A Study of Rock Coast Erosion on the Atlantic Coast of Ireland

Submitted for the degree of Doctor of Philosophy

2019

Niamh D. Cullen

Trinity College Dublin
Coláiste na Tríonóide, Baile Átha Cliath
The University of Dublin

Declaration

I declare that this thesis has not been submitted as an exercise for a degree at this or any other university and it is entirely my own work.

I agree to deposit this thesis in the University's open access institutional repository or allow the library to do so on my behalf, subject to Irish Copyright Legislation and Trinity College Library conditions of use and acknowledgement.

Niamh D. Cullen

A Study of Rock Coast Erosion on the Atlantic Coast of Ireland

Niamh D. Cullen

Abstract

The rate and processes of erosion on a coastal rock cliff on the west coast of Ireland are investigated. The links between site characteristics (wave climate, nearshore bathymetry, foreshore characteristics (platform roughness, elevation) and cliff and platform erosion are explored. This integrated approach gives new insights into controls on the spatial distribution of erosion on rock coasts.

This is achieved through high resolution measurements of cliff and platform topography using Terrestrial Laser Scanning and Structure from Motion Photogrammetry respectively, empirical assessment of rock mass characteristics (discontinuities), wave modelling, and characterization of the nearshore and foreshore environment using Digital Elevation Models and topographic surveys.

This work provides the following new insights: (1) The current rate of erosion at the study site is two orders of magnitude greater than previously estimated for Ireland's rock coastline. (2) Rock discontinuities exert a strong control on the rate and spatial distribution of erosion at the study site. (3) Nearshore bathymetry and foreshore characteristics have a strong influence of the alongshore distribution of wave energy available for erosion of the cliff. (4) Abrasion by clast transport is a geomorphologically significant process of platform erosion at the study site. (5) The type of abrasion feature observed is determined by the clast transport mode, which itself is strongly influenced by platform roughness. (6) Important links exist between cliff and platform erosion. (7) Cross scalar measurements of platform erosion using Structure from

Motion Photogrammetry presents a significant opportunity for bridging the gap between micro and meso scale studies of platform erosion.

The implication of this study is that integrated studies of rock mass, foreshore and nearshore characteristics are required to effectively explain the spatial variability of erosion on rock coasts.

Acknowledgements

The past four years have been one enjoyable challenge after another. One thing that has constantly surprised and delighted me throughout the four years of my PhD is the willingness of family, friends, colleagues and strangers to give up their time and to help me achieve my goal. I have found the kindness of people and their readiness to help in any way they can a constant and ongoing source of motivation. I would like to sincerely thank everyone who has helped and inspired me on this journey:

Firstly, I have been truly lucky to have been mentored and supervised by Dr. Mary Bourke. I will be forever grateful for her constant belief in my abilities and her incredible support and advice throughout. Thank you for always seeing in me what I sometimes I could not. It has been a privilege.

Thank you to all of the staff in the Department of Geography for all of the support given throughout my time at Trinity College Dublin (TCD). Thank you to Dr. Elaine Treacy (TCD) and Terrence Dunne (TCD) for all things equipment related, training, maintenance, laboratory access, purchasing, bookings and everything else.

My thanks to Dr. Larissa Naylor (University of Glasgow) for ideas and inspiration. To Prof. Heather Viles and the staff at the Rock Breakdown Laboratory at Oxford University for my first introduction to rock breakdown equipment. To Dr Carlos Loureiro (Ulster University, Colraine) for SWAN training and support. To Dr. Arian Riquelme for guidance using DSE software and for providing an executable compatible with MatLab educational edition. To Dr. Partick Belmont for giving up his time and equipment to collect the bathymetry data.

I am grateful to the following organisations for providing funding for the research included in this thesis: Trinity Postgraduate Research Studentship, The Department of Geography Trinity

College, the Earth and Planetary Processes Research Group (TCD), the Geological Survey of Ireland, the British Society for Geomorphology, the Estuarine and Coastal Science Association, the Irish Geomorphology Group (IGGy) and the Marine Institute.

For fun times friendship: My fellow postgraduate students past and present. To Dr. Kevin Lougheed who was always on hand to answer GIS questions and available for a pint. To fellow PhD student, office buddy and sounding board Jane Maher. To research group pal and fellow PhD student Ankit Verma who I was lucky to collaborate with and whose PhD research gave me opportunity to travel to Arizona and the Natural History Museum in London. Thank you. To fellow postgraduate representative and conference buddy Ciara Flemming (University College Dublin).

To my friends Sarah, Seona, Cliona, Emma and Andrea who never complained about my complaining and were always there to make me laugh. You have helped more than you will ever know.

For help in the field: To the many people who gave up their time to come on fieldwork with me despite the sometimes less than ideal conditions; Kevin, Sahar, Mary, Larissa, Archie, Ciaran, Floriano, Caoimhe and my mam. To Noreen, my west coast pal whom I met on my first visit to my field site. Charger of batteries, maker of tea, and with Danny, retriever of giant boulders for my experiments. Who always had a warm scone and joke ready after a long, hard day in the field. To Noreen's cousin Joseph, who allowed me to install a fence and a weather station in the middle of his field, and who protected it from nosy cows when I wasn't there. To John Givens for allowing me the use of his house in Quilty for fieldwork and to Susan and Iseult Stokes who welcomed me and the wet, smelly dog with open arms whenever the Quilty house was unavailable.

Family: To my brothers, Niall and Darragh who live far away but will always be close.

My greatest thanks go to my partner, Karl, and my mam, Anne. Karl, who for the past 15 years has supported me in everything that I have ever wanted to do and whose patience, understanding and sense of humour have pulled me through. You would have been out by now. My mam, I have no words that would do justice to what you have done for me. The kindest, bravest, most wonderful woman alive. Thank you.

Finally, to my dad, Derek, who sadly died 20 years ago this year. It was from him I got my love of all things outdoors and science and his graduation picture in the red and gold of Trinity College is a constant source of inspiration. This thesis is dedicated to him.

For Dad

Table of Contents

Chapter 1: General Introduction

1. Introduction to rock coasts

1.1 Rock coasts

Rock coasts are defined by Sunamura (1992) as being composed of consolidated material (rock) of varying strength. They are predominantly erosional coastal landforms (Naylor et al. 2010). This distinguishes them from soft coasts such as beaches and dunes which are primarily depositional in nature. An estimated 80% of global coastlines are classified as 'rocky' (Emery and Kuhn, 1982). Cliffs are characteristic features of rocky coasts and are comprised of materials which vary in strength along a continuum from soft cohesive clay and consolidated gravel to hard rock such as granite (Stephenson et al., 2013). The term coastal cliff is defined here as a steep slope > 40˚, often vertical and sometimes overhanging, located where the sea meets the elevated land (Goudie, 2004, Hampton et al., 2004).

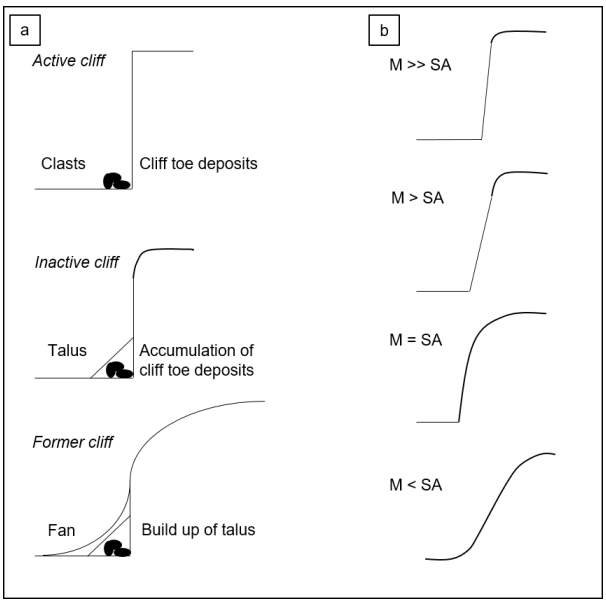

Figure 1. Illustration showing (a) the geological evolution of idealised sea cliff profiles and (b) the relationship between cliff profile and the relative efficacy of marine (M) and sub aerial (SA) processes. Adapted from Emery and Kuhn (1982) and Stephenson (2013).

Another prominent feature of rock coasts are shore platforms, although globally, the percentage of coast having shore platforms is unknown (Naylor et al. 2010). Shore platforms commonly front sea cliffs however they may also be backed by beaches or sand dunes. They have been broadly classified as Type A or Type B by Sunamura (1992). Type A platforms are gently sloping surfaces, commonly 1-5˚ (Stephenson and Kirk, 2005) (Figure 2). Type B platforms consist of near horizontal surfaces which often, but not always, terminate at their seaward edge in a sub tidal cliff (Figure 2). Whether platforms are of Type A or Type B is considered to be a function of tidal range with Type A platforms dominating in macrotidal areas (Trenhaile, 1987). Although Sunamura's classification is broadly cited, this simplistic designation belies the wide range of platform morphologies that can be observed (Figure 3). The platform studied as part of this thesis terminates at its seaward edge in a subtidal cliff, hence is designated as Type B. However, the slope of the platform is similar to that of Type B platforms (1-5 ˚). The platform morphology is also highly variable (chapter 4) ranging from areas with very low roughness (topographic variability < 0.1 m) to areas characterized by high macro roughness (topographic variability > 1 m).

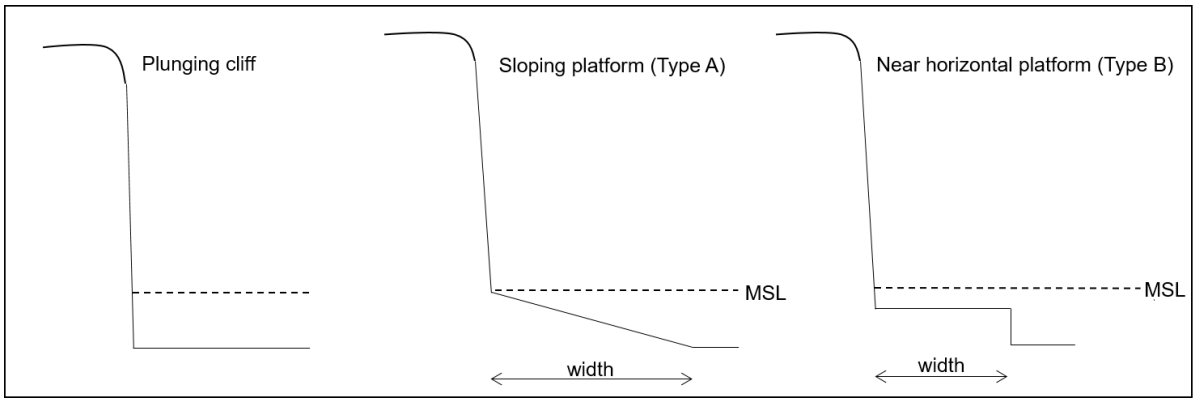

Figure 2. Illustration of platform types showing relation to Mean Sea Level (MSL) adapted from Sunamura (1992)

Figure 3. (a-f) Images of shore platforms demonstrating the range of platform morphologies observed along the Irish coastline. (a) Dissected limestone platform with low topographic variability at Fanore, Co. Clare. (b) Stepped platform with irregular topography due to dissolution of limestone at Doolin, Co. Clare. (c) Sandstone platform dissected by channel at Breaffa South, Co. Clare. (d) Washboard morphology with beds dipping seaward at Spanish Point. (e) Washboard morphology with beds dipping landward at Quilty, Co. Clare and (f) washboard type morphology with near vertical bedding at Myrtleville, Co. Cork. (g) The location of platforms in a-f from north to south respectively.

Photos by N.D. Cullen. and M.C. Bourke.

1.2 Ireland's rock coast

Although Emery and Kuhns (1982) 80% figure for the percentage of the world's coastlines dominated by rocky coastline is widely cited, this has not been validated (Naylor et al. 2010). Of Ireland's ~5,400 km long coastline (McCartney et al., 2010), approximately 56 % is rock dominated (EUrosion, 2004) with approximately 1,288 km of this classified as cliff, and a further 170 km of composite cliffs comprised of both hard and soft materials (Barron et al., 2011) (Figure 4).

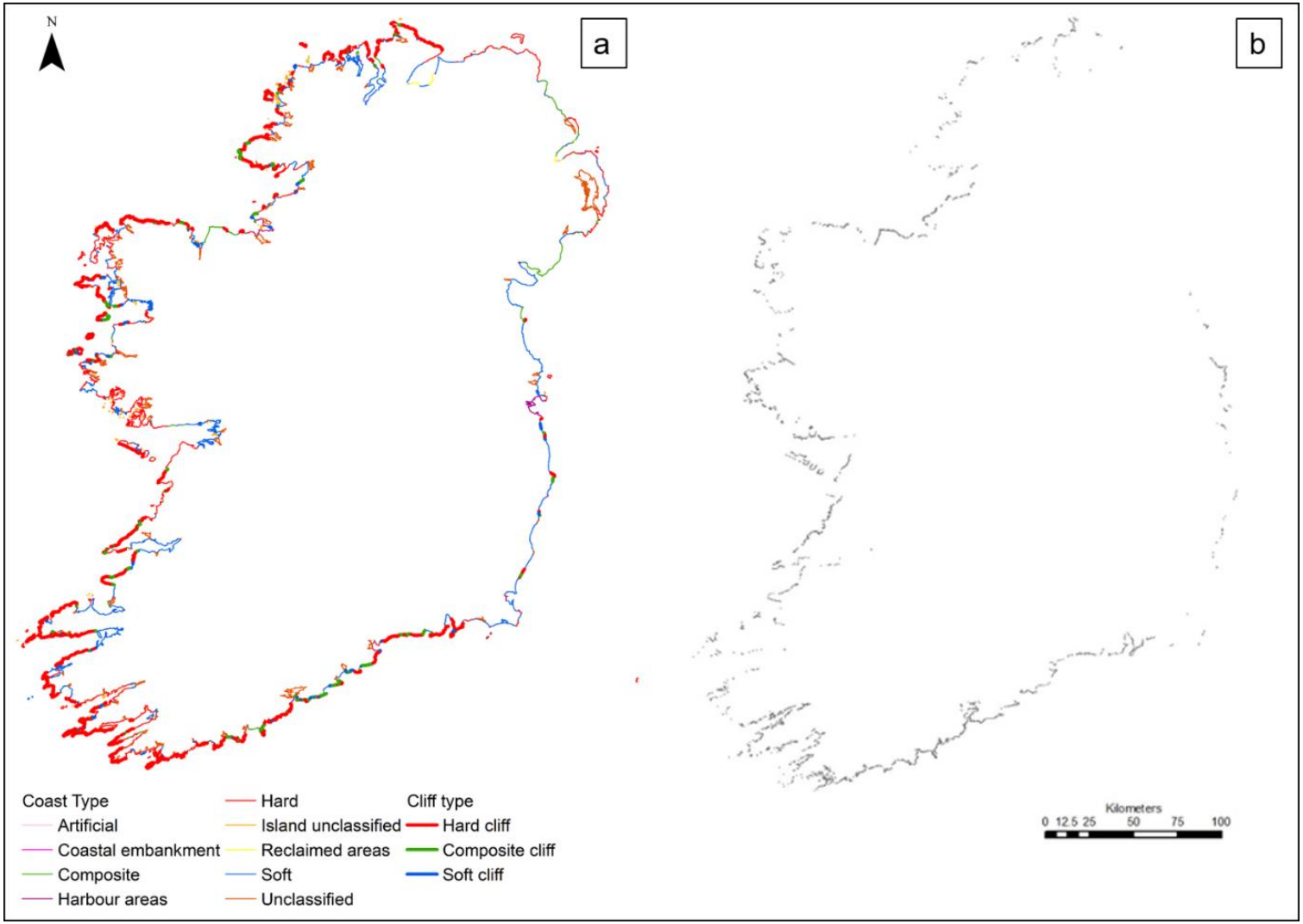

Figure 4. a) Ireland's coastline classified by coast type (Adapted from EUrosion, 2004 and Barron et al. 2011) and b) the distribution of shore platforms (Bourke et al., 2016. Reproduced with permission).

1.3 Erosion of rock coasts

Prior to the 21st century hard rock coasts had received relatively little attention compared to soft coasts (Naylor et al., 2010). Rock breakdown (weathering + erosion) processes that contribute to erosion of rock coasts encompass a wide range of land-sea interactions. These processes include sub-aerial e.g. seepage, precipitation and weathering (chemical, physical and biological) and marine processes, e.g. hydraulic action and wave quarrying, which ultimately result in a reduction of rock strength, instability, failure and removal of material at a range of spatial and temporal scales. Erosion rates on rocky coasts are less well defined than those of soft coasts owing to the longer time scales involved (McKenna et al., 1992). However, the growing number of rock coast researchers, as evidenced by the increase in the number of publications (see chapter 4), has produced increasingly better data on rates of change on rock coasts. For example, microscale measurements of shore platform erosion now extend to decades (e.g. Stephenson et al., 2010, Stephenson and Kirk, 1996), while the application of laser scanning for monitoring of coastal cliffs has provided unprecedented temporal and spatial resolution of cliff erosion (e.g. Rosser et al., 2005, Rosser et al., 2007, Lim et al., 2010, Williams et al., 2018). These data have increased spatial and temporal resolution of erosion data over progressively longer periods. However, understanding of long-term development of rock coasts remains a challenge (Naylor et al. 2010).

Globally, the mean annual rate of erosion of rock coasts varies between 1 cm yr^{-1} for hard rock lithologies up to 0.1 m yr^{-1} for softer rock (Prémaillon et al., 2017). Retreat rates for rock cliffs in Ireland are relatively unknown (McKenna et al., 1992). However, the presence of shorelines raised during the Quaternary (> 200,000 years old) suggest that rates of retreat may be as low as 0.01m per century (Devoy, 2008). On shore platforms, global annual mean rates of downwearing, measured using the micro erosion meter (chapter 5), are 0.397, 1.282 and 0.625 mm yr^{-1} for igneous, sedimentary and metamorphic rocks respectively (Dasgupta, 2010 and references therin).

While rock coast research has increased significantly in recent decades, some areas have received less attention. For example, although the influence of rock control in coastal environments has received considerable theoretical consideration (e.g. Edwards, 1941, Johnson, 1919, Yatsu, 1966, 1988, Sunamura, 1992, Suzuki, 2002), only quite recently has the influence of structural and geomorphological controls on rock coast erosion been demonstrated (e.g. Cruslock et al., 2010, Naylor and Stephenson, 2010, Stephenson and Naylor, 2011a, 2011b, Naylor, 2016), with Naylor and Stephenson (2010) providing the first robust empirical evidence of the strong role that discontinuities (joints, fractures bedding planes etc) play in mediating platform erosion. A recent study by Prémaillon et al. (2017) examining global rates of cliff retreat concluded that lithology had the strongest influence on rates of erosion. However, the authors highlighted the lack of critical data on parameters such as cliff height and rock mass characteristics, including weathering and discontinuities, which are useful for understanding cliff evolution dynamics. Researchers have attempted to explain variations in coastal cliff erosion in relation to environmental factors (e.g. Rosser et al., 2013, Prémaillon et al., 2017) however few, if any, studies have applied Naylor and Stephenson's (2010) approach to coastal cliffs in order to determine the influence of discontinuities in mediating cliff erosion.

Another limiting approach of rock coast research has been a tendency for research to focus on either the shore platform or the cliff (Naylor et al., 2010), despite the two components being inextricably linked. For example, only in recent decades have researchers started to investigate the transformation of wave energy across the platform (Farrell et al., 2009, Ogawa et al., 2011, 2012, 2013), the influence of platform morphology (Marshall and Stephenson, 2011, Poate et al., 2018) and subsequent delivery to the cliff toe (Van Jones et al., 2018).

Rock coasts research has also been inclined towards investigation of landforms in microscale process-based studies and macro or evolutionary scale inquiries (Naylor et al. 2010), with a lesser focus on meso scale (cm – 10^1 m) processes (Cullen and Bourke, 2018). A key limitation of this tendency is the gap that remains between microscale processes and landforms and

our understanding of, and relationships to, long term macro-scale landform evolution. Addressing this relative lack of information on meso scale processes can only assist with more meaningful upscaling of field and laboratory data for informing theoretical and numerical models of long term landform evolution.

Despite the dominance of rocky coastlines, growing recognition of their importance and the increasing number of rock coasts geomorphologists whose research has significantly advanced our understanding, research into the rates and processes of erosion on rocky shorelines still lags far behind that of soft coasts. This is particularly the case for Ireland where very limited research has been carried out and little is known about the rates and processes of erosion on Ireland's rock dominated coastline. Even less is known about how Irelands rock coasts will respond to predicted changes in climate such as increasing sea levels, increased storm intensity and changes in precipitation and temperature regimes.

1.4 Aims of this study

This thesis is aimed at addressing some of the gaps in rock coast research outlined above. The main aims of this research are as follows:

1. To measure the current rate of erosion on a coastal cliff on the west coast of Ireland and investigate the role of discontinuities in the spatial distribution of erosion.

2. To investigate the role of wave energy in the rate and spatial distribution of cliff erosion.

3. To quantify the efficacy of mesoscale erosion on platform erosion and explore the importance of links between cliff and platform erosion.

4. To assess and compare methods for measuring erosion on shore platforms and develop a means for cross scalar investigations.

1.4 Structure of thesis

The core chapters in this thesis (Chapters 2-6) are prepared in manuscript format for submission to academic journals. Relevant citations for published manuscripts are provided. The abstract and discussion for each of the core chapters are self-contained. Author contributions are explicitly stated at the beginning of each chapter. A brief description of the core chapters (2-5) is given below. A synthesis of the core chapter findings and conclusions are given in Chapter 6.

1.4.1 Chapter 2

The role of discontinuities in mediating the spatial distribution of coastal cliff erosion

Chapter 2 is focused on addressing the first aim of this thesis. The rate of erosion on a coastal cliff is measured using repeat Terrestrial Laser Scanning (TLS) surveys to measure the volume and spatial distribution of cliff erosion. The characteristics of discontinuity sets (spacing, density orientation etc.) are determined through semi-automated discontinuity set extraction from the TLS point clouds. The relationships between discontinuity set characteristics, the rockfall inventory and the spatial distribution of erosion are evaluated. The data in this chapter represent the first high resolution measurements of coastal cliff erosion in an Irish context in addition to the first empirical assessment of the role of discontinuities in mediating the spatial distribution of erosion of a coastal cliff.

1.4.2 Chapter 3

Variability in alongshore distribution of wave energy on an embayed coastline and its relationship to the spatial distribution of erosion

This chapter uses numerical modelling to investigate the variability in wave energy distribution at the study site using a range of offshore wave conditions. The focus is to determine the range in alongshore significant wave height. This is then used as a proxy for wave energy and is compared to the spatial distribution and rate of cliff erosion (Aim 2). The data highlight the importance of specific and local-scale nearshore characteristics in the generation of alongshore variability of wave energy and the influence of foreshore characteristics in the delivery of wave energy to the cliff. The data provide further evidence for the strong influence of discontinuities in mediating the spatial distribution of coastal cliff erosion.

1.4.4 Chapter 4

Clast abrasion of a rock shore platform on the west coast of Ireland

The focus of chapter 4 is quantification of meso scale erosion on a shore platform via abrasion by clast transport (Aim 3). This chapter explores the influence of platform morphometry on clast transport dynamics and abrasion of the platform. It highlights the links between cliff erosion and sediment supply and platform erosion. These data represent the first empirical measurement of platform erosion via this process and provides new information on the important influence of platform morphology on clast transport dynamics.

1.4.5 Chapter 5

A comparison of Structure from Motion Photogrammetry and the Traversing Micro Erosion Meter for measuring erosion on shore platforms.

Chapter 5 compares the longstanding method of measuring erosion on shore platforms to a newer method of geomorphic change detection using Structure from Motion (SfM) Photogrammetry (Aim 4). This chapter provides a detailed comparison of the Micro Erosion

Meter (and its successor the Traversing Micro Erosion Meter) to SfM Photogrammetry. This chapter also tests a new method for cross scalar measurement of erosion on shore platforms using a Structure from Motion Photogrammetry based approach. The chapter details the development and manufacture of a coordinate reference system which allows the generation of high resolution (sub-mm) DEMs for geomorphic change detection.

1.4.6 Chapter 6

Synthesis

Chapter 6 contains a synthesis of chapters 2, 3, 4 and 5 and summarizes the results and implications of the findings in the broader context of rock coast research. The synthesis also contains recommendations for future work.

References

BARRON, S., DELANEY, A., PERRIN, P., MARTIN, J., O'NEILL, F., DE JONGH, A., O'NEILL, L., PERRIN, P., BARRON, S. & ROCHE, J. 2011. *National survey and assessment of the conservation status of Irish sea cliffs*, National Parks and Wildlife Service.

BOURKE, M. C., NAYLOR, L. A., FLOOD, R., NASH, C., CULLEN, N. D., GOFFO, F. & MIGGE, K. 2016. Investigation of Ireland's Shore Platforms: Location, type and coastal protection. . *Geological Survey of Ireland Shortcall Reports.* Dublin, Ireland: Geological Survey of Ireland.

CRUSLOCK, E. M., NAYLOR, L. A., FOOTE, Y. L. & SWANTESSON, J. O. 2010. Geomorphologic equifinality: A comparison between shore platforms in Höga Kusten and Fårö, Sweden and the Vale of Glamorgan, South Wales, UK. *Geomorphology,* 114, 78-88.

DASGUPTA, R. 2010. Whither shore platforms? *Progress in Physical Geography*.

DEVOY, R. J. 2008. Coastal vulnerability and the implications of sea-level rise for Ireland. *Journal of Coastal research*, 325-341.

EDWARDS, A. B. 1941. Storm-wave platforms. *Jour. Geomorphology,* 4, 223-236.

EUROSION 2004. Living with coastal erosion in Europe: Sediment and Space for Sustainability. Part 2 Maps and Statistics. . *Commissioned by the Directorate General Environement European Commission* Europe.

FARRELL, E. J., GRANJA, H., CAPPIETTI, L., ELLIS, J. T., LI, B. & SHERMAN, D. J. 2009. Wave transformation across a rock platform, Belinho, Portugal. *Journal of Coastal Research*, 44-48.

GOUDIE, A. 2004. *Encyclopedia of geomorphology*, Psychology Press.

HAMPTON, M. A., GRIGGS, G. B., EDIL, T. B., GUY, D. E., KELLEY, J. T., KOMAR, P. D., MICKELSON, D. M. & SHIPMAN, H. M. 2004. Processes that govern the formation and evolution of coastal cliffs. *US Geological Survey professional paper,* 1693, 7-38.

JOHNSON, D. W. 1919. *Shore processes and shoreline development*, John Wiley & Sons, Incorporated.

JONES, E. V., ROSSER, N. & BRAIN, M. 2018. Alongshore variability in wave energy transfer to coastal cliffs. *Geomorphology*.

LIM, M., ROSSER, N. J., ALLISON, R. J. & PETLEY, D. N. 2010. Erosional processes in the hard rock coastal cliffs at Staithes, North Yorkshire. *Geomorphology,* 114, 12-21.

MARSHALL, R. J. & STEPHENSON, W. J. 2011. The morphodynamics of shore platforms in a micro-tidal setting: Interactions between waves and morphology. *Marine Geology,* 288, 18-31.

MCCARTNEY, M., ABERNETHY, G. & GAULT, L. 2010. The Divider Dimensions of the Irish Coast. *Irish Geography,* 43, 277-284.

MCKENNA, J., CARTER, R. & BARTLETT, D. 1992. Coast Erosion in Northeast Ireland:-Part II Cliffs and Shore Platforms. *Irish Geography,* 25, 111-128.

NAYLOR, L. 2016. Geomorphological control on boulder transport and coastal erosion before, during and after an extreme extra-tropical cyclone. *Earth Surface Processes and Landforms*.

NAYLOR, L. & STEPHENSON, W. 2010. On the role of discontinuities in mediating shore platform erosion. *Geomorphology,* 114, 89-100.

NAYLOR, L., STEPHENSON, W. & TRENHAILE, A. 2010. Rock coast geomorphology: recent advances and future research directions. *Geomorphology,* 114, 3-11.

OGAWA, H. 2013. Observation of wave transformation on a sloping type B shore platform under wind-wave and swell conditions. *Geo-Marine Letters,* 33, 1-11.

OGAWA, H., DICKSON, M. & KENCH, P. 2011. Wave transformation on a sub-horizontal shore platform, Tatapouri, North Island, New Zealand. *Continental Shelf Research,* 31, 1409-1419.

OGAWA, H., KENCH, P. & DICKSON, M. 2012. Field Measurements of Wave Characteristics on a Near-Horizontal Shore Platform, Mahia Peninsula, North Island, New Zealand. *Geographical Research,* 50, 179-192.

POATE, T., MASSELINK, G., AUSTIN, M. J., DICKSON, M. & MCCALL, R. 2018. The role of bed roughness in wave transformation across sloping rock shore platforms. *Journal of Geophysical Research: Earth Surface,* 123, 97-123.

PRÉMAILLON, M., REGARD, V. & DEWEZ, T. How to explain variations in sea cliff erosion rate? EGU General Assembly Conference Abstracts, 2017. 8012.

ROSSER, N., LIM, M., PETLEY, D., DUNNING, S. & ALLISON, R. 2007. Patterns of precursory rockfall prior to slope failure. *Journal of geophysical research: earth surface,* 112.

ROSSER, N. J., BRAIN, M. J., PETLEY, D. N., LIM, M. & NORMAN, E. C. 2013. Coastline retreat via progressive failure of rocky coastal cliffs. *Geology,* 41, 939-942.

ROSSER, N. J., PETLEY, D. N., LIM, M., DUNNING, S. & ALLISON, R. J. 2005. Terrestrial laser scanning for monitoring the process of hard rock coastal cliff erosion. *Quarterly Journal of Engineering Geology and Hydrogeology,* 38, 363-375.

STEPHENSON, W., KIRK, R., HEMMINGSEN, S. & HEMMINGSEN, M. 2010. Decadal scale micro erosion rates on shore platforms. *Geomorphology,* 114, 22-29.

STEPHENSON, W. & NAYLOR, L. 2011a. Geological controls on boulder production in a rock coast setting: insights from South Wales, UK. *Marine Geology,* 283, 12-24.

STEPHENSON, W. & NAYLOR, L. 2011b. Within site geological contingency and its effect on rock coast erosion. *Journal of Coastal Research,* 61, 831-835.

STEPHENSON, W. J., DICKSON, M. E. & TRENHAILE, A. S. 2013. Rock Coasts. *In:* SHRODER, J. F. (ed.) *Treatise on Geomorphology.* 1st ed.: Elsevier.

STEPHENSON, W. J. & KIRK, R. M. 1996. Measuring erosion rates using the micro-erosion meter: 20 years of data from shore platforms, Kaikoura Peninsula, South Island, New Zealand. *Marine Geology,* 131, 209-218.

SUNAMURA, T. 1992. *Geomorphology of rocky coasts*, John Wiley & Son Ltd.

SUZUKI, T. 2002. Rock control in geomorphological processes: research history in Japan and perspective. *Transactions, Japanese Geomorphological Union,* 23, 161-199.

TRENHAILE, A. S. 1987. *The geomorphology of rock coasts*, Oxford University Press, USA.

WILLIAMS, J. G., ROSSER, N. J., HARDY, R. J., BRAIN, M. J. & AFANA, A. A. 2018. Optimising 4-D surface change detection: an approach for capturing rockfall magnitude–frequency. *Earth surface dynamics.,* 6, 101-119.

YATSU, E. 1966. *Rock control in geomorphology*, Sozosha.

YATSU, E. 1988. *The nature of weathering: an introduction*, Sozosha Tokyo.

Chapter 2: The role of discontinuities in mediating the spatial distribution of coastal cliff erosion

Abstract

A recent review of global erosion rates for rock coasts has highlighted the lack of critical data on parameters which drive the evolution of rock coasts such as cliff height, weathering and discontinuities. The role of discontinuities in reducing the resisting force of coastal cliffs is widely acknowledged. However, our understanding of the way in which discontinuities influence the rate of coastal cliff erosion remains poor, with a tendency for coastal researchers to focus on lithology and mechanical strength. Here we present the results of a study utilising advances in data capture with terrestrial laser scanning (TLS), and recently developed software Discontinuity Set Extractor (DSE) for semi-automated extraction of discontinuity set characteristics from TLS point clouds. We test this approach on a coastal cliff on the west coast of Ireland to determine whether analysis of discontinuity set characteristics can help to explain the differential rates of erosion by rockfall on coastal cliffs.

Our results indicate that DSE is a useful tool which can characterize discontinuity sets on near vertical cliffs with relative ease. The approach largely removes the sampling bias and limitations associated with traditional approaches. We find that discontinuity characteristics exert a strong control on the spatial distribution of rockfall cliff erosion at the study site. Our data indicate that spacing density plays an important role in mediating the size of rockfall events, with smaller rockfalls associated with higher discontinuity densities, and larger rockfalls associated with lower spacing density. Our results also imply that larger, less frequent rockfall events have a greater influence on the rate of erosion than smaller, higher frequency rockfalls. This suggests the significant role that

discontinuities play in mediating the spatial distribution of erosion. Further, it demonstrates the need to incorporate discontinuity set characteristics to explain variations in erosion rates of coastal cliffs.

Key words

Rock coast cliff, erosion, discontinuities, point cloud, rockfall.

Author contributions

N.D.C wrote the body of the manuscript with contributions from M.C.B. N.D.C carried out the analysis. M.C.B edited the final manuscript.

2.1 Introduction

The rock masses which comprise coastal cliffs and shore platforms are comprised of discontinuous, inhomogeneous, anisotropic and non-linearly elastic (DIANE) materials (Hudson and Harrison, 1997). Sunamura (1995) identified two dominant forces acting on rock coasts; the attacking force of waves (F_W) and the resisting force of the rock (F_R), with erosion occurring when the F_W exceeds F_R. F_R is determined by lithology, mechanical strength and discontinuity characteristics such as orientation, spacing, and density (Sunamura, 1995). Despite acknowledgement of the influence of discontinuities on coastal cliff erosion (Rosser et al., 2007, Lim et al., 2010, Rosser et al., 2013), coastal geomorphologists have tended to focus on lithology and mechanical strength (Naylor and Stephenson, 2010). In a study which demonstrated the importance of discontinuities in mediating shore platform erosion Naylor and Stephenson (2010) called for greater inclusion of empirical measurements of rock mass properties, e.g. discontinuities, in order to improve geomorphological understanding (Yatsu, 1966).

Over the last decade, the application of techniques such as Light Detection and Ranging (LiDAR) and Structure from Motion (SfM) Photogrammetry in studies of coastal rock cliff erosion have allowed researchers to capture erosion of the entire cliff face at unprecedented spatial and temporal resolution. This has revealed the complex erosion patterns which challenge the traditional model of rock cliff erosion. This was proposed by Trenhaile (1987) and Sunamura (1992) whereby the cliff retreats through undercutting at the cliff toe by waves and subsequent failure of the overhanging rock through cantilever collapse. High spatial and temporal resolution studies (e.g. Rosser et al., 2007, Lim et al., 2010, Rosser et al., 2013) have verified the significant influence that rock strength and structure play in controlling rock fall characteristics at coasts. The role of discontinuities in mediating shore platform erosion has also been demonstrated (Cruslock et al., 2010, Stephenson and Naylor, 2011b). While the influence of waves and other variables (e.g.

climate, weathering, rock saturation etc.) are important, the role of structural controls on the spatial variability of coastal rock cliff erosion merits greater attention. Indeed, a recent study highlighted the lack of critical data such as cliff height and rock mass characteristics, including weathering and discontinuities, for understanding cliff evolution dynamics (Prémaillon et al., 2018).

Coastal cliffs and their contiguous platforms can be difficult to access and researchers have previously been restricted to collecting discontinuity data in the field using scan lines and cell mapping (Priest and Hudson, 1981). These approaches have both advantages and limitations (Slob et al., 2005). Scan line surveys provide detailed information on discontinuity characteristics while cell mapping provides only average information on discontinuity sets. In addition, cell mapping is less time consuming and can be conducted in locations where direct access is not possible (Kemeny and Post, 2003). For both methods however, sampling difficulties and human bias can introduce large errors in data sets (Kemeny and Post, 2003).

Advances in data collection using Terrestrial Laser Scanning (TLS) techniques and Unmanned Aerial Vehicles (UAVs) allow relatively easy collection of data from which high density (mm – cm resolution) point clouds are obtained. These techniques have been widely adopted in geomorphological research for generating high resolution Digital Elevation Models (DEMs) and detection of geomorphic change across a wide range of scales and terrains (Brasington et al., 2000, Balaguer-Puig et al., 2017, Verma and Bourke, 2018, Cullen and Bourke, 2018). Advances in software programming permit semi-automated analysis of rock mass characteristics such as the number, spacing, orientation and persistence of discontinuities in quarry and other inland cliff exposures (e.g. Slob et al., 2002, 2005, Riquelme et al., 2014, 2015, 2016, 2018, Buyer and Schubert, 2016). The approach provides a more robust characterisation of rock mass discontinuities than using traditional methods (Riquelme et al., 2014, 2015, Kemeny and Post, 2003). In addition, the

approach would reduce or remove sampling bias, human error and accessibility issues. This approach has not yet been applied to coastal cliff sections. Here we apply the approach to a coastal cliff on the west coast of Ireland. We determine the spatial distribution of rock fall erosion. Finally, we assess the usefulness of semi-automated extraction of discontinuity sets from point clouds for spatial analysis of erosion patterns.

2.1.1 The study site

The site is a coastal cliff at Ballard Bay on the Loop Head peninsula, Co. Clare on the west coast of Ireland (Figure 1). The study site is comprised of a cliff with a maximum height of approximately 50 m (above 0 m OD Malin Head) fronted by a gently sloping (2-5˚) type B shore platform with a maximum width of approximately 200 m. The site lithology is comprised of two Upper Carboniferous (Namurian) sedimentary sequences, the Tullig (exposed on the platform) and Kilkee (exposed in the cliff) cyclothems, which form part of the larger Central Clare Group of sedimentary rocks (Hodson and Lewarne, 1961, Rider, 1974, Pulham, 1989, Collinson et al., 1991). High subsidence and sedimentation rates during the early Namurian produced dewatering structures such as sand volcanoes and slumped horizons overlain by siltstones and sandstones of continental slope and shelf origin (Wignall and Best, 2000). As the basin shallowed a deltaic depositional environment, analogous to that of the modern-day Mississippi Delta, dominated (Wignall and Best, 2000) and many of these features are observed at the study site. As such, the site was identified as being largely representative of the coastal cliff type for this area on the west coast of Ireland with the Kilkee Cyclothem, of which the cliff is comprised, described as a broadly lateral equivalent of what is observed in the lower part of the Cliffs of Moher (Parkes et al., 2005). The site was also selected based on the presence of a shore platform and accessibility of both the cliff and the platform for deployment of equipment. Furthermore, within site alongshore variability of cliff and platform characteristics (e.g. lithology, structure etc.) represented a unique opportunity to observe the role of alongshore

variability of cliff and platform characteristics on cliff and platform dynamics while keeping wave climate consistent.

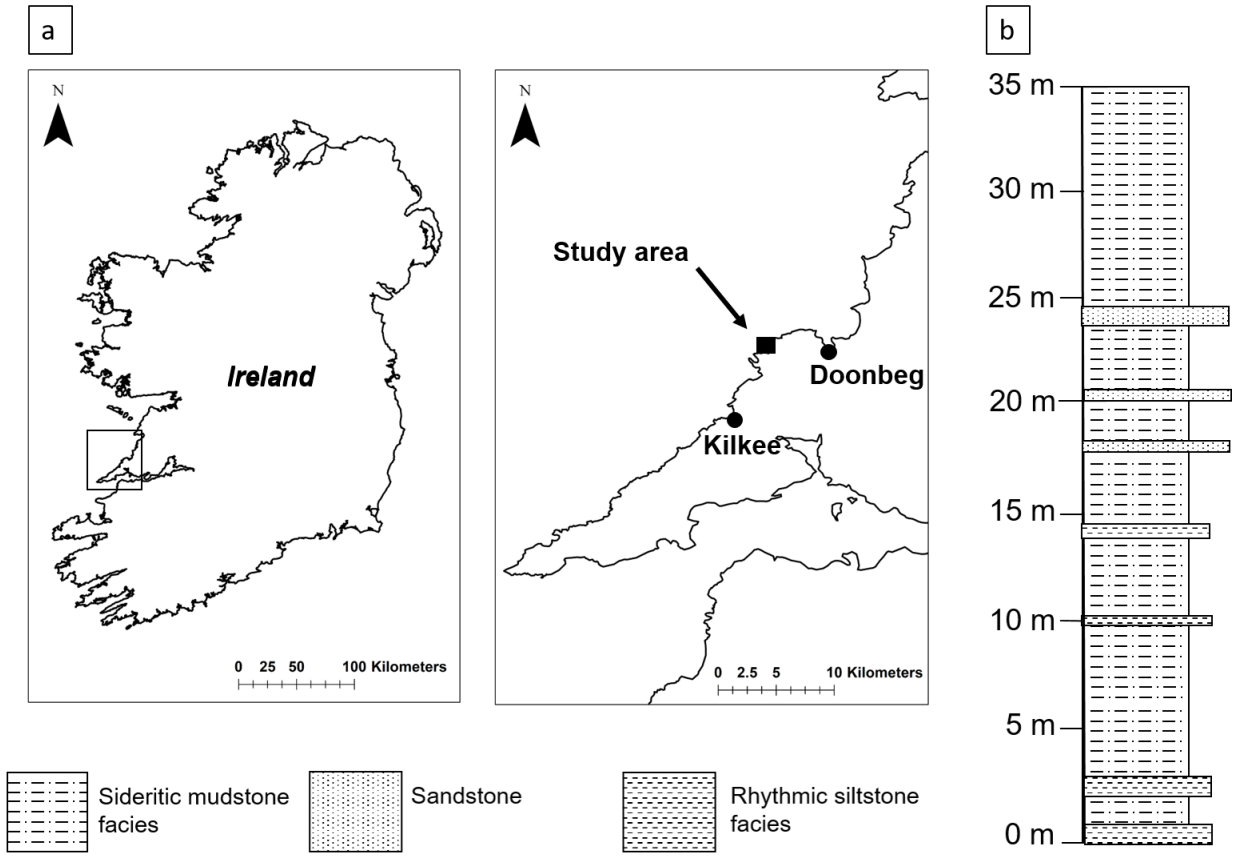

Figure 1. (a) Maps showing the location of the study site at Ballard Bay, Co Clare on the west coast of Ireland and (b) A typical geological section of the cliff exposure. Height shown is from the base of the cliff which varies between 5 and 9 m above 0 m OD Malin Head.

Figure 2. (a) Plan view of the study site at Ballard Bay, (b) view of the cliff and platform looking from north to south, (c) aerial view looking south to north and (d) view from the sea looking ENE.

The cliff structure is highly fractured i.e. characterised by numerous discontinuities. These discontinuities include bedding planes, joints and fractures in the cliff and occur at a range of scales from large scale (10^{-1}– 10^{2} m) (Figure 3) to very small scale (10^{-2} m) discontinuities. Discontinuities vary in orientation, spacing and density along the cliff.

The predominant style of mass wasting from the cliff is rockfall. In general, rockfalls occur along failure planes which are associated with discontinuity surfaces (Figures 3 and 4). The scale of rockfalls varies from smaller (10^{-1} m) to much larger magnitude events (10^{2} m) as evidenced by the presence of rockfall scars and cliff toe deposits of varying scales (Figure 3 and 4). Seepage of groundwater frequently occurs in association with discontinuities (Figure 4). Evidence for wave action at the base of the cliff (i.e. at the cliff toe) is demonstrated by the presence of notching (Figure 3). Undercutting at the cliff toe is generally restricted to the northern half of the bay and is greatest at the northern most end.

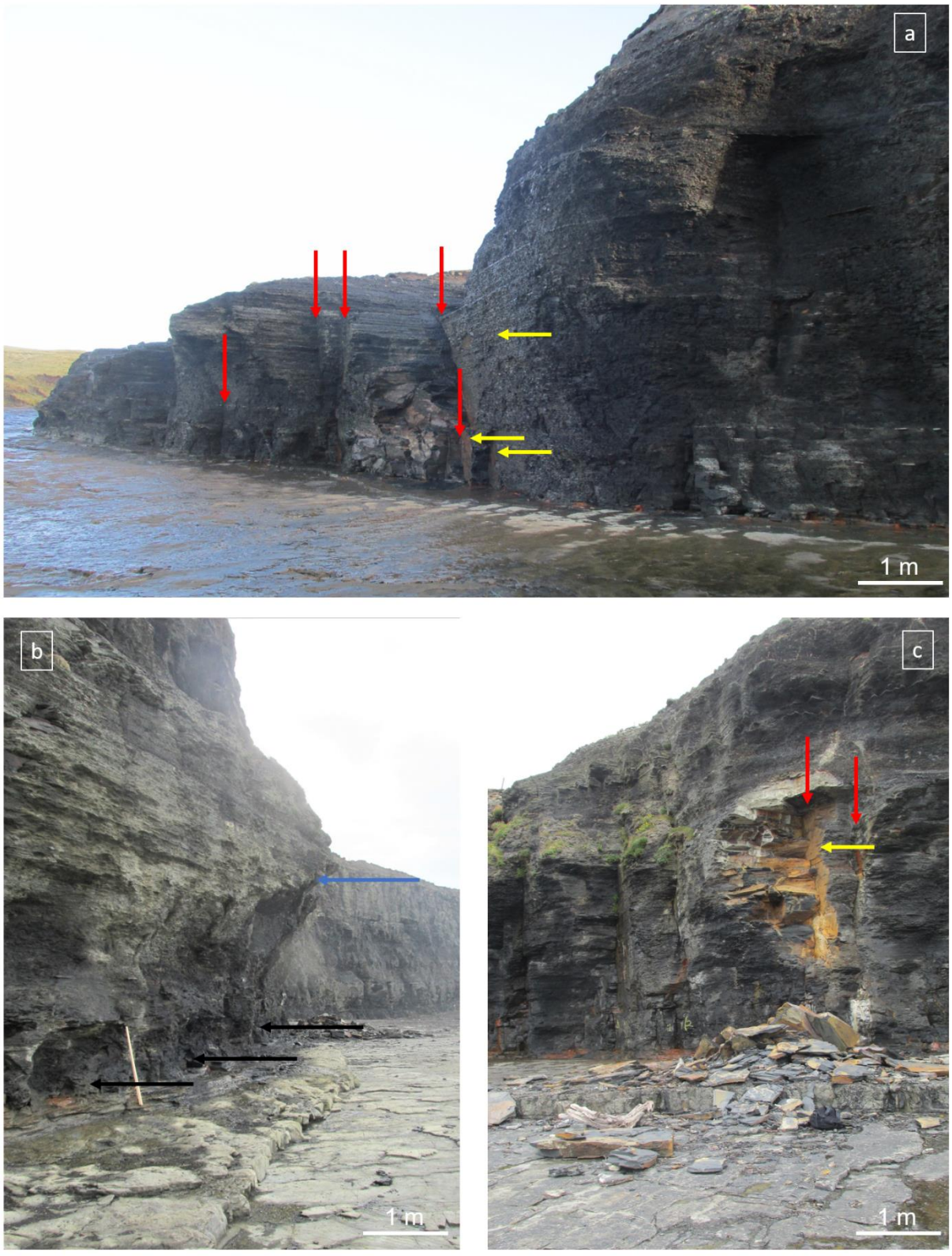

Figure 3. (a) Example of large scale discontinuities (jointing) present in the cliff (red arrows) and failure planes (yellow arrows), (b) evidence of wave action at the cliff toe in the form

of notching (black arrows) and the overhanging rock mass (blue arrow) in cliff section 1 and (c) mass wasting of overhanging rock mass along discontinuities (red arrows) and the failure plane (yellow arrow).

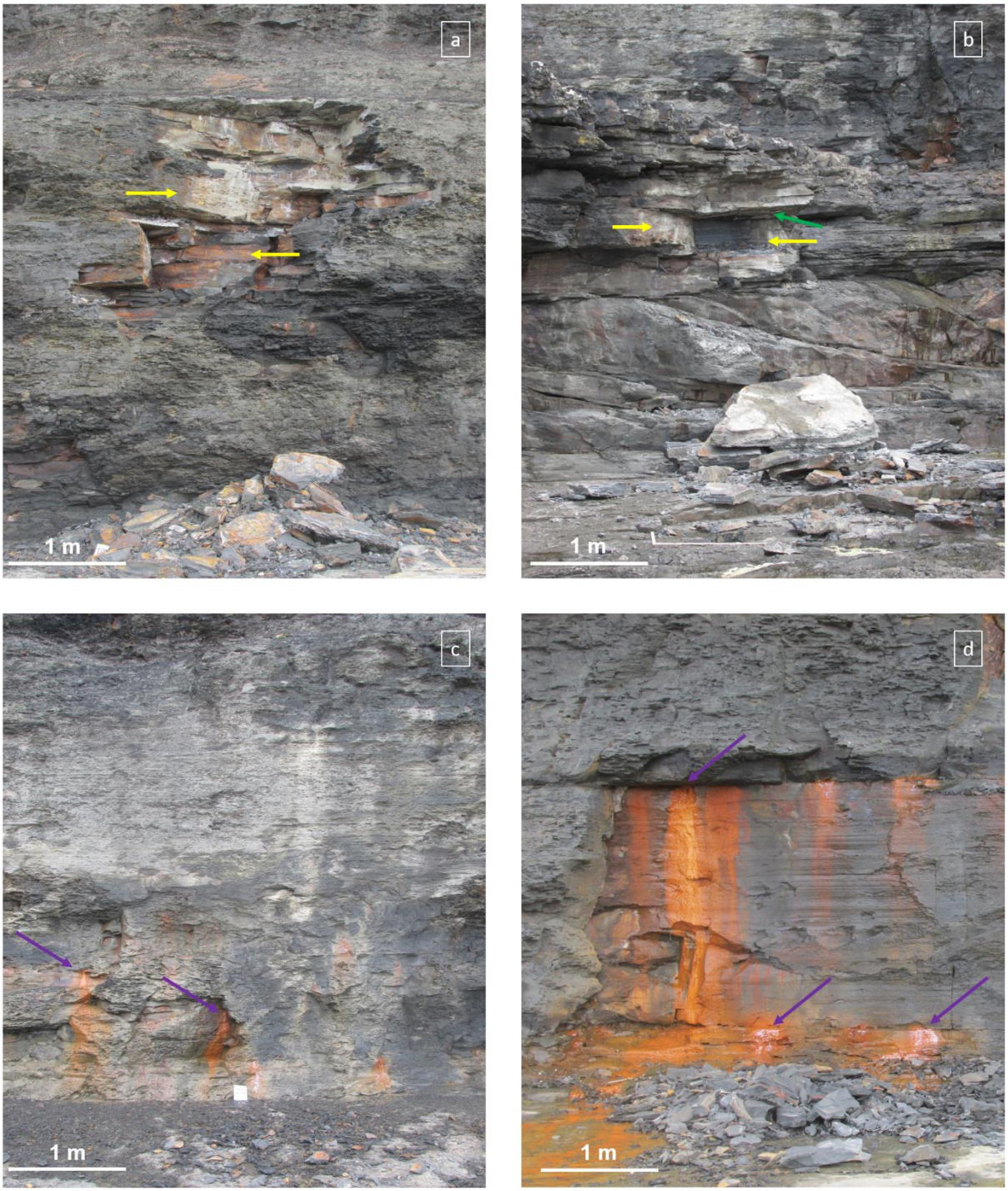

Figure 4. Examples of mass wasting from the cliff which predominantly occur as rockfalls (a and b) large failure of overhanging rock mass along discontinuity planes of differently oriented discontinuity sets (yellow arrows). Green arrow in b indicates discontinuity associated with bedding plane. Relatively smaller scale rockfalls in foreground of c and d.

Groundwater seepage associated with discontinuities (purple arrows in c and d). Orange staining is due to precipitation of ferric oxide.

Monthly temperatures in the region range from a mean minimum of 3.3˚ C in February to a maximum of 19.6˚ C in July. Absolute minimum temperatures between 1971 and 2000 of - 8.2˚ C occurred in January with absolute max of 31.6℃ in July. The annual mean number of days with air frost for the same period was 18.6 days with 71.6 days of ground frost. Average annual wind speeds were 9.4 knots with max wind speeds of 83 knots recorded. The mean annual rainfall is 964.7mm with max mean monthly rainfall (105.4mm) occurring in December and minimum mean monthly receipts (56.1mm) occurring in April (Met Éireann, 2015)

The location is exposed to high energy North Atlantic storms with an annual mean significant wave height of 3 - 4 m (Gallagher et al., 2014). Spring tidal range is 4.4 m (0 m OD Malin Head ± 2.2 m). Normal tidal range reaches between 30 and 50 m from the cliff toe. However, prevailing onshore winds and a predominantly W-SW incoming wave direction (Gallagher et al., 2014) produces waves which frequently reach the cliff toe as evidenced by rapid removal of cliff toe deposits (Cullen and Bourke, 2018). During the last Glacial Maximum ~ 24,000 Cal BP the study area was covered by the British Irish Ice Sheet (BIIS) (Peters et al., 2016). The western margins of the BIIS retreated from the area ~15.5 ± 1.0 ka BP (Bowen et al., 2002). Current rates of isostatic rebound for the area are estimated at -0.1 mm yr^{-1} (Stockamp et al., 2015).

2.2 Methodology

2.2.1 Data collection

2.2.2.1 Terrestrial Laser scanning

TLS data of the cliff face were collected in March 2016 using a Faro Focus 3D X330 and in March 2017 using a Leica P20. A total of 19 alongshore TLS stations were set up prior to the survey with a distance of less than 60 m between stations (to ensure good overlap). The distance of each TLS survey station to the cliff was less than 50 m. At each TLS station, a 0.016 m diameter hole was drilled to a depth of approximately 5 cm into the platform so that the steel rods were stable once inserted into the drill holes. A single drill hole was located approximately 6–8 m north, south, east and west of the central point (Figure 5). The position of each drill hole was measured using a differential Global Positioning system (dGPS) (Trimble Global Navigation Satellite System (GNSS) R8-3) (horizontal error = ± 0.015 m, vertical error = ± 0.020 m. A 0.016 m x 1m steel rod top was inserted into and fixed in place in each of the 4 pre-drilled holes and a spirit level was used to ensure each rod was vertical. A sphere with a magnetic base was fixed to a metal washer located at the top of each of the four steel rods. The distance (m) from the platform surface to the base of each sphere at each drill site was measured and recorded. For each scan the Faro Focus 3D X330 was located at the centre point of each TLS survey station and the position marked for easy relocation during the next survey. Scan resolution was set to 0.063 mm at 10 m distance. This was repeated for 19 stations. The procedure was replicated for the second scan in March 2017.

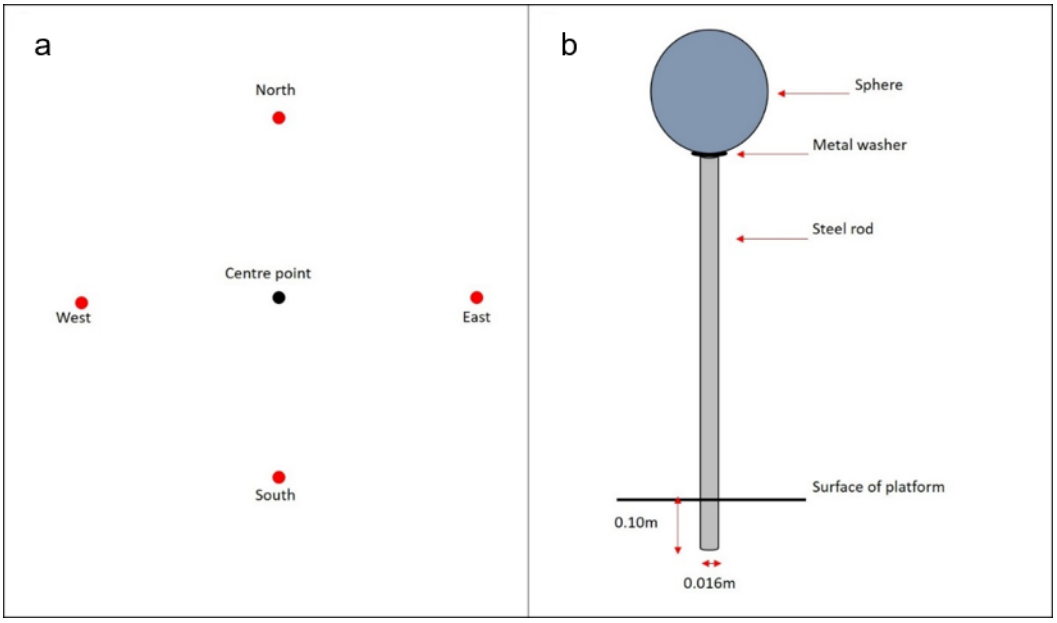

Figure 5. (a) The TLS survey station set up with a single drill hole approximately 6 m north, south, east and west of the station centre point and (B) Image depicting one of the steel rod and sphere units, that were placed at the 4 cardinal points and used for alignment and co registration of individual scans.

2.2.2 Data processing

2.2.2.1 Primary processing of point clouds

The primary processing (co registration of individual scans, noise filtering and subsampling) of the 2016 TLS point cloud was carried out by David Rogers (Ulster University, Coleraine) using *Faro Scene* (version 6.2) (Faro, 2016). The primary processing (co registration of individual scans) of the 2017 TLS point cloud was carried out by Donal Lennon (University College Dublin using *Leica Cyclone* (version 9.1.3*)* (Leica, 2015). The following steps were carried out in CloudCompare (Cloud Compare, 2013).

2.2.2.2 Secondary processing of point clouds

(1) Point cloud georeferencing

Each individual scan performed as part of an overall survey contains points that are common to both scans. Both the Faro Focus and Leica Scanner software, *Faro Scene 6.2* (Faro, 2016) and *Leica Cyclone* (Leica, 2015) respectively, perform registration of the individual scans using a system of constraints. These constraints are overlapping or equivalent objects in each scan, in this case the spheres positioned 6 – 8 m north, east, south and west of the TLS scanner. The software(s) compute an optimal alignment transformation for each target resulting in a single point cloud. For the 0316 survey the ground point at each target was surveyed using dGPS and the point cloud was retrospectively georeferenced in CloudCompare using the dGPS survey points. For the 0417 survey a series of targets were fixed in position along the cliff face and surveyed using dGPS. The point cloud was retrospectively georeferenced in CloudCompare using the dGPS survey points.

(2) Cloud cleaning

The Statistical Outlier Removal (SOR) tool in CloudCompare was applied to the point clouds to remove unwanted points or 'noise'. The algorithm calculates the average distance from each point to its neighbors considering *k* nearest neighbors. Points that are further than the average distance plus user defined *n* times the standard deviation are rejected. The default values of $k = 8$ and $n = 1$ were applied.

(3) Alignment of point clouds

The *point pairs picking* tool was used to roughly align the two point clouds. This approach uses a series of user defined points in each point cloud to roughly align the two entities.

An Iterative Closest Points (ICP) algorithm was then applied in to finely register the two point clouds in CloudCompare.

(4) Segmentation

Following alignment of the points cloud, each point cloud was divided into five cliff sections (Figure 6). Each cliff section (S01 -S05) were selected based on perceived differences in cliff discontinuity characteristics (spacing, orientation, density) and platform morphology (roughness) identified during field surveys. Each cliff section represents a sub sample of the cliff face.

Figure 6. Aerial view of the study site showing the location and lateral extent of cliff sections 1 - 5 (S01-S05).

The delineation between cliff sections one and two was based on the apparent difference in the orientation and spacing of the dominant set of near vertical discontinuities in the cliff face. In cliff section 1 these discontinuities are widely spaced (> 1 m) and the cliff line orientation is approximately NNW - SSE compared to cliff section two which was perceived to have more closely spaced near vertical discontinuities in the cliff face (<1 m) with a dominant cliff line orientation of NNE – SSW (Figure 6). The platform fronting both cliff sections one and two has very low macroscale topographic variability (< 0.1 m) (See chapter 4 for descriptions of platform morphology types and examples) and the transition between sections was determined by a shore normal step in the platform which runs from the base of the cliff to the seaward edge of the platform. At the cliff toe this step coincides with the transition from a NNW-SSE orientated cliff line to a NNE – SSW orientated cliff line.

The delineation between cliff sections two and three was based on the transition from a predominantly NNE – SSW orientated cliff line with only one identifiable discontinuity set in cliff section two, to two cross cutting near vertical discontinuity sets in cliff section three with apparent orientations of NNE-SSW and NNW -SSE. This transition in the orientation of discontinuities on the cliff coincides with a marked change platform morphology from very low macroscale topographic variability to high topographic variability (>1 m) characterised by stepped platform morphology.

The delineation between cliff sections three and four was based on the apparent transition from two cross cutting near vertical discontinuity sets in cliff section three, to one dominant near vertical discontinuity set in cliff section four, in addition to the presence of a supra tidal platform with a maximum width of 50 m in front of the cliff toe. Similarly, the delineation between cliff sections four and five were based on a transition to a near vertical dominant discontinuity set with an apparent change in orientation to that of cliff section four and a marked difference in platform morphology which also coincided with the transition to the

apparent change in orientation of the dominant near vertical discontinuity sets between sections.

Point clouds for each cliff section were extracted using the *segment* tool in CloudCompare. The surface area of each cliff section was calculated using the cliff section length and height measured in CloudCompare. Cliff height was calculated from the mean of three vertical lines at the start, middle and end of each cliff section. Cliff length was calculated as the mean of three horizontal lines measuring the cliff length at the base middle and top of each cliff section.

(5) Subsampling

To reduce the processing time and obtain a more uniform point density between scans, both point clouds were subsampled at 1 cm resolution using the *subsample* tool in CloudCompare.

2.2.3 Data analysis

2.2.3.1 Change detection – Multiscale Cloud to Cloud Comparison (M3C2)

Multiscale Cloud to Cloud Comparison (M3C2) (Lague et al., 2013) allows direct comparison of point clouds in 3D. The algorithm estimates surface normals and orientation in a scale consistent with local roughness and measures the surface change along the normal direction with an explicit calculation of a local confidence interval (Lague et al., 2013). This approach has demonstrated higher accuracy compared to other methods such as DEMs of Difference (DoDs) (e.g. Lane et al., 2003, Milan et al., 2007) direct cloud-to-cloud comparison (C2C) using closest point technique (e.g. Girardeau-Montaut et al., 2005) and cloud to mesh distance (C2M) (e.g. Cignoni et al., 1998, Kazhdan and Hoppe,

2013). The main limitations associated with these approaches are difficulty in capturing very complex topography, such as overhangs, in the case of DoDs and C2C, as well as inability to determine a confidence interval, in the case of C2M (Lague et al., 2013).

A brief outline of the principles of M3C2 and the steps used in the M3C2 analysis are outlined below. The reader is referred to Lague et al. (2013) for a more detailed description.

(1) Estimation of normal scale

The normal scale is the distance at which the first point cloud looks for change in the next. On complex 3D topographies this is complicated by the fact that the surface normal can change from one point to the next depending on surface roughness. Where surface roughness is of similar scale to the surface normal scale, the orientation of the surface normal can fluctuate and result in overestimation of the distance between the two point clouds (Earlie, 2015). The M3C2 offers an option to apply a uniform normal scale the the whole point cloud however this may result in surface smoothing and can miss change in surface orientation. M3C2 also offers a second option whereby a gradually increasing scale is applied and the most suitable scale is selected. The scale is selected using Principle Components Analysis (PCA) of the nearest neighbors to a point *i* based in a sphere of radius *d.* The 1st, 2nd and 3rd eigenvalues of the covariance matrix resulting from the PCA are ordered in decreasing magnitude and all three are needed for analysis of the variance in the 1st, 2nd and 3rd dimensions respectively. The relative contribution of each eigenvalue to the total variance determines how 1D, 2D or 3D the point cloud appears at a particular scale. The scale at which the proportion of the variance of the third eigenvalue is smallest, i.e. where the scale normal to the cliff surface with its origin orientated towards the scanner, is chosen (Brodu and Lague, 2012, Lague et al., 2013). In this case the *guess parameters* tool was used to estimate the optimum normal scale.

(2) Estimation of projection scale and depth

The projection scale is the diameter of the base of a cylinder which is projected from one cloud to the other and used to estimate the surface change (Lague et al., 2013). The cylinder must contain more than four core points in either cloud to calculate the surface distance. The projection depth is the maximum distance at which one cloud can be projected to the next. Lower values reduce the processing time but must be large enough to capture the maximum difference between the point clouds. In this case the *guess parameters* tool was used to estimate the optimum projection scale and depth.

(3) Registration and alignment error

Prior to calculation of distance between point clouds (see below) an error term is added to allow for registration and alignment errors. The accuracy of registration varies depending on the horizontal and vertical error accuracy of the dGPS points used to georeference the point clouds. In this case an RMS error of 0.10 m to account for errors in registration of, and alignment between, the point clouds in CloudCompare was applied to all cliff sections. The M3C2 plugin was used to identify areas of significant change in each cliff section at a 95% confidence interval (Lague et al., 2013). Areas of significant change were validated using field surveys and aerial images of the cliff to identify rockfall scars.

(4) Calculation of distance between point clouds

After defining the normal and projected scales and depth the distance is calculated from the intercept of each set of points defined by the diameter of the cylinder. The position of the points in each point cloud are calculated along the cloud normal. The standard deviation of the points is used to determine the surface roughness in the normal direction.

(5) Confidence interval

For each distance calculated the algorithm estimates a confidence interval, defined at 95%. The confidence interval is used to determine the accuracy of the calculated distances depending on the registration error and the standard deviation i.e. surface roughness. This allows identification of significant change rather than change due to registration error or surface roughness. We applied a conservative maximum RMS error of 0.1 m to account for errors in registration and alignment. This allows detection of rockfalls with a minimum volume of 0.001 mm^3 at a 95% confidence interval.

2.2.3.2 Calculation of rockfall volume

We then used the 2.5D volume calculation tool in cloud compare to calculate the volume and surface areas of significant change i.e. rockfalls. A polygon was drawn around the areas of significant change (identified using M3C2) on point clouds and extracted using the segment tool. The 2.5D volume tool was used to calculate the surface area and volume of each area of significant change i.e. rockfall.

2.2.3.3 *Rockfall inventory characteristics.*

We recorded the total number of rockfalls in each cliff section in addition to the surface area and volume of each rockfall. Rockfalls were validated in the field and using aerial images of the cliff face to identify rockfall scars. The relative frequency of rockfalls in a section was calculated as the number rockfalls per unit area (n m^{-2}). From the rockfall inventory we calculated the minimum, maximum, mean and mode rockfall volume and surface area for the entire inventory and for each cliff section individually.

2.2.3.4 Erosion rate

Erosion rate (cm yr^{-1}) was calculated for the entire site and for each cliff section using the equation:

$$ER = 100 \frac{\mathrm{Vol}}{\left(\frac{\mathrm{SA}}{t}\right)} \quad (1)$$

where Vol is the total volume (m^3) of rockfalls in an inventory (site or cliff section), SA is the surface area (m^{-2}) of interest (site or cliff section) and t = 1 year.

2.2.3.5 Rockfall surface area - volume distribution

We adopted techniques used in existing landslide and rockfall research (e.g. Dussauge-Peisser et al., 2002, Malamud et al., 2004, Guzzetti et al., 2009, Larsen et al., 2010) to analyse volume, surface area and frequency distribution of rockfalls in our inventory and to explore relationships with the characteristics the discontinuity sets. The relationship between rockfall surface area (m^2) and rockfall volume (m^3) is expected to follow a power law distribution according to the equation:

$$Vol = a\, SA^b \quad (2)$$

Where *a* is a constant and *b* is the power law exponent. The fit to and deviation from the fitted power law trendline can be used to explore changes in failure mechanism as a function of volume (Guzzetti et al., 2009, Larsen et al., 2010). Here we use it to explore the influence of discontinuity spacing on the relationship between surface area and volume. Rock falls which plot below the fitted power law trendline have a relatively lower volume per surface area i.e. relatively shallow failures. Rockfalls which plot above the fitted

power law trendline have relatively higher volume per surface area i.e. relatively deeper failures.

2.2.3.6 Rockfall volume - cumulative frequency distribution

The Magnitude - Cumulative Frequency (MCF) is widely used in natural hazards science (Hungr et al., 1999). The relationship between rockfall volume and frequency has been demonstrated to follow a power law distribution (Gardner, 1980, Gardner, 1983, Hungr et al., 1999, Dussauge-Peisser et al., 2002) and is assumed to be represented as:

$$CumFreq. = a\, Vol^{-\beta} \tag{3}$$

Where *CumFreq.* is the cumulative frequency, *a* is a constant and the β is the volume - frequency power law exponent. Values of β are indicative of the size distribution of rockfalls with higher values of β indicating a higher proportion of smaller rockfalls in an inventory (Malamud et al., 2004). The constant *a* is highly variable (Hungr et al., 1999) and β is found to range between 0.4 – 1.1 for rockfalls in general (Santana et al., 2012), although higher values (β = 0.71 – 2.37) have been observed in coastal cliffs with similar lithology to the cliff in this study (Whadcoat, 2017, Barlow et al., 2012, Williams et al., 2018, Rosser et al., 2007).

2.2.3.7 Discontinuity set extraction

To determine discontinuity set characteristics we used freely available software Discontinuity Set Extractor (DSE) developed by Riquelme et al. (2014, 2015) using the baseline TLS point cloud (TLS 0316) (see section 2.2.2. for details of cloud georeferencing, cleaning, segmentation of cliff sections and sub sampling procedure). A discontinuity 'set' refers to a group of discontinuities which are determined to have similar characteristics (i.e. orientation, spacing etc.).

The point clouds for each section (S01 - S05) were imported to DSE. For each section we followed the recommended workflow outlined in (Riquelme et al., 2014, 2015) (Figure 7). Details of the parameters used at each stage of the workflow are shown in Table 1. The main steps taken for extraction of discontinuity sets are (1) Local curvature calculation (2) Statistical analysis of the planes and (3) Cluster analysis. This is followed by extraction of the discontinuity set characteristics (mean, maximum, minimum spacing and maximum spacing density). A brief description of the steps is given below. For a more detailed explanation of the of DSE used the reader is referred to Riquelme et al. (2014, 2015).

(1) Local curvature calculation

A normal is calculated for each 3D point. This is achieved by first identifying the *k* nearest neighbours for each point in the point cloud. A coplanarity test is carried out using PCA to determine whether a set of points lies on the same plane i.e. belong to the same discontinuity set. The step calculates the orientation of the coplanar set of points by calculating the best-fit adjustment plane according to the equation

$$Ax + By + Cz + D = 0 \quad 4$$

where A, B and C are the components of the normal vector to the plane and D gives the perpendicular distance from the origin to the plane (Riquelme et al., 2014).

(2) Statistical analysis of the planes

Each set of coplanar points comprises a plane. The normal vector of each plane is converted to a stereographic projection i.e. pole. Statistical analysis is carried out to determine the density of poles for each region of the stereographic projection using Kernel Density Estimation (KDE) and the local maxima. Usually the density function analysis

results in identification of many local maximums however, only a few are principle poles (Riquelme et al., 2014). The user then defines two parameters for assignment of principle pole classification (i) the cone filter where the angle formed by two vectors must be higher that this value and (ii) the maximum number of principle poles (i.e. the maximum number of discontinuity sets). Following the assignment of principle poles in DSE and prior to cluster analysis, a visual inspection of extracted discontinuity sets for each cliff section was carried out in CloudCompare to identify incorrectly identified discontinuity sets. Typical errors included weathered surfaces (approx. dip 44˚), which were known from site surveys and from aerial images collected using a UAV (Phantom 3 Pro). These errors were manually removed using the *edit poles* tool in DSE and principle poles assignment was repeated. Cluster analysis was carried out on the remaining discontinuity sets.

(3) Cluster analysis

For each discontinuity set, the data subset comprised of groups of planar clusters is required. Each of the clusters is a member of the discontinuity set and is defined in space according to its plane equation (Eqtn. 4). Clustering of the 3D data is achieved using the Density Based Scan Algorithm with Noise (DBSCAN) (Ester et al., 1996). Once the clusters in a discontinuity set are determined the user is offered an option to increase the minimum number of points within a cluster and discarding small clusters. We defined the minimum number of points in a cluster as 500 based on recommendation by Riquelme (2018, Pers comm). This is followed by plane generation. Each plane is determined by the set of points which belong to a discontinuity set and the points belonging to the clusters which constitute a subset of the discontinuity set.

(4) Discontinuity set characteristics

After the above steps have been carried out and discontinuity sets, their clusters and planes have been determined, the characteristics of the discontinuity sets are extracted using the *spacing* calculation tool. This method employs two approaches to calculate the characteristics of the discontinuity sets. The first assumes full persistence of discontinuities i.e. that discontinuity planes extend continuously through the rock mass. For example, this assumption is used where scan lines are employed to determine discontinuity sets for rock mass characterisation. Where scan lines intersect discontinuity, this discontinuity is assumed to be persistent beyond the extent of the scan line intersection. The second approach assumes that discontinuities do not persist throughout the rock mass and only uses the identified discontinuity planes for calculation of the discontinuity set characteristics. The statistical analysis using the KDE technique (Silverman, 2018) calculates the non-parametric distribution of discontinuity spacing and the following population statistics for each discontinuity set: min, mode, mean, max spacing, maximum spacing density and standard deviation.

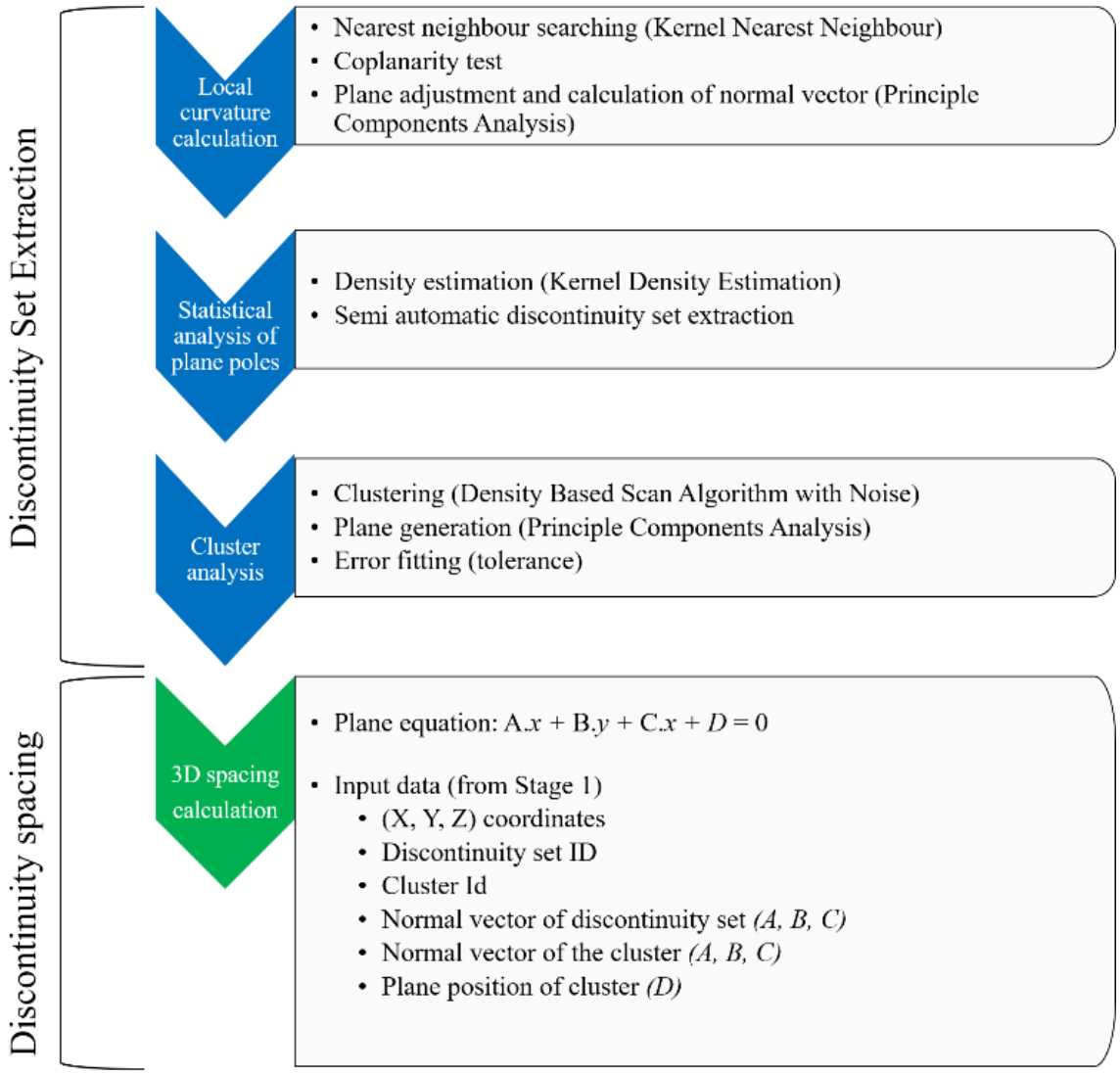

Figure 7. Workflow for discontinuity set extraction using DSE and spacing analysis with the details of processing methods used for each stage (Adapted from Riquelme et al., 2014, 2015).

Table 1. Details of the parameters and values used to extract discontinuity sets.

Parameter	**Value**
Calculation of normal vectors and corresponding poles	
k nearest neighbours (knn)	30

Tolerance for coplaniarity test (eta)	0.2
Calculation of poles density	
Number of bins for kernel density test (nbins)	64
Minimum angle between normal vectors of the discontinuity set (anglevppal)	30˚
Assignment of a discontinuity set to a point	
Cone	30˚
Cluster analysis	
K sigmas	1.5
Minimum number of points per cluster	500

2.2.3.8 Relationships between the discontinuity set characteristics, rockfall inventories and the spatial distribution of erosion.

We explored relationships between discontinuity set characteristics (dip direction, dip angle, max, min, mean, mode and maximum density of spacing), rockfall inventories (max, min, mean volume) and the spatial distribution of erosion (erosion rate, rockfall volume - surface area distribution, rockfall volume - frequency distribution) with multiple and single regression techniques using statistical analysis software XLSTAT (XLSTAT, 2017).

2.3 Results

This section contains the results of the data analysis described above. The results of the M3C2 analysis for identification of areas of significant change i.e. rockfalls are shown and the characteristics of the rockfall inventory (volume, surface area, frequency) are described. This is followed by the output of the discontinuity set extractor software and a description of the discontinuity set characteristics. Finally, analysis of the relationships

between the rockfall inventory characteristics, erosion rate and the discontinuity set characteristics are presented.

2.3.1 Multiscale Cloud to Cloud Comparison (M3C2)

The RMS error for registration and alignment of the point clouds is shown in table 2. The maximum RMS error of 0.10 m was applied for M3C2 significant change detection for all cliff sections allowing detection of rockfalls with a minimum volume of 0.001 m^3 to be detected at the 95% confidence interval.

Table 2. The RMS registration error of point cloud registration

Section ID	RMS error (m)
S01	0.07
S02	0.09
S03	0.08
S04	0.1
S05	0.09

The output of the of the M3C2 analysis for cliff sections 1-5 (S01 -S05) are shown in figures 8 -12 respectively. The M3C2 distance and distance uncertainty for each section are shown in table 3. Each cliff section showed areas of significant change at the 95% confidence interval. Significant (negative) change, i.e. volume loss, is interpreted as rockfall. Rockfalls occurred across the entire cliff face during the study period.

Table 3. The M3C2 distance and distance uncertainty for cliff sections 1 -5 (S01 -S05).

Cliff section	M3C2 distance	M3C2 distance uncertainty	
		Min	Max
	m	m	m
S01	± 0.625	0.197	0.222
S02	± 0.600	0.099	0.125
S03	± 0.125	0.196	0.221
S04	± 0.625	0.196	0.222
S05	-0.125 - 0.063	0.196	0.23

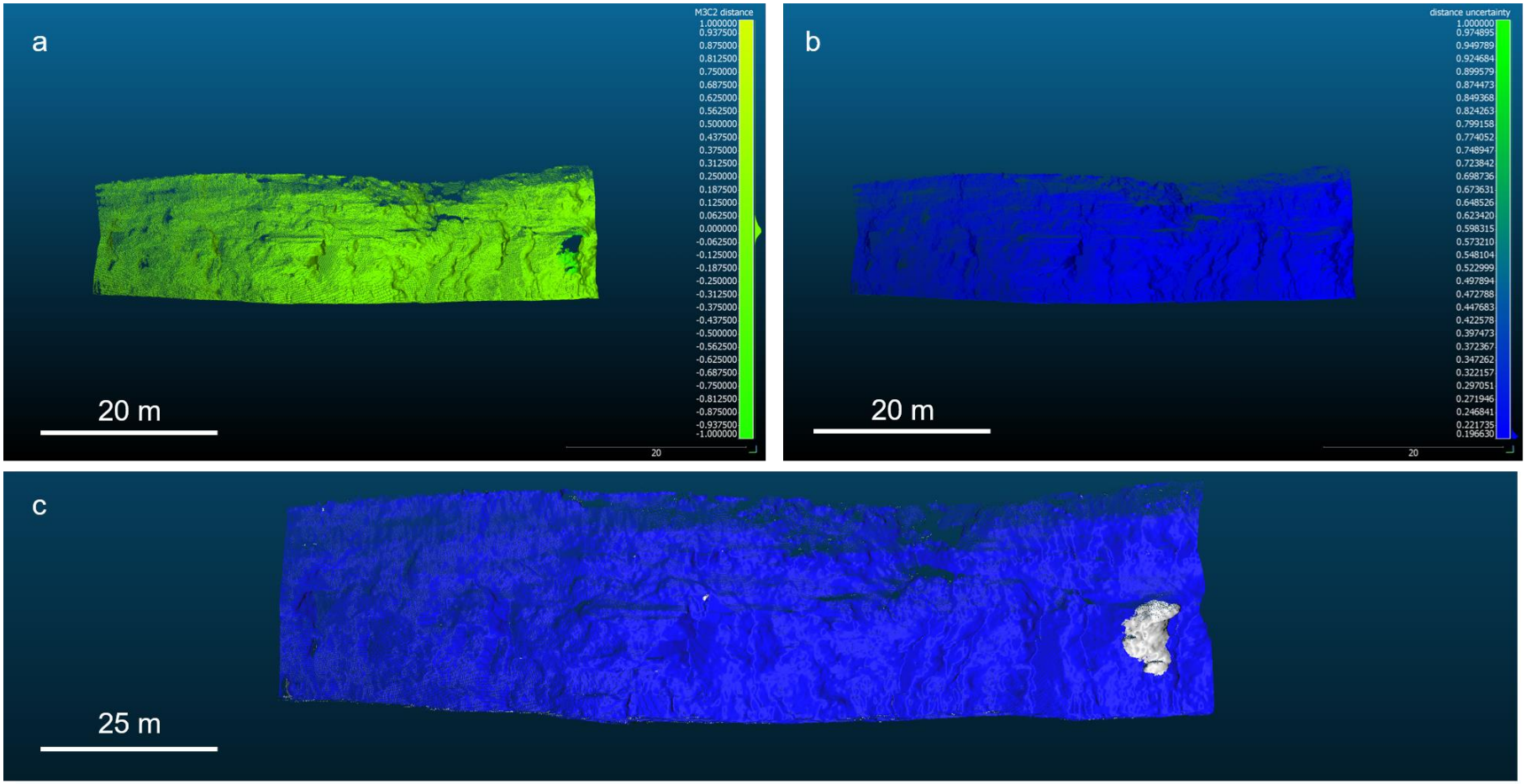

Figure 8. The M3C2 distance (a) and distance uncertainty (b) for cliff section 1 (Scale bar values are shown in table 3) and (c) M3C2 areas of significant change at 95% confidence interval (white areas).

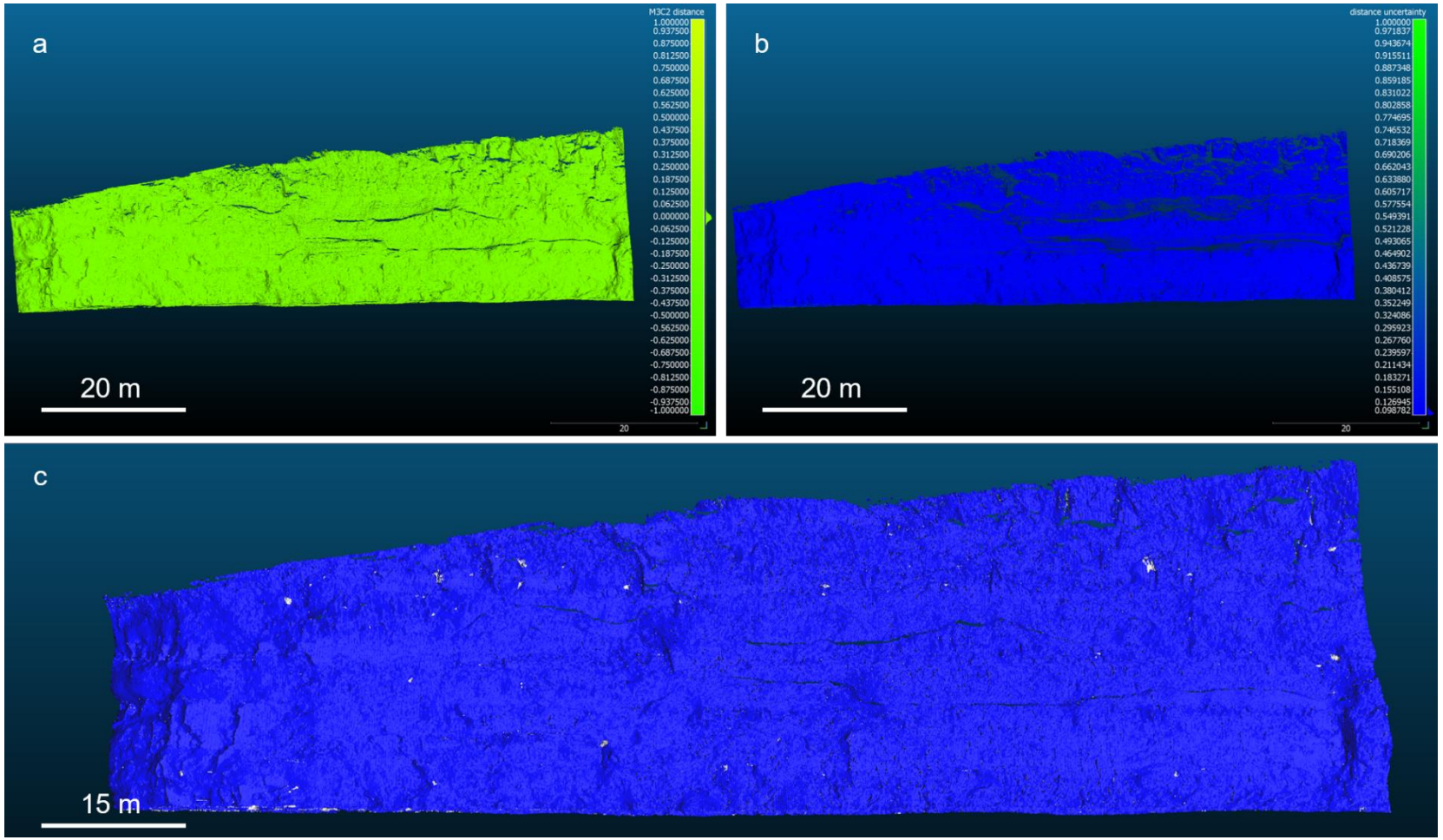

Figure 9. The M3C2 distance (a) and distance uncertainty (b) for cliff section 2 (Scale bar values are shown in table 3) and (c) M3C2 areas of significant change at 95% confidence interval (white areas).

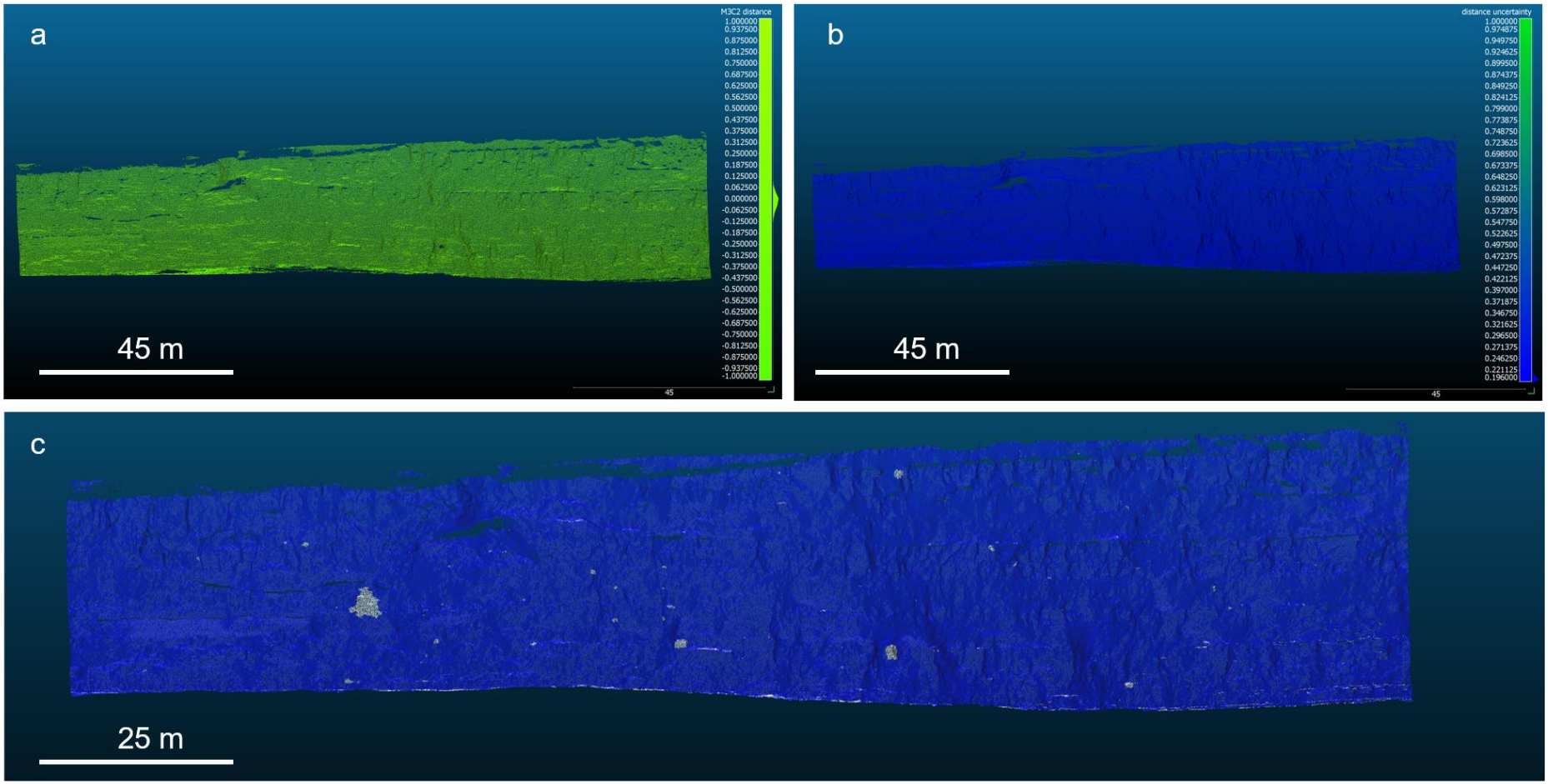

Figure 10. The M3C2 distance (a) and distance uncertainty (b) for cliff section 3 (Scale bar values are shown in table 3) and (c) M3C2 areas of significant change at 95% confidence interval (white areas).

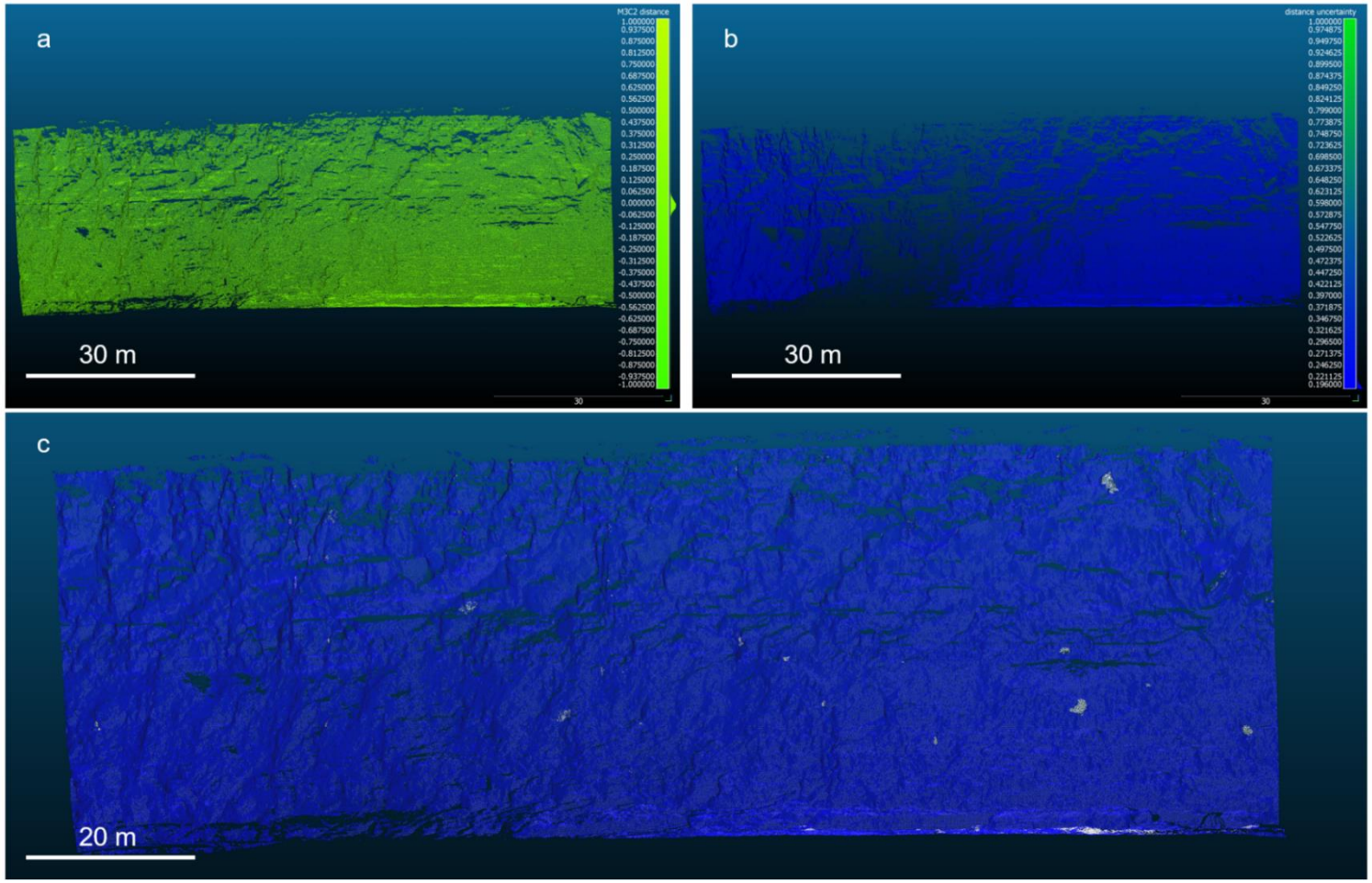

Figure 11. The M3C2 distance (a) and distance uncertainty (b) for cliff section 4 (Scale bar values are shown in table 3) and (c) M3C2 areas of significant change at 95% confidence interval (white areas).

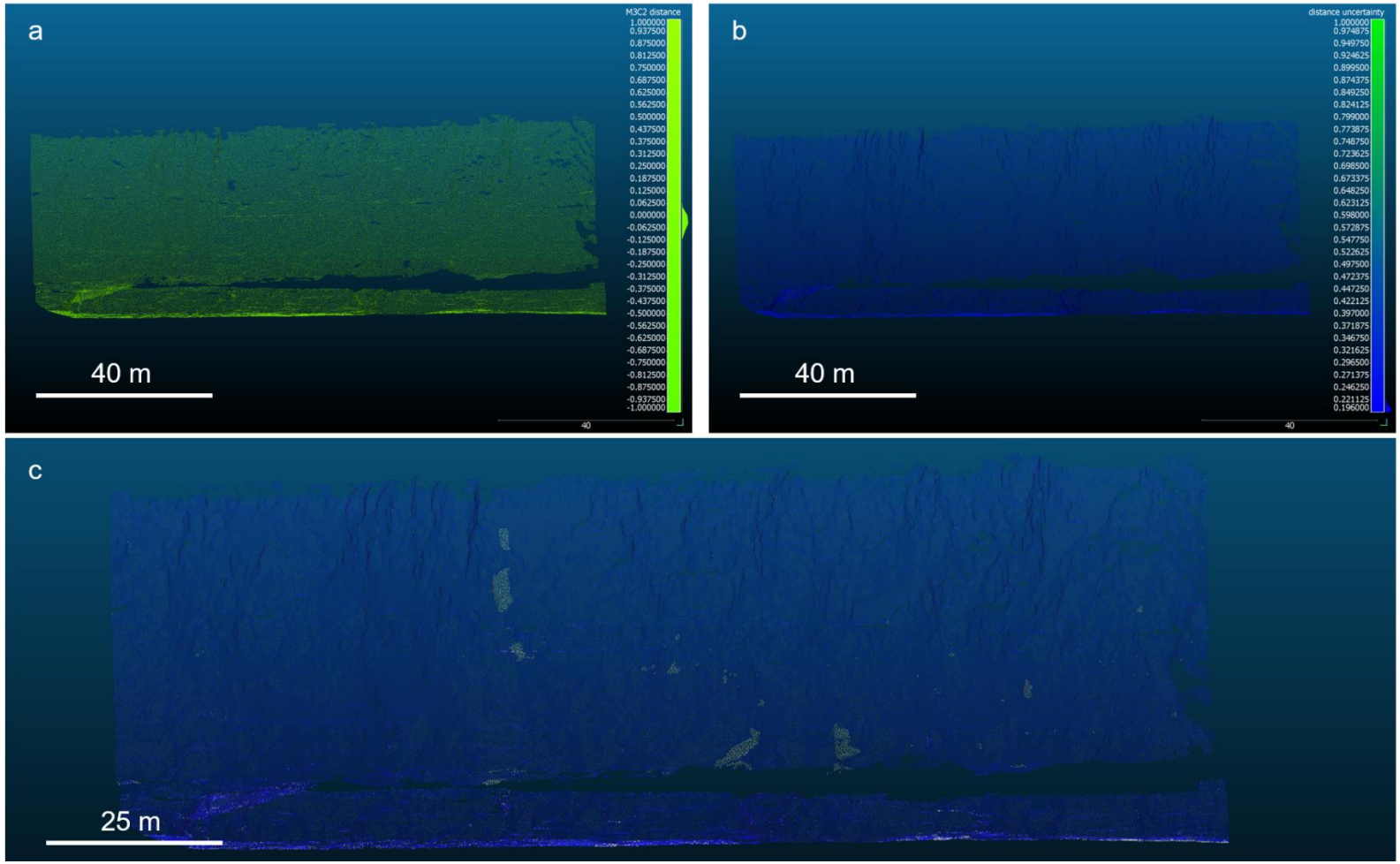

Figure 12. The M3C2 distance (a) and distance uncertainty (b) for cliff section 5 (Scale bar values are shown in table 3) and (c) M3C2 areas of significant change at 95% confidence interval (white areas).

2.3.2 Rockfall inventory characteristics

List of abbreviations used to describe rockfall inventory characteristics

RF*Relfreq* - relative frequency of rockfalls

Rf*SA* – rockfall surface area

RF*Vol* - rockfall volume

RFVol_{min} - minimum rockfall volume

RFVol_{max} – maximum rockfall volume

RFVol_{mean} – mean rockfall volume

RfVol_{StDev} – standard deviation of rockfall volume

A total of 540 rockfalls were identified across all cliff sections (S01-S05) (Table 4) with a surface area of 156 m^2, 1% of the total area studied. The highest frequency of rockfalls occurred in S03 (n = 193) and the lowest frequency of rockfalls in S01 (n = 31). When normalized to account for surface area the highest relative frequency of rockfalls (RF*Relfreq.)* was found in S02 (0.09 RF m^{-2}) and the lowest RF*Relfreq* in S05 (0.02 RF m^{-2}). The smallest detectable rockfall volume (RFVol_{min} = 0.001 m^3) had the highest frequency of occurrence in all inventories. The largest rockfall volume (RFVol_{max}) detected was 11.56 m^3 in S01. Mean rockfall volume (RFVol_{mean}) ranges from 0.01 in S02 to 0.40 in S01. The variability of rockfall volume, measured as the standard deviation from the mean volume, (RfVol_{StDev}) is greatest in S01 (2.11) and lowest in S02 (0.02).

Table 4. Characteristics of the rockfall inventory. SA is surface area, ER is erosion rate.

Section ID	**Section SA**	**Rockfall**			**Rockfall volume**						***ER***
		Freq.	*Rel freq.*	*SA*	*Total*	*Max*	*Min*	*Mode*	*μ*	*σ*	
	m^2	n	n m^{-2} yr^{-1}	m^2	m^3	m^3	m^3	m^3	m^3	m^3	cm yr^{-1}
S01	799	31	0.04	18.6	11.92	11.56	0.001	0.002	0.40	2.11	1.5
S02	1,651	148	0.09	17.6	1.50	0.21	0.001	0.001	0.01	0.02	0.1
S03	4,628	193	0.04	38.6	12.00	4.53	0.001	0.001	0.06	0.35	0.3
S04	3,680	94	0.03	20.8	3.68	0.75	0.001	0.001	0.04	0.11	0.1
S05	4,515	77	0.02	60.0	27.19	7.01	0.001	0.001	0.35	1.21	0.6
Net	15,274	540	N/A	156	56	N/A	0.001	0.001	N/A	N/A	0.37

2.3.3 Erosion rate

A total volume of 56 m^3 of material was removed from the cliff via rockfall during the study period (t = 1 yr). The net erosion rate for the entire cliff was calculated at 0.36 cm yr^{-1} (Table 4) however the erosion rate varies between cliff sections. S01 had the highest erosion rate (1.5 cm yr^{-1}) while the lowest erosion rate was observed in S02 and S04 (0.1 cm yr^{-1}).

2.3.4 Rockfall surface area– volume distribution

A statistically significant relationship was observed between rockfall surface area (Rf*SA)* and rockfall volume (Rf*Vol*) (R^2 = 0.704, P < 0.001) for the entire rockfall inventory and for the cliff section (Figure 13, Table 5). The strongest relationship between Rf*SA* and Rf*Vol* was found in S03 and the weakest, but still statistically significant relationship in S04 (R^2 = 0.549, P < 0.001). S02 also exhibited a weak but statistically significant relationship between Rf*SA* and Rf*Vol* (R^2 = 0.622, P < 0.001).

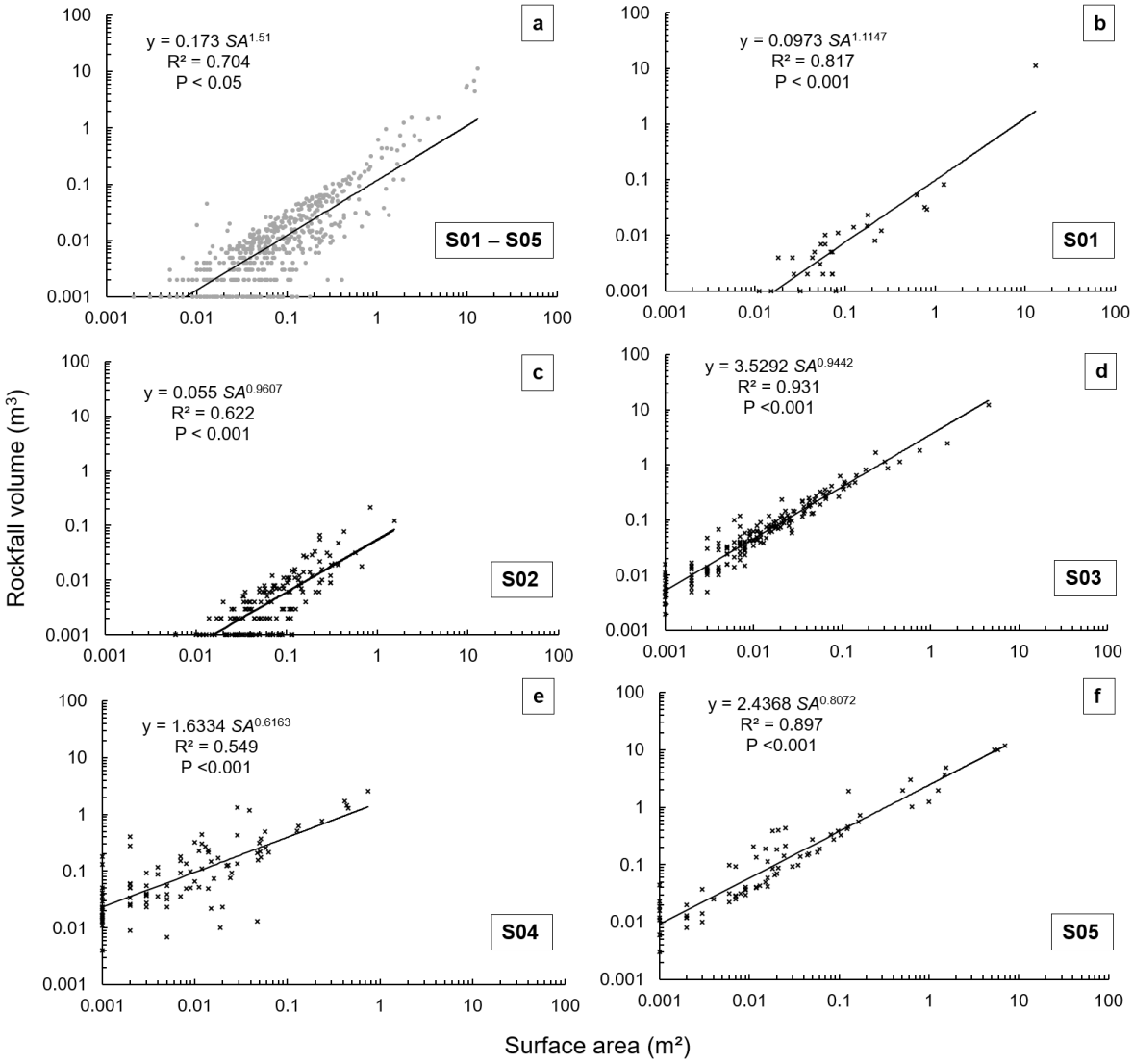

Figure 13. (a) Log–log scale plot of rockfall surface area - volume distribution with the fitted power law trendline for the full rockfall inventory (S01- S05) and (b-f) the log-log plots of rockfall surface area – volume distribution with the fitted power law trendline (solid black line) for individual rock sections.

Table 5. The surface area – volume distribution exponent *b* values, R^2 and P values for the fitted power law trendlines for the entire rockfall inventory (All) and cliff section inventories (S01-S05).

Section ID	*b*	R^2	P
All	1.510	0.704	<0.001
S01	1.115	0.817	<0.001
S02	0.961	0.622	<0.001
S03	0.944	0.931	<0.001
S04	0.616	0.549	<0.001
S05	0.807	0.897	<0.001

2.3.5 Rockfall volume – frequency distribution (Rf*Vol* – Freq.)

The fitted power law trendlines for the full rockfall inventory for all cliff sections and within cliff sections exhibit a range of β values (β = 0.42 – 1.224) (Figure 14, Table 6). The total rockfall inventory and the inventory within each cliff section exhibit a rollover in the rockfall volume – frequency distribution at the lower end of the Rf*Vol* spectrum (≤0.01 m^3). Additional power law trendlines have been fitted to characterize these sub-populations. Three sub-populations were identified in the overall inventory (Figure 14) with two sub-populations in each of the cliff section inventories. The exponent β representing rockfalls above the rollover threshold of 0.01 m^3 (Table 6) was used to explore relationships between the proportion of smaller rockfalls within an inventory and the other characteristics of the discontinuity sets and erosion rate (see section 3.3.6). For rockfall volumes above the rollover threshold, S02 has the highest proportion of smaller rockfalls within its inventory (β = 1.224) which also coincides with the highest relative frequency of rockfalls within a cliff section inventory. The lowest proportion of smaller rockfalls in an inventory was found in S01 (β = 0.375).

Table 6. The volume – frequency exponent β, R^2 and P values for the fitted power law trendlines for the entire rockfall inventory (All) and cliff section inventories (S01-S05). β values used in analysis are highlighted in bold and represent the rockfall sub-population which falls above the rollover threshold.

Section ID	**β**	**R^2**	**P**
All (S01-S05)	-0.668	0.816	<0.001
sub pop 1	-0.419	0.816	<0.005
sub pop 2	-0.692	0.823	<0.001
sub pop 3	-1.647	0.9916	<0.001
S01	-0.402	0.876	<0.001
sub pop 1	-0.308	0.959	<0.001
sub pop 2	**-0.375**	0.8245	<0.001
S02	-1.045	0.97	<0.001
sub pop 1	-0.468	0.993	<0.001
sub pop 2	**-1.224**	0.998	<0.001
S03	-0.762	0.98	<0.001
sub pop 1	-0.22	0.989	<0.001
sub pop 2	**-0.837**	0.992	<0.001
S04	-0.716	0.948	<0.001
sub pop 1	-0.348	0.997	<0.001
sub pop 2	**-0.821**	0.95	<0.001
S05	-0.464	0.955	<0.001
sub pop 1	-0.148	0.975	<0.001
sub pop 2	**-0.504**	0.953	<0.001

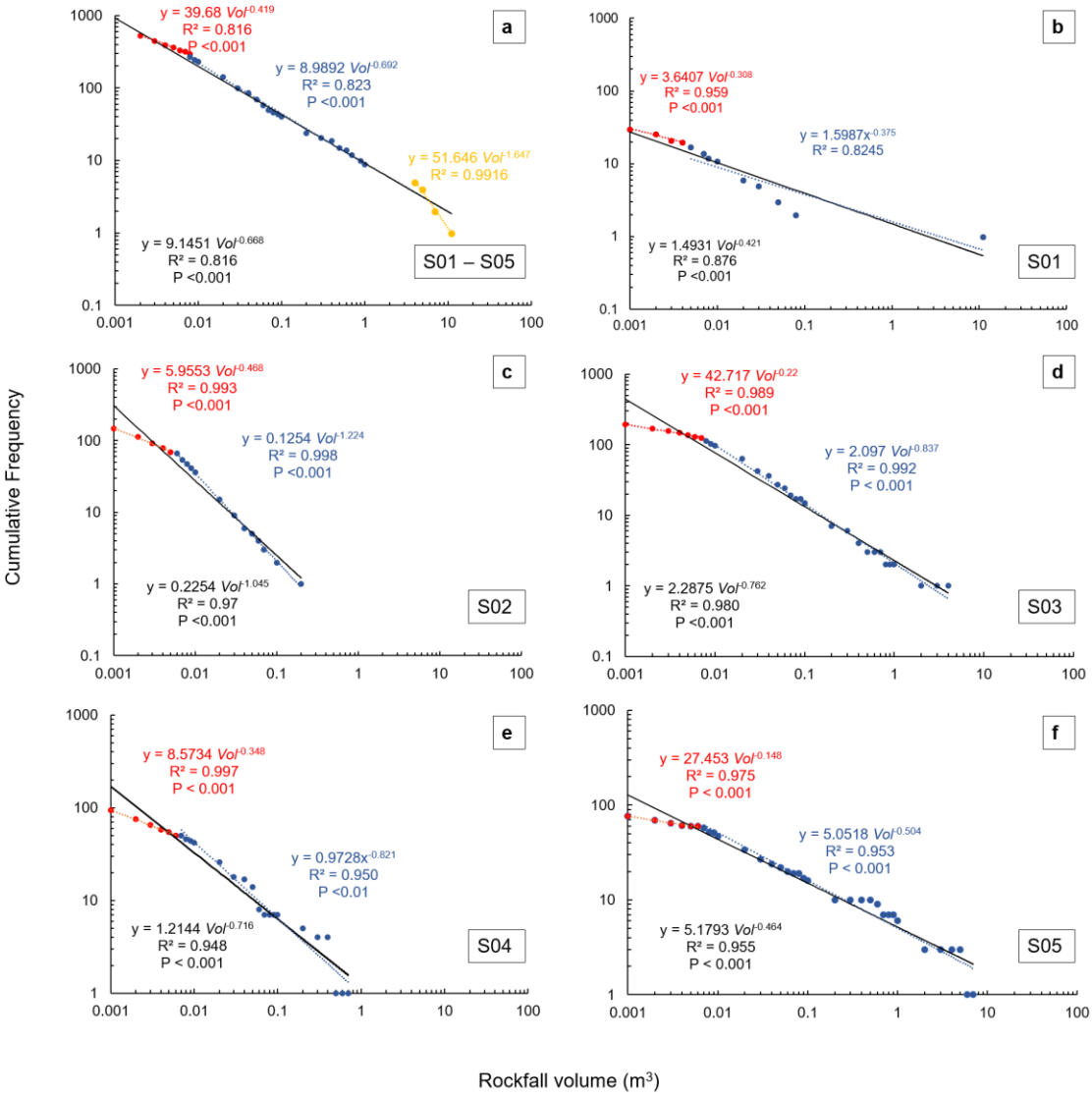

Figure 14. (a) Log-log scale plot of the cumulative frequency – rockfall volume distribution with the fitted power law trendline (solid black line) for entire cliff face and (b-f) for each section (S01–S05 respectively). Additional power law trendlines are fitted for different sub populations of the volume spectrum (red, blue and yellow dotted lines) with the corresponding power law equation, R^2 and P values (text is colour coded to associated trendline). Blue dotted trendline and associated β were used for analysis.

2.3.6 Discontinuity set extraction

The results of the discontinuity set extraction are given on a cliff section by section basis followed by a description of discontinuity set characteristics.

Cliff section 1 (S01)

Discontinuity set extraction identified 3 discontinuity sets in S01. The 1st (J1, Figure 15) are discontinuities associated with bedding planes (based on dip of 3.88˚). The 2nd (DS_1) and 3rd (DS_2) are near vertical discontinuity sets with a dip of 84˚ and dip direction of 104 and 194˚ respectively (Table 7). A total of 12, 62 and 43 clusters were identified in J1, DS_1 and DS_2 respectively. With respect to the total number of points in the point cloud for S01, the percentage of points assigned to J1, DS_1 and DS_2 were 6, 23 and 11% respectively. Therefore, DS_1 is designated as the dominant discontinuity set (i.e. the discontinuity set having the greatest influence) and this discontinuity set is used in further analysis (Figure 16). The same procedure is used to identify the dominant discontinuity sets for each cliff section.

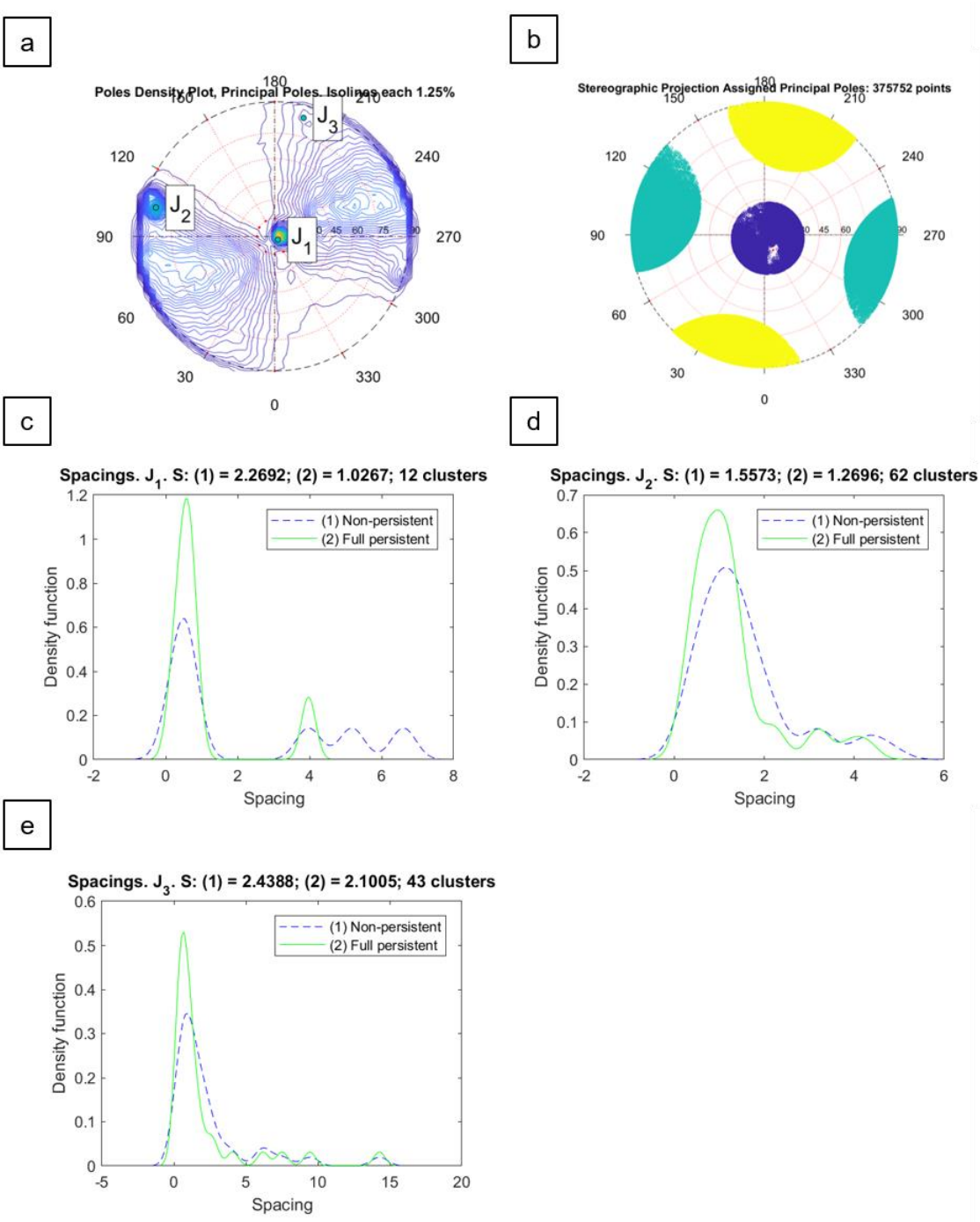

Figure 15. (a) Discontinuity Set Extractor poles density and principle poles assignment for cliff S01 (b) Stereographic projection of principle poles, (c, d and e) Density function of discontinuity spacing assuming non-persistence of discontinuities (blue dashed line) and full persistence of discontinuities (green solid line) for J1 (Bedding plane), J2 (DS_1) and J3 (DS_2) respectively. The number of clusters in each discontinuity set is also shown.

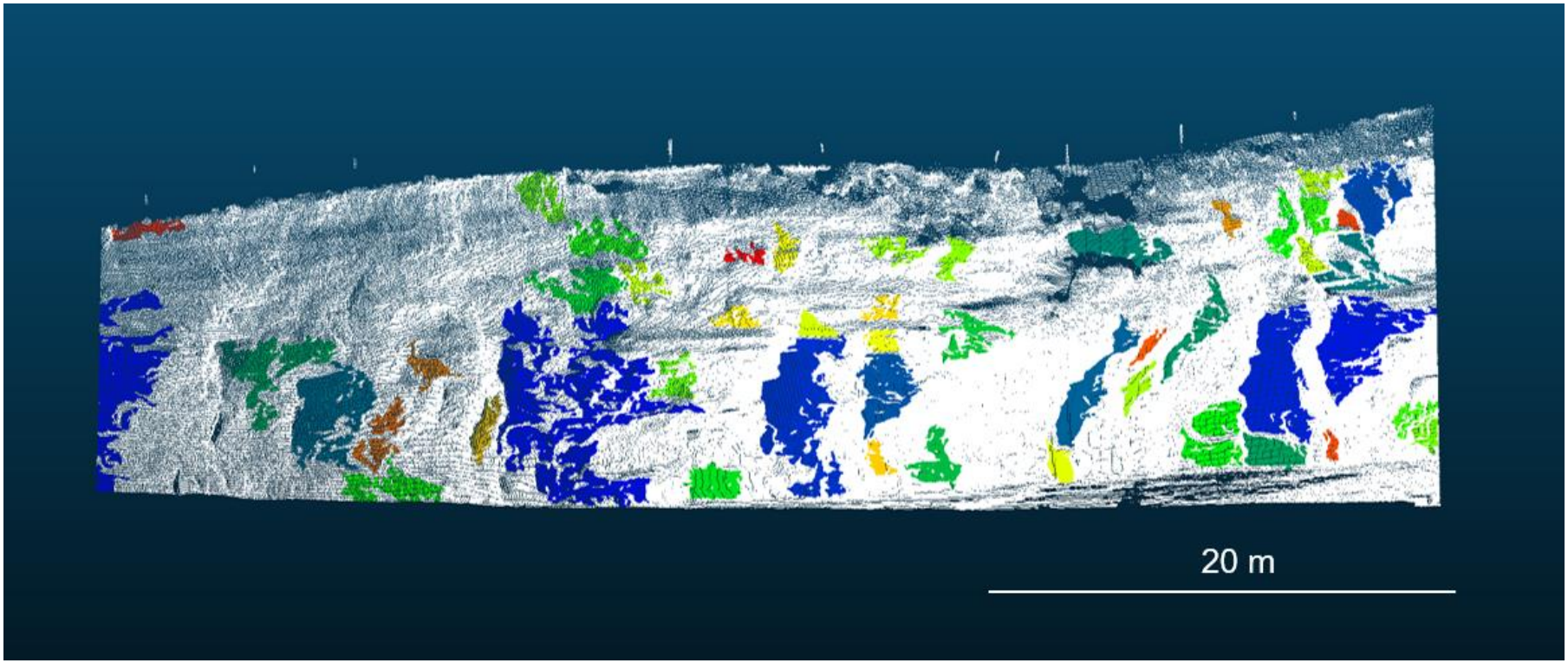

Figure 16. Cloud compare image of clusters in the dominant discontinuity set (DS_1) derived from DSE analysis for S01. Each colour represents a different cluster of points in the same discontinuity set, in this case DS_1.

Cliff section 2 (S02)

Two discontinuity sets were identified in S02. Discontinuities in J1 (Figure 17) are identified as bedding planes based on a dip of 3.86˚. The 2nd discontinuity set (DS_1) has a near vertical dip of 84˚and a dip direction of 104˚ m (Table 7). The total number of clusters in each discontinuity were 23 (J1) and 88 (DS_1). Of the total number of points, 14% were assigned to clusters in J1 and 46% to clusters in DS_1. As such, DS_1 was assigned as the dominant discontinuity set (Figure 18).

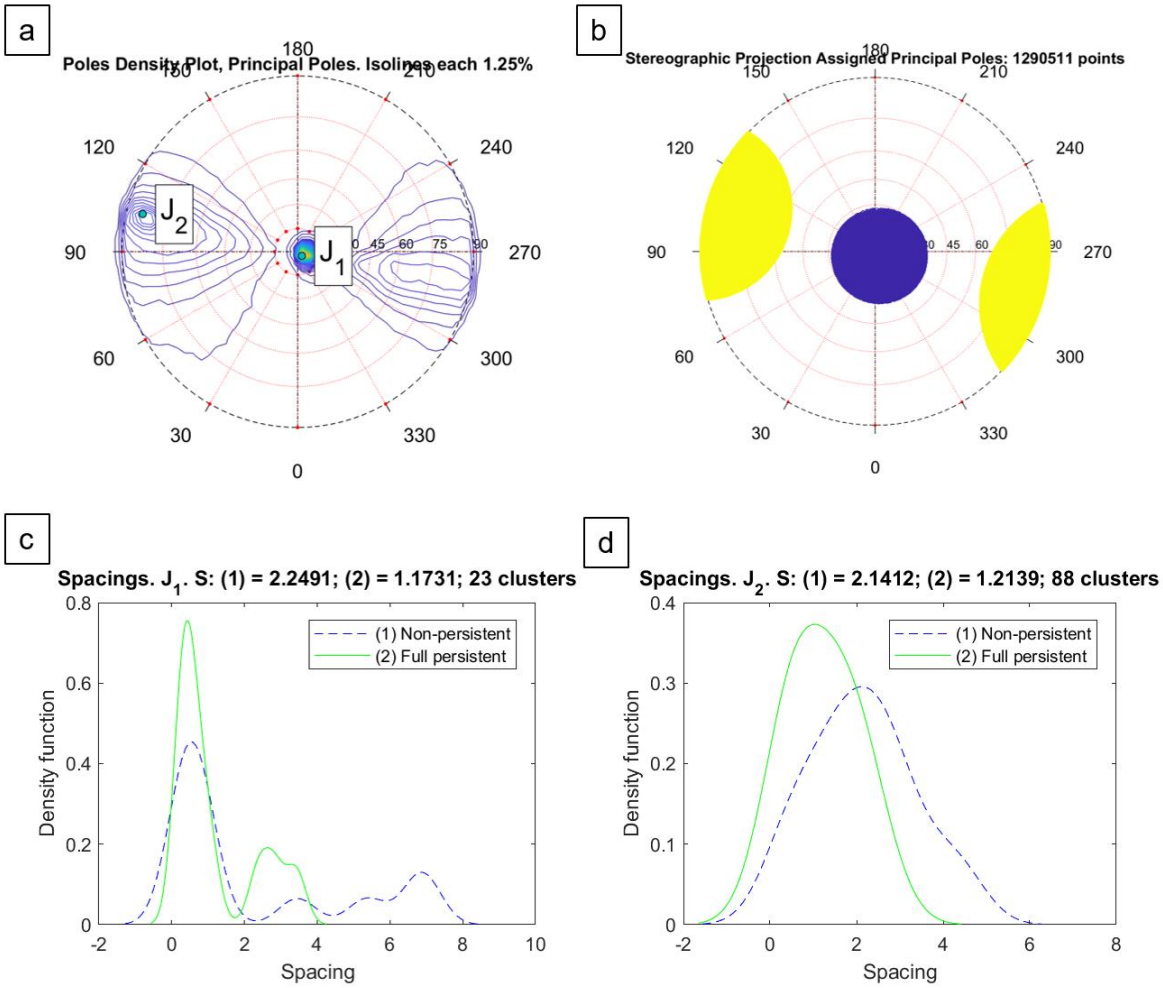

Figure 17. (a) Discontinuity Set Extractor pole density and principle poles assignment for cliff S02 (b) Stereographic projection of principle poles, (c and d) Density function of discontinuity spacing assuming non-persistence of discontinuities (blue dashed line) and full persistence of discontinuities (green solid line) for J1 (Bedding plane) and J2 (DS_1) respectively.

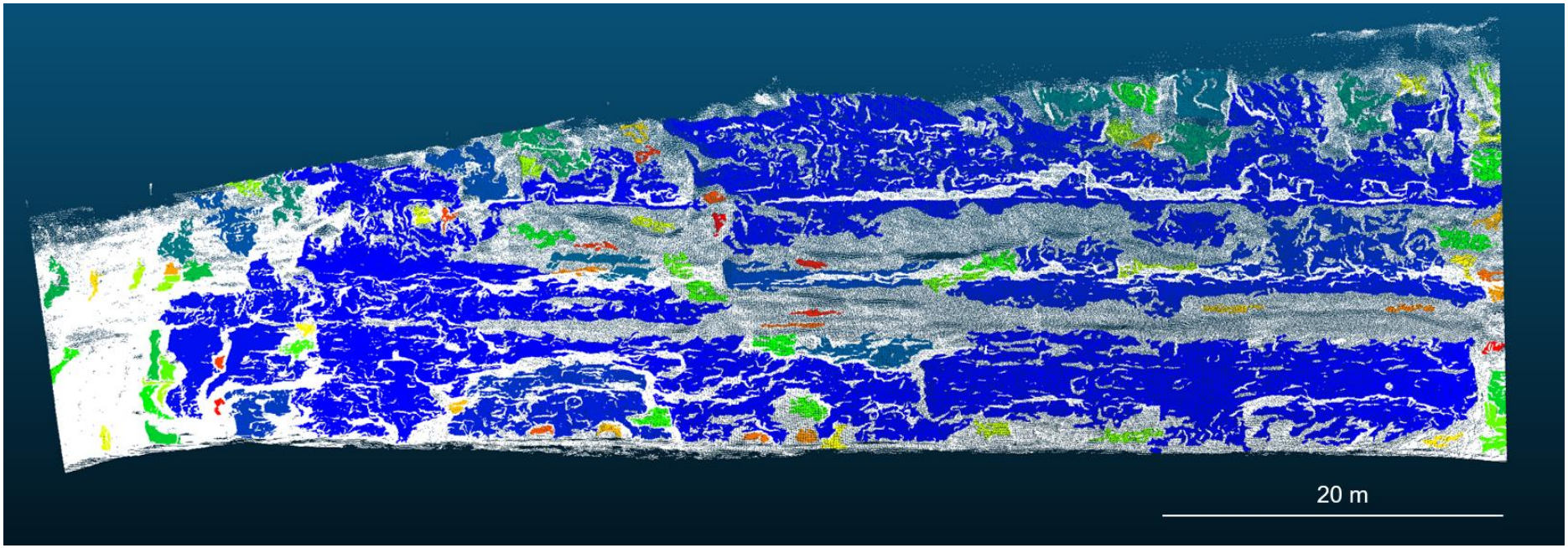

Figure18. Cloud compare image of clusters in the dominant discontinuity set (DS_1) derived from DSE analysis for S02. Each colour represents a different cluster of points in the same discontinuity set, in this case DS_1.

Cliff section 3 (S03)

Three discontinuity sets were identified in S03. Discontinuities in J1 (Figure 19) are identified as bedding planes based on a dip of 3.86˚. The 2nd discontinuity set (DS_1) has a near vertical dip of 74˚ and a dip direction of 279˚. The 3rd discontinuity set (DS_2) has a dip of 76 and dip direction of 92˚ (Table 7). The total number of clusters in each discontinuity were 55 (J1), 406 (DS_1) and 550 (DS_2). Of the total number of points 11% were assigned to clusters in J1, 28% to clusters in DS_1 and 31% to clusters in DS_2. Therefore, DS_2 was identified as the dominant discontinuity set (Figure 20).

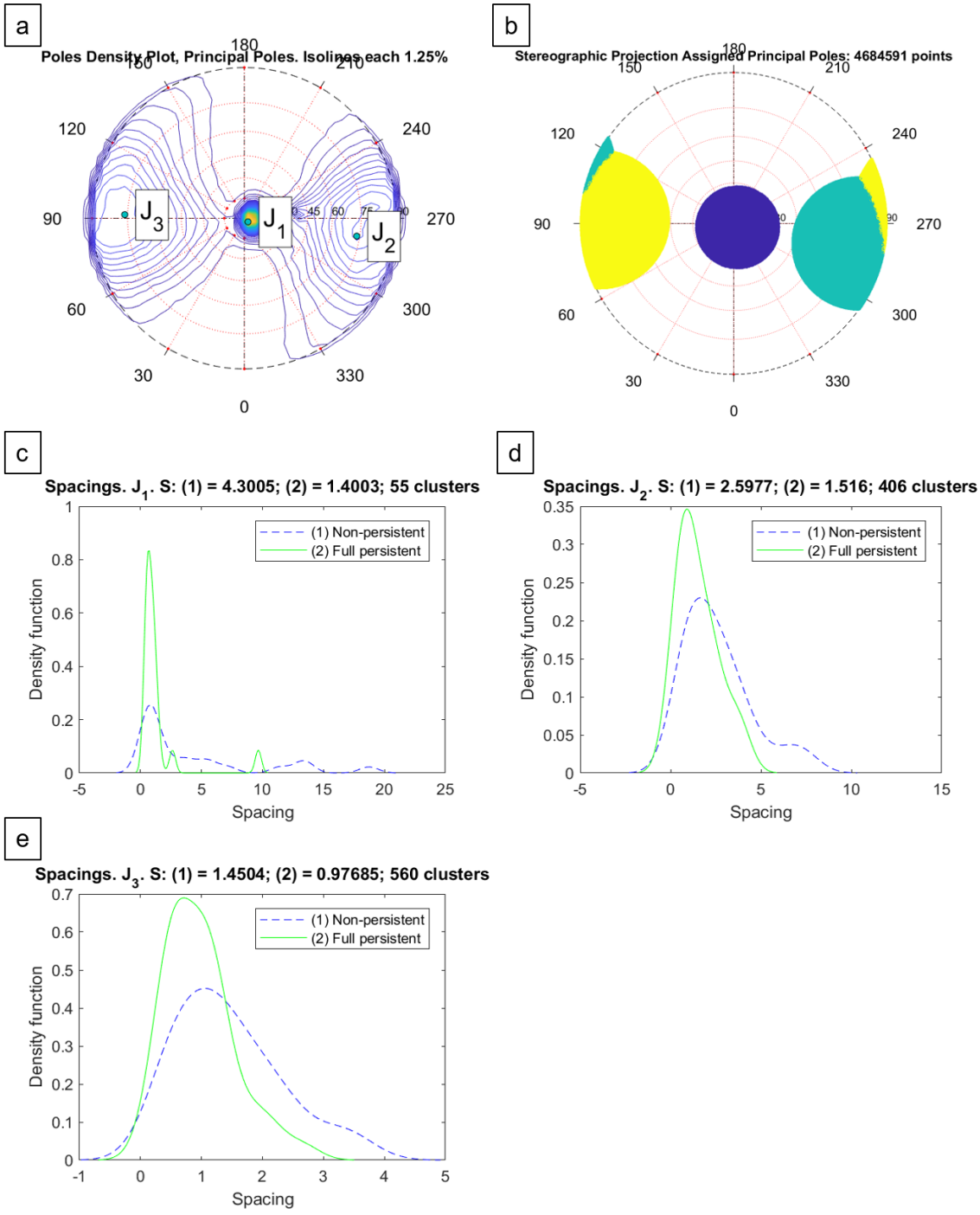

Figure 19. Discontinuity Set Extractor pole density and principle poles assignment for S03, (b) Stereographic projection of principle poles, (c, d and e) Density function of discontinuity spacing assuming non-persistence of discontinuities (blue dashed line) and full persistence of discontinuities (green solid line) for J1 (Bedding plane), J2 (DS_1) and J3 (DS_2) respectively.

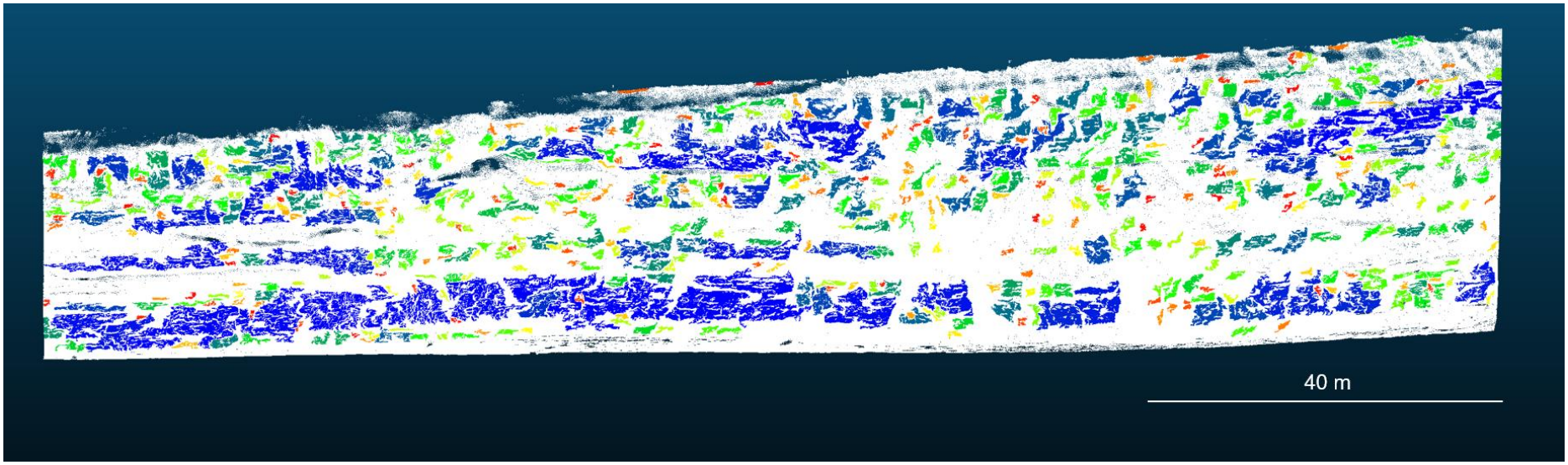

Figure 20. Cloud compare image of clusters in the dominant discontinuity set (DS_2) derived from DSE analysis for S03. Each colour represents a different cluster of points in the same discontinuity set, in this case DS_2.

Cliff section 4 (S04)

Discontinuity set extraction identified three discontinuity sets in S04. The 1st (J1) are discontinuities associated with bedding planes (based on dip of 3.86˚). The 2nd discontinuity set (DS_1) is a near vertical discontinuity set with a dip of 70˚ and dip direction of 268˚ (Table 7). A total of 12 and 37 and 213 clusters were identified in J1 and DS_1 (Figure 21) respectively. The percentage of points assigned to J1 and DS_2 were 34 and 28% respectively. Despite J1 being assigned a greater number of the total points, in order to compare cliff sections based on a like for like basis i.e. on near vertical discontinuities rather than bedding planes, we designated DS_1 as the dominant discontinuity set (Figure 22).

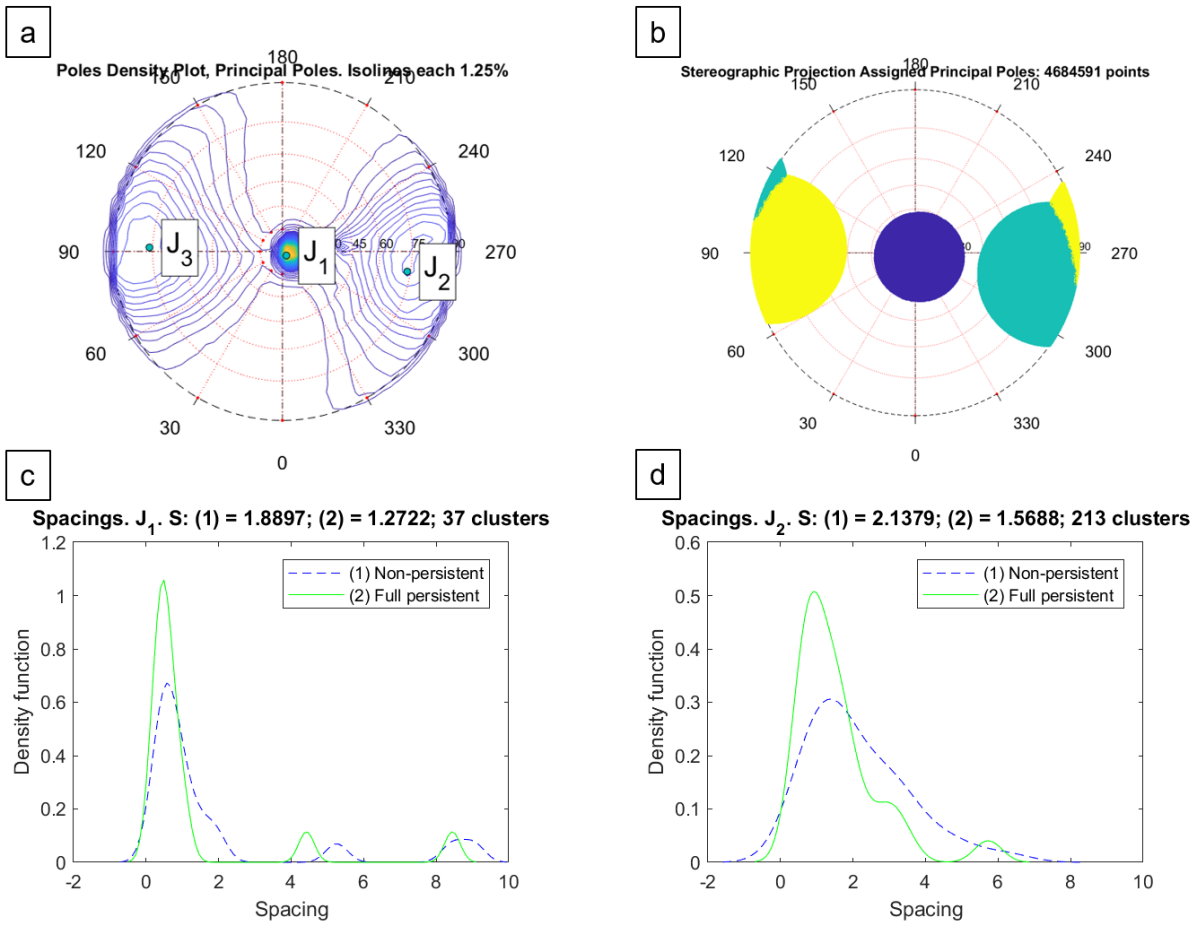

Figure 21. (a) Discontinuity Set Extractor pole density and principle poles assignment for S04, (b) Stereographic projection of principle poles, (c and d) Density function of discontinuity spacing assuming non-persistence of discontinuities (blue dashed line) and full persistence of discontinuities (green solid line) for J1 (bedding plane) and J2 (DS_1) respectively.

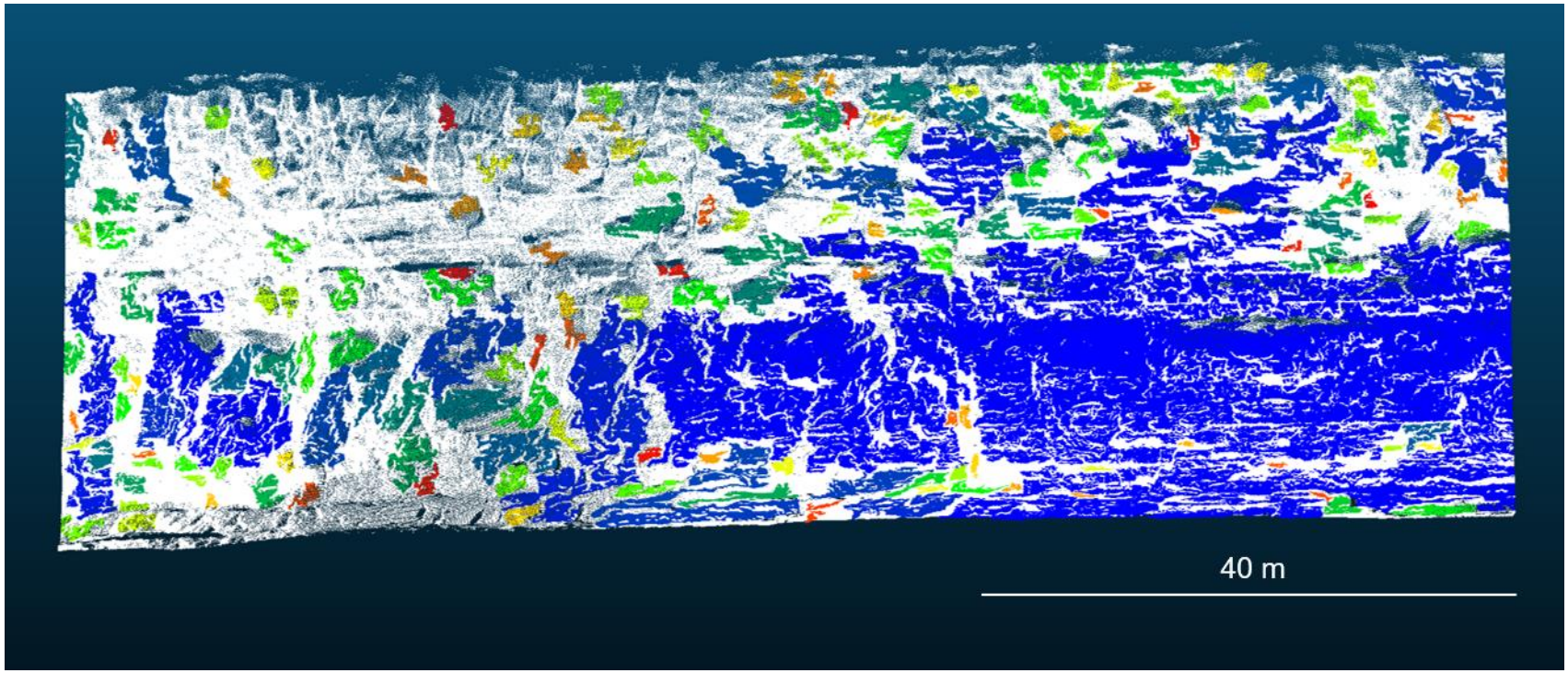

Figure 22. Cloud compare image of clusters in the dominant discontinuity set (DS_1) derived from DSE analysis for S04. Each colour represents a different cluster of points in the same discontinuity set, in this case DS_1.

Cliff section 5 (S05)

Two discontinuity sets were identified in S05. Discontinuities in J1 are identified as bedding planes based on a dip of 3.86˚. The 2nd discontinuity set (DS_1) has a near vertical dip of 80˚and a dip direction of 88˚ m (Table 7). The total number of clusters in each discontinuity were 51 (J1) and 440 (DS_1) (Figure 23). Of the total number of points, 6% were assigned to clusters in J1 and 43% to clusters in DS_1 (Table 7). As such DS_1 was assigned as the dominant discontinuity set (Figure 24).

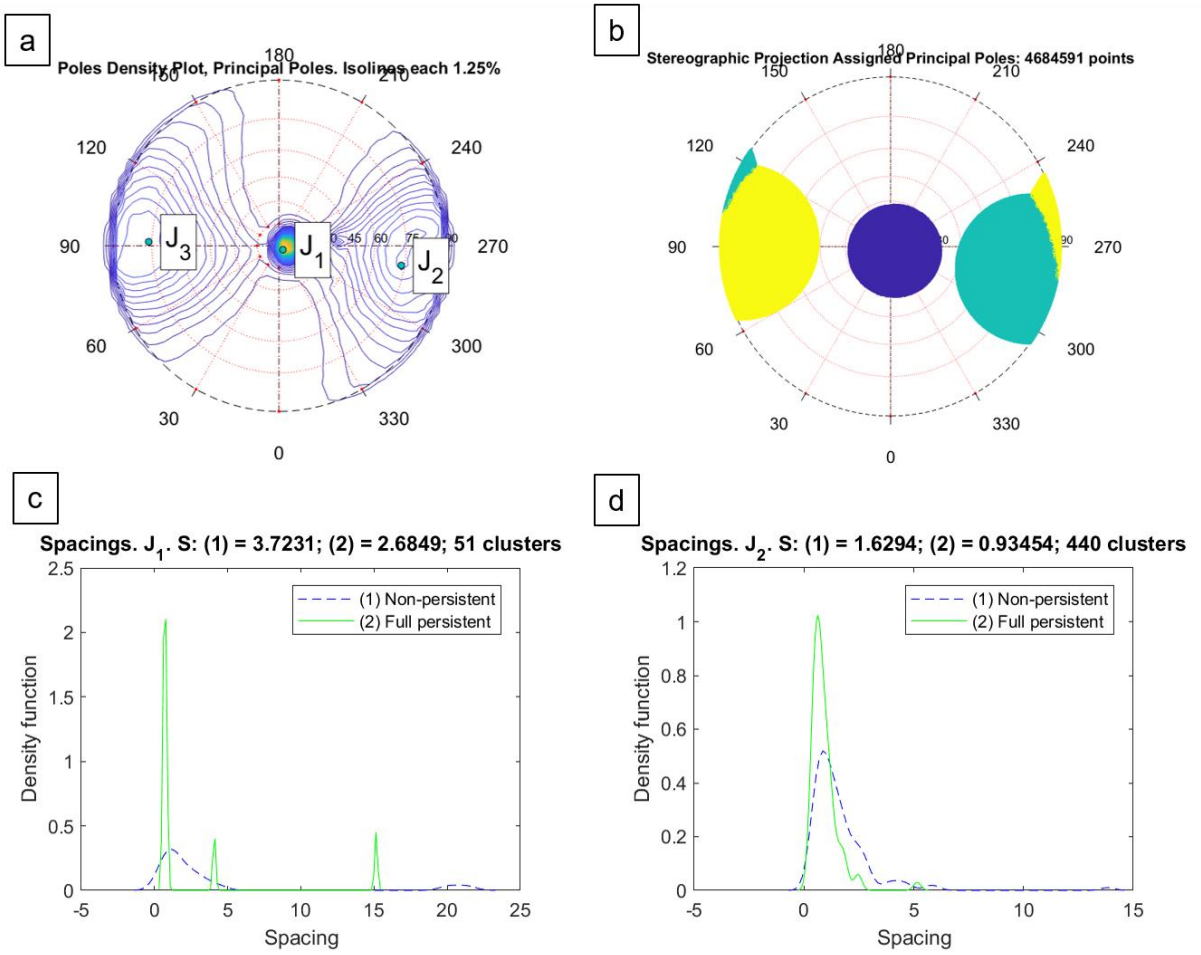

Figure 23. (a) Discontinuity Set Extractor pole density and principle poles assignment for S05, (b) Stereographic projection of principle poles, (c and) Density function of spacings density assuming non-persistence of discontinuities (blue dashed line) and full persistence of discontinuities (green solid line) for J1 (Bedding plane) and J2 (DS_1) respectively.

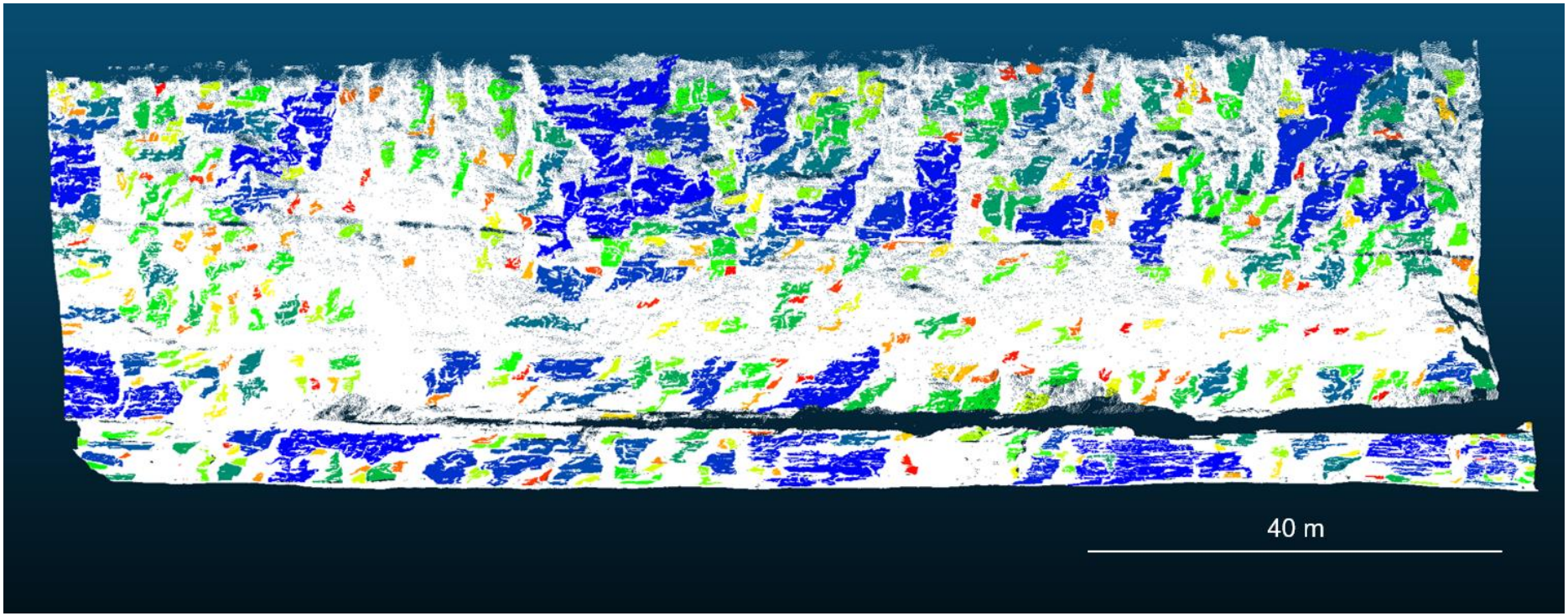

Figure 24. Cloud compare image of clusters in the dominant discontinuity (DS_1) set derived from DSE analysis for S05. Each colour represents a different cluster of points in the same discontinuity set, in this case DS_1.

Discontinuity set characteristics

List of abbreviations used to describe discontinuity set characteristics

S_{min} - minimum spacing

S_{max} – maximum spacing

S_{Mode} – mode spacing

$S\mu$ - mean spacing

SD_{max} - maximum spacing density

Prefix NP refers to assumption of non-persistence of discontinuities

Prefix FP refers to assumption of full persistence of discontinues

The statistics of the discontinuity sets are shown in Table 7. Assuming non-persistence (NP) of discontinuities, the minimum spacing (NPS_{min}) within a DS ranges from 0.15 m (S01/DS_1) to 0.46 m (S03/DS_1). Maximum distance between discontinuities within a DS (NPS_{max}), ranges from 4.40 m (S02/DS_1) to maximum of 14.28 m (S01/DS_2). The maximum density of discontinuities within a DS (NPSD_{max}), varies between 0.56 m in S01/DS_1 to a maximum of 1.57 in S02/DS_1. Mode spacing (NPS_{Mode}) ranged from 0.15 m to 0.46 m. Mean (NP$S\mu$) discontinuity spacing varies between 1.41 m in S01/DS_1 to 2.47 m in S01/DS_2.

Assuming the full persistence (FP) of discontinuities, the minimum spacing (FPS_{min}) within a DS ranges from 0.14 m (S03/DS_2) to 0.44 m (S04/DS_1). The maximum distance between discontinuities within a DS (FPS_{max}), ranges from 2.67 m (S03/DS_2) to maximum of 14.28 m (S01/DS_2). The maximum density of discontinuities within a DS (FPSD_{max}), varies between 0.48 m in S05/DS_1 to a maximum of 1.57 in S02/DS_1. Mode spacing (FPS_{Mode}) ranges from 0.14 m to 0.44 m. Mean (FP$S\mu$) discontinuity spacing varies between 0.98 m in S03/DS_2 to 2.17 m in S01/DS_2. For all discontinuity sets identified, spacing values that consider full

persistence of discontinuities are less than (or equal to) those that assume non-persistence of discontinuities (Table 7).

Table 7. Characteristics of the principle discontinuity sets in each section extracted from TLS point clouds using DSE (Riquelme et al. 2015). Discontinuity sets classified as horizontal bedding are not shown. NP and FP indicate assumption of non persistence and full persistence of discontinuities respectively. Dominant DS (% of total points) in each cliff section is highlighted in bold.

DS characteristics	**S01**				**S02**		**S03**				**S04**		**S05**	
	DS_1		*DS_2*		*DS_1*		*DS_1*		*DS_2*		*DS_1*		*DS_1*	
Spacing	(m)	(m)	(m)	(m)	(m)	(m)	(m)	(m)	(m)	(m)	(m)	(m)	(m)	(m)
Persistence	NP	FP	NP	FP	NP	FP	NP	FP	NP	FP	NP	FP	NP	FP
Min	0.15	0.15	0.22	0.22	0.31	0.31	0.46	0.20	0.30	0.14	0.44	0.44	0.26	0.22
Max	4.67	4.34	14.28	14.28	4.40	2.69	8.10	4.00	3.64	2.67	6.24	5.73	13.86	5.18
Max density	0.56	0.49	0.83	0.69	1.57	1.09	1.39	0.65	1.05	0.71m	1.39	0.90	0.82	0.48
Mode	0.15	0.15	0.22	0.22	0.31	0.31	0.46	0.20	0.30	0.14	0.44	0.44	0.26	0.22
μ	1.41	1.24	2.47	2.17	1.96	1.30	2.19	1.33	1.45	0.98	2.14	1.57	1.45	0.77
σ	1.25	1.18	3.03	3.14	1.25	0.78	1.69	1.06	0.85	0.56	1.36	1.17	1.46	0.59
Clusters (n)	46		42		84		427		560		213		441	
Dip direction (°)	104		194		104		279		92		268		88	
Dip angle (°)	84		84		84		75		76		69		80	
% of total points	**23**		11		**46**		28		**31**		**28**		**43**	

2.3.7 Relationships between discontinuity sets, the rockfall inventory, erosion rate and the spatial distribution of erosion.

Rockfall inventory

Multiple regression analysis of the dependent variable RfVol_{max} indicated that 100% of the variability was explained by the Dom*DS* variables D*Dir*, NPS_{min} and NPSD_{max}. NPSD_{max} had the greatest influence (R^2 = 0.98, P < 0.01) with RfVol_{max} decreasing as NPSD_{max} increases (Figure 25). No significant relationship was found between RfVol_{max} and Dom*DS* variables which assumed full persistence of discontinuities. Multiple regression of dependent variable RfVol_{mean} showed that 100% of the variability was explained by the Dom*DS* variables D*Dir*, NPS_{mode} and NPSD_{max} with NPSD_{max} having the greatest influence (R^2 = 0.84, P < 0.05) (Figure 25). No significant relationship was found between RfVol_{mean} and Dom*DS* variables which assumed full persistence of discontinuities.

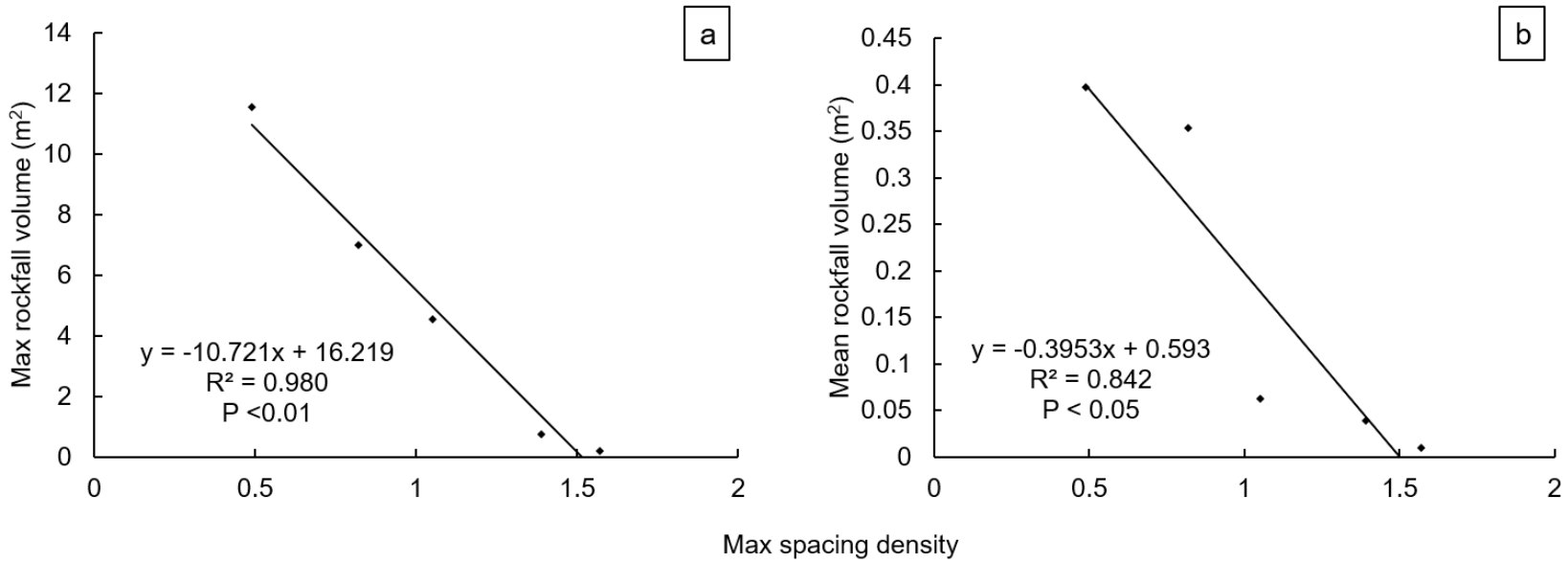

Figure 25. Linear regression of DS*Dom* maximum spacing density in S01–S05 and (a) maximum rockfall volume and (b) mean rockfall volume.

Multiple regression of dependent variable RF$RelI_{freq}$ indicates that 100% of the variability was explained by the variables Dir, NPS_{mode}, NPSD_{max} with NPSD_{max} having the most influence however the relationship is not statistically significant (P > 0.05).

Erosion rate

A significant negative power law relationship was also found between ER and NPDS_{max} (R^2 = 0.978, P <0.01) with ER decreasing with increasing NPDS_{max} (Figure 26). A statistically significant relationship (R^2 = 0.84, P < 0.05) was found between ER and RfVol_{max} with ER increasing exponentially with increasing values of RfVol_{max} (Figure 26). No significant relationship was found between ER and any DS characteristics which assumed full persistence of discontinuities.

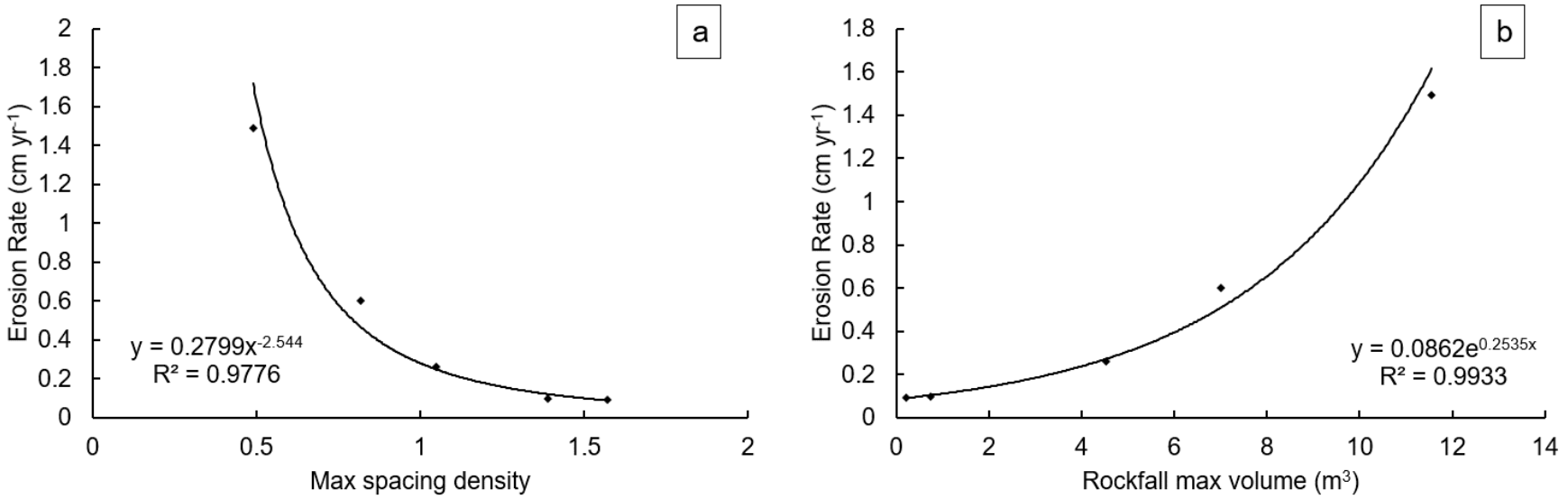

Figure 26. (a) Erosion rate - maximum spacing density distribution with fitted power law trendline and (b) exponential trendline fitted to the erosion rate – maximum rockfall volume distribution.

Surface area - Volume distribution

A statistically significant power law relationship was found between the variability around the Rf*SA* -Rf*Vol* fitted power law trendline and the StDev, i.e. variability, around the mean of discontinuity set spacing (Figure 27). No significant relationship was found between SA - Vol and any DS characteristics which assumed full persistence of discontinuities.

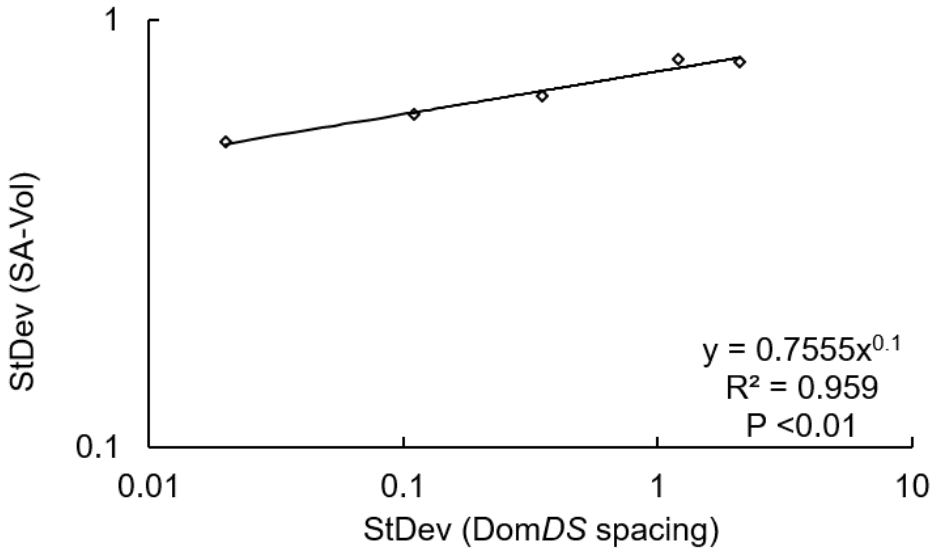

Figure 27. Log-log scale plot of the variability around the surface area – volume distribution fitted power law trendline and the standard deviation of spacing for the dominant discontinuity set in each cliff section.

Volume – Frequency distribution

Multiple regression analysis indicates that 100% of the variability in exponent β (i.e. where higher values of β indicate proportionally frequency of smaller rockfalls in an inventory) was explained by the variables DS*Dir*, NPD_{max}, NPSD_{max} with NPSD_{max} having the greatest influence (R^2 = 0.907, P < 0.05) (Figure 28).

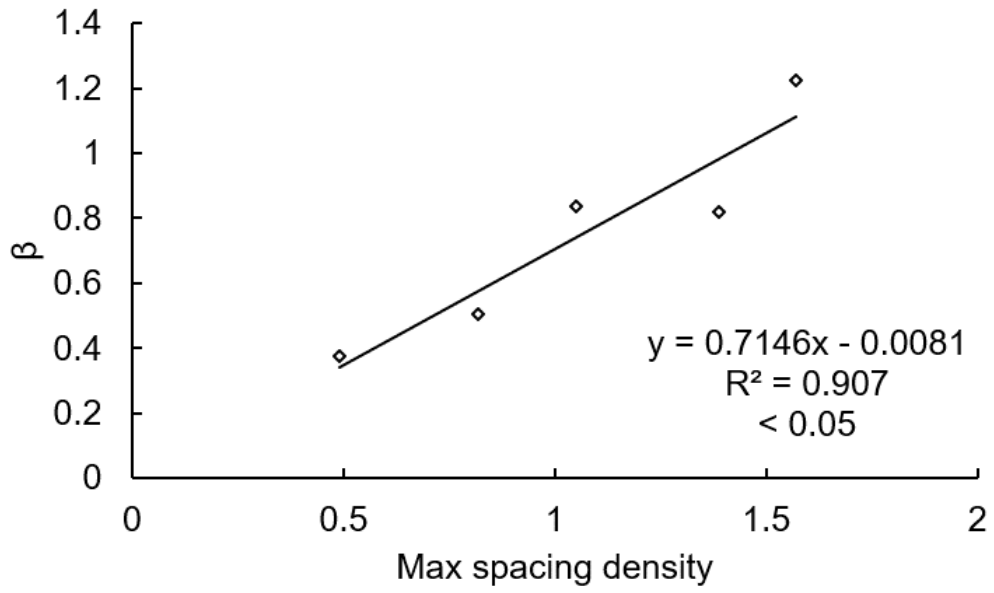

Figure 28. Linear plot of exponent β as a function of maximum spacing density of discontinuity sets for each section.

A significant power law relationship between exponent β and ER (R^2 = 0.827, P < 0.05), RfVol_{mean} (R^2 = 0.967, P < 0.05) and RfVol_{max} (R^2 = 0.772, P < 0.05) (Figure 29). All three variables exhibit a strong negative power law relationship to values of β i.e. to the proportion of smaller rockfalls within an inventory (Figure 29). No significant relationship was found between β and any DS characteristics which assumed full persistence of discontinuities.

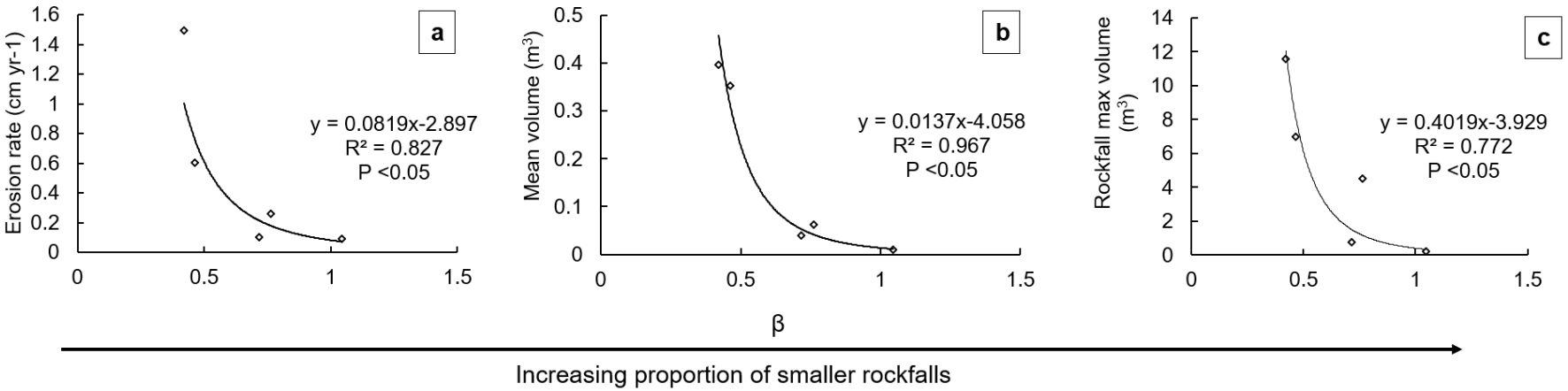

Figure 29. Power law trendline fitted to (a) β - erosion rate, (b) β – mean rockfall volume and (c) β – maximum rockfall volume distributions.

3.4 Discussion

Rockfall inventory

The rockfall inventory reveals differences in the relative frequency, mean and maximum rockfall volumes between cliff sections. We hypothesised that differences in the rockfall inventory characteristics between sections were due to differences in the characteristics of discontinuity sets. We find that the maximum density of discontinuities, assuming the non-persistence of discontinuities hypothesis, has the greatest influence on the mean and maximum volume of rockfalls in each of the cliff section inventories (discussed further below).

Although the orientation of discontinuities was found to explain some of the variability associated with the maximum and mean rockfall volume, the relationship was not found to be significant. Naylor and Stephenson (2010) found that the orientation of discontinuities can exert a significant influence of the rate and scale of blocks quarried by waves from shore platforms. We propose that the lack of any significant relationship between the orientation of discontinuities and other variables examined in this study is due to the overall orientation of discontinuities at the study site and to the mechanism of failure. Firstly, none of the discontinuity sets are orientated normal (perpendicular) to the shoreline and are thus largely perpendicular to the dominant incoming wave direction which reduces the potential for compression in discontinuities at the base of the cliff. Secondly, the hydraulic forces which can exploit discontinuity orientation on cliffs are not applicable above the reach of waves, hence the mechanism of detachment is very different. For locations where the orientation of discontinuities is different to that of the study site, the overall influence of orientation will also differ. The influence of discontinuity orientation at the study site is demonstrated on the platform where largescale discontinuities orientated ENE – SSW (near parallel to incoming wave directions) have been exploited and preferentially eroded, resulting in dissection of the platform along these discontinuities. The combined influence of wave action (chapter 3) and

discontinuities is also observed where undercutting at the cliff toe resulted in an overhanging rock mass which subsequently failed along discontinuity planes.

The lack of any significant relationship between the dependant variables investigated and discontinuity characteristics which assumed the full persistence are important. These findings suggest that the assumption of full persistence of discontinuities in rock masses (e.g. Slob, 2010) may be inappropriate for highly fractured, heterogenous rock masses such as the cliff in this study. This highlights one of the main advantages of semi-automated discontinuity set extraction from point clouds, as the approach is not subject to the same limitations, i.e. sampling bias and human error, as manual collection of discontinuity data in the field, thus providing a more accurate representation of discontinuities in the rock mass.

Rockfall surface area– volume distribution

Deviation from the fitted SA – Vol power-law trendline is indicative of failure mechanism with higher values of the exponent *b* (>1.2-1.3) interpreted as a dominance of deep seated failures along shear planes (Guzzetti et al., 2009, Larsen et al., 2010) and lower values where tensile stresses dominate (Rosser et. Al. 2007; Williams et al. 2018). With this in mind, we have interpreted the deviation from the power-law between rockfall inventories for a given cliff section as an indication of rockfall depth rather than failure mechanism, with smaller volumes relative to surface area (i.e. shallow failures) plotting below the line and higher volumes relative to surface area (i.e. deeper failures) plotting above the line. Using this interpretation, the strong relationship between the standard deviation from the SA-Vol power-law trendline and the standard deviation of discontinuity set spacing in each cliff section suggests that variability in discontinuity spacing contributes to the variability around the SA-Vol distribution trendline. Greater variability in the spacing of discontinuities would favor greater variability in the depth of rock fall relative to the surface area and thus, greater variability around the fitted power-law trendline, however more work is needed to validate this.

Rockfall volume – frequency distribution

The range of volume frequency distribution β values observed (β = 0.4 – 1.2) is similar to values observed for rockfalls in general (β = 0.4 – 1.1) (Santana et al., 2012) and for rockfalls in coastal cliffs with similar lithology on the north east coast of England (β = 0.71 – 2.37) (Rosser et al., 2007, Barlow et al., 2012, Whadcoat, 2017, Williams et al., 2018). A strong linear relationship between β and spacing density shows the influence of spacing density on the proportion of smaller rockfalls within an inventory, with higher proportions of smaller rockfalls associated with higher density of discontinuity spacing. This suggests that a higher density of spacing facilitates a relatively higher occurrence of smaller rockfalls. The strong negative power-law relationship that exists between β and mean rockfall volume is expected as a higher proportion of smaller rockfalls will have the effect of lowering the mean volume of the overall inventory. The strong relationship between maximum rockfall volume and maximum density of discontinuity spacing supports our previously stated finding regarding the influence of spacing density on the rockfall surface area – volume relationship i.e. higher spacing density yields a higher frequency of smaller rockfalls; lower spacing density results in larger, less frequent rockfalls. By way of example, S02 has the highest proportion of smaller rockfalls within its inventory, lowest maximum rockfall volume and the highest density of discontinuities, while S01 has the lowest proportion of smaller rockfalls within its inventory, highest maximum rockfall volume and the lowest density of discontinuities.

The rollover at the lower end of the volume spectrum observed is also similar to that observed in previous studies (e.g. Dussauge-Peisser et al., 2002, Corominas et al., 2017) For inventories using aerial images and at a larger scale (km -10^2 km) this may be due to incompleteness of record, i.e. failure to detect small failures (Hovius et al., 2000, Hungr et al., 2008). A similar trend was observed by Guthrie and Evans (2004) and Guzzetti et al. (2002). However, the authors concluded that other physical causes may be responsible as the rollover occurred at sizes well above the minimum size consistently mapped. We suggest that under

sampling is unlikely to be the cause as we also observed the rollover at volumes which are well represented in the inventories (< 0.01 m^3). At this time, we cannot identify the physical cause that may be responsible. A recent study which analysed very small detachments (<0.001 m^3) from a rock shore platform (Swirad et al., *In review*) also identified a rollover at the lower end of the volume spectrum and a complex shape to the overall distribution curve, which the authors attributed to the superimposition of successive smaller detachments between surveys. Due to the limitations of the sampling method, i.e. time interval between surveys, we cannot exclude the influence of superimposition of rockfall on the volume - frequency distribution. Williams et al. (2018) demonstrated that very high temporal resolution monitoring of coastal cliff erosion significantly increases the number of smaller rockfalls (<0.1 m^3) detected. They found a 67 to 98% increase in volume contributed by smaller rockfalls when the time interval between surveys was increased from 30 days to 1 hour. However, the authors also noted that for assessment of erosion rates longer intervals may be enough. Although our sampling interval represents a limitation, because we have compared our data between sections on a like for like basis we do not envisage that the sampling resolution has had a significant impact on the overall findings.

Erosion rate

The highest rate of erosion was found in S01 which coincides with the lowest density of discontinuities. The lowest erosion rate(s) were found in S02 and S04 which coincide with the 1st and 2nd highest density of discontinuity spacing respectively. However, our measured erosion rate demonstrates a statistically significant relationship to the maximum volume of rockfalls in an inventory, with higher rates of erosion having a strong positive relationship with increasing maximum rockfall volume in a cliff section. A similar relationship between erosion rate and maximum rockfall volume was also demonstrated by Matasci et al. (2015) in a study of the impact of fracturing patterns on the erosion rate of stratified limestone, where increasing maximum rockfall volume showed a strong positive relationship to erosion rate. The

relationship between erosion rate and maximum rockfall volume suggests that larger, less frequent rockfalls have a greater influence on the erosion rate than relatively higher frequency, lower volume rockfalls. This is also supported by the rockfall volume - cumulative frequency distributions. S01, where the highest rate of erosion occurred, had a lower proportion of smaller rockfalls in its inventory. S02 and S04, where the largest proportions of smaller rockfalls occurred, had the lowest erosion rates. Furthermore, maximum rock fall volume and the maximum spacing of discontinuities also exhibit a statistically significant relationship, with maximum density of discontinuity spacing inversely correlated to maximum rockfall volume on a linear scale, providing further evidence that larger rockfalls, facilitated by less densely fractured rock, have a greater influence on the overall rate of coastal cliff erosion.

The net rate of cliff erosion measured (0.037 m yr^{-1}) is at least two orders of magnitude greater than previous estimates for Ireland's rock coastline (0.001 m yr^{-1}) (Devoy, 2008). It is important to note that the study duration (t = 1 yr) is short compared to the timescale of erosion processes on rock coasts. These data may only be extrapolated to longer timescales with caution. It does however highlight a critical need for more long-term empirical measurements of erosion rates along Ireland's rock dominated coastline for a range of different lithologies (and wave regimes).

With respect to global measurements of rock coast retreat, the rate of erosion at the study site is an order of magnitude lower than the median rate calculated for soft rock such as chalks (0.2 m yr^{-1}) , and slightly higher than the median rate for hard rock lithologies (0.029 m yr^{-1}) (Prémaillon et al., 2018 and references therin). Given that the lithology of the site would be considered somewhere between medium and hard based on the classification used by Prémaillon et al. (2018), we suggest that the rate calculated here is within realistic estimates for coastal cliffs of this rock type based on the measured rates globally. Despite this, and given the stochastic nature of rock coast erosion, we acknowledge that more accurate estimation of longer-term rates of erosion will only be possible with additional longer-term monitoring at this

and other locations. Furthermore, although calculation of a mean erosion rate is useful and indeed necessary, given the variability of erosion rates at this one site we also apply a cautionary note to application of mean erosion rates for any given lithology between locations without a greater understanding of dominant controls on the spatial distribution of erosion (e.g. the role of discontinuities, degree of weathering and wave climate).

The role of discontinuities in mediating the spatial distribution of cliff erosion also has implications for subsequent erosion of contiguous shore platforms. A recent study by Cullen et al. (2018) (see chapter 4) demonstrated a positive feedback between cliff and platform erosion, where material supplied by the cliff was shown to abrade the platform surface via abrasion by clast transport. The variation in location, size and frequency of clasts supplied from the cliff to the platform will produce variable impacts of clast abrasion and rates of erosion across the platform. Hence, the characteristics of discontinuities which control the spatial distribution of erosion of the cliff, have a secondary influence on erosion of the platform.

Discontinuity set extraction

Identifying and determining the characteristics of the most relevant discontinuities for a given process remains a major challenge in relating field measured discontinuity characteristics to erosion rates (Scott and Wohl, 2018). The application of DSE for extraction of discontinuity sets does require some degree of expertise in rock mechanics, and perhaps some previous knowledge of the location of interest. We observed incorrectly identified discontinuity sets which would have significantly affected the results of our analysis had they not been removed. Despite this, DSE provides an extremely useful tool for extraction of discontinuity set characteristics from point clouds that is also very user friendly. The semi-automated nature of the software means that the user still has full control over the results. In our case this allowed us to identify and remove ‘false’ discontinuity sets providing a more accurate characterization of the rock mass structure. Although not employed in this study, recent developments in the

software (e.g. Riquelme et al., 2018) also allow calculation of discontinuity persistence. Application of this tool will be useful to investigate our interpretation that the assumption of the full persistence of discontinuities in rock mass characterization studies may be inappropriate for highly fractured rock masses.

An additional and significant advantage of the overall approach is the potential for retrospective analysis of previously collected data to contribute to questions which remain regarding controls on the variability of coastal cliff erosion rates, particularly where longer-term data sets with higher temporal resolution are available. Furthermore, the approach is also valid for SfM derived point clouds generated from UAV images (Riquelme et al., 2015), which means that locations not accessible for TLS can also be characterized with relative ease. Combined with geomorphic change detection techniques which also utilize SfM Photogrammetry from UAV, this will permit unprecedented characterization of rock masses in difficult to access terrains. This will improve our understanding of controls on the spatial distribution of erosion and hence advance predictive models of erosion rates and coastal evolution. There is added potential to characterize large swathes of coastal cliffs if the semi-automated discontinuity set extraction technique can be applied to high resolution satellite data e.g., from European Space Agency Copernicus suite, although the resolution may only pick up large scale discontinuities.

3.5 Conclusions

This study is the first empirical assessment of the influence of discontinuities on rock coast cliff erosion rates. The results demonstrate the importance of discontinuity set characteristics in mediating the spatial distribution of erosion.

1. We find that spacing density has the greatest influence on rockfall inventory characteristics and erosion rate. Higher spacing density is associated with a higher proportion of smaller rockfalls in an inventory and lower rates of erosion. Lower spacing density is associated with higher maximum rockfall volume and higher rates of erosion. These findings indicate that high magnitude, low frequency rockfalls have a greater influence on the rate of erosion than higher frequency, lower magnitude rockfalls.

2. The net rate of erosion calculated here is two orders of magnitude greater than that previously estimated for Ireland's rock coast.

3. The results also indicate that assumption of discontinuity persistence in characterization of rock masses for slope stability assessment may be inappropriate for highly fractured, heterogenous rock masses.

4. In this study we have employed semi-automated discontinuity set extraction from points clouds using freely available software DSE. This approach, while requiring a degree of scrutiny, provides an extremely useful tool for rock coast geomorphologists for characterization of discontinuity sets in coastal cliffs. This study demonstrates the critical importance of incorporating empirical measurements of discontinuity set characteristics when trying to explain variations in the spatial distribution of erosion for rock dominated coastal cliffs.

Acknowledgments

The authors would like to thank Dr. Adrian Riquelme (University of Alicante) for his guidance on using DSE software and for providing a DSE executable compatible with MatLab educational version.

References

BALAGUER-PUIG, M., MARQUÉS-MATEU, Á., LERMA, J. L. & IBÁÑEZ-ASENSIO, S. 2017. Estimation of small-scale soil erosion in laboratory experiments with Structure from Motion photogrammetry. *Geomorphology*.

BARLOW, J., LIM, M., ROSSER, N., PETLEY, D., BRAIN, M., NORMAN, E. & GEER, M. 2012. Modeling cliff erosion using negative power law scaling of rockfalls. *Geomorphology,* 139**,** 416-424.

BOWEN, D., PHILLIPS, F., MCCABE, A., KNUTZ, P. & SYKES, G. 2002. New data for the last glacial maximum in Great Britain and Ireland. *Quaternary Science Reviews,* 21**,** 89-101.

BRASINGTON, J., RUMSBY, B. & MCVEY, R. 2000. Monitoring and modelling morphological change in a braided gravel-bed river using high resolution GPS-based survey. *Earth Surface Processes and Landforms,* 25**,** 973-990.

BRODU, N. & LAGUE, D. 2012. 3D terrestrial lidar data classification of complex natural scenes using a multi-scale dimensionality criterion: Applications in geomorphology. *ISPRS Journal of Photogrammetry and Remote Sensing,* 68**,** 121-134.

BUYER, A. & SCHUBERT, W. 2016. Extraction of discontinuity orientations in point clouds. *Rock Mechanics and Rock Engineering: From the Past to the Future,* 2**,** 1133-1138.

CIGNONI, P., ROCCHINI, C. & SCOPIGNO, R. Metro: measuring error on simplified surfaces. Computer Graphics Forum, 1998. Wiley Online Library, 167-174.

COLLINSON, J. D., MARTINSEN, O., BAKKEN, B. & KLOSTER, A. 1991. Early fill of the Western Irish Namurian Basin: a complex relationship between turbidites and deltas. *Basin Research,* 3**,** 223-242.

COMPARE, C. 2013. Cloud Compare.

COROMINAS, J., MAVROULI, O. & RUIZ-CARULLA, R. 2017. Magnitude and frequency relations: are there geological constraints to the rockfall size? *Landslides***,** 1-17.

CRUSLOCK, E. M., NAYLOR, L. A., FOOTE, Y. L. & SWANTESSON, J. O. 2010. Geomorphologic equifinality: A comparison between shore platforms in Höga Kusten and Fårö, Sweden and the Vale of Glamorgan, South Wales, UK. *Geomorphology,* 114**,** 78-88.

CULLEN, N. D. & BOURKE, M. C. 2018. Clast abrasion of a rock shore platform on the Atlantic coast of Ireland. *Earth Surface Processes and Landforms,* 43 (12) 2627-2641.

DEVOY, R. J. 2008. Coastal vulnerability and the implications of sea-level rise for Ireland. *Journal of Coastal research***,** 325-341.

DUSSAUGE-PEISSER, C., HELMSTETTER, A., GRASSO, J.-R., HANTZ, D., DESVARREUX, P., JEANNIN, M. & GIRAUD, A. 2002. Probabilistic approach to rock fall hazard assessment: potential of historical data analysis. *Natural Hazards and Earth System Science,* 2**,** 15-26.

EARLIE, C. S. 2015. Field observations of wave induced coastal cliff erosion, Cornwall, UK.

ÉIREANN, M. 2015. Met Eireann. Shannon Airport 1971–2000 averages Dublin, Ireland.: Met Éireann.

ESTER, M., KRIEGEL, H.-P., SANDER, J. & XU, X. A density-based algorithm for discovering clusters in large spatial databases with noise. Kdd, 1996. 226-231.

FARO 2016. *Faro Scene cloud processing software* (version 6.2) [software] Available at https://www.faro.com/products/product-design/faro-scene.

GALLAGHER, S., TIRON, R. & DIAS, F. 2014. A long-term nearshore wave hindcast for Ireland: Atlantic and Irish Sea coasts (1979–2012). *Ocean Dynamics,* 64**,** 1163-1180.

GARDNER, J. 1983. Rockfall frequency and distribution in the Highwood Pass area, Canadian Rocky Mountains. *Zeitshrift fur Geomorphologie, NF,* 27**,** 311-324.

GARDNER, J. S. 1980. Frequency, magnitude and spatial distribution of mountain rockfalls and rockslides in the Highwood Pass area, Alberta, Canada. *Thresholds in Geomorphology. Allen and Unwin, New York***,** 267-295.

GIRARDEAU-MONTAUT, D., ROUX, M., MARC, R. & THIBAULT, G. 2005. Change detection on points cloud data acquired with a ground laser scanner. *International Archives of Photogrammetry, Remote Sensing and Spatial Information Sciences,* 36**,** W19.

GUTHRIE, R. & EVANS, S. 2004. Magnitude and frequency of landslides triggered by a storm event, Loughborough Inlet, British Columbia. *Natural Hazards and Earth System Science,* 4**,** 475-483.

GUZZETTI, F., ARDIZZONE, F., CARDINALI, M., ROSSI, M. & VALIGI, D. 2009. Landslide volumes and landslide mobilization rates in Umbria, central Italy. *Earth and Planetary Science Letters,* 279**,** 222-229.

GUZZETTI, F., MALAMUD, B. D., TURCOTTE, D. L. & REICHENBACH, P. 2002. Power-law correlations of landslide areas in central Italy. *Earth and Planetary Science Letters,* 195**,** 169-183.

HODSON, F. & LEWARNE, G. C. 1961. A mid-Carboniferous (Namurian) basin in parts of the counties of Limerick and Clare, Ireland. *Quarterly Journal of the Geological Society,* 117**,** 307-333.

HOVIUS, N., STARK, C. P., HAO-TSU, C. & JIUN-CHUAN, L. 2000. Supply and removal of sediment in a landslide-dominated mountain belt: Central Range, Taiwan. *The Journal of Geology,* 108**,** 73-89.

HUDSON, J. A. & HARRISON, J. 1997. Engineering rock mechanics, vol. I. Pergamon.

HUNGR, O., EVANS, S. & HAZZARD, J. 1999. Magnitude and frequency of rock falls and rock slides along the main transportation corridors of southwestern British Columbia. *Canadian Geotechnical Journal,* 36**,** 224-238.

HUNGR, O., MCDOUGALL, S., WISE, M. & CULLEN, M. 2008. Magnitude–frequency relationships of debris flows and debris avalanches in relation to slope relief. *Geomorphology,* 96**,** 355-365.

KAZHDAN, M. & HOPPE, H. 2013. Screened poisson surface reconstruction. *ACM Transactions on Graphics (ToG),* 32**,** 29.

KEMENY, J. & POST, R. 2003. Estimating three-dimensional rock discontinuity orientation from digital images of fracture traces. *Computers & Geosciences,* 29**,** 65-77.

LAGUE, D., BRODU, N. & LEROUX, J. 2013. Accurate 3D comparison of complex topography with terrestrial laser scanner: Application to the Rangitikei canyon (NZ). *ISPRS journal of photogrammetry and remote sensing,* 82**,** 10-26.

LANE, S. N., WESTAWAY, R. M. & MURRAY HICKS, D. 2003. Estimation of erosion and deposition volumes in a large, gravel-bed, braided river using synoptic remote sensing. *Earth Surface Processes and Landforms,* 28**,** 249-271.

LARSEN, I. J., MONTGOMERY, D. R. & KORUP, O. 2010. Landslide erosion controlled by hillslope material. *Nature Geoscience,* 3**,** 247.

LEICA 2015. *Leica Cyclone, 3D point cloud processing software*. (version 8.1) [software] Available at http://hds.leica-geosystems.com/en/Leica-Cyclone_6515.htm.

LIM, M., ROSSER, N. J., ALLISON, R. J. & PETLEY, D. N. 2010. Erosional processes in the hard rock coastal cliffs at Staithes, North Yorkshire. *Geomorphology,* 114**,** 12-21.

MALAMUD, B. D., TURCOTTE, D. L., GUZZETTI, F. & REICHENBACH, P. 2004. Landslide inventories and their statistical properties. *Earth Surface Processes and Landforms,* 29**,** 687-711.

MATASCI, B., JABOYEDOFF, M., LOYE, A., PEDRAZZINI, A., DERRON, M.-H. & PEDROZZI, G. 2015. Impacts of fracturing patterns on the rockfall susceptibility and erosion rate of stratified limestone. *Geomorphology,* 241**,** 83-97.

MILAN, D. J., HERITAGE, G. L. & HETHERINGTON, D. 2007. Application of a 3D laser scanner in the assessment of erosion and deposition volumes and channel change in a proglacial river. *Earth Surface Processes and Landforms: The Journal of the British Geomorphological Research Group,* 32**,** 1657-1674.

NAYLOR, L. & STEPHENSON, W. 2010. On the role of discontinuities in mediating shore platform erosion. *Geomorphology,* 114**,** 89-100.

PETERS, J. L., BENETTI, S., DUNLOP, P., COFAIGH, C. Ó., MORETON, S. G., WHEELER, A. J. & CLARK, C. D. 2016. Sedimentology and chronology of the advance and retreat of the last British-Irish Ice Sheet on the continental shelf west of Ireland. *Quaternary Science Reviews,* 140**,** 101-124.

PRÉMAILLON, M., REGARD, V., DEWEZ, T. J. & AUDA, Y. 2018. GlobR2C2 (Global Recession Rates of Coastal Cliffs): a global relational database to investigate coastal rocky cliff erosion rate variations. *Earth Surface Dynamics,* 6**,** 651-668.

PRIEST, S. & HUDSON, J. Estimation of discontinuity spacing and trace length using scanline surveys. International Journal of Rock Mechanics and Mining Sciences & Geomechanics Abstracts, 1981. Elsevier, 183-197.

PULHAM, A. 1989. Controls on internal structure and architecture of sandstone bodies within Upper Carboniferous fluvial-dominated deltas, County Clare, western Ireland. *Geological Society, London, Special Publications,* 41**,** 179-203.

RIDER, M. The Namurian of West County Clare. Proceedings of the Royal Irish Academy. Section B: Biological, Geological, and Chemical Science, 1974. JSTOR, 125-142.

RIQUELME, A., TOMÁS, R., CANO, M., PASTOR, J. L. & ABELLÁN, A. 2018. Automatic Mapping of Discontinuity Persistence on Rock Masses Using 3D Point Clouds. *Rock Mechanics and Rock Engineering***,** 1-24.

RIQUELME, A. J., ABELLÁN, A. & TOMÁS, R. 2015. Discontinuity spacing analysis in rock masses using 3D point clouds. *Engineering Geology,* 195**,** 185-195.

RIQUELME, A. J., ABELLÁN, A., TOMÁS, R. & JABOYEDOFF, M. 2014. A new approach for semi-automatic rock mass joints recognition from 3D point clouds. *Computers & Geosciences,* 68**,** 38-52.

RIQUELME, A. J., TOMÁS, R. & ABELLÁN, A. 2016. Characterization of rock slopes through slope mass rating using 3D point clouds. *International Journal of Rock Mechanics and Mining Sciences,* 84**,** 165-176.

ROSSER, N., LIM, M., PETLEY, D., DUNNING, S. & ALLISON, R. 2007. Patterns of precursory rockfall prior to slope failure. *Journal of geophysical research: earth surface,* 112.

ROSSER, N. J., BRAIN, M. J., PETLEY, D. N., LIM, M. & NORMAN, E. C. 2013. Coastline retreat via progressive failure of rocky coastal cliffs. *Geology,* 41**,** 939-942.

SANTANA, D., COROMINAS, J., MAVROULI, O. & GARCIA-SELLÉS, D. 2012. Magnitude–frequency relation for rockfall scars using a Terrestrial Laser Scanner. *Engineering geology,* 145**,** 50-64.

SCOTT, D. N. & WOHL, E. E. 2018. Bedrock Fracture Influences on Geomorphic Process and Form Across Process Domains and Scales. *Earth Surface Processes and Landforms*.

SILVERMAN, B. W. 2018. *Density estimation for statistics and data analysis*, Routledge.

SLOB, S. 2010. *Automated rock mass characterisation using 3-D terrestrial laser scanning.* TU Delft, Delft University of Technology.

SLOB, S., HACK, R. & TURNER, A. K. An approach to automate discontinuity measurements of rock faces using laser scanning techniques. ISRM International Symposium-EUROCK 2002, 2002. International Society for Rock Mechanics and Rock Engineering.

SLOB, S., VAN KNAPEN, B., HACK, R., TURNER, K. & KEMENY, J. 2005. Method for automated discontinuity analysis of rock slopes with three-dimensional laser scanning. *Transportation research record: journal of the transportation research board*, 187-194.

STEPHENSON, W. & NAYLOR, L. 2011. Within site geological contingency and its effect on rock coast erosion. *Journal of Coastal Research,* 61, 831-835.

STOCKAMP, J., LI, Z., BISHOP, P., HANSOM, J., RENNIE, A., PETRIE, E., TANAKA, A., BINGLEY, R. & HANSEN, D. Investigating Glacial Isostatic Adjustment in Scotland with InSAR and GPS Observations. Proceedings of FRINGE, 2015.

SUNAMURA, T. 1992. *Geomorphology of rocky coasts*, John Wiley & Son Ltd.

SUNAMURA, T. Rock control in coastal geomorphic processes. International Journal of Rock Mechanics and Mining Sciences and Geomechanics Abstracts, 1995. 103A.

SWIRAD, Z., ROSSER, N. & BRAIN, M. *In review*. Identifying mechanisms of shore platform erosion using Structure-from-Motion (SfM) Photogrammetry. *Earth surface Processes and Landforms*.

TRENHAILE, A. S. 1987. *The geomorphology of rock coasts*, Oxford University Press, USA.

VERMA, A. K. & BOURKE, M. C. 2018. A Structure from Motion photogrammetry-based method to generate sub-millimetre resolution Digital Elevation Models for investigating rock breakdown features. *Earth Surf. Dynam. Discuss.,* 4, 5.

WHADCOAT, S. K. 2017. *Numerical modelling of rockfall evolution in hard rock slopes.* Durham University.

WILLIAMS, J. G., ROSSER, N. J., HARDY, R. J., BRAIN, M. J. & AFANA, A. A. 2018. Optimising 4-D surface change detection: an approach for capturing rockfall magnitude–frequency. *Earth surface dynamics.,* 6**,** 101-119.

XLSTAT 2017. Data Analysis and Statistical Solution for Microsoft Excel. . Paris, France.: Addinsoft.

YATSU, E. 1966. *Rock control in geomorphology*, Sozosha.

3.6 Supplementary tables

Table S1. Rockfall (RF) ID, surface area (SA) and volume (Vol) of rockfalls in the inventory.

RF ID	SA m^2	Vol $-m^3$	RF ID	SA m^2	Vol m^3	RF ID	SA m^2	Vol m^3
S01_RF_01	0.18	0.024	S02_RF_01	0.142	0.009	S02_RF_31	0.277	0.032
S01_RF_02	1.259	0.085	S02_RF_02	0.027	0.002	S02_RF_32	0.052	0.002
S01_RF_03	0.772	0.033	S02_RF_03	0.066	0.002	S02_RF_33	0.044	0.002
S01_RF_04	0.214	0.008	S02_RF_04	0.116	0.003	S02_RF_34	0.028	0.001
S01_RF_05	0.083	0.011	S02_RF_05	0.307	0.009	S02_RF_35	0.136	0.01
S01_RF_06	0.177	0.015	S02_RF_06	0.303	0.009	S02_RF_36	0.024	0.002
S01_RF_07	0.079	0.001	S02_RF_07	0.245	0.01	S02_RF_37	0.034	0.005
S01_RF_08	0.054	0.007	S02_RF_08	0.085	0.001	S02_RF_38	0.369	0.048
S01_RF_09	0.631	0.055	S02_RF_09	0.315	0.019	S02_RF_39	0.019	0.002
S01_RF_10	0.06	0.007	S02_RF_10	0.18	0.014	S02_RF_40	0.077	0.007
S01_RF_11	0.046	0.005	S02_RF_11	0.106	0.006	S02_RF_41	0.073	0.008
S01_RF_12	0.027	0.002	S02_RF_12	0.162	0.004	S02_RF_42	0.039	0.003
S01_RF_13	0.018	0.004	S02_RF_13	0.228	0.006	S02_RF_43	0.101	0.009
S01_RF_14	0.026	0.004	S02_RF_14	0.061	0.002	S02_RF_44	0.189	0.012
S01_RF_15	0.057	0.002	S02_RF_15	0.11	0.002	S02_RF_45	0.068	0.004
S01_RF_16	0.125	0.014	S02_RF_16	0.306	0.012	S02_RF_46	0.04	0.004
S01_RF_17	0.806	0.03	S02_RF_17	0.041	0.003	S02_RF_47	0.371	0.019
S01_RF_18	0.072	0.002	S02_RF_18	0.081	0.001	S02_RF_48	0.313	0.019
S01_RF_19	0.072	0.002	S02_RF_19	0.026	0.002	S02_RF_49	0.106	0.01
S01_RF_20	0.072	0.005	S02_RF_20	0.061	0.005	S02_RF_50	1.545	0.123
S01_RF_21	0.038	0.002	S02_RF_21	0.029	0.002	S02_RF_51	0.092	0.007
S01_RF_22	0.011	0.001	S02_RF_22	0.578	0.032	S02_RF_52	0.058	0.006
S01_RF_23	0.015	0.001	S02_RF_23	0.337	0.02	S02_RF_53	0.124	0.011
S01_RF_24	0.032	0.001	S02_RF_24	0.071	0.001	S02_RF_54	0.044	0.004
S01_RF_25	0.043	0.004	S02_RF_25	0.021	0.001	S02_RF_55	0.05	0.007
S01_RF_26	0.07	0.005	S02_RF_26	0.151	0.006	S02_RF_56	0.039	0.001
S01_RF_27	0.06	0.01	S02_RF_27	0.05	0.006	S02_RF_57	0.041	0.001
S01_RF_28	0.053	0.003	S02_RF_28	0.02	0.004	S02_RF_58	0.012	0.001
S01_RF_29	0.252	0.012	S02_RF_29	0.071	0.007	S02_RF_59	0.013	0.001
S01_RF_30	13.151	11.56	S02_RF_30	0.039	0.001	S02_RF_60	0.07	0.006

Table S1 continued.

RF ID	SA m2	Vol m3	RF ID	SA m2	Vol m3	RF ID	SA m2	Vol m3
S02_RF_61	0.017	0.002	S02_RF_95	0.029	0.002	S02_RF_125	0.058	0.007
S02_RF_64	0.058	0.006	S02_RF_96	0.062	0.001	S02_RF_126	0.114	0.015
S02_RF_65	0.431	0.078	S02_RF_97	0.109	0.006	S02_RF_127	0.011	0.001
S02_RF_66	0.022	0.001	S02_RF_98	0.104	0.002	S02_RF_128	0.036	0.004
S02_RF_67	0.107	0.003	S02_RF_99	0.033	0.001	S02_RF_129	0.035	0.006
S02_RF_68	0.016	0.001	S02_RF_100	0.033	0.002	S02_RF_130	0.014	0.002
S02_RF_69	0.019	0.002	S02_RF_101	0.298	0.028	S02_RF_131	0.165	0.026
S02_RF_70	0.153	0.028	S02_RF_102	0.153	0.014	S02_RF_132	0.205	0.033
S02_RF_71	0.01	0.001	S02_RF_103	0.022	0.001	S02_RF_133	0.232	0.009
S02_RF_72	0.138	0.012	S02_RF_104	0.044	0.002	S02_RF_134	0.146	0.007
S02_RF_73	0.112	0.001	S02_RF_105	0.107	0.011	S02_RF_135	0.123	0.016
S02_RF_74	0.191	0.029	S02_RF_106	0.116	0.001	S02_RF_136	0.231	0.066
S02_RF_75	0.101	0.011	S02_RF_107	0.064	0.006	S02_RF_137	0.083	0.007
S02_RF_76	0.039	0.003	S02_RF_108	0.025	0.003	S02_RF_138	0.072	0.008
S02_RF_77	0.033	0.005	S02_RF_109	0.039	0.004	S02_RF_139	0.07	0.012
S02_RF_78	0.247	0.016	S02_RF_110	0.034	0.004	S02_RF_140	0.035	0.003
S02_RF_79	0.091	0.008	S02_RF_111	0.057	0.008	S02_RF_141	0.207	0.006
S02_RF_80	0.233	0.055	S02_RF_112	0.092	0.011	S02_RF_142	0.037	0.001
S02_RF_81	0.036	0.003	S02_RF_113	0.103	0.002	S02_RF_143	0.041	0.001
S02_RF_82	0.049	0.002	S02_RF_114	0.027	0.001	S02_RF_144	0.121	0.014
S02_RF_83	0.231	0.022	S02_RF_115	0.046	0.001	S02_RF_145	0.05	0.001
S02_RF_84	0.066	0.001	S02_RF_116	0.11	0.003	S02_RF_146	0.026	0.003
S02_RF_87	0.028	0.001	S02_RF_117	0.032	0.001	S02_RF_147	0.062	0.004
S02_RF_88	0.011	0.001	S02_RF_118	0.077	0.002	S02_RF_148	0.006	0.001
S02_RF_89	0.015	0.001	S02_RF_119	0.137	0.008	S02_RF_149	0.127	0.003
S02_RF_90	0.09	0.001	S02_RF_120	0.052	0.004	S02_RF_150	0.057	0.002
S02_RF_91	0.074	0.008	S02_RF_121	0.089	0.003	S02_RF_151	0.025	0.001
S02_RF_92	0.055	0.006	S02_RF_122	0.04	0.001	S03_RF_01	0.264	0.066
S02_RF_93	0.027	0.001	S02_RF_123	0.093	0.003	S03_RF_02	0.112	0.025
S02_RF_94	0.674	0.018	S02_RF_124	0.842	0.213	S03_RF_03	0.068	0.004
						S03_RF_04	0.058	0.008

Table S1 continued

RF ID	SA m2	Vol m3	RF ID	SA m2	Vol m3	RF ID	SA m2	Vol m3
S03_RF_05	0.033	0.005	S03_RF_36	0.095	0.025	S03_RF_69	0.007	0.002
S03_RF_06	0.048	0.003	S03_RF_37	0.003	0.001	S03_RF_70	0.06	0.015
S03_RF_07	0.016	0.001	S03_RF_39	0.005	0.001	S03_RF_71	0.814	0.185
S03_RF_08	0.077	0.007	S03_RF_40	0.013	0.002	S03_RF_72	0.294	0.062
S03_RF_09	0.148	0.028	S03_RF_41	0.222	0.043	S03_RF_73	0.061	0.01
S03_RF_10	0.495	0.106	S03_RF_42	0.247	0.042	S03_RF_74	0.104	0.022
S03_RF_11	0.039	0.004	S03_RF_43	0.177	0.037	S03_RF_75	0.629	0.096
S03_RF_12	0.03	0.003	S03_RF_44	0.049	0.011	S03_RF_76	0.108	0.025
S03_RF_13	0.011	0.001	S03_RF_45	0.017	0.002	S03_RF_77	0.049	0.012
S03_RF_14	0.031	0.005	S03_RF_46	0.012	0.003	S03_RF_78	1.128	0.451
S03_RF_15	0.038	0.007	S03_RF_47	0.279	0.065	S03_RF_79	0.039	0.007
S03_RF_16	0.095	0.018	S03_RF_48	0.005	0.001	S03_RF_81	0.03	0.005
S03_RF_17	0.072	0.015	S03_RF_49	0.027	0.007	S03_RF_82	0.043	0.011
S03_RF_18	12.222	4.534	S03_RF_51	0.03	0.006	S03_RF_83	0.015	0.002
S03_RF_19	0.033	0.004	S03_RF_52	0.322	0.057	S03_RF_84	0.04	0.008
S03_RF_20	0.652	0.146	S03_RF_53	1.684	0.239	S03_RF_85	0.042	0.009
S03_RF_21	0.124	0.021	S03_RF_54	0.01	0.001	S03_RF_86	0.003	0.001
S03_RF_22	0.235	0.021	S03_RF_55	0.273	0.051	S03_RF_87	0.033	0.007
S03_RF_23	0.005	0.001	S03_RF_56	0.425	0.12	S03_RF_88	0.08	0.015
S03_RF_24	0.043	0.009	S03_RF_57	0.175	0.042	S03_RF_89	0.073	0.014
S03_RF_25	0.237	0.049	S03_RF_58	0.323	0.072	S03_RF_90	0.267	0.092
S03_RF_26	0.045	0.011	S03_RF_59	0.075	0.017	S03_RF_91	0.087	0.022
S03_RF_27	0.057	0.009	S03_RF_60	0.068	0.015	S03_RF_92	0.006	0.001
S03_RF_28	0.041	0.007	S03_RF_61	0.002	0.001	S03_RF_93	0.063	0.011
S03_RF_29	0.061	0.011	S03_RF_62	0.003	0.001	S03_RF_94	0.124	0.024
S03_RF_30	0.469	0.109	S03_RF_63	0.009	0.001	S03_RF_95	0.008	0.002
S03_RF_31	0.06	0.012	S03_RF_64	0.186	0.042	S03_RF_96	2.436	1.557
S03_RF_32	0.024	0.005	S03_RF_65	0.055	0.012	S03_RF_97	0.486	0.14
S03_RF_33	0.091	0.012	S03_RF_66	0.4	0.102	S03_RF_98	0.049	0.011
S03_RF_34	0.025	0.005	S03_RF_67	0.145	0.038	S03_RF_99	0.09	0.017
S03_RF_35	0.005	0.001	S03_RF_68	1.809	0.762	S03_RF_100	0.22	0.036

Table S1 continued

RF ID	SA m2	Vol m3	RF ID	SA m2	Vol m3	RF ID	SA m2	Vol m3
S03_RF_101	0.076	0.016	S03_RF_133	0.856	0.329	S03_RF_166	0.011	0.003
S03_RF_102	0.062	0.016	S03_RF_134	0.003	0.001	S03_RF_167	0.079	0.025
S03_RF_103	0.189	0.057	S03_RF_135	0.071	0.018	S03_RF_168	0.01	0.002
S03_RF_104	0.063	0.009	S03_RF_136	0.014	0.002	S03_RF_169	0.016	0.005
S03_RF_105	0.023	0.007	S03_RF_137	0.042	0.01	S03_RF_170	0.004	0.001
S03_RF_106	0.007	0.001	S03_RF_138	0.088	0.021	S03_RF_171	0.073	0.02
S03_RF_107	0.003	0.001	S03_RF_139	0.069	0.019	S03_RF_172	0.013	0.004
S03_RF_108	0.051	0.009	S03_RF_140	0.033	0.008	S03_RF_174	0.021	0.006
S03_RF_109	0.116	0.036	S03_RF_141	0.009	0.001	S03_RF_175	0.04	0.012
S03_RF_111	0.216	0.036	S03_RF_142	0.106	0.022	S03_RF_176	0.007	0.002
S03_RF_112	0.14	0.029	S03_RF_143	0.014	0.003	S03_RF_179	0.05	0.007
S03_RF_113	0.075	0.018	S03_RF_144	0.013	0.003	S03_RF_180	0.108	0.02
S03_RF_114	0.004	0.001	S03_RF_145	0.003	0.001	S03_RF_181	0.047	0.014
S03_RF_115	0.028	0.008	S03_RF_146	0.144	0.023	S03_RF_182	0.005	0.001
S03_RF_116	0.029	0.004	S03_RF_147	0.014	0.006	S03_RF_183	0.019	0.007
S03_RF_117	0.079	0.011	S03_RF_148	0.039	0.013	S03_RF_184	0.023	0.008
S03_RF_118	0.005	0.001	S03_RF_149	0.12	0.015	S03_RF_186	0.001	0.001
S03_RF_119	0.04	0.006	S03_RF_150	0.034	0.007	S03_RF_187	0.034	0.01
S03_RF_120	1.128	0.307	S03_RF_151	0.031	0.008	S03_RF_188	0.073	0.018
S03_RF_121	0.098	0.006	S03_RF_152	0.043	0.01	S03_RF_189	0.37	0.105
S03_RF_122	0.009	0.002	S03_RF_153	0.207	0.049	S03_RF_190	0.007	0.002
S03_RF_123	0.014	0.004	S03_RF_154	0.029	0.008	S03_RF_191	0.005	0.002
S03_RF_124	0.242	0.066	S03_RF_155	0.097	0.027	S03_RF_192	0.128	0.045
S03_RF_125	0.134	0.037	S03_RF_156	0.016	0.005	S03_RF_193	0.01	0.003
S03_RF_126	0.041	0.008	S03_RF_158	0.004	0.001	S03_RF_194	0.066	0.027
S03_RF_127	0.037	0.007	S03_RF_159	0.012	0.003	S03_RF_195	0.028	0.008
S03_RF_128	0.356	0.064	S03_RF_160	0.003	0.001	S03_RF_196	0.135	0.047
S03_RF_129	0.412	0.076	S03_RF_162	0.012	0.004	S03_RF_197	0.058	0.027
S03_RF_130	0.097	0.025	S03_RF_163	0.073	0.02	S03_RF_198	0.012	0.004
S03_RF_131	0.042	0.009	S03_RF_164	0.185	0.044	S03_RF_199	0.005	0.003
S03_RF_132	0.119	0.007	S03_RF_165	0.01	0.004	S03_RF_200	0.015	0.008

Table S1 continued

RF ID	SA m2	Vol m3	RF ID	SA m2	Vol m3	RF ID	SA m2	Vol m3
S03_RF_201	0.006	0.002	S04_RF_29	1.447	0.437	S04_RF_64	0.315	0.05
S03_RF_202	0.012	0.004	S04_RF_30	1.277	0.451	S04_RF_65	0.041	0.001
S03_RF_204	0.079	0.017	S04_RF_31	0.367	0.052	S04_RF_66	0.074	0.016
S04_RF_01	0.037	0.003	S04_RF_32	0.01	0.019	S04_RF_67	0.176	0.052
S04_RF_02	0.022	0.001	S04_RF_34	0.18	0.001	S04_RF_68	0.224	0.051
S04_RF_03	0.014	0.001	S04_RF_36	0.049	0.014	S04_RF_69	1.691	0.413
S04_RF_04	0.158	0.048	S04_RF_37	0.099	0.009	S04_RF_70	0.137	0.029
S04_RF_05	0.052	0.011	S04_RF_38	0.023	0.005	S04_RF_71	0.626	0.133
S04_RF_06	0.009	0.002	S04_RF_39	0.209	0.047	S04_RF_72	0.051	0.001
S04_RF_07	0.05	0.002	S04_RF_40	0.036	0.007	S04_RF_73	0.134	0.008
S04_RF_08	0.023	0.003	S04_RF_41	0.051	0.002	S04_RF_74	0.04	0.003
S04_RF_09	0.492	0.057	S04_RF_42	0.05	0.009	S04_RF_75	0.025	0.002
S04_RF_10	0.128	0.023	S04_RF_43	0.034	0.002	S04_RF_76	2.585	0.746
S04_RF_100	0.013	0.001	S04_RF_44	0.011	0.001	S04_RF_77	0.267	0.013
S04_RF_11	0.004	0.001	S04_RF_45	0.023	0.02	S04_RF_78	0.036	0.004
S04_RF_12	0.092	0.025	S04_RF_46	0.427	0.029	S04_RF_79	0.056	0.003
S04_RF_13	0.075	0.024	S04_RF_47	0.029	0.001	S04_RF_80	0.059	0.002
S04_RF_14	0.026	0.002	S04_RF_48	0.019	0.001	S04_RF_81	0.235	0.014
S04_RF_15	0.065	0.01	S04_RF_49	0.089	0.004	S04_RF_83	0.281	0.002
S04_RF_16	0.124	0.022	S04_RF_50	0.038	0.003	S04_RF_84	0.169	0.018
S04_RF_17	0.093	0.007	S04_RF_51	0.18	0.007	S04_RF_85	0.308	0.012
S04_RF_18	0.112	0.012	S04_RF_52	0.44	0.012	S04_RF_86	0.056	0.005
S04_RF_19	0.023	0.001	S04_RF_53	0.116	0.004	S04_RF_87	0.13	0.001
S04_RF_20	0.228	0.011	S04_RF_54	0.215	0.014	S04_RF_88	0.092	0.003
S04_RF_21	0.036	0.001	S04_RF_55	0.322	0.01	S04_RF_89	0.028	0.003
S04_RF_22	1.34	0.029	S04_RF_56	0.023	0.001	S04_RF_90	0.049	0.008
S04_RF_23	0.148	0.015	S04_RF_58	1.188	0.039	S04_RF_91	0.022	0.015
S04_RF_24	0.039	0.005	S04_RF_59	0.517	0.127	S04_RF_92	0.016	0.001
S04_RF_25	0.15	0.007	S04_RF_60	0.217	0.063	S04_RF_93	0.016	0.001
S04_RF_26	0.017	0.001	S04_RF_61	0.255	0.058	S04_RF_94	0.77	0.236
S04_RF_27	0.013	0.001	S04_RF_63	0.032	0.005	S04_RF_95	0.06	0.002

Table S1 continued

RF ID	SA m2	Vol m3	RF ID	SA m2	Vol m3	RF ID	SA m2	Vol m3
S04_RF_96	0.007	0.005	S05_RF_29	0.041	0.012	S05_RF_61	0.334	0.08
S04_RF_97	0.017	0.001	S05_RF_30	0.029	0.007	S05_RF_62	0.07	0.02
S04_RF_98	0.406	0.002	S05_RF_31	0.146	0.044	S05_RF_63	0.097	0.035
S04_RF_99	0.013	0.047	S05_RF_32	0.273	0.086	S05_RF_64	0.031	0.006
S05_RF_01	0.388	0.018	S05_RF_33	0.029	0.007	S05_RF_65	0.03	0.009
S05_RF_02	0.037	0.003	S05_RF_34	0.037	0.009	S05_RF_66	0.014	0.003
S05_RF_03	0.137	0.037	S05_RF_35	0.042	0.016	S05_RF_67	0.058	0.016
S05_RF_04	0.093	0.03	S05_RF_36	0.458	0.124	S05_RF_68	0.025	0.004
S05_RF_05	0.094	0.007	S05_RF_37	9.945	5.83	S05_RF_69	0.722	0.17
S05_RF_06	0.142	0.024	S05_RF_38	1.97	1.264	S05_RF_70	0.012	0.002
S05_RF_07	0.019	0.001	S05_RF_39	3.022	0.623	S05_RF_71	0.012	0.002
S05_RF_08	0.394	0.021	S05_RF_40	1.022	0.639	S05_RF_72	0.013	0.002
S05_RF_09	3.656	1.497	S05_RF_41	9.848	5.357	S05_RF_74	0.006	0.001
S05_RF_10	11.97	7.006	S05_RF_42	1.254	0.996	S05_RF_75	0.02	0.002
S05_RF_11	0.191	0.06	S05_RF_43	0.039	0.012	S05_RF_76	0.011	0.001
S05_RF_12	4.849	1.56	S05_RF_44	0.191	0.015	S05_RF_77	0.135	0.012
S05_RF_13	0.427	0.025	S05_RF_45	0.012	0.001	S05_RF_78	0.186	0.02
S05_RF_14	0.208	0.011	S05_RF_46	0.164	0.057	S05_RF_79	0.112	0.016
S05_RF_15	0.088	0.021	S05_RF_47	0.031	0.008	S05_RF_80	0.215	0.025
S05_RF_16	0.275	0.05	S05_RF_48	0.043	0.013			
S05_RF_17	0.016	0.001	S05_RF_49	0.324	0.105			
S05_RF_18	0.008	0.002	S05_RF_50	0.01	0.003			
S05_RF_20	0.044	0.001	S05_RF_51	0.028	0.007			
S05_RF_21	0.422	0.122	S05_RF_53	0.025	0.007			
S05_RF_22	0.099	0.006	S05_RF_54	0.086	0.018			
S05_RF_23	1.986	0.506	S05_RF_55	1.93	0.1261			
S05_RF_24	0.153	0.046	S05_RF_56	0.065	0.019			
S05_RF_25	0.388	0.097	S05_RF_57	0.04	0.009			
S05_RF_26	0.049	0.015	S05_RF_58	0.558	0.163			
S05_RF_27	0.023	0.001	S05_RF_59	0.036	0.009			
S05_RF_28	0.003	0.001	S05_RF_60	0.022	0.006			

Chapter 3: Variability in alongshore distribution of wave energy on an embayed coastline and relationship to the spatial distribution of erosion

Cullen. N.D.[1], Bourke. M.C.[1]

[1]Department of Geography, University of Dublin, Trinity College, Dublin, Ireland.

Abstract

The role of wave energy has long been cited as the dominant control on erosion of rock coasts. Recent research has demonstrated the influence of nearshore and foreshore topography on alongshore variability of wave energy, however the direct relationship to rates of coastal cliff erosion has not been demonstrated. We present the findings of a study which investigates the influence of macroscale coastline geometry, near and foreshore characteristics on the alongshore variability of wave energy on an embayed coastline, and the relationship to rates of cliff erosion. We find that offshore wave climate and nearshore characteristics exert a strong control on the alongshore variability of wave energy at the study site. We do not find any significant relationship between alongshore wave energy variability and cliff erosion rates. Further, we conclude that foreshore characteristics, specifically cliff toe elevation, exerts a strong influence on the wave energy magnitude to reach the cliff toe.

Key words

Wave energy variability, embayed coastline, SWAN, coastal Rock cliff erosion.

Author Contributions

N.D.C. wrote the body of the manuscript with contributions from M.C.B. M.C.B and P.B. collected the nearshore bathymetry data, N.D.C. assisted with all aspects of data collection in the field. PB undertook primary data processing of bathymetry, NDC and carried out all post primary data processing, built the bathymetry model and conducted the wave modelling. M.C.B. edited the final manuscript.

3.1 Introduction

3.1.1 The role of waves in erosion of rock coasts

The early conceptual models of Sunamura (1992) and Trenhaile (1987) proposed that waves were the dominant erosive force on rocky coastlines. For decades the relationship between waves and cliff retreat has been considered as the principle driver in the shaping and erosion of rock coastlines (e.g. Hutchinson, 1972, Sanders, 1968, Sunamura, 1977, Hansom et al., 2008, Sallenger Jr et al., 2002, Lim et al., 2011). Sunamura (1992) proposed that the erosion of rock coasts is a function of the interaction between the assailing force of waves (F_W) and the resisting force of the rock (F_R) (Sunamura, 1992, Equation 3.1).

$$x = f(F_W, F_R, t) \quad 1$$

where *x* is the eroded distance, *t* is time with erosion only occurring when $F_W > F_R$. The process of cliff undercutting by waves and subsequent cantilever failure of the overlying cliff has been considered to be the dominant mechanism by which sea cliffs are modified regardless of lithology (Young and Ashford, 2008). With respect to F_W, variations in the distribution of wave energy, as a result of differences in deep water wave height and nearshore bathymetry (Sunamura, 1995), are believed to exert a strong control on the spatial distribution of coastal cliff erosion (e.g. Sallenger et al. 2002; Murray and Aston, 2013). Despite this, limited research has focused on linking rates of coastal cliff retreat to wave climate (Earlie, 2015). It is only in recent decades that researchers have begun to explore the relationship between the offshore wave field and coastal cliff erosion through analysis of micro seismic motions of the cliff (swaying, vibrating and shaking) during wave impact (Adams et al., 2002, 2005, Young et al., 2011, 2012, 2013, Dickson and Pentney, 2012). With a few notable exceptions (e.g. Adams et al., 2005, Brain et al., 2014, Norman et al., 2013, Earlie, 2015) the geomorphic and geotechnical response to these motions are relatively unexplored. A number of studies have analytically estimated the wave energy available for the erosion of rock coasts (e.g.

Stephenson and Kirk, 2000, Trenhaile and Kanyaya, 2007). Others have taken an empirical approach and measured the cross shore distribution of wave energy and determined the influence of foreshore characteristics (Ogawa et al., 2011, 2013, Stephenson et al., 2018, Poate et al., 2018). However, to date, studies have not examined the alongshore variability in near and foreshore characteristics, wave height, wave velocity and wave power, the resultant potential energy transfer to the cliff (Jones et al., 2018) and relationship to measured cliff erosion rates.

In contrast, the role of waves in the erosion and evolution of shore platforms has received significantly greater attention. Studies in this respect are numerous and incorporate a range of processes and scales including; the effects of waves and tides on the rate of platform downwearing, platform morphology and evolution (e.g. Stephenson and Kirk, 2000, Kanyaya and Trenhaile, 2005, Trenhaile, 2000, 2008, Marshall and Stephenson, 2011, Trenhaile and Porter, 2007, Trenhaile and Kanyaya, 2007) , wave transformation across the platform (Farrell et al., 2009, Beetham and Kench, 2011, Ogawa et al., 2011, 2012, Ogawa, 2012, 2013, Poate et al., 2018), meso scale erosion of shore platforms via quarrying of clasts and clasts transport dynamics (Nott, 2003, Etienne and Paris, 2010, Goto et al., 2009, 2010, 2011, Imamura et al., 2008, Hall, 2011b, Mastronuzzi and Sansò, 2004, Nandasena et al., 2011, Cox et al., 2012, Nandasena and Tanaka, 2013, Naylor et al., 2016b, Erdmann et al., 2018) and associated abrasion of the platform by via clast transport (Cullen and Bourke, 2018). The volume of research on the role of waves in mediating platform erosion only serves to highlight the relative paucity of studies relating to geomorphological and geotechnical implications of wave impact on cliff erosion, while the relative importance of coastline and foreshore geometry on wave energy distribution remains uncertain (Jones et al., 2018).

Here we assess the alongshore variability in wave energy distribution on an embayed coastline which is typical of the 5,400km long Irish coastline. We use significant wave height as a proxy for wave energy and model for a range of typical offshore wave conditions

(significant wave height, period and direction). We explore the relationship between alongshore wave energy distribution, macroscale coastline geometry and near and foreshore geometry and relate these to the spatial distribution of coastal cliff erosion.

3.1.2 Wave climate on the west coast of Ireland

The North East Atlantic has some of the highest wave energy levels in the world. Gallagher et al. (2014) produced a long term near shore hind-cast for the west coast of Ireland characterising the wave climate from 1979 – 2012. The authors report an annual mean significant wave height (HSig) of 3 m with a mean winter (Dec/Jan /Feb) HSig up to 5 m. The lowest HSig (0 – 2.5 m) occurs in the summer months (Jun/Jul/Aug) with a similar range of HSig values (0 – 3m) in Spring (Feb/Mar/Apr) and Autumn (Sep/Oct/Nov). The largest waves ever documented off the west coast occurred in February 2014 during Storm Darwin when a HSig of 12 m was recorded. The dominant incoming wave direction exhibits very little seasonal variability ranging from W – SW and extending only 10˚ - 20˚ from west. At the study site (introduced in chapter 2) the maximum tidal range is 4.4 m (0 m ± 2.2 m). Normal tidal range reaches between 30 m and 50 m from the cliff toe, depending on platform width and slope. However, the prevailing incoming wave direction combined with a predominantly westerly (onshore) wind direction produces waves which often reach the cliff toe, as evidenced by rapid (weeks to months) removal of cliff toe deposits (Cullen and Bourke, 2018).

3.2 Methodology

3.2.1 Data collection

Onshore - Terrestrial Laser Scanning

Terrestrial Laser Scanning (TLS) data were collected in March 2016 by David Rogers (Ulster University, Coleraine) using a Faro Focus 3D X330. A total of 19 alongshore TLS stations were set up prior to surveying with a maximum distance of 60 m between stations (to ensure good overlap). Further details of TLS data collection are described in chapter two. Horizontal error for the TLS point cloud was calculated as $\sqrt{(a_{xy}^2 + b_{xy}^2)}$ where a_{xy} is the reported ranging error of the Faro Focus 3D laser scanner and b_{xy} is the xy error of the Trimble dGPS used to georeference the TLS point cloud. Vertical error was calculated as $\sqrt{(a_z^2 + b_z^2)}$ where a_z is the reported ranging error of the Faro Focus 3D laser scanner and b_z is the reported accuracy of the Trimble dGPS.

Onshore– Digital Surface Model

A Digital Surface Model (DSM) for the areas of the cliff line (i.e. the cliff edge in plan view) and the coastline to the north and south of the bay which were not captured by the TLS scanner were purchased from BlueSky (www.bluesky-world.ie). Vertical and horizontal errors are ± 1 m.

Nearshore - Bathymetry

A bathymetric survey of the bay was carried out in March 2017. We used a RiverRay ADCP (Teledyne Marine) with a Hemisphere Eclipse A325 Smart GPS Antenna. The RiverRay uses a vertical beam for precise characterization of the seafloor. The survey transects across and along the bay were carried out at high spring tide to ensure that water was deep enough to capture the bathymetry at the platform edge. This ensured maximum overlap between the nearshore bathymetric survey data and the onshore TLS survey data to reduce interpolation

errors. The maximum vertical (Z) error of the nearshore bathymetry was calculated using the reported depth error for the vertical beam measurements of ±1% of the recorded depth (bed elevation corrected to account for tidal range of ±2.2 m). Horizontal (XY) error reported for the Hemisphere dGPS is ±0.02 m.

Offshore - Bathymetry

Offshore bathymetry was provided by the INtegrated Mapping FOr the Sustainable Development of Ireland's MArine Resource (INFOMAR) project. Details of bathymetric data collection and processing procedures can be found at http://www.infomar.ie/data/DataProcessing.php. The bathymetry was obtained at 10 m resolution in the same coordinate system as the TLS, DSM and Bathymetry data (ETRS89 UTM Z29 N, OD Malin Head).

3.2.2 Data processing

3.2.2.1 Onshore, near and offshore data

Terrestrial laser scan (TLS) point cloud

The primary processing (co registration of individual scans, noise filtering and subsampling) of the TLS point cloud was carried out by David Rogers (Ulster University, Coleraine) using *Faro Scene* (version 6.2) (Faro, 2016). Point clouds were retrospectively georeferenced using GCPs collected using a differential Global Positioning System (dGPS) (Trimble Global Navigation Satellite System (GNSS) R8-3) (horizontal error = ± 0.015 m, vertical error = ± 0.020 m) (see chapter 2 section 2.2.2.2 for more details on point cloud processing procedure). Each cloud was sub-sampled at 0.10 m to increase to reduce processing time. The processed

cloud was converted to an LAS file and exported to ArcMap (version 10.5.2). The LAS file was converted to a multipoint file using the *LAS to multipoint* tool in ArcMap.

Digital Surface Model (DSM)

The DSM was downloaded as a georeferenced raster (ETRS 89 UTM Zone 29 N) and imported to ArcMap. The DSM was converted to a multipoint file using the *raster to multipoint* tool in ArcMap.

Nearshore bathymetric data

Nearshore bathymetric data were processed to correct for seawater depth (Teledyne, 2015) by Dr. Patrick Belmont and Bruce Call (Utah State University). The bathymetry point file was imported to ArcMap and converted to a multipoint file using the *raster to multipoint* tool.

Offshore bathymetric data

The offshore bathymetric raster was converted to a multipoint file using the *raster to multipoint* tool in ArcMap.

3.2.2.2 Interpolation of offshore, nearshore and onshore topography

All multipoint files (TLS, DSM, nearshore and offshore bathymetry) were merged to a single multipoint file in ArcMap. To interpolate a surface from the merged multipoint file of the TLS, DSM, near and offshore bathymetry elevation data, we used Inverse Distance Weighted (IDW) interpolation with Natural Neighbour (NN) geometric estimation. IDW predicts elevation of an unmeasured point based on the measured values surrounding it. IDW assumes that measured

values closest to the unmeasured point have a greater influence than measured points further away, while also assuming that the influence of the nearest measured points decreases with increasing distance from the unmeasured point. Utilising the NN geometric estimation within the IDW method is considered suitable for sample data that are unevenly or sparsely distributed (GIS Resources, 2014) (which is the case for the nearshore bathymetric data collected here using the RiverRay ADCP), while also being suitable for point data with a more uniform distribution (GIS Resources, 2014) (as is the case for the offshore bathymetric and onshore TLS data used here) . Limitations of the IDW approach to surface interpolation include an inability to assess prediction errors and a reduction in interpolation accuracy as the density of point data decreases.

Two grids were interpolated, a 10 m resolution grid incorporating the offshore and nearshore bathymetric data, and onshore TLS and DSM data and (2) a 1 m resolution grid incorporating the nearshore bathymetry and the onshore TLS and DSM elevation points. IDW produced best results given the number of points in the merged datasets.

Accounting for the different errors in the individual data sets (offshore, nearshore and TLS) is important as they occur at orders of magnitude difference. When combining the data sets this was not fully considered. Therefore, the model output is indicative rather than predictive. Future work will include all errors in model calculation.

IDW validation

Interpolated elevation values for the 1 m resolution grid were validated using independent dGPS survey points which were not used in the interpolation. IDW error was calculated as the

mean of the difference (estimated – measured) between the measured and interpolated values.

Near and foreshore geometry

A series of across shore profiles (n = 7) were derived from the interpolated 1 m resolution Digital Elevation Model to characterise foreshore geometry.

3.2.2.3 SWAN simulations

Model setup

We used SWAN (Booji et al. 1999) to model significant wave heights which we use here as a proxy for wave energy.

SWAN is a third-generation wave model for simulation of waves in shallow water. The model accounts for propagation, generation, dissipation and non-linear wave-wave interactions (Booij et al., 1999). The model does not account for diffraction but does include depth induced wave breaking, triad wave-wave interactions and current effects (Booij et al., 1999)

SWAN simulates the development of the wave spectrum according to:

$$\frac{\partial N}{\partial t} + \frac{\partial (c_x N)}{\partial x} + \frac{\partial \left(c_y N\right)}{\partial y} + \frac{\partial (c_\sigma N)}{\partial \sigma} + \frac{\partial (c_\theta N)}{\partial \theta} = \frac{S}{\sigma} \qquad 3.2$$

Where the action density = $N(\sigma, \theta) = E(\sigma, \theta)/\sigma$, t is time, x and y are the cross and alongshore coordinates respectively, σ is the wave radian frequency and θ is the wave direction, c_x, c_y,

and c_z are the wave group velocities in the x, y, σ and θ space respectively, and S is the source and sink term according to:

$$S = S_{in} + S_{nl} + S_{ds} \quad 3.3$$

Where S_{in} incorporates wind waves, S_{nl} is non-linear triad and quartet interactions and S_{ds} includes energy dissipation via white capping, bottom friction and wave breaking (Gorrell et al., 2011).

All computations were performed on a HP Pavilion Power Laptop with Intel ® Core™ i7-7700HQ 64bit processor with 32 GB RAM and NVIDIA GEFORCE GTX graphics. The simulations were performed on two grids. The first was a coarse grid (20 m resolution) which covers the area from the MK3 wave buoy approximately 6 km WNW of the study site and incorporates the area approximately 2km south and 1 km north of the study site in addition to the bay (Figure 1). The bottom (bathymetry) grid used was 10 m resolution. The second grid was 10 m resolution grid (the highest resolution which could be achieved by the processor at this scale) which covers the area inside the bay (Figure 1) and which utilised the 1 m interpolated bathymetry grid. The model was run in stationary mode (i.e. where the first term in equation 3.2 is equal to zero). This mode assumes that the wave propagates instantaneously throughout the model domain and is considered suitable for small domains such as the one in this study For short spatial scales and water depths, such as those considered here, non-linear triad interactions are significantly greater (Freilich and Guza, 1984, Elgar and Guza, 1985, Gorrell et al., 2011), as such we have excluded non-linear quartet interactions from the model runs and applied the SWAN default nonlinear triad interactions source term of Eldeberky and Battjes (1996). For wind wave generation and white capping, the source term of Janssen (1989, 1991) was applied. We used the SWAN default expression for bottom dissipation (JONSWAP) after Hasselmann et al. (1973). The default source term of Battjes and Janssen (1978) was applied for estimation of depth induced breaking. The shape

of the wave spectra was defined using the JONSWAP spectrum (Hasselmann et al., 1973), with the width of directional spreading expressed as a power (3). To determine the variability of wave energy along the shoreline, the boundary conditions of the 10m grids were obtained from nested 10 m grids in the 20m grid simulation.

Wave parameters

Boundary conditions for SWAN simulations (significant wave height, direction and period) were obtained from the MK3 wave buoy record for the period March 2016 – April 2017. This is the same period used to measure the rate of cliff erosion (see chapter 2). These data were used to calculate the mean wave period and mean wave direction for each significant wave height (HSig) used in the simulations, we averaged the values of wave period and wave direction for a 20 cm range of HSig. For example, mean wave direction and mean period for values of HSig between 0.9m and 1.1m were used to calculate the mean wave period and wave direction for a significant wave height of 1m. We generated models for a range of HSig at 1m intervals from 1m (i.e. low wave energy conditions) to 8m (i.e. storm wave energy conditions). HSig for each simulation was calculated at maximum spring tidal range (+2.2 m OD Malin Head).

3.2.2.4 Alongshore variability of HSig, nearshore bathymetry and foreshore characteristics.

To assess the influence of nearshore bathymetry of HSig, a series of shore normal profiles (n = 8) of the nearshore change in HSig (modelled for offshore Hsig of 1 m) and a corresponding profile of the nearshore change in bathymetry were extracted from the HSig raster and the interpolated digital elevation model (DEM) respectively. The profiles were chosen based on modelled differences in alongshore HSig i.e. where we observed notable or relatively little change in modelled alongshore HSig. This was done to investigate what features of the alongshore bathymetry (e.g. abrupt steps, gentle slopes etc.) produced the change, or relative

lack of change, in HSig. The alongshore variability of the nearshore bathymetry was determined from the standard deviation of each profile. The range of standard deviations observed for the profiles selected (see results section 3.3.4) indicate a good representation of alongshore topographic variability in the selected profiles. To assess the influence of foreshore characteristics i.e. cliff toe elevation, a second series of profiles (n =7) were extracted from the interpolated DEM to determine the alongshore variability of cliff toe elevation.

3.2.2.5 Spatial distribution of cliff erosion

The methods for the measurement and calculation of cliff erosion rate are described in chapter 2.

3.3 Results

3.3.1. IDW interpolation and validation

3.3.1.1 IDW interpolation of bathymetric and onshore points.

The results of the IDW interpolations are shown in Figure 1. Maximum depth offshore was -73 m OD and maximum onshore cliff height was 80 m. With respect to nearshore bathymetry, bottom depth within the bay varies from north to south with shallowing occurring further seaward in the northern half of the bay. (Figure 1 and 2)

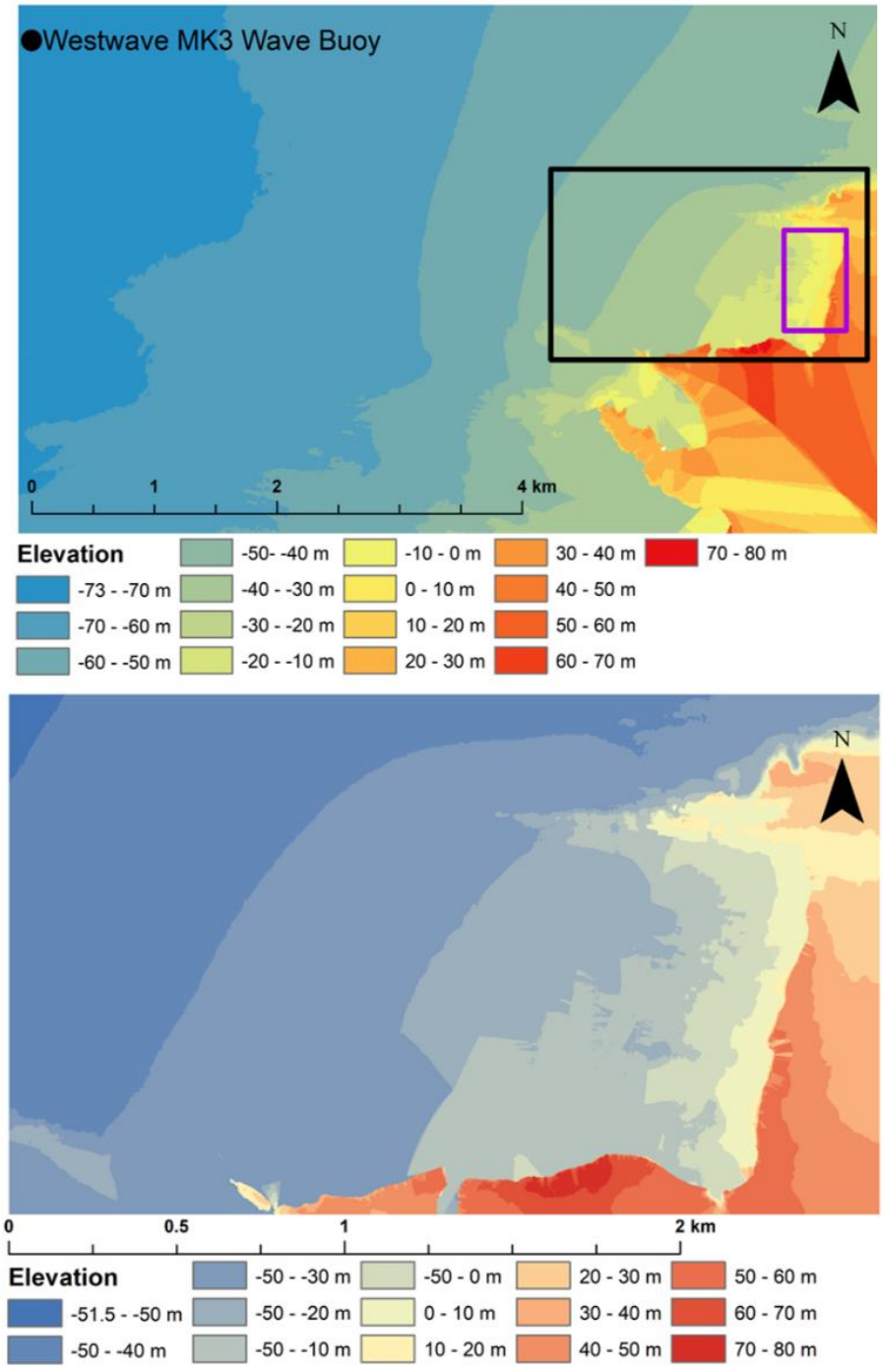

Figure 1. Inverse Weighted Distance interpolation of offshore and nearshore bathymetric data with onshore TLS and DSM data at (a) 10 m resolution, (b) 1 m resolution. Black box in a indicates the extent of the 1 m resolution interpolated bathymetry grid shown in b. Purple box in a shows the extent of the nested grid used for the SWAN simulation of HSig at 1 m grid resolution.

3.3.1.2 IDW validation

A total of 24 dGPS survey points were used to validate the 1 m resolution IDW interpolation (Figure 1, Table 1). Mean IDW error is calculated at ± 0.07m. Maximum IDW error was 1.7 m and minimum IDW error was 0.01 m. In general, IDW error was less than 0.20 m.

Table 1. dGPS point interpolated (IDW) elevation points (OD Malin Head). dGPS z error is ± 0.02 m.

Point ID	Eastings	Northings	dGPS Elevation (m OD)	IDW Elevation (m OD)	Difference (m)
1	91624.7	166686.4	6.7	6.9	0.1
2	91521.5	166699.1	-1.3	-1.4	-0.1
3	91669.1	166694.9	2.7	2.8	0.1
4	91612.4	166609.1	8.5	8.7	0.2
5	91605.3	166629.5	-1.3	-1.9	-0.6
6	91565.3	166621.7	4.4	4.5	0.1
7	91599.2	166534.0	8.6	8.9	0.2
8	91492.5	166569.6	-0.8	-0.3	0.4
9	91568.8	166546.8	5.2	5.4	0.2
10	91536.3	166376.5	6.6	6.6	0.0
11	91461.7	166399.5	-0.8	-0.9	-0.1
12	91491.2	166391.3	2.0	2.2	0.2
13	91515.7	166334.6	5.7	5.5	-0.2
14	91436.8	166357.1	-1.1	-1.0	0.1
15	91488.0	166343.5	2.7	2.7	0.0
16	91504.0	166311.0	5.4	5.5	0.1
17	91432.6	166338.6	-1.0	-1.1	-0.1
18	91484.4	166318.8	3.7	3.7	-0.1
19	91475.9	166264.4	5.1	5.1	0.0
20	91411.1	166290.1	-0.2	0.3	0.6
21	91443.8	166274.9	2.9	2.6	-0.2
22	91480.1	166233.6	5.1	4.9	-0.2
23	91389.2	166252.9	-0.2	1.0	1.2
24	91444.7	166239.5	3.1	3.0	-0.1
Mean					0.07

3.3.3 SWAN model runs

3.3.3.1 Wave boundary conditions

The significant wave height recorded by the Westwave MK3 Wave Buoy range from a minimum of 0.38 m in May 2016 to a maximum of 9.83 m in September 2016 although HSig only exceeded 9 m on one other occasion in December 2016. Generally, the highest HSig occur in the winter months (December to February) while the lowest HSig occur in Summer months (June – August). Mean wave period for HSig between 1 and 8 m ranges from 10 s to a maximum of 16 s for a HSig of 8m (Table 2). Mean incoming wave direction varied between 276° and 293° for HSig of 1 and 8 m respectively. The general trend is for larger waves to come from an increasingly northerly direction. It is important to note that the wave boundary conditions are based on one year of data and may not be representative of wave conditions over longer timescales.

Table 2. Parameters used in the SWAN model runs to estimate wave energy variability along the shoreline at the study site. Range of HSig values are derived from Westwave MK3 wave buoy record from 01/03/2016 to 5/04/2017 available at *www.datamarine.ie.*

SWAN Set Level	Hsig (m)	Mean Period* (s)	Mean Direction* (°)
2.2 m OD	1	10	276
2.2 m OD	2	10	279
2.2 m OD	3	12	281
2.2 m OD	4	12	280
2.2 m OD	5	14	284
2.2 m OD	6	14	290
2.2 m OD	7	15	291
2.2 m OD	8	16	294

**Values derived by averaging the values at relevant HSig ± 0.1 m.*

3.3.3.2 SWAN simulations

20 m grid

The simulated values of HSig at 20 m resolution using the boundary conditions derived from table 2 (HSig 1-8 m) at maximum tidal range (2.2 m OD) are shown in figure 2. Considerable variability on HSig is observed for all offshore HSig. The boundary conditions used for 1 m resolution simulations (HSig 1-8 m) are shown in figure 2. Nearshore HSig is generally highest in the southern half of the bay and lowest in the northern half of the bay. For all simulations HSig increases as waves approach the shore and is lowest at the maximum tidal range. At offshore HSig ranging from 1 – 5 m, simulated HSig is greatest within 500 m of the maximum tidal range. At offshore HSig of 6 m simulated HSig increases approximately 1 km from maximum tidal range which extends to 2 km offshore for offshore HSig of 8 m.

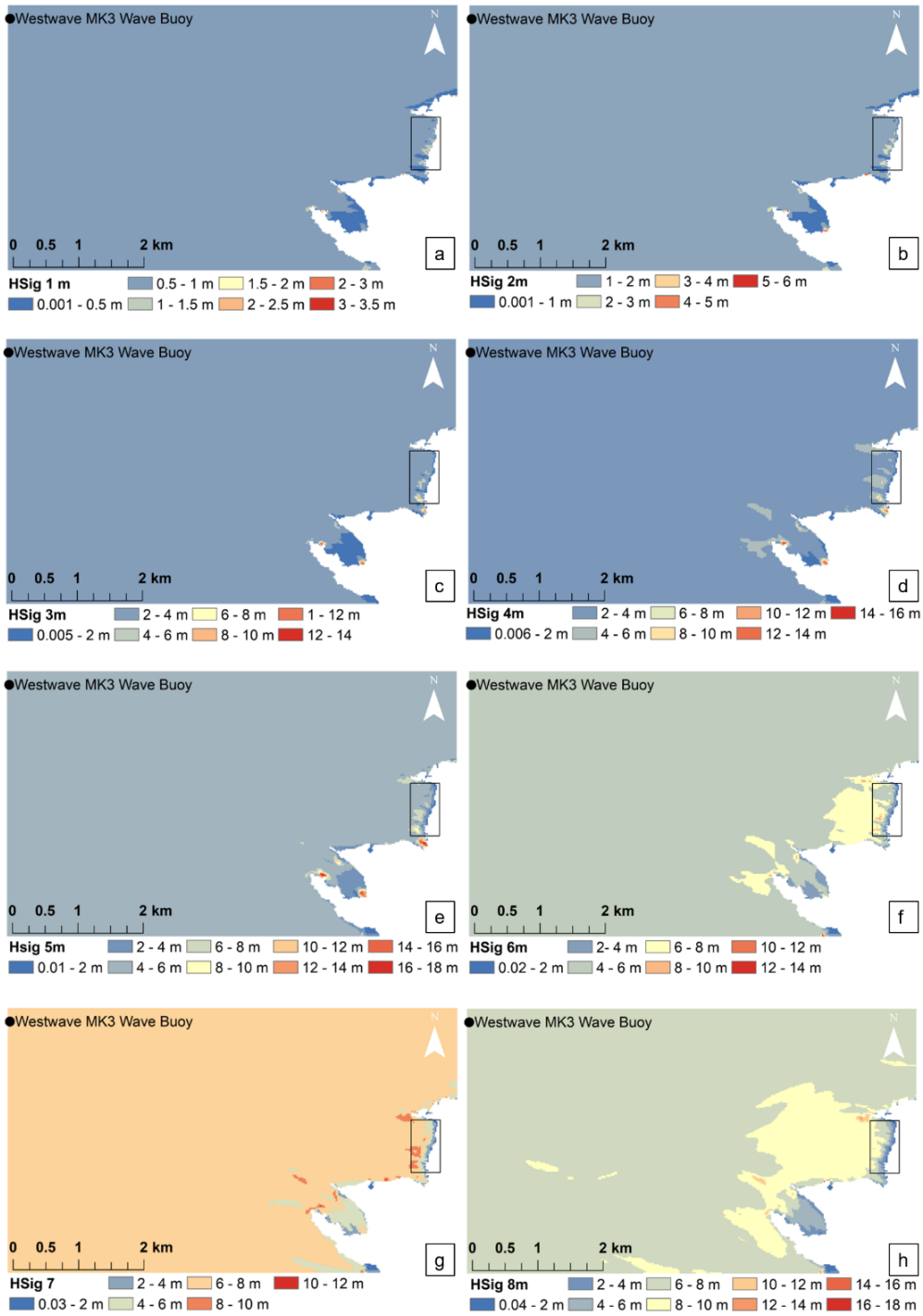

Figure 2. The results of the 20 m resolution simulation used to obtain the boundary conditions (black box in a-h) for the 1 m resolution simulations (Figs. 3-6). Boundary conditions for the 20 m resolutions simulations are derived from table 2.

10 m grid

Using the boundary conditions from the nested grid for offshore HSig of 1 m (Table 2) the range of HSig at the maximum tidal range within the bay ranges from a minimum of 0.001 m at the northern end of the bay to a maximum of 0.8 m at the southern end of the bay . At HSig of 2 m values of modelled HSig at 2.2 m OD in the bay range between 0.001 m and 2.2 m. For HSig of 3, 4 and 5 m, simulated HSig in the bay ranges from a minimum of 0.01, 0.02 and 0.01 m respectively, to a maximum of 3, 3.4 and 4.4m respectively. The largest ranges of simulated HSig in the bay (0.02 – 9 m and 0. 2 – 9.4 m) were observed for the highest offshore HSig, (7 and 8 m respectively). Regardless of incoming wave direction, simulated HSig was lowest at the northern end of the bay for all model simulations and highest at the southern end (Figs. 3-6). Simulated HSig increases northward with increasing offshore wave height.

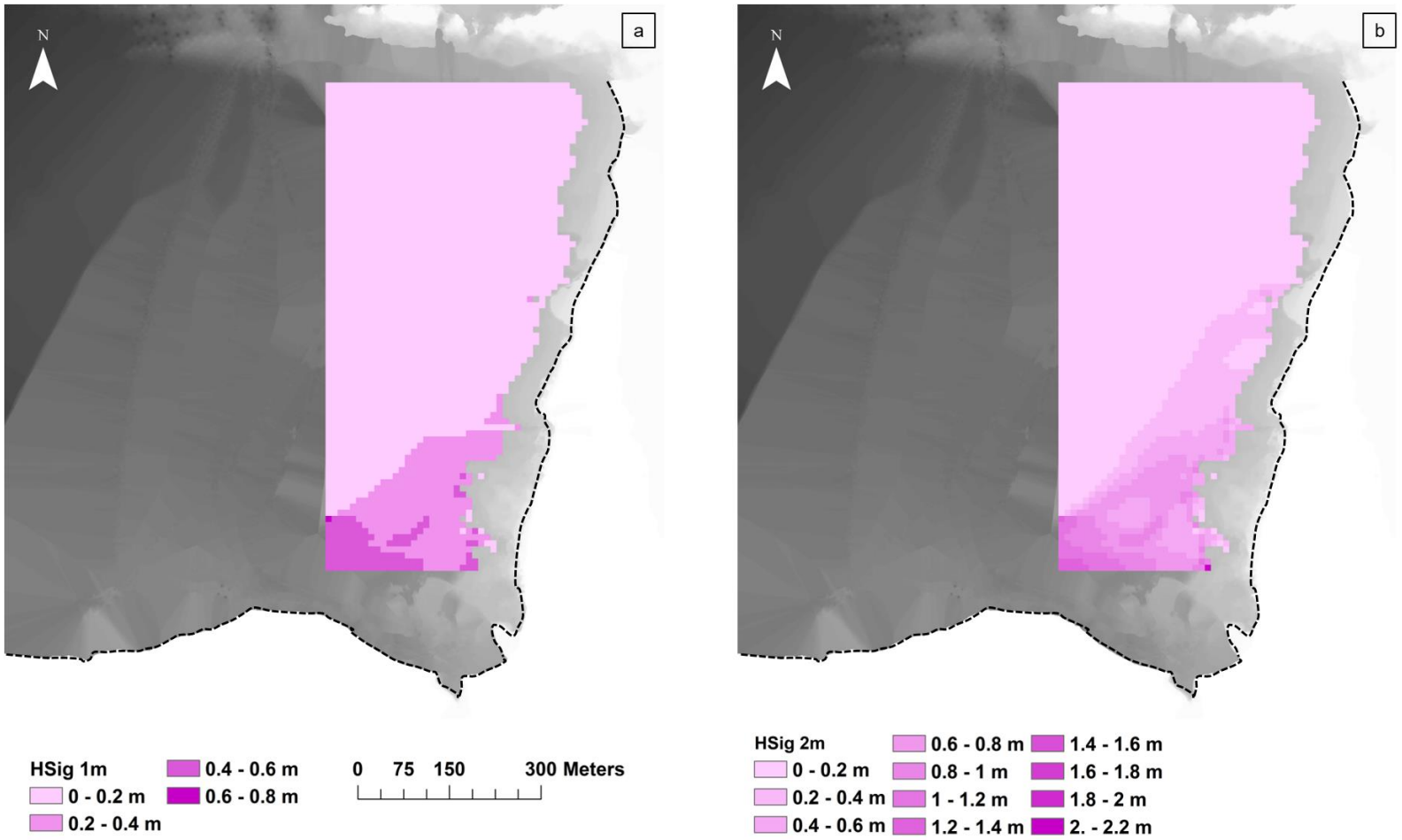

Figure 3. Simulated alongshore HSig variability within the bay at offshore HSig of 1 m and 2 m (a and b respectively) overlaid on the 1 m resolution interpolated Digital Elevation Model (DEM) of the study site. Dashed black line is the cliff line.

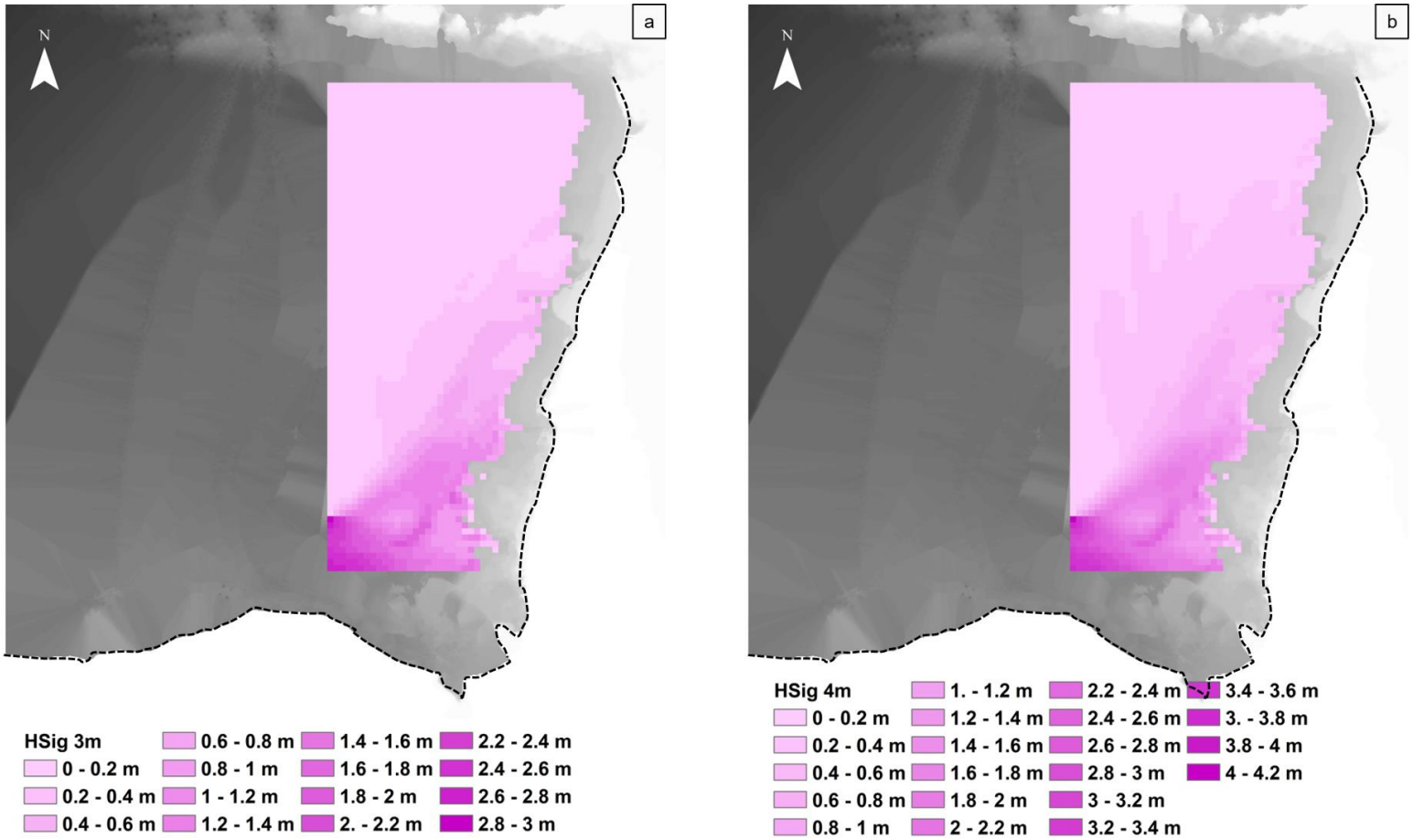

Figure 4. Simulated alongshore HSig variability within the bay at offshore HSig of 3 m and 4 m (a and b respectively) overlaid on the 1 m resolution interpolated DEM of the study site. Dashed black line is the cliff line.

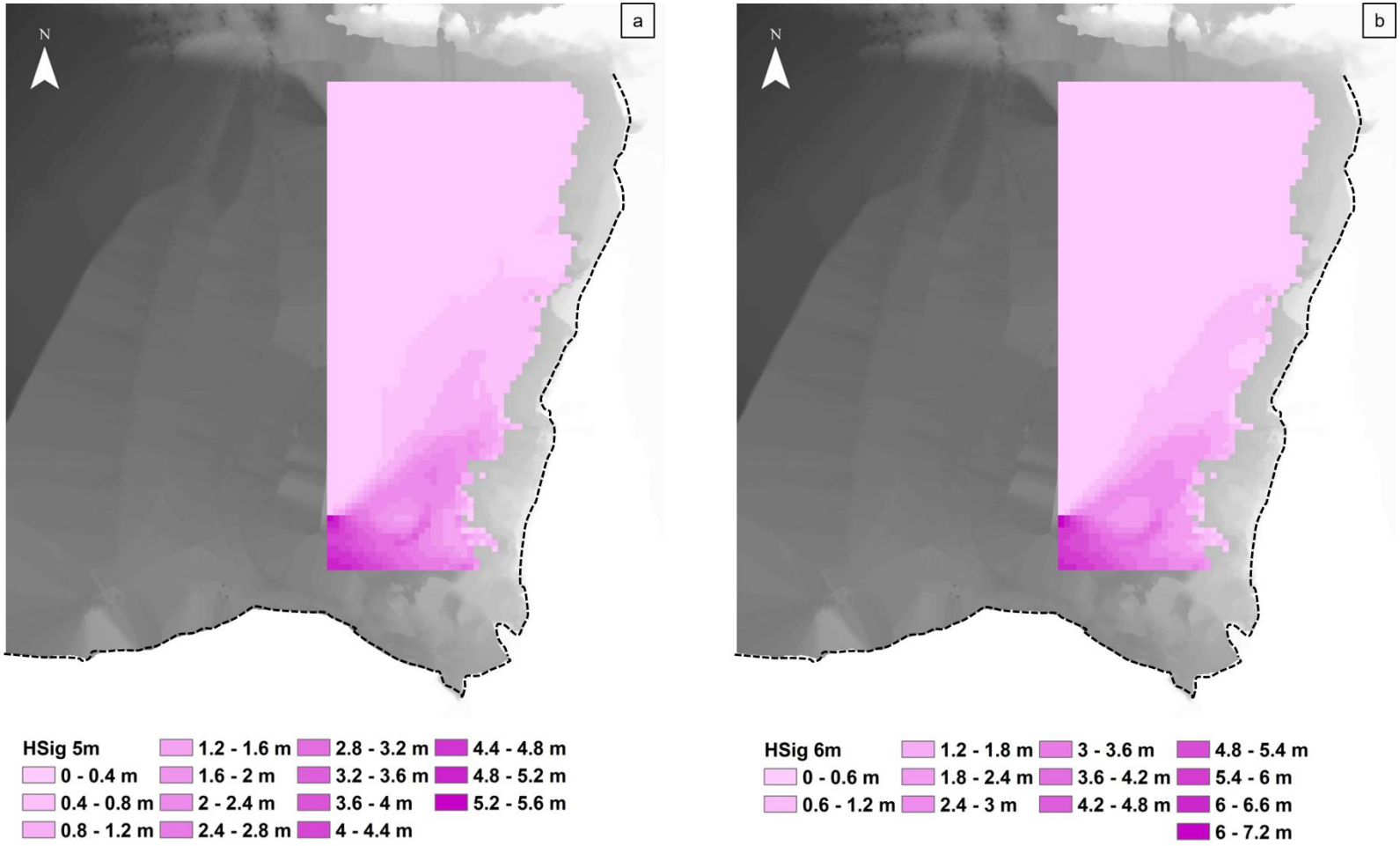

Figure 5. Simulated alongshore HSig variability within the bay at offshore HSig of 5 m and 6 m (a and b respectively) overlaid on the 1 m resolution interpolated DEM of the study site. Dashed black line is the cliff line.

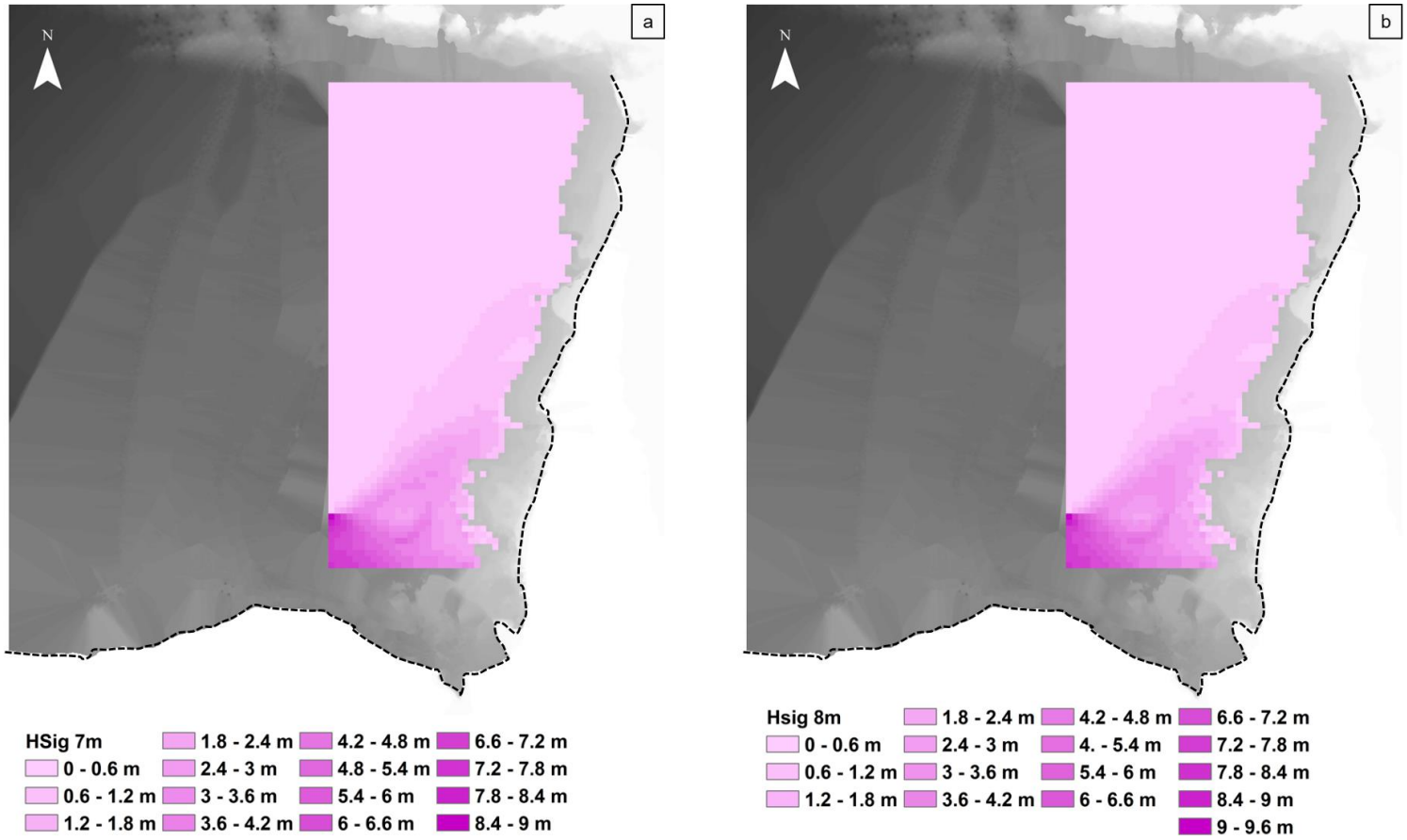

Figure 6. Simulated alongshore HSig variability within the bay at offshore HSig of 7 m and 8 m (a and b respectively) overlaid on the 1 m resolution interpolated DEM of the study site. Dashed black line is the cliff line.

3.3.4 Alongshore variability of HSig and nearshore bathymetry

The location of the shore normal transects used to extract the alongshore HSig and bathymetry profiles are shown in figure 7.

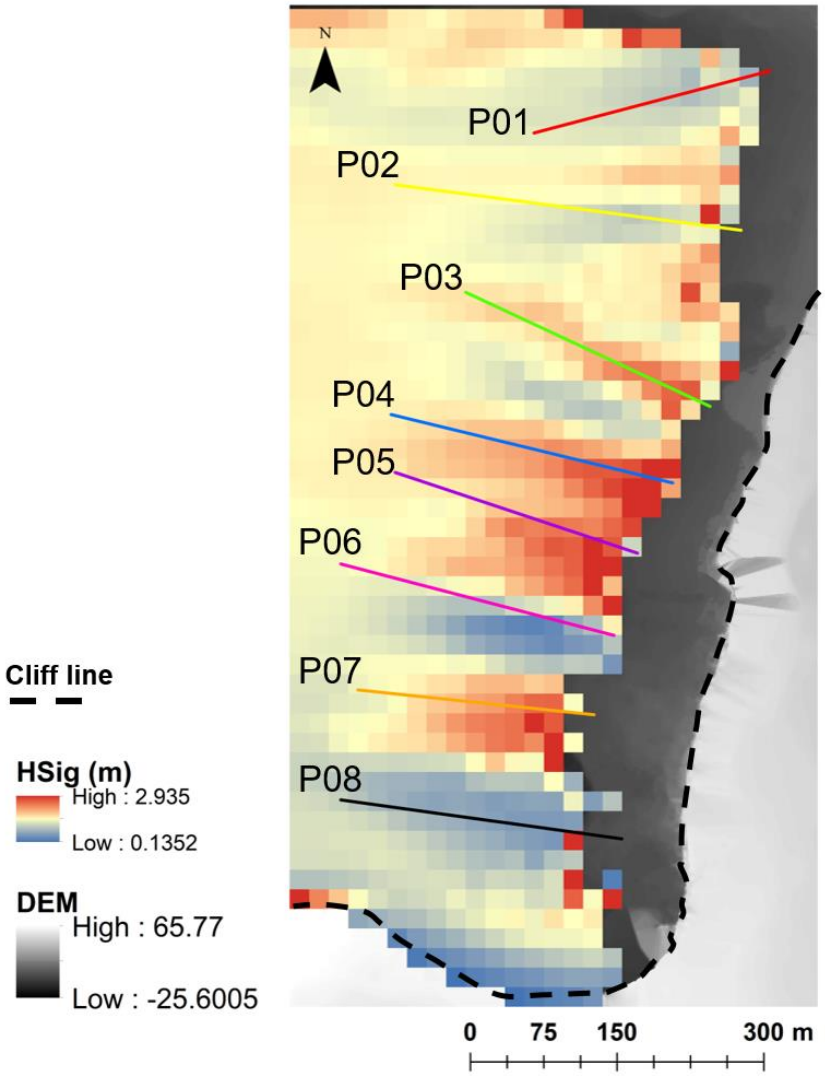

Figure 7. The location of the shore normal profiles of HSig and nearshore bathymetry from north to south (P01 to P08 respectively).

The smallest increases in HSig occur in association with bathymetry which exhibits the least amount of nearshore topographic variability, as measured by the standard deviation (StDev) of the bathymetric profile. For P01 and P02 in the northernmost end of the bay (Figs. 7 and 8), HSig increases from a minimum of 0.43 m and 0.52 m to a maximum of 0.63 m and 0.66 m on P01 and P02 respectively. The equivalent bathymetric profiles have a StDev of 3.99 m (T01) and 4.52 m (T02) (Figure 8). For P03 and P04 (Figs. 7 and 9), HSig increases from a minimum of 0.75 m (P03) and 0.73 m (P04) to a maximum of 1.1 and 1.4 respectively. The StDev for the corresponding bathymetric profiles are 4.54 m (P03) and 4.85 m (P04). Towards the southern end of the bay on P05 and P06 (Figs. 7 and 10), HSig increase from a minimum of 0.55 m and 0.23 m to a maximum of 1.36 m and 0.65 m respectively. The corresponding StDev of the bathymetric profiles are 6.13 (P05) and 8.83 (P06). At the southernmost end of the bay HSig increases from a minimum of 0.59 m to a maximum of 1.19 m on P07 (Figs. 7 and 11) and from 0.31 m to 1.5 m on P08 (Figs. 7 and 11). The StDev of the equivalent bathymetric profiles (Figure 11) are 5.71 (T07) and 5.16 (T08).

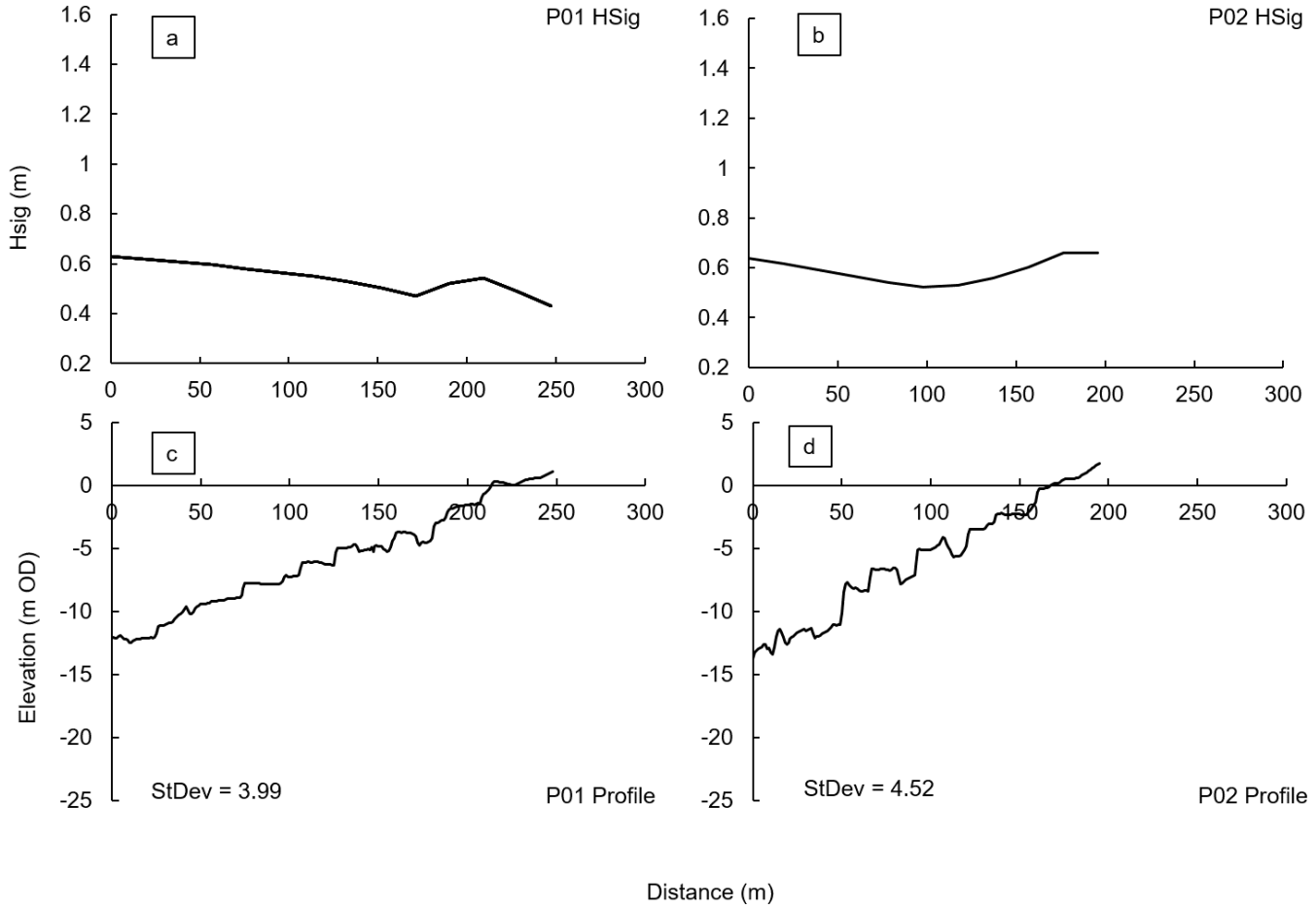

Figure 8. Cross shore profiles HSig on P01 and P02 (a and b) showing the shoaling of waves and increase in HSig as waves reach shallower bottom depths. The corresponding nearshore bathymetric profiles and their respective StDev are shown in c and d (P01 and P02 respectively).

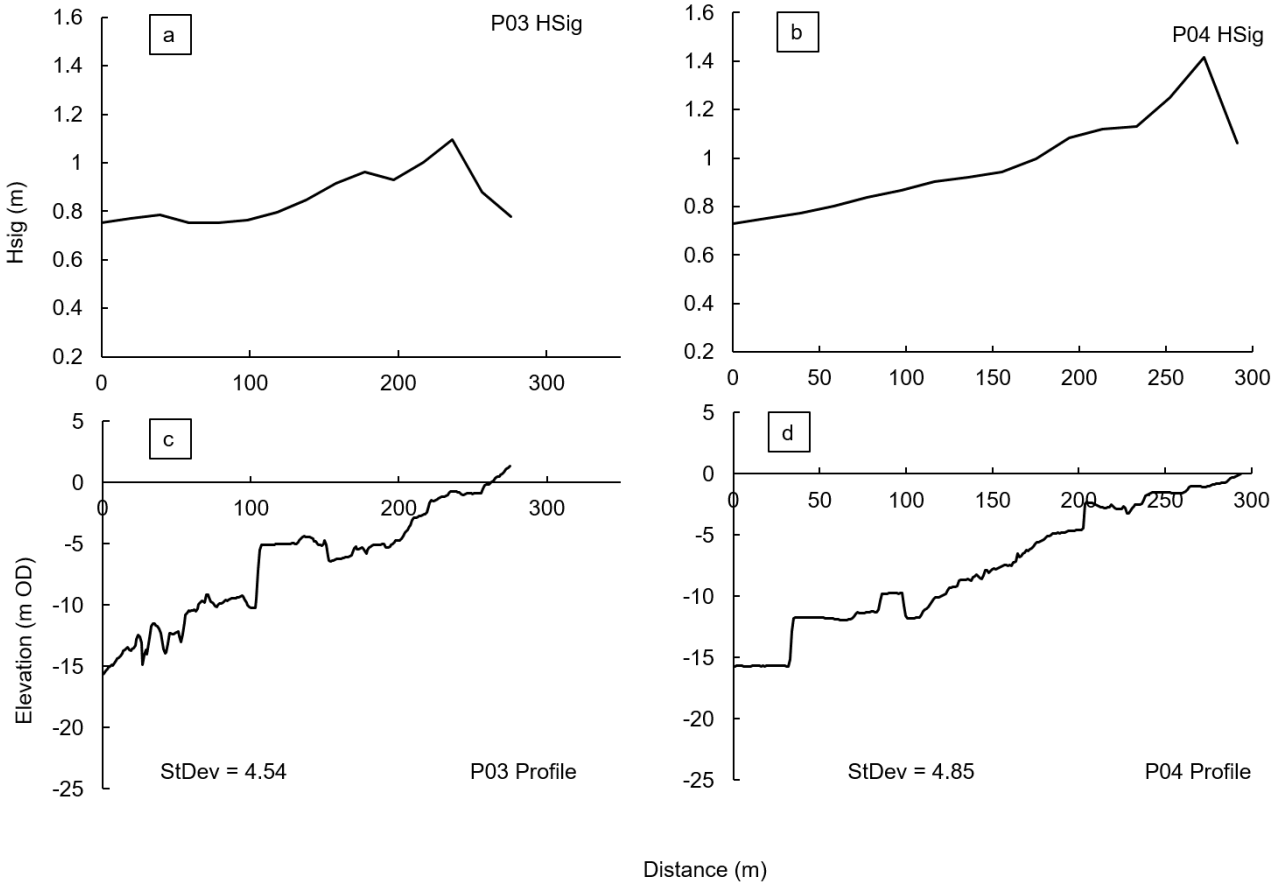

Figure 9. Cross shore profiles HSig on P03 and P04 (a and b) showing the shoaling of waves and increase in HSig as waves reach shallower bottom depths. The corresponding nearshore bathymetric profiles and their respective StDev are shown in c and d (P03 and P04 respectively).

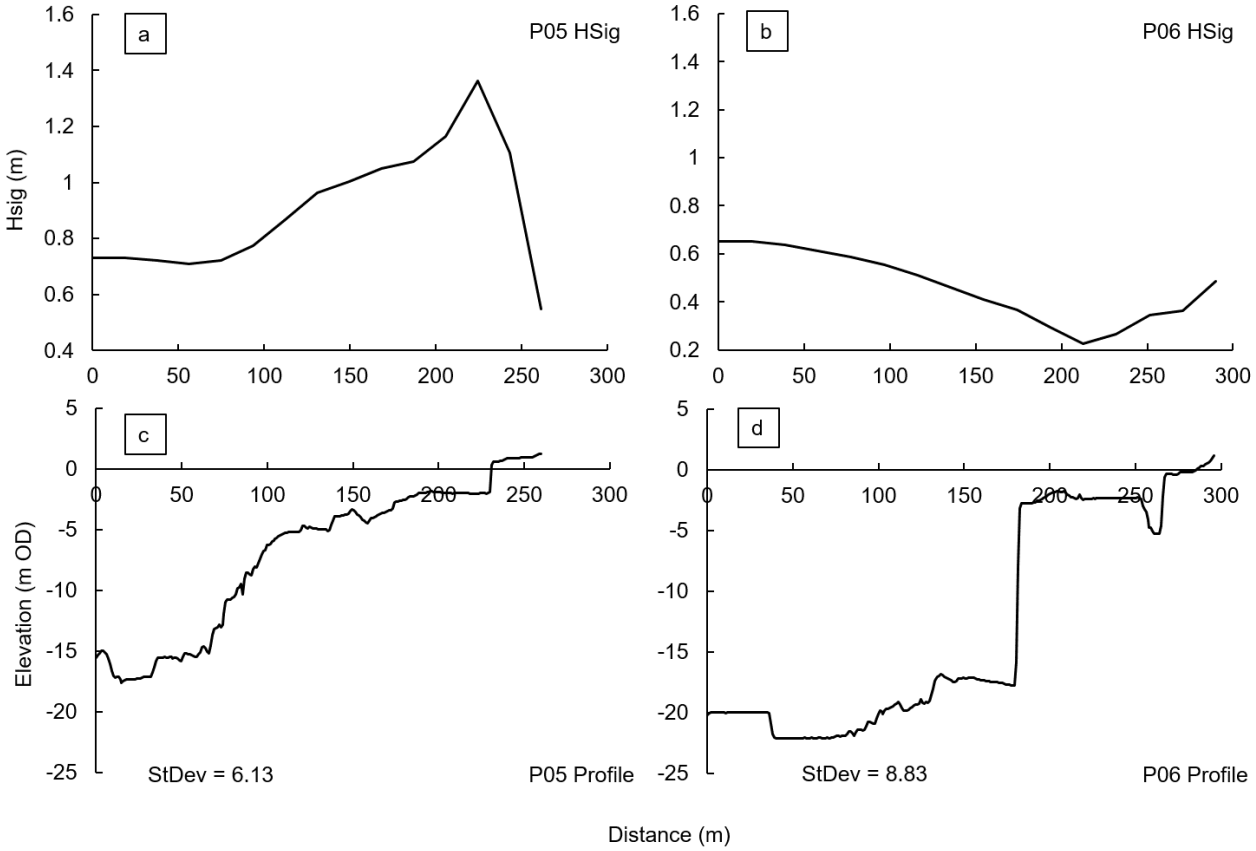

Figure 10. Cross shore profiles HSig on P05 and P06 (a and b) showing the shoaling of waves and increase in HSig as waves reach shallower bottom depths. The corresponding nearshore bathymetric profiles and their respective StDev for are shown in c and d (P05 and P06 respectively).

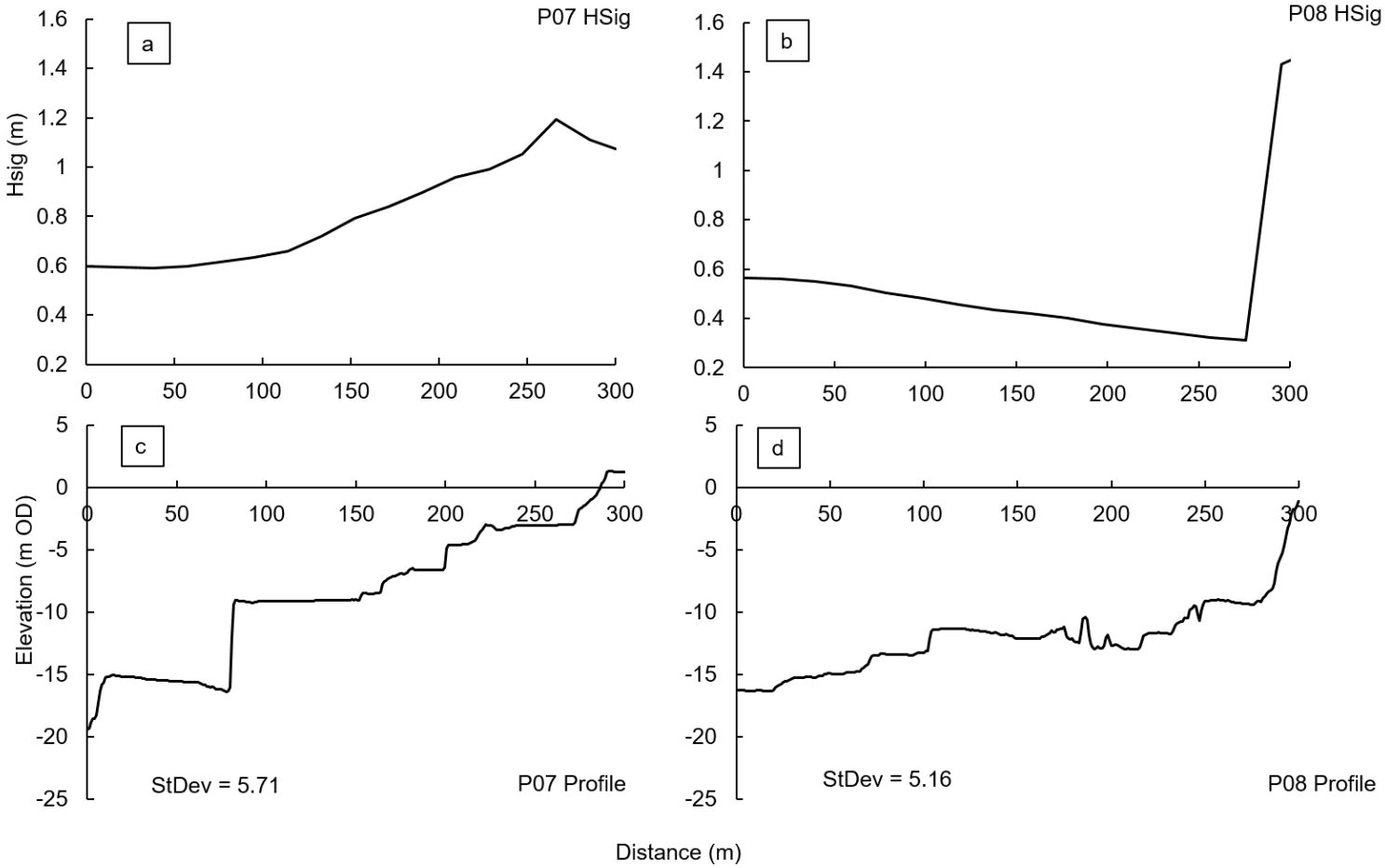

Figure 11. Cross shore profiles HSig on P07 and P08 (a and b) showing the shoaling of waves and increase in HSig as waves reach shallower bottom depths. The corresponding nearshore bathymetric profiles and their respective StDev are shown in c and d (P07 and P08 respectively).

Alongshore variability of cliff toe elevation.

Seven across shore profiles (Figure 12) show the variability in the position of the cliff toe alongshore relative to the maximum tidal range (2.2 m OD). The elevation of the cliff toe varies significantly alongshore and is lowest at the northern end of the site (5 m OD) (Figure 12), increasing southward to maximum of 13 m OD. The exception to this is the southern corner of the bay where the cliff toe elevation is 2 m OD. .

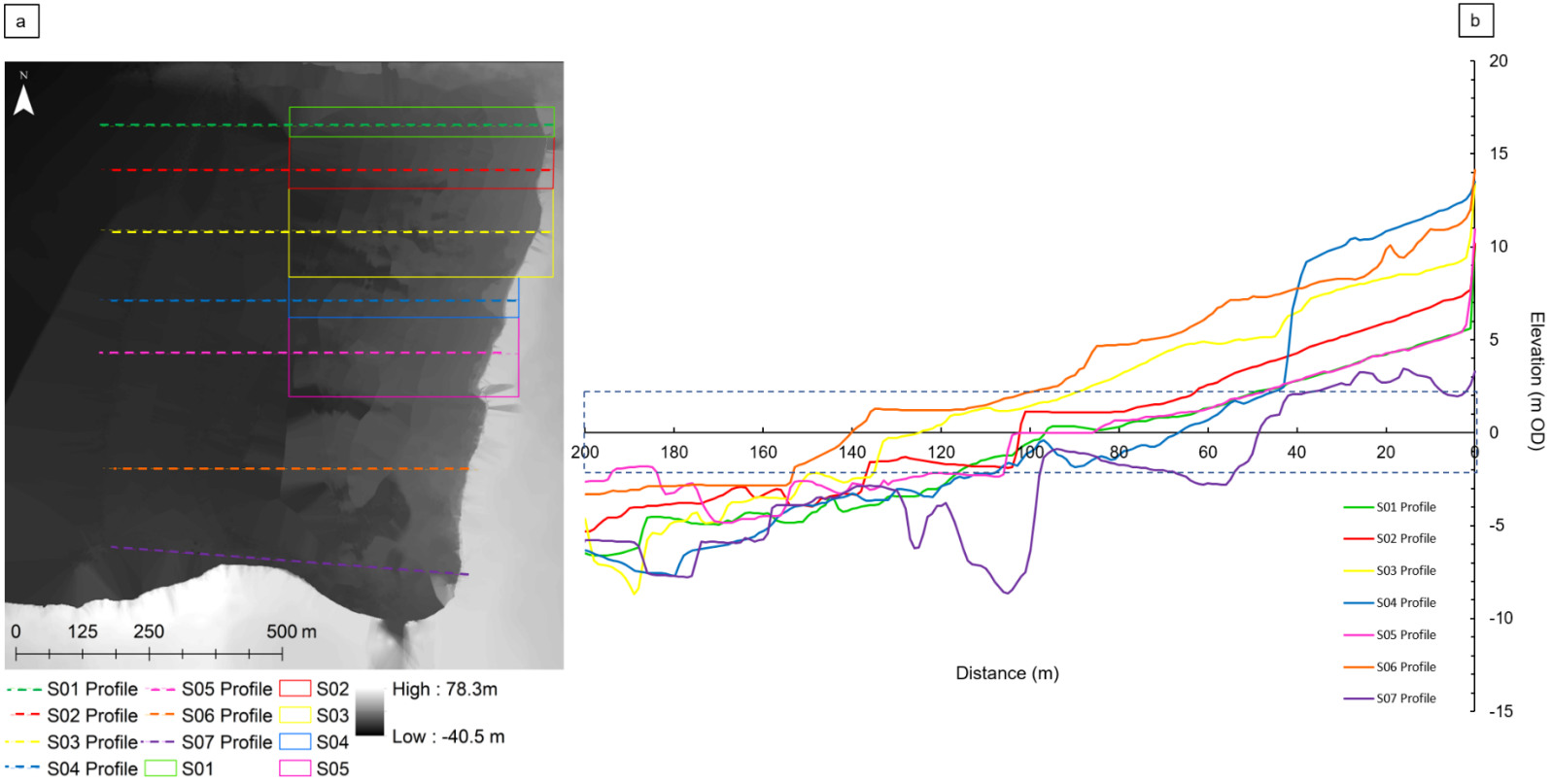

Figure 12. (a) the location of the cliff toe elevation profiles (dashed lines) from north to south (S01 Profile – S07 Profile respectively) and their location with respect to cliff sections where erosion rates were measured (chapter 2) (coloured boxes in a, from north to south S01 -S05 respectively). Topographic profiles showing the variation in cliff toe elevations alongshore are shown in b.

3.3.5 Spatial distribution of cliff erosion.

The rate of cliff erosion at the study site has been shown to vary between cliff sections (Figure 12) A total of 56 m^3 of cliff material was eroded via rockfall during the study period (March 2016 to Apr 2017). The net erosion rate for the entire cliff was calculated at 0.37 cm yr^{-1}. S01, located at the northern end of the bay had the highest erosion rate (1.5 cm yr^{-1}) (chapter 2). The lowest erosion rate was observed in S02 and S04 (0.1 cm yr^{-1}). The erosion rate at the southern end of the bay (S05, chapter 2) was 0.6 cm yr^{-1} (chapter 2). It is important to note that the erosion rates calculated here are for a period of one year which is short with respect to the timescale of erosion on rock coasts. Hence, we apply a note of caution with respect to extrapolation of this figure over longer time scales. We do note however, that the rate of erosion calculated here is within the range expected for this rock type (medium hardness) based on the global median rates of coastal cliff erosion calculated by of Prémaillon et al. (2018).

3.4 Discussion

Macroscale coastal geometry and nearshore bathymetry

The model simulations show variability in alongshore HSig within the bay. Regardless of simulated offshore incoming wave direction, period or HSig during the study period, the highest HSig at the maximum tidal range is consistently found at the southern half of the bay. The low range of values of HSig approaching the nearshore suggest that the overall macroscale geometry of the coastline does not have a controlling effect on the distribution of HSig, (and hence wave energy) within the bay. Our findings are consistent with a recent study by Jones et al. (2018) who monitored high frequency cliff top motions using seismometers along a stretch of coastline between Staithes and Port Mulgrave on the NE coast of the UK to

determine the alongshore variability of wave energy. The site was similar to that studied here with a 570 m bay with two adjacent headlands. The authors concluded that the macroscale geometry of the coastline had little effect on variability of wave energy delivery to the cliff in the bay studied when compared to that of the nearshore morphology. Indeed, our findings strongly suggest that it is the nearshore morphology and the offshore HSig that appear to have the greatest influence on the variability of the alongshore distribution of wave energy (HSig) within the bay. Here we state an important limitation of the model runs with respect to the inland limits that were used i.e. high-water spring tide (+2.2 m OD). Waves here are likely to behave as a wave bore rather than as waves and hence modelled conditions may deviate from the actual conditions. Any further work will require that the inland limits for the model runs stop further out and that wave transformation across the foreshore is modelled using additional more suitable software (e.g. XBeach) which is capable of resolving this transformation more accurately.

The StDev of the nearshore bathymetric profile, used here as a measure of the variability of nearshore morphology, increases from north to south consistent with an overall increase in the HSig from north to south. The scale of variability of the nearshore bathymetric profiles has a strong influence on the magnitude of shoaling and on the relative increase in HSig. Greater shoaling occurs in the southern half of the bay where the Stdev of the nearshore profiles, and hence the magnitude of variability in the nearshore bathymetry, is greatest. In the northern half of the bay and particularly in the northernmost end, relatively low nearshore bathymetric variability is associated which relatively lower magnitude of wave shoaling and lower HSig.

Our data show that the alongshore wave energy variability decreases during large swell events (i.e. where offshore HSig is greatest) compared to lower energy, or even average conditions (Jones et al., 2018). Despite the lower variability in alongshore HSig at the maximum tidal range under storm conditions, modelled HSig remains lowest at the northern end of the bay,

highlighting again the influence of nearshore bathymetry on alongshore wave energy variability.

Foreshore characteristics

We have not measured the transformation of wave energy across the foreshore. However, foreshore characteristics (e.g. width, morphology, gradient) and the elevation of the foreshore and cliff toe relative to the tidal frame, have been demonstrated to exert a strong control on the cross shore distribution of wave energy (Ogawa et al., 2011, Ogawa et al., 2016, Poate et al., 2016, Stephenson et al., 2018). Tidal level, combined with bottom depth and wave height, controls the distance from the cliff at which waves break. Stephenson et al. (2018) demonstrated that tidal level during high tide waves < 2 m were able to travel further across the platform before breaking, resulting in a narrow surf zone close to the cliff and relatively less wave energy dissipation compared to low tide. In a microtidal environment, Marshall and Stephenson (2011) found that water depth and foreshore gradient had a greater influence on dissipation of wave energy across the foreshore than foreshore width. With respect to platform width and elevation, Ogawa et al. (2016) found that in micro tidal environments, platform width and gradient had the greatest influence on the cross shore distribution of wave energy. On narrower, lower elevation platforms, greater water depths allowed greater gravity wave to propagate across the platform. On wider platforms with a higher elevation relative to the tidal frame, waves break further from the cliff toe and greater energy is dissipated across the platform (Beetham and Kench, 2011, Ogawa et al., 2016). The importance of storm surge in elevating wave processes was not investigated here. Future work will benefit from incorporating storm surge into model runs. Coupling of the SWAN model with a second model which is capable of modelling wave energy transformation across the foreshore to the cliff toe (e.g. XBeach or similar) may also be useful in this regard.

The elevation of the cliff toe relative to the tidal frame also exerts a strong control on the delivery of wave energy to the cliff (Ogawa et al., 2011, 2016, Poate et al., 2016, Stephenson et al., 2018). At our study site, variability in alongshore cliff toe elevation clearly plays a critical role in wave energy delivered to the cliff. This variability in cliff toe elevation may partially explain the lack of any obvious relationship between the alongshore wave energy distribution and the spatial distribution of erosion (discussed below). Higher elevations receive proportionally less wave energy than lower elevations. Therefore, given the trend for increasing cliff toe elevation from north to south, we might expect to see greater erosion rates at the northern end of the bay where cliff toe elevation is lower.

Erosion rates

Our measurements of cliff erosion do not extend to the southernmost end of the bay which were inaccessible but where modelled HSig is greatest. However, the overall planform of the bay (Figure 1) supports the finding of chapter 2 which demonstrated that the highest rates of cliff erosion occurred in the northeast end of the bay. The planform of the bay therefore also suggests that the rate of cliff erosion (retreat) decreases moving southwards, except for the southernmost corner of the bay. This area coincides with an area of the bay where the present-day platform is largely absent and hence nearshore bottom depth is relativity greater. This produces waves which firstly, break closer to the cliff and secondly, are not dissipated across a wide platform. As such waves in this area can deliver proportionally greater amounts of wave energy to the cliff toe. Furthermore, at this location the cliff toe elevation is within normal tidal range and as such, receives a proportionally higher frequency of wave impacts compared to any other cliff toe location alongshore. The apparently greater inferred rate of erosion in the southern corner of the bay combined with these factors provide further support for the

importance of nearshore and foreshore morphology and cliff toe elevation relative to the tidal frame when considering controls on the rate of coastal cliff erosion.

Our results indicate that near and foreshore characteristics have a significant influence on the variability of alongshore wave energy distribution and delivery to the cliff. The macroscale coastline geometry has little effect on the significant wave height variability within the bay. The alongshore variability in HSig is strongly influenced by the scale of variability of the nearshore bathymetry. While cliff erosion rates also vary alongshore we did not observe any relationship between the non-linear spatial distribution of cliff erosion and the alongshore variability of wave energy. We propose that this is due to the strong influence of discontinuity set characteristics (Chapter 2) in addition to the influence of cliff toe elevation relative to the tidal range.

3.5 Conclusions

We have modelled alongshore variability of wave energy, using significant wave height as a proxy, on an embayed coastline on the west coast of Ireland under varying offshore wave conditions to explore the relationships between wave climate, near and foreshore characteristics and the spatial distribution of rock cliff erosion.

1.We find that HSig varies considerably alongshore within the bay and that this variability is controlled by the nearshore bathymetry. Relatively greater shoaling and relatively larger HSig are associated with nearshore bathymetry that exhibits greater variability with respect to the scale of topographic change.

2. We do not find a significant relationship between cliff erosion rates and along shore wave energy distribution. In this instance we conclude that this is due to the influence foreshore characteristics, specifically cliff toe elevation with respect to the tidal frame, in addition to the

strong influence of discontinuity set characteristics (Chapter 2). However, we also note the limitations of the short time scale used to measure the erosion rate relative to the time scale of erosive processes operating on rock coasts and the influence this may have had on the results.

3. Our data highlight the importance of nearshore bathymetry on the alongshore distribution of wave energy and wave energy delivery to the cliff toe (e.g. Jones et al., 2018).

4. Our findings demonstrated the critical role of cliff toe elevation relative to the tidal frame (Ogawa, 2013, Poate et al., 2016, Stephenson et al., 2018). Further study of nearshore and foreshore characteristics will determine the influence of bay configuration on wave energy and rates of coastal cliff retreat. Although for some locations it is anticipated that rock mass characteristics such as lithology, discontinuities and weathering are more important.

Acknowledgements

We would like to thank Dr. Patrick Belmont for providing equipment and carrying out collection of bathymetry data. Thanks to Bruce Call for initial processing of bathymetric data. We would also like to thank David Rogers (Ulster University) for expertise and guidance during TLS data collection in the field during what were sometimes very difficult conditions, and also for initial processing of the TLS data. Thank you to David Hardy and Niall Finn at the Geological survey of Ireland for initial processing of the offshore bathymetric data. A special thank you to Dr Carlos Loureiro (Ulster University) for his tremendous instruction on all aspects of wave modelling using SWAN and for his continued help with the simulations throughout the preparation of this manuscript.

References

ADAMS, P. N. 2005. Nearshore wave-induced cyclical flexing of sea cliffs. *Journal of Geophysical Research,* 110.

ADAMS, P. N., ANDERSON, R. S. & REVENAUGH, J. 2002. Microseismic measurement of wave-energy delivery to a rocky coast. *Geology,* 30**,** 895-898.

ADAMS, P. N., STORLAZZI, C. D. & ANDERSON, R. S. 2005. Nearshore wave-induced cyclical flexing of sea cliffs. *Journal of Geophysical Research: Earth Surface (2003–2012),* 110.

BATTJES, J. A. & JANSSEN, J. 1978. Energy loss and set-up due to breaking of random waves. *Coastal Engineering 1978.*

BEETHAM, E. P. & KENCH, P. S. 2011. Field observations of infragravity waves and their behaviour on rock shore platforms. *Earth Surface Processes and Landforms,* 36**,** 1872-1888.

BOOIJ, N., RIS, R. & HOLTHUIJSEN, L. H. 1999. A third-generation wave model for coastal regions: 1. Model description and validation. *Journal of geophysical research: Oceans,* 104**,** 7649-7666.

BRAIN, M. J., ROSSER, N. J., NORMAN, E. C. & PETLEY, D. N. 2014. Are microseismic ground displacements a significant geomorphic agent? *Geomorphology,* 207**,** 161-173.

COX, R., ZENTNER, D. B., KIRCHNER, B. J. & COOK, M. S. 2012. Boulder ridges on the Aran Islands (Ireland): recent movements caused by storm waves, not tsunamis. *The Journal of geology,* 120**,** 249-272.

CULLEN, N. D. & BOURKE, M. C. 2018. Clast abrasion of a rock shore platform on the Atlantic coast of Ireland. *Earth Surface Processes and Landforms,* 43 (12) 2627-2641.

DICKSON, M. E. & PENTNEY, R. 2012. Micro-seismic measurements of cliff motion under wave impact and implications for the development of near-horizontal shore platforms. *Geomorphology,* 151-152**,** 27-38.

EARLIE, C. S. 2015. Field observations of wave induced coastal cliff erosion, Cornwall, UK.

ELDEBERKY, Y. & BATTJES, J. A. 1996. Spectral modeling of wave breaking: Application to Boussinesq equations. *Journal of Geophysical Research: Oceans,* 101**,** 1253-1264.

ELGAR, S. & GUZA, R. 1985. Observations of bispectra of shoaling surface gravity waves. *Journal of Fluid Mechanics,* 161**,** 425-448.

ERDMANN, W., KELLETAT, D. & SCHEFFERS, A. 2018. Boulder transport by storms–Extreme-waves in the coastal zone of the Irish west coast. *Marine Geology*.

ETIENNE, S. & PARIS, R. 2010. Boulder accumulations related to storms on the south coast of the Reykjanes Peninsula (Iceland). *Geomorphology,* 114**,** 55-70.

FARO 2016. *Faro Scene cloud processing software* (version 6.2) [software] Available at https://www.faro.com/products/product-design/faro-scene.

FARRELL, E. J., GRANJA, H., CAPPIETTI, L., ELLIS, J. T., LI, B. & SHERMAN, D. J. 2009. Wave transformation across a rock platform, Belinho, Portugal. *Journal of Coastal Research***,** 44-48.

FREILICH, M. & GUZA, R. 1984. Nonlinear effects on shoaling surface gravity waves. *Phil. Trans. R. Soc. Lond. A,* 311**,** 1-41.

GALLAGHER, S., TIRON, R. & DIAS, F. 2014. A long-term nearshore wave hindcast for Ireland: Atlantic and Irish Sea coasts (1979–2012). *Ocean Dynamics,* 64**,** 1163-1180.

GORRELL, L., RAUBENHEIMER, B., ELGAR, S. & GUZA, R. 2011. SWAN predictions of waves observed in shallow water onshore of complex bathymetry. *Coastal Engineering,* 58**,** 510-516.

GOTO, K., MIYAGI, K., KAWANA, T., TAKAHASHI, J. & IMAMURA, F. 2011. Emplacement and movement of boulders by known storm waves—field evidence from the Okinawa Islands, Japan. *Marine Geology,* 283**,** 66-78.

GOTO, K., OKADA, K. & IMAMURA, F. 2009. Characteristics and hydrodynamics of boulders transported by storm waves at Kudaka Island, Japan. *Marine Geology,* 262**,** 14-24.

GOTO, K., OKADA, K. & IMAMURA, F. 2010. Numerical analysis of boulder transport by the 2004 Indian Ocean tsunami at Pakarang Cape, Thailand. *Marine Geology,* 268**,** 97-105.

HALL, A. M. 2011. Storm wave currents, boulder movement and shore platform development: A case study from East Lothian, Scotland. *Marine Geology,* 283**,** 98-105.

HANSOM, J., BARLTROP, N. & HALL, A. 2008. Modelling the processes of cliff-top erosion and deposition under extreme storm waves. *Marine Geology,* 253**,** 36-50.

HASSELMANN, K., BARNETT, T., BOUWS, E., CARLSON, H., CARTWRIGHT, D., ENKE, K., EWING, J., GIENAPP, H., HASSELMANN, D. & KRUSEMAN, P. 1973. Measurements of

wind-wave growth and swell decay during the Joint North Sea Wave Project (JONSWAP). *Ergänzungsheft 8-12*.

HUTCHINSON, J. Field and laboratory studies of a fall in Upper Chalk cliffs at Joss Bay, Isle of Thanet. Proceedings of the Roscoe Memorial Symposium, 1972, 1972. 692-706.

IMAMURA, F., GOTO, K. & OHKUBO, S. 2008. A numerical model for the transport of a boulder by tsunami. *Journal of Geophysical Research: Oceans,* 113.

JANSSEN, P. A. 1989. Wave-induced stress and the drag of air flow over sea waves. *Journal of Physical Oceanography,* 19**,** 745-754.

JANSSEN, P. A. 1991. Quasi-linear theory of wind-wave generation applied to wave forecasting. *Journal of Physical Oceanography,* 21**,** 1631-1642.

JONES, E. V., ROSSER, N. & BRAIN, M. 2018. Alongshore variability in wave energy transfer to coastal cliffs. *Geomorphology*.

KANYAYA, J. I. & TRENHAILE, A. S. 2005. Tidal wetting and drying on shore platforms: an experimental assessment. *Geomorphology,* 70**,** 129-146.

LIM, M., ROSSER, N. J., PETLEY, D. N. & KEEN, M. 2011. Quantifying the controls and influence of tide and wave impacts on coastal rock cliff erosion. *Journal of Coastal Research,* 27**,** 46-56.

MARSHALL, R. J. & STEPHENSON, W. J. 2011. The morphodynamics of shore platforms in a micro-tidal setting: Interactions between waves and morphology. *Marine Geology,* 288**,** 18-31.

MASTRONUZZI, G. & SANSÒ, P. 2004. Large boulder accumulations by extreme waves along the Adriatic coast of southern Apulia (Italy). *Quaternary International,* 120**,** 173-184.

NANDASENA, N., PARIS, R. & TANAKA, N. 2011. Numerical assessment of boulder transport by the 2004 Indian ocean tsunami in Lhok Nga, West Banda Aceh (Sumatra, Indonesia). *Computers & geosciences,* 37**,** 1391-1399.

NANDASENA, N. & TANAKA, N. 2013. Boulder transport by high energy: Numerical model-fitting experimental observations. *Ocean Engineering,* 57**,** 163-179.

NAYLOR, L. A., STEPHENSON, W. J., SMITH, H. C., WAY, O., MENDELSSOHN, J. & COWLEY, A. 2016. Geomorphological control on boulder transport and coastal erosion before, during and after an extreme extra-tropical cyclone. *Earth Surface Processes and Landforms,* 41**,** 685-700.

NORMAN, E. C., ROSSER, N. J., BRAIN, M. J., PETLEY, D. N. & LIM, M. 2013. Coastal cliff-top ground motions as proxies for environmental processes. *Journal of Geophysical Research: Oceans,* 118**,** 6807-6823.

NOTT, J. 2003. Waves, coastal boulder deposits and the importance of the pre-transport setting. *Earth and Planetary Science Letters,* 210**,** 269-276.

OGAWA, H. 2012. Observation of wave transformation on a sloping type B shore platform under wind-wave and swell conditions. *Geo-Marine Letters,* 33**,** 1-11.

OGAWA, H. 2013. Observation of wave transformation on a sloping type B shore platform under wind-wave and swell conditions. *Geo-Marine Letters,* 33**,** 1-11.

OGAWA, H., DICKSON, M. & KENCH, P. 2011. Wave transformation on a sub-horizontal shore platform, Tatapouri, North Island, New Zealand. *Continental Shelf Research,* 31**,** 1409-1419.

OGAWA, H., DICKSON, M. E. & KENCH, P. S. 2016. Generalised observations of wave characteristics on near-horizontal shore platforms: Synthesis of six case studies from the North Island, New Zealand. *New Zealand Geographer,* 72**,** 107-121.

OGAWA, H., KENCH, P. & DICKSON, M. 2012. Field Measurements of Wave Characteristics on a Near-Horizontal Shore Platform, Mahia Peninsula, North Island, New Zealand. *Geographical Research,* 50**,** 179-192.

POATE, T., MASSELINK, G., AUSTIN, M., DICKSON, M. & KENCH, P. 2016. Observation of Wave Transformation on Macro-tidal Rocky Platforms. *Journal of Coastal Research,* 75**,** 602-606.

POATE, T., MASSELINK, G., AUSTIN, M. J., DICKSON, M. & MCCALL, R. 2018. The role of bed roughness in wave transformation across sloping rock shore platforms. *Journal of Geophysical Research: Earth Surface,* 123**,** 97-123.

SALLENGER JR, A. H., KRABILL, W., BROCK, J., SWIFT, R., MANIZADE, S. & STOCKDON, H. 2002. Sea-cliff erosion as a function of beach changes and extreme wave runup during the 1997–1998 El Niño. *Marine Geology,* 187**,** 279-297.

SANDERS, N. Wave tank experiments on erosion of rocky coasts. Papers and Proceedings of the Royal Society of Tasmania, 1968. 11-18.

STEPHENSON, W. J. & KIRK, R. M. 2000. Development of shore platforms on Kaikoura Peninsula, South Island, New Zealand: Part one: the role of waves. *Geomorphology,* 32**,** 21-41.

STEPHENSON, W. J., NAYLOR, L. A., SMITH, H., CHEN, B. & BRAYNE, R. P. 2018. Wave transformation across a macrotidal shore platform under low to moderate energy conditions. *Earth Surface Processes and Landforms,* 43**,** 298-311.

SUNAMURA, T. 1977. A relationship between wave-induced cliff erosion and erosive force of waves. *The Journal of Geology,* 85**,** 613-618.

SUNAMURA, T. 1992. *Geomorphology of rocky coasts*, John Wiley & Son Ltd.

SUNAMURA, T. Rock control in coastal geomorphic processes. International Journal of Rock Mechanics and Mining Sciences and Geomechanics Abstracts, 1995. 103A.

TELEDYNE 2015. River Ray ADCP Guide.

Teledyne Marine.

TRENHAILE, A. 2000. Modeling the development of wave-cut shore platforms. *Marine Geology,* 166**,** 163-178.

TRENHAILE, A. & PORTER, N. J. 2007. Can shore platforms be produced solely by weathering processes? *Marine Geology,* 241**,** 79-92.

TRENHAILE, A. S. 1987. *The geomorphology of rock coasts*, Oxford University Press, USA.

TRENHAILE, A. S. 2008. The development of subhorizontal shore platforms by waves and weathering in microtidal environments. *Zeitschrift für Geomorphologie,* 52**,** 105-124.

TRENHAILE, A. S. & KANYAYA, J. I. 2007. The role of wave erosion on sloping and horizontal shore platforms in macro-and mesotidal environments. *Journal of Coastal Research***,** 298-309.

YOUNG, A. P., ADAMS, P. N., O'REILLY, W. C., FLICK, R. E. & GUZA, R. 2011. Coastal cliff ground motions from local ocean swell and infragravity waves in southern California. *Journal of Geophysical Research: Oceans,* 116.

YOUNG, A. P. & ASHFORD, S. A. 2008. Instability investigation of cantilevered seacliffs. *Earth Surface Processes and Landforms: The Journal of the British Geomorphological Research Group,* 33**,** 1661-1677.

YOUNG, A. P., GUZA, R. T., ADAMS, P. N., O'REILLY, W. C. & FLICK, R. E. 2012. Cross-shore decay of cliff top ground motions driven by local ocean swell and infragravity waves. *Journal of Geophysical Research,* 117.

YOUNG, A. P., GUZA, R. T., DICKSON, M. E., O'REILLY, W. C. & FLICK, R. E. 2013. Ground motions on rocky, cliffed, and sandy shorelines generated by ocean waves. *Journal of Geophysical Research: Oceans,* 118**,** 6590-6602.

Chapter 4: Clast abrasion of a rock shore platform on the Atlantic coast of Ireland

Cullen, N.D.[1] and Bourke, M.C.[1] 2018 Clast abrasion of a rock shore platform on the Atlantic coast of Ireland. *Earth Surface Processes and Landforms*, 43 (12), 2626 – 2641, doi:10.1002/esp.4421

[1]Department of Geography, Trinity College Dublin, The University of Dublin, 2 College Green, Dublin 2, Ireland.

Abstract

The abrasion of coastal rock platforms by individual or clusters of clasts during transport has not been quantitatively assessed. We present a study which identifies the types of abrasion and quantifies erosion due to the transport of clasts during three storms in February and March 2016. We explore relationships between platform roughness, determined by the Fractal Dimension (*D*) of the topographic profiles, geomorphic controls and the type and frequency of abrasion feature observed. Clast transport experiments were undertaken in conjunction with the measurement of wave energy to assess transport dynamics under summer and winter (non-storm) conditions.

Platform abrasion occurred extensively during the storms. We identify two types of clast abrasion trails: simple and complex. In addition, we find two forms of erosion occur on these trails: Scratch marks and Percussion marks. An estimated 13.6 m^2 of the platform surface (representing < 1% of the total surface area) was eroded by clast abrasion on simple abrasion trails during the three storms. We attribute approximately two thirds of this to scratch-type abrasion. The total volume of material removed by abrasion was 67,808 cm^3. Despite the larger surface area affected by scratch marks, we find that the volume of material removed through percussion impact was almost seven times greater. We also find that the type and frequency of abrasion features is strongly influenced by the effect of platform morphometry on

transport mode, with impact-type abrasion dominating areas of higher platform roughness. Results of the clast transport experiments indicate that abrasion occurs under non-storm wave energy conditions with observable geomorphological effects. We suggest that abrasion by clasts is an important component of platform erosion on high energy Atlantic coastlines, particularly over longer time scales, and that the morphogenetic link between the cliff and the platform is important in this context as the sediment supplied by the cliff is used to abrade the platform.

Keywords

Shore platforms, abrasion, clast transport, Atlantic coast.

Author Contributions

N.D.C. wrote the body of the manuscript with contributions from M.C.B. N.D.C carried out the analysis. M.C.B edited the final manuscript

4.1 Introduction

4.1.1 Shore platform research

Shore platforms form conspicuous components of rocky coasts which, until recent decades, were largely ignored by coastal scientists (Dasgupta, 2011). Stephenson (2000) identified four emergent themes in shore platform research, specifically: (1) the role of marine and subaerial processes on the platform development; (2) platform morphology; (3) modelling platform development and (4) measurement of erosion rates on platforms. More recently, geo informatics have been applied to elucidate dynamics between shore platforms and cliffs (Palamara et al., 2007, Dornbusch et al., 2008). A comprehensive, but not exhaustive, review of the literature on shore platforms (n = 95) from 1968 to present (Figure 1) has highlighted the tendency for research to focus on microscale processes (e.g. sweeping abrasion, salt weathering), and macro-scale or modelling studies of controls on platform development (e.g. tidal inundation period and geological contingency), a trend that has also been noted by Stephenson and Naylor (2011b). In comparison, meso-scale processes have received less attention, although research at this scale has increased significantly in the last two decades (Figure 1b). Elucidating controls on clast production and clast transport dynamics are the dominant themes at this scale (e.g. Cruslock et al., 2010, Hall, 2011a, Knight and Burningham, 2011, Stephenson and Naylor, 2011a, Naylor et al., 2016a).

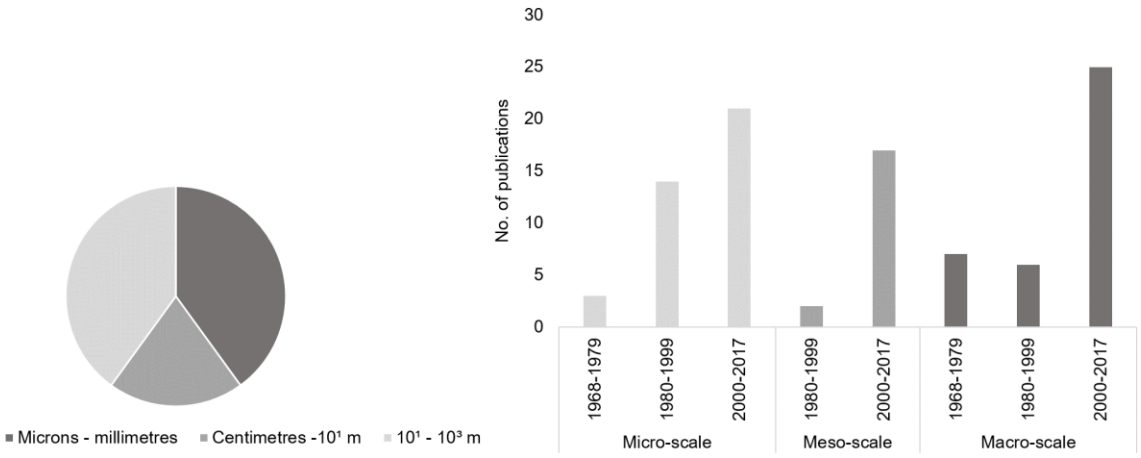

Figure 1. a) The intensity of research at different scales based on a review of 95 publications from 1968 – 2017 and b) trends in the scale of study over time.

Scale issues in geomorphology have already been highlighted by a number of researchers (e.g. Viles, 2001, Warke and McKinley, 2011). What the data in Figure 1 show is a clear need to focus greater attention on meso-scale erosion processes. Bridging the gap between the two end member scales of investigation can only improve prospects for more meaningful 'up' and 'down' scaling of microscale field and laboratory data and macro-scale landform development studies.

4.1.2 Meso-scale abrasion by clast transport

Abrasion trails are erosional lineations on the surface of coastal rock platforms formed by the movement of traction-load clasts across platforms by waves (Figure 2). They have been referred to in the literature as collections of '*impact marks, striations and crescentic marks'*

(Hall et al., 2008), *'trails of impact marks'* (Hall et al., 2008) *'linear abrasion scars'* (Knight et al., 2009) *'striations and scratches'* (Erdmann et al., 2018) and '*abrasion trails*' (Moses, 2014).

Figure 2. Abrasion trail formed by the transport of a clast across a supra tidal section of the shore platform at field site.

These abrasion trails, herein called clast abrasion trails (CATs), have been observed by numerous researchers (e.g. McKenna et al., 1992, Hall et al., 2008, Knight et al., 2009, Cruslock et al., 2010, Cox et al., 2012, Pérez-Alberti et al., 2012, Erdmann et al., 2018). Previous descriptions of CATs are primarily qualitative and are generally restricted to observations of maximum length (M_l) and the types of abrasion features observed e.g. scratch and crescentic marks. One exception to this is Moses (1993 cited by Moses, 2014) who

described narrow abrasion trails on a limestone platform on the west coast of Ireland where up to 90% of the surface rock had been fractured off exposing fresh bedrock. Despite the increasing number of studies that examine factors which control the entrainment and transport of boulders across shore platforms, the contribution of CATs to the erosion of shore platforms has not been quantitatively assessed (Moses, 2014).

Clast transport on intertidal shore platforms has been demonstrated to be a highly dynamic process (e.g. McKenna, 1990, Naylor et al., 2016a). Here we differentiate between cobble to boulder sized clasts (after Wentworth, 1922) found on intertidal platforms, Cliff Top Storm Deposits (CTSD) and mega-clasts. The latter two are the subject of much research but are not the focus of this study.

Factors affecting clast entrainment and transport include size, shape, transport mode, pre-transport setting, slope, topography and surface roughness (Nott, 2003, Imamura et al., 2008, Nandasena et al., 2011, 2013, Weiss and Diplas, 2015). Of these, slope, topography and surface roughness have been described as key factors (Nandasena et al., 2011, 2013, Weiss and Diplas, 2015). Yet, there is a need for increased quantity, quality and temporal resolution of field data from a range of sites in order to improve existing equations of boulder entrainment and transport (Paris et al., 2011, Naylor et al., 2016a). With the exception of Naylor et al. (2016a) observations of clast movement typically report movement months to years after a storm which reproduces poor time coupling between wave conditions and clast movement (Naylor et al., 2016a). Apart from McKenna (1990), there are no detailed observations of clast transport under non-storm conditions.

This paper is structured in two parts. The first part addresses the relative lack of quantitative data on meso-scale processes of erosion on shore platforms. The focus is meso-scale

abrasion caused by the transport of clasts. The primary aim in the first part is to provide the first quantitative assessment of abrasion on shore platforms via this process. This is achieved through measuring the volume of abrasion caused by the transport of clasts during three storms, defined as "*deep and active areas of low pressure associated with strong winds and precipitation*" (UK Met Office, 2018), in February and March 2016. The second aim is to provide an assessment of geomorphological controls and their relationship to clast transport dynamics and the type of abrasion feature observed. To this end, we provide a classification of abrasion feature types and combine this with a quantitative assessment of platform morphometry, using the Fractal Dimensional (*D*) as a measure of platform roughness.

The second part of this paper sets out to determine the potential for this abrasion process to operate under a range of wave energy regimes. Equivalent to our observation of the need for increased research at meso-scale, we suggest that clast transport studies would benefit from research which encompasses different 'scales' of wave energy. Combined with high resolution (daily) monitoring of clast transport, this will provide greater time coupling between wave conditions and clast transport dynamics. Therefore, the second part of this paper aims to determine threshold wave energy conditions required to entrain and transport clasts of known size and shape, and to assess the geomorphic effect. To this end, clast transport experiments were carried out under summer and winter wave energy conditions.

Study area

The study was conducted on an intertidal rock shore platform located at Ballard Bay on the Loop Head Peninsula, Co. Clare, Ireland (Figure 3). The location is exposed to high energy storms from the North Atlantic with annual mean significant wave heights of 3 – 4 m (Gallagher et al., 2013). The area is subject to semi-diurnal tides with a tidal range of 4.5 m. The study site is a 1 km long, sandstone cliffed coastline fronted by a gently sloping (2-5˚) platform with

a maximum width of 200 m terminating in a cliff at its seaward edge. This is similar to a Type B platform after Sunamura (1992). Normal tidal range reaches within 30-50 m of the cliff toe, depending on platform slope. However, prevailing westerly (onshore) winds and a predominantly W-SW incoming wave direction (Gallagher et al., 2014) produce waves which often reach the cliff toe, as evidenced by rapid (weeks to months) removal of cliff toe deposits.

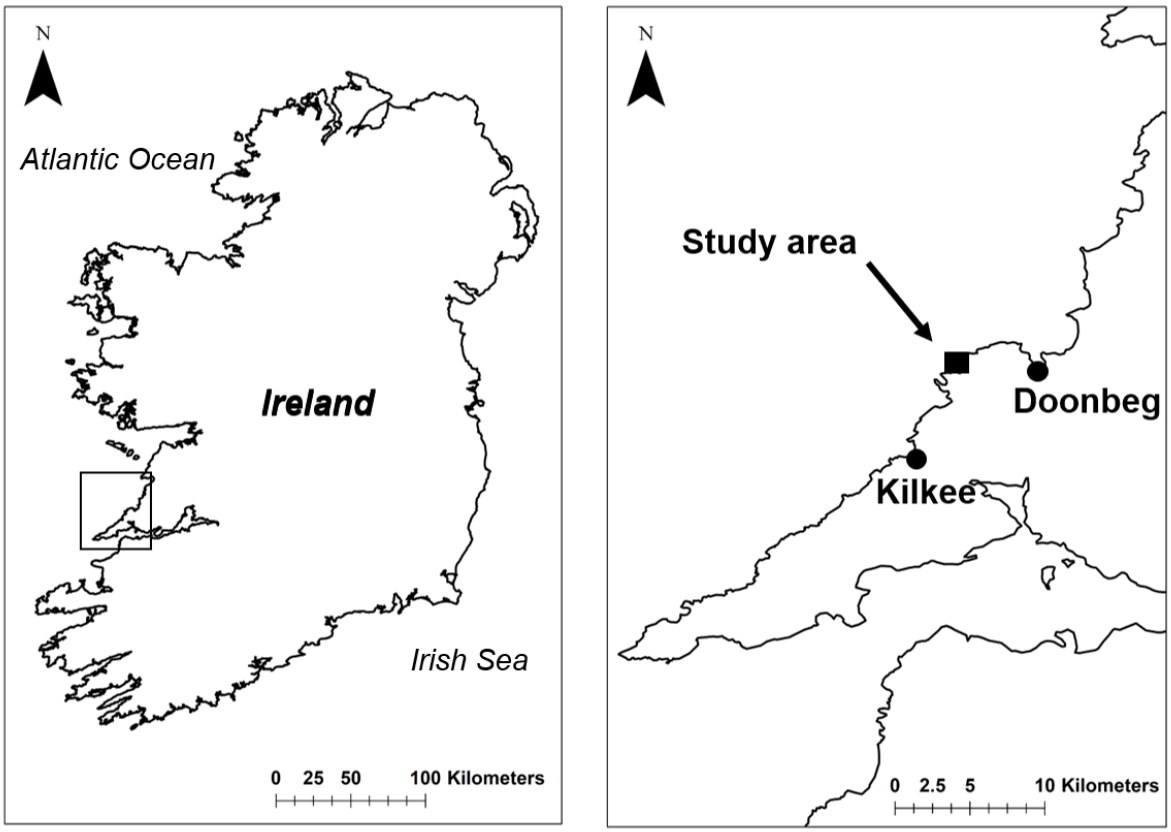

Figure 3. The location of the sites mentioned in the text. Maps throughout this manuscript were created using ArcGIS® software (version 10.4) by ESRI.

The study site is composed of two Upper Carboniferous sedimentary sequences, the Tullig (exposed on the platform) and Kilkee (exposed in the cliff) cyclothems, which form part of the

larger Central Clare Group (Hodson and Lewarne, 1961, Rider, 1974, Pulham, 1989, Collinson et al., 1991). During the Last Glacial Maximum ~24,000 Cal BP the study area was covered by the British Irish Ice Sheet (BIIS) (Peters et al., 2016). The western margins of the BIIS retreated from the area ~15.5 ± 1.0 ka BP (Bowen et al., 2002). Current rates of glacial isostatic rebound for the west coast of Ireland are estimated at -0.1 mm yr^{-1} (Stockamp et al., 2015).

Two widely spaced ENE trending faults dissect the platform into north, central and southern components. The southern platform is inaccessible. The lithology of the northern platform is characterised by a sandstone facies with a blocky internal structure and intermittent thin (<1 mm) clay seams which define bed layers of variable thickness (0.3 m – 0.5 m) within the sandstone body (Figure 4a). The thickness of the uppermost bed layer varies between 0.10 m and 0.40 m at visible exposures. The internal blocky structure is expressed at the surface as non-systematic discontinuities (i.e. discontinuities with non-systematic spacing, abrupt terminations and range of orientations) with a dominant NE to SW direction (Figure 4b). These discontinuities are intersected by widely spaced (1-3 m) NNW-SSE orientated systematic discontinuities (i.e. discontinuities with preferred orientation and systematic spacing) (Figure 4c). The thickness of the sandstone facies ranges from 3 m on the northern platform, to 0.3 m on the central platform. On the northern platform, the sandstone overlies 3 m of alternating siltstone and mudstone facies (Figure 4d). On the central platform it caps a 4 m-high, 2 m-wide step of listric faulted sandstone in front of the main cliff (Figure 4e). This step is fronted by an intertidal platform largely comprised of deformed delta slope deposits of siltstone and mudstone, with hummocky relief and no definable bed layers (Figure 4f). This transitions to a blocky sandstone, akin to that of the northern platform, near the southernmost end of the central platform.

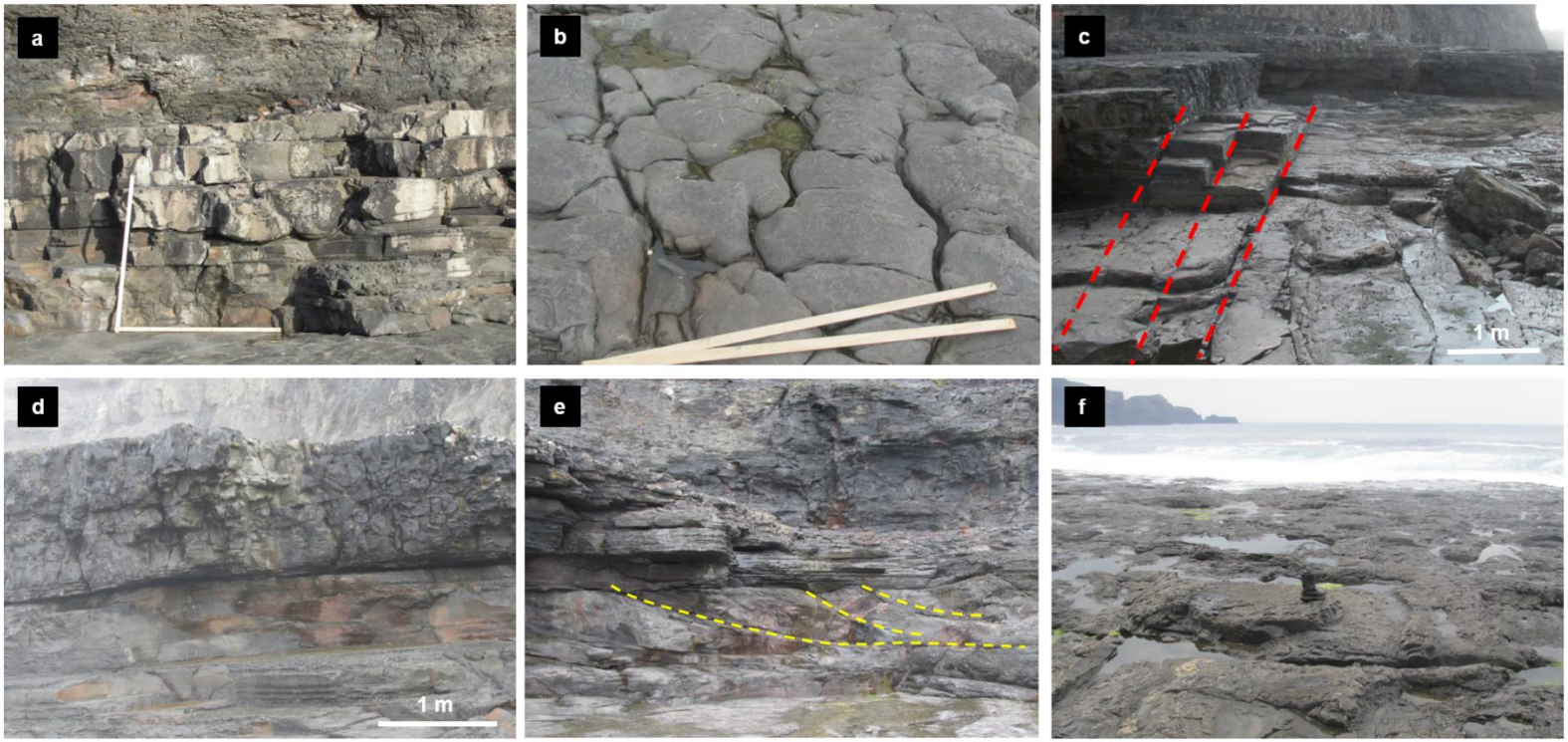

Figure 4. a) blocky internal structure of sandstone beds comprising the northern platform (stick is 1 m x 1m for scale), b) internal structure expressed at the surface as non-systematic discontinuities (stick is 1 m x 1m for scale) intersected by systematic discontinuities shown in c (red dashed lines). d) Blocky sandstone overlying interbedded silt and mudstone facies, e) blocky sandstone capping step of listric faulted sandstone (yellow dashed lines) in front of the main cliff and fronted by deformed delta slope deposits with hummocky morphology shown in f (boot in centre foreground for scale).

Repeat seasonal surveys of the study site since August 2015 have demonstrated a frequent supply (via cliff fall) of sediment to the platform and a relatively short residence time (days to months) of cliff and platform derived material on the platform. We have also observed mass movements from the cliff and the quarrying of boulders from the platform during storms.

Three significant storms occurred in Ireland in February and March 2016. These are detailed in Table 1 with the wind and wave data for the clast transport experiments. Maximum wave height recorded by the Westwave MK3 wave buoy (6 km west north west of the study) during the storms site was 23 m compared to 1.9 m for the clast transport experiments. No wind data were available from the nearest weather buoy for all three storms and clast experiments. Therefore, we used data recorded by the Shannon Airport weather station, approx. 80 km east of the study site for easier comparison.

Table 1. Wind and offshore wave data for the three storms and the clast transport experiments (CTE). *Shannon Airport. ** Westwave MK3.

Storm	**Date**	**Wind ***			**Wave ****		
		Mean speed (km/hr)	Max speed (km/hr)	Mean dir. (˚)	Sig. hgt. (m)	Max height (m)	Mean dir. (˚)
Henry	01/02/16	51	104	236	8	21	279
Imogen	08/02/16	49	106	247	11	23	276
Jake	02/03/16	41	117	289	No data	No data	No data
CTE	06/08/16	32	41	82	0.9	1.9	271
CTE	19/11/16	8.0	14	159	2.3	No data	310

4.2 Methods

4.2.1 Characterisation and volumetric analysis of post-storm CATs

Shortly following the three coastal storms in February and March 2016 (Table 1), fresh CATs were observed on the northern and central platforms. Initial mapping identified two types of CATs. Complex CATs occurred where one or more CATs form in multiple directions often crossing each other, leading to the complete surface abrasion of patches. Simple CATs occurred where individual trails were easily identifiable (see Figure 2 for example). Simple CATs form approximately 60% of all CATs identified on the platform. For practicality, only simple CATs were used to estimate the surface area and volume of material eroded by clast transport. As such, values for volume and surface area are an underestimate of the total formed during the storm activity. Simple CATs (n = 35) were mapped, measured and photographed. CAT pathways and length were mapped using a hand-held GPS (Garmin etrex. Error ± 6 m). The total error for CAT length was calculated as the square root of the sum of the squared errors for the beginning and end GPS coordinates of all CATs. A sub-sample of CATs (n = 10, 28% of total) was selected to represent the following population attributes: 1. The variability in track length and 2. The location on the variable platform morphology. This sub-sample of CATs were mapped using a high precision Trimble Global Navigation Satellite System (GNSS) R8-3 (horizontal error = ± 0.015 m, vertical error = ± 0.020 m). The GPS coordinates of all simple CATs formed during the storms were plotted using ESRI ArcMap 10.4.1. Individual, mean and total track length were calculated in ArcMap. Each of the 10 sub-sampled CATs were photographed at close range along their entire length, in nadir view using a Nikon D3000 (10.2 mega pixels) with scale and markers to allow measurement of the eroded surface area.

The styles of abrasion were categorised using the concept of tool marks where flow-parallel structures are cut into a bed (Allen, 1982). We adopted the terminology of Richardson and

Carling (2005) and identified two types of tool marks on the CATs: scratch marks and percussion marks (Figure 5). Scratch marks (simple, looped and parallel) are linear tool marks formed by clasts in contact with the platform surface during wave motion. They varied in length and were often intermittent. Percussion marks are erosional features (up to a few cm) formed by the chipping away of a rock fragment by the ballistic impact of a bedload clast.

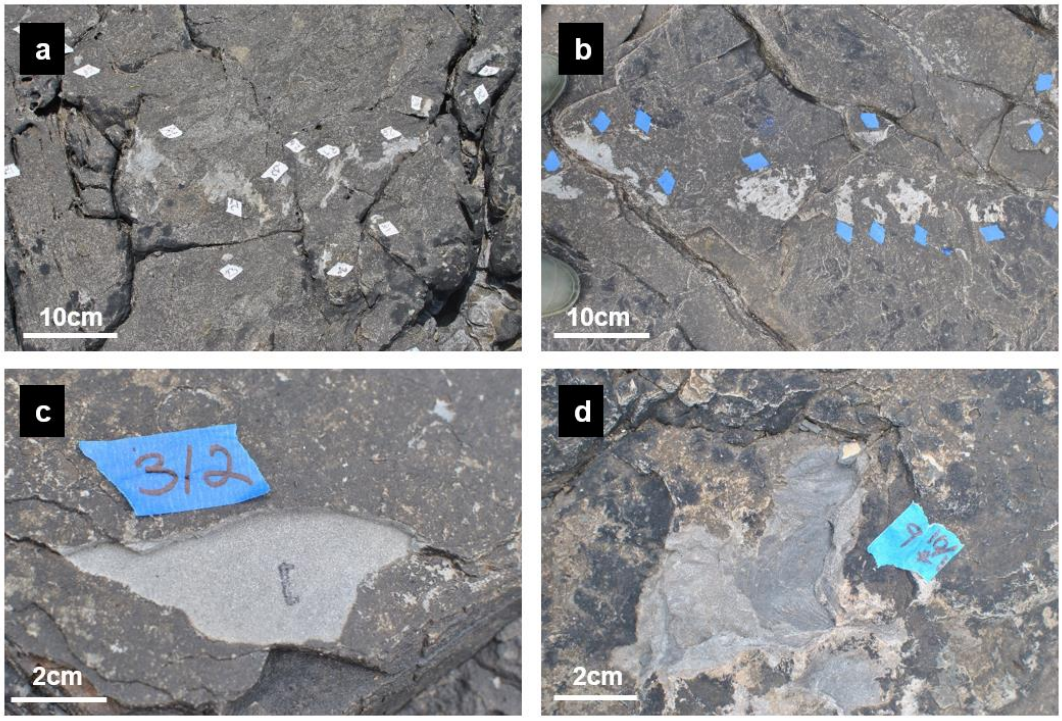

Figure 5. Examples of scratches (a and b) and percussion fracture facets (Bourke et al., 2007) on the edge (c) and face (d) found on clast abrasion trails at the study site. White and blue tape is 2 cm wide.

The eroded surface area for all scratch marks on each sub-sampled CAT was calculated from the images using the measure tool in open source software Fiji (Schindelin et al., 2012). The

total scratched surface area was averaged per metre of CAT length and this figure then applied to the full population of simple CATs to derive an estimate of platform surface area affected by scratch-type abrasion. The volume of sediment eroded was estimated by assuming the removal of 3 sandstone grains (300 µm dimeter – medium to coarse sandstone after Wentworth, 1922) from the floor of the scratch marks (i.e. scratch depth of 900 µm). This assumption is based on observations of the scratch marks.

We determined the volume of platform sediment eroded from percussion marks by undertaking high resolution volume estimates along individual CATs. Thirty-five percussion marks, representing 16% of the total number of percussions in the sub-sample were selected to incorporate the range of size and style of feature (e.g. percussion fracture facets on the face and edge). Individual percussion marks were imaged at close range (<1m) employing basic principles of Structure-from-Motion (SfM) Photogrammetry (Micheletti et al., 2015b) and a local coordinate system in order to build high resolution digital elevation models (DEMs). Quality of images was assessed using the 'estimate image quality' tool in AgiSoft PhotoScan (2013. Version 1.2.4). Removal of low-quality images, i.e. images with a Q value < 0.5 resulted in 29 of the 35 imaged percussions being included for DEM analysis. Images were processed using Agisoft and the local co-ordinate system was used to generate DEMs and orthophotographs of each percussion mark. Triangular Irregular Network (TIN) surfaces were generated within ArcMap using DEMs as the input. The volume for percussion marks was calculated using the polygon volume tool and the relevant orthophotograph as a reference for percussion outline. Negligible change in slope below the reference plane was assumed in this calculation. Percussion volume error (± 7%) was calculated as the mean percentage error of sampled percussion volumes based on the mean of the difference between measured and estimated XY + Z error values for each SfM derived percussion DEM.

We used the average volume of sampled percussions and the average number of percussions per metre of CAT and applied these values to the total simple CAT length for the platform population to provide an estimate the volume of sediment eroded from percussion marks.

4.2.2 Clast Transport Experiments

To determine the threshold wave energy for entrainment and transport of clasts of known size and shape and evaluate the potential for abrasion by clast transport under summer and winter non-storm wave energy conditions, we undertook clast transport experiments during spring tide in August (summer) and November (winter) 2016. Pressure transducers (PTs) were installed during each deployment to measure wave energy. Due to lack of clasts on the platform, a range of coarse clast sizes were collected from a boulder beach at Quilty, 16 km north of the study site. Clasts were classified based on size, using an adapted version of the Wentworth scale after Blair and McPherson (1999), and shape (after Zingg, 1935). Each clast was paired with a similar size and shape clast (blade, disc, sphere after Zingg, 1935) to limit the influence of different clast shapes on transport dynamics. Clasts were deployed in two alongshore arrays on two previously surveyed platform transects (T1 and T2) in August and November 2016. See figures 5 - 7, 13 and 14 for transect and clast deployment locations. The experiments ran for 2 tidal cycles (24 hrs). Clast start and finish positions were recorded using a Trimble GNSS. Evidence of abrasion caused by clast transport during the monitoring period was imaged by a hand-held camera (iPhone 5S).

Figure 6. Experimental set up for clast transport experiment (November). Location of pressure transducer indicated by black arrow.

For the August experiment, four clast pairs were deployed. One clast from each pair was placed in an alongshore array on each transect (T1 and T2) at 0 m OD, approximately 120 m

from the cliff toe. Tidal range during the experiment was 4.4 m (-2.2 to 2.2 m OD) (Marine Institute, 2016).

For the November experiment, seven clast pairs were deployed. These included larger clasts up to 17.5 kg because of expected higher wave energy conditions. These were also the largest size that could be manually carried to the platform. Wave conditions inhibited deployment at 0m OD. One clast from each pair were deployed 1.5 m and 1.4 m OD on T1 and T2 respectively, approximately 100 m from the cliff toe (Figure 6). Tidal range during the experiment was 3.6 m (-1.7 to 1.9 m OD) (Marine Institute, 2016).

4.2.3 Wave energy

Wave energy was measured during the experiments using two PTs (RBR Solo Wave). PTs were deployed with the sensor flush to the surface of the platform on both transects at 0 m OD during August and at 1.5 m and 1.4 m OD on T1 and T2 respectively during November (Figure 6). PTs were set to sample at 4 Hz at 4096 (17.2 mins) with a sample interval of 30 mins.

4.2.4 Platform roughness and surface morphology classification.

In order to assess the role of geomorphological setting on clast transport and abrasion feature type, topographic data, field observations and aerial images were used to quantify platform roughness and develop a general platform morphological classification. A Trimble GNSS rover was used to acquire five shore-normal topographic surveys. Topographic profiles were sampled at 0.1 – 0.5 m intervals from approximately 5 m from the cliff to the furthest accessible seaward point. We used the fractal dimension of the representative morphological type profiles

as a quantitative measure of relative roughness (Table 2 and Figure 8). Although TLS data of the platform surface was available, this approach was used for easier comparison in future studies of roughness data between sites for which TLS data may not be available. The roughness of each profile was determined by calculating the fractal dimension (*D*) using the method outlined in Dasgupta (2013). This approach applies the roughness-length method described by Malinverno (1990) to topographic profile data to calculate the Hurst Coefficient (H) and the Fractal Dimension (*D*).

$$\mathrm{D} = 2 - \mathrm{H} \tag{1}$$

Roughness (RMS) values were determined for different window lengths based on the following equation.

$$RMS\,(w) = \frac{1}{n_w} \sum_{i=1}^{n_w} \sqrt{\frac{1}{m_i - 2} \sum_{j \in w_i} \left(z_j - \bar{z}\right)^2} \tag{2}$$

where n_w = total number of windows of length w; m_i = number of points in the i^{th} window, w_i and z_j = residuals from the trend and $\bar{z}$ is the mean residual for that window (Dasgupta, 2013).

$$RMS\,(w) = \frac{1}{n_w} \sum_{i=1}^{n_w} \delta_i \tag{3}$$

where δ_i = the standard deviation of the i^{th} window =

$$\sqrt{\frac{1}{m_i - 2}} \sum_{j \in w_i} \left(z_j - \bar{z}\right)^2 \quad (4)$$

The longest, shortest and effective (final) window lengths were calculated based on Malinverno's recommendation that the longest window length should *"vary between 20% of the total length of the series and the shortest span containing at least ten points"* (Malinverno, 1990: 1954). The calculated mean effective window length and their corresponding RMS values were plotted on a log-log scale. The *D* value for the profile was calculated using equation (1) where the slope of the least square linear regression line = H.

Using field observations, photographs, aerial images and roughness data (Table 2 and Figures 7 and 8), four broad types of platform morphology were identified. These are; type A - high macro-roughness, type B – medium macro-roughness, type C - low macro-roughness and type D - very low macro-roughness. The boundaries between morphological types are transitional and we also note that there is some variability within each morphological type.

Table 2. Description of the morphological types identified at the study site.

Morphogenic type	Macro scale roughness (relative)	Characteristics
Type A	High	High macro roughness resulting from stepped platform topography. Steps range in height from centimetres to >1m depending on bed thickness to. Zone of active boulder quarrying demonstrated by numerous fresh sockets.
Type B	Medium	Strong influence of rock structures. Common mud mounds and distorted bedding form hummocky terrain with differences in topographic highs and lows of up to 1m.
Type C	Low	Highly weathered, platform surface where uneven removal of thin (<25cm) bed layers increases overall roughness. Generally restricted to higher elevations alongshore such as in front of the cliff toe.
Type D	Very low	Relatively planar surface with low microtopographic variability (<10cm).

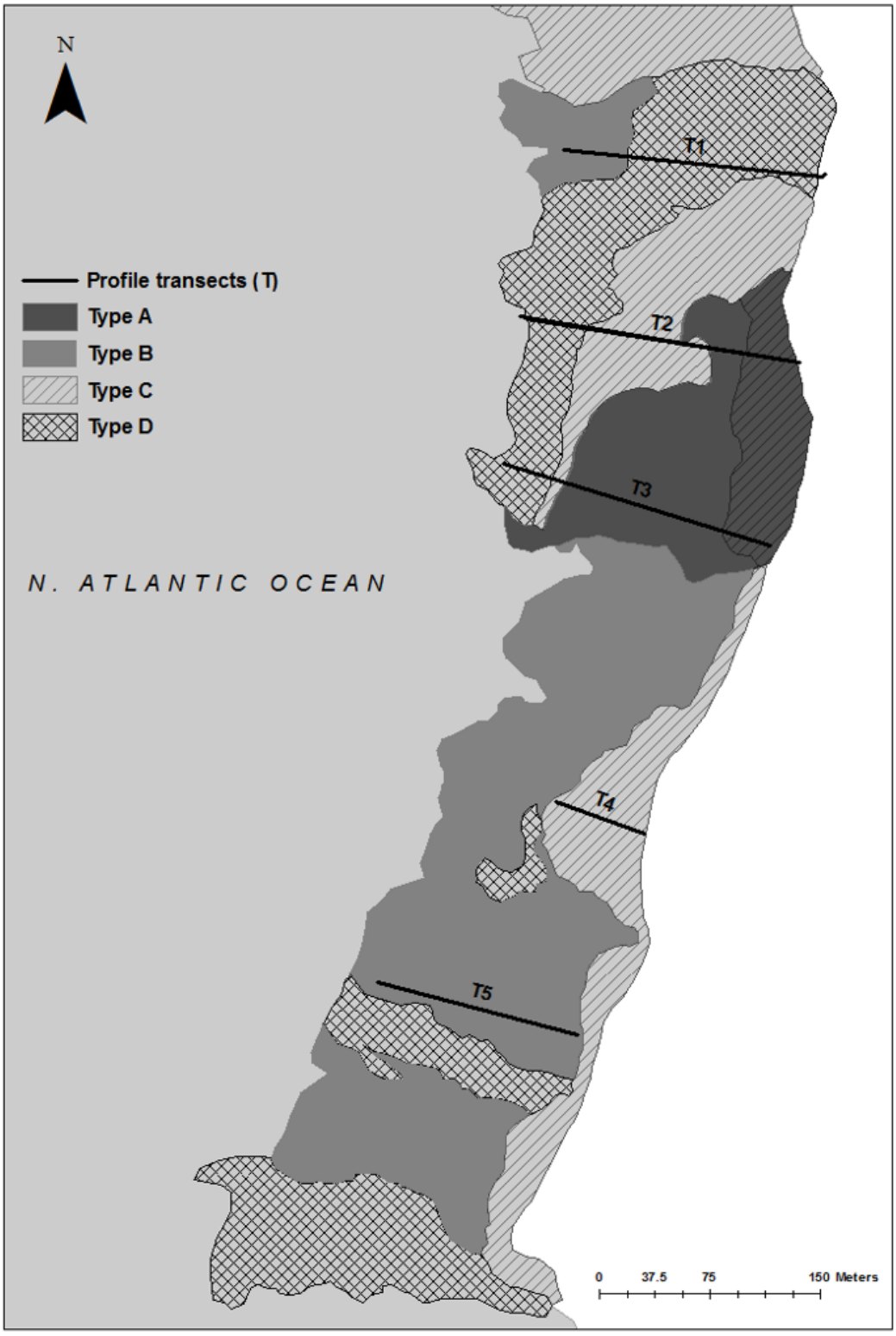

Figure 7. The distribution of morphological types A-D at the study site and the location of the topographic survey transects 1-5.

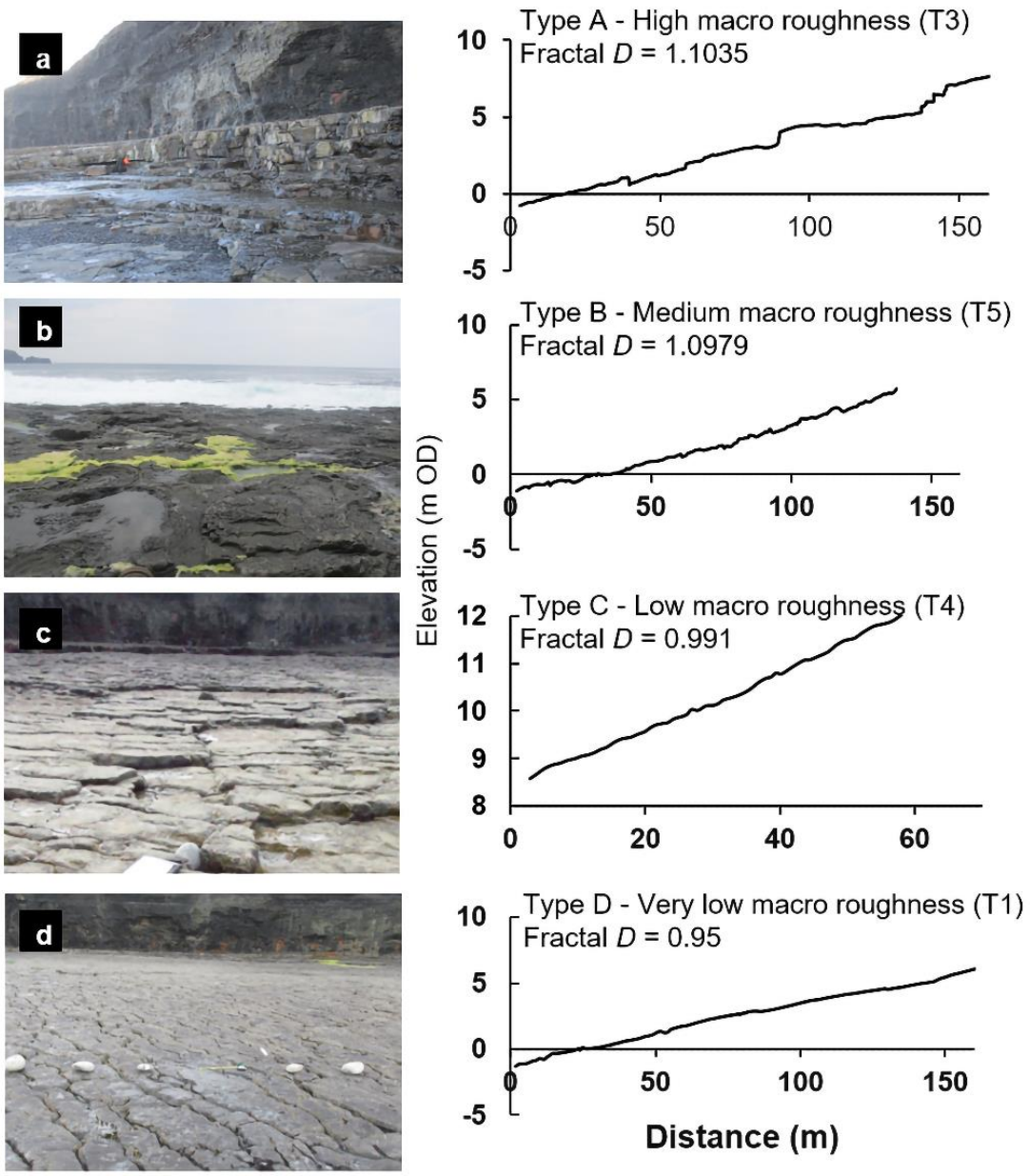

Figure 8. The different morphological types described in Table 2, their topographic profiles and calculated Fractal *D* values.

4.3 Results

4.3.1 CAT morphometry

Thirty-five simple CATs distributed across an area of 0.4 km^2 were mapped (Figure 8a). While the exact origin of the clasts which formed the CATs is sometimes unclear, previous observations and the origin of mapped CATs indicates that there are two sources of clasts. Many CATs begin at, or close to, freshly quarried sockets on the platform at elevations between 3 m and 7 m OD. This points to plucking of platform material during high energy wave conditions as one source of clasts on the platform. Many CATs also appear to have their origin near the cliff toe (<10 m), suggesting that mass movements from the cliff are also a source of clasts on the platform. This is supported by evidence of fresh rockfall scars on the cliff face and the absence of cliff toe deposits observed during previous surveys.

The total length of CATs was 1.51 km (± 0.05 km). Maximum and minimum CAT length were 92 m and 11 m respectively with a mean length of 42 m. CATs demonstrated numerous changes in direction (Figure 9a and b) with a net transport direction off shore (270º). CATs were distributed across the width of the platform from the cliff toe at 8 m OD to 120 m from the cliff toe at 0 m OD. Maximum and minimum lengths of the sub-sampled CATs were 92 m and 16 m, respectively. Mean sub-sampled CAT length was 38 m, slightly lower than that of the total population (42 m).

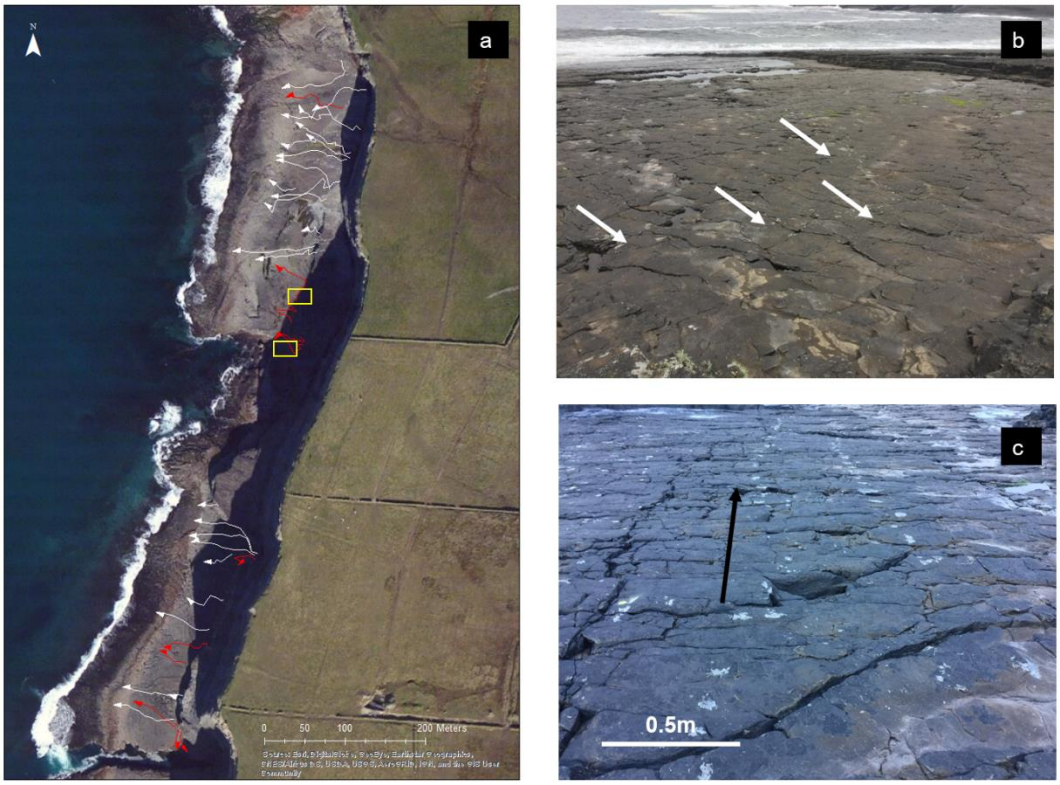

Figure 9. a) Map of the 35 CATs surveyed (arrows indicate the direction of transport). The red arrows are the 10 CATs selected for detailed measurements. Yellow boxes show the location of panels b and c. b) Zoomed in perspective of CAT in (top yellow box in a). c) Example of a parallel CAT (lower yellow box in a).

Although excluded from the CAT survey due to the difficulty of identifying individual abrasion trails, complex CATs form a significant proportion (~40%) of CATs at the study site and also have abrasion forms similar to those identified for simple CATs. Figure 10 shows examples of abrasion in these 'patches'. These abrasion 'hotspots' are highly localised on the platform and would have higher sediment abrasion volumes than simple CATs. In general, complex CATs become less obvious in the intertidal zone where bioprotection (by *Chthalamus monatgui*, *Chthalamus stellatus*, micro and macro algae) was effective (Figure 9c).

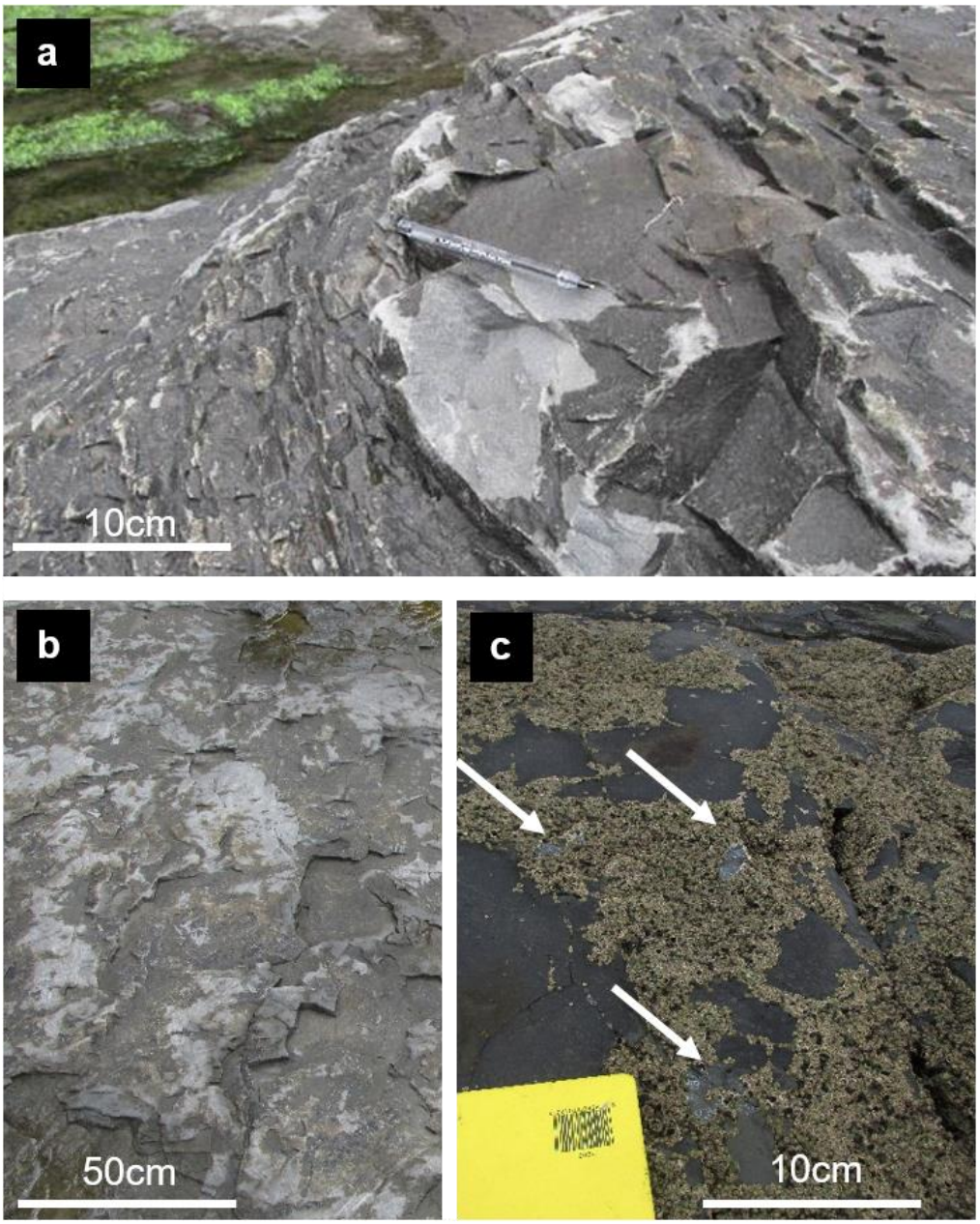

Figure 10. Complex CATs. a) Example of percussion abrasion and b) abraded platform 'patches' which were not included in the analysis. c) Example of bioprotection in the intertidal zone where *Chthalamus monatgui* and *Chthalamus stellatus* prevented contact between the moving clast and the platform surface. White arrows indicate where *Chthalamus monatgui* and *Chthalamus stellatus* have been removed by contact with the moving clast.

4.3.2 Surface area and volume analysis of sub-sampled CATs

We estimated the surface area and volume of platform material eroded via clast abrasion for a) scratches and b) percussion marks (Table 3). A total of 2520 scratches were measured. The surface area of scratch marks in the sampled CATs was 2.4 m^2. The mean surface area of scratch marks per metre of track was 0.006 m^2/m. When applied to the total length of the CAT population (1,510 m) the total surface area of the platform affected by scratch mark abrasion was 9.5 m^2. The calculated volume for scratch type abrasion for the sub-sampled CATs was 2160 cm^3. When we averaged this figure per metre of simple CAT and applied to the population, the volume of platform sediment abraded via scratch marks was 8,605 cm^3, equivalent to 900 $cm^3\ m^{-2}$ or 21.6 kg of sediment. The lowest frequency of scratches occurred on morphological types A and D. The highest frequency of scratches occurred on morphological type B and a combination of type B and D (Figure 11).

Table 3. Results of surface area and volume analysis of sub-sampled CATs * indicates where a CAT crosses more than one morphological zone, the dominant zone, i.e. zone in which the majority of CAT was located, is stated first.

CAT	Type	Length	Scratches				Percussions			
			Total	Sd.	SA	Vol.	Total	Sampled	SA	Vol.
		(m)	(n)	(n)	(m^2)	(cm^3)	(n)	(n)	(m^2)	(cm^3)
1	A	92	152	152	0.81	729	40	6	0.26	480
2	A	31	126	126	0.34	306	42	2	0.17	30
3	A	39	114	114	0.16	144	8	2	0.08	300
4	D	16	133	133	0.18	162	9	4	0.03	50
5	D	18	205	205	0.19	171	0	0	0	0
6	BD	40	653	653	0.23	207	17	5	0.07	960
7	B	38	294	294	0.11	99	39	5	0.24	180
8	BD	23	376	376	0.15	135	30	1	0.01	10
9	B	30	239	239	0.11	99	19	1	0.05	20
10	D	51	228	228	0.11	99	10	3	0.01	20
Total (10)	N/A	379	2,520	2,520	2.4	2,160	214	29	1.02	14,860
Population total (35)	N/A	1,510	10,040	N/A	9.5	8,605	853	N/A	4.1	59,203

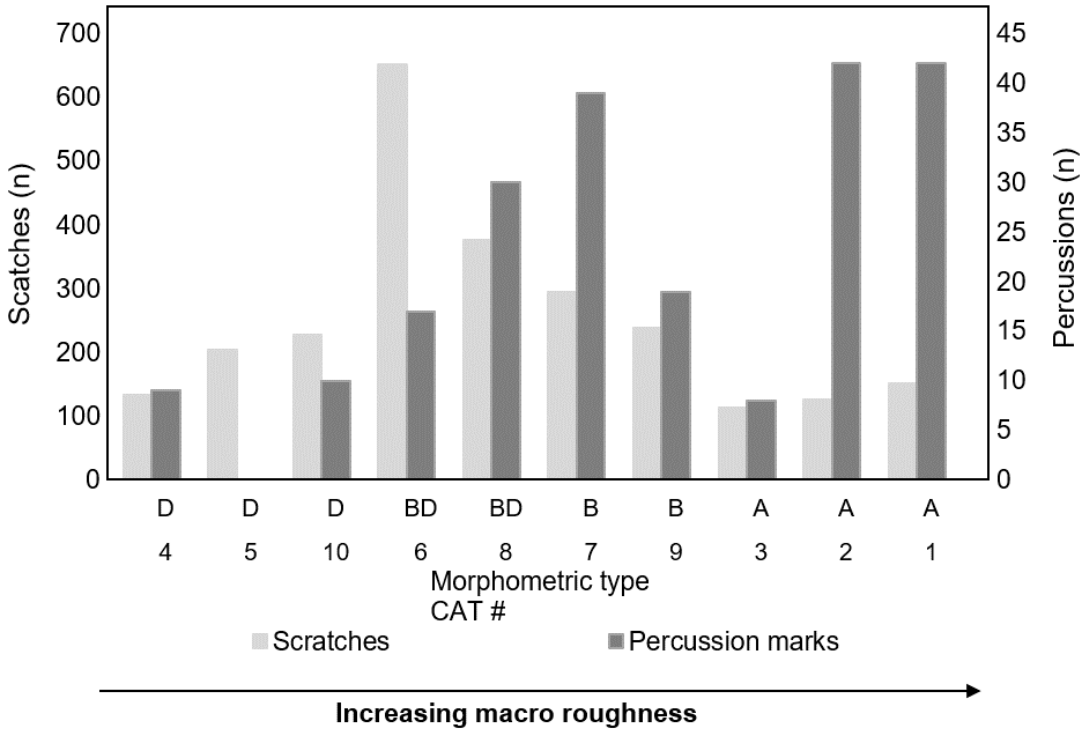

Figure 11. The frequency of scratches and percussions on different morphological types (A-D) in the sub sampled CATs (1-10). * indicates CATs whose pathways cross more than one morphological type. Dominant type shown first.

The surface area of percussion marks in the sampled CATs was 1 m^2. The mean surface area of sampled percussions (n=29) was 0.003 m^2 m^{-1}. When applied to the total length of the CAT population (1,510 m) the total surface area of the platform affected by percussion mark abrasion was 4.1 m^2. The calculated volume for percussion type abrasion for the sub-sampled CATs was 14,860 cm^3. When averaged per metre of CAT and applied to the population the total volume of percussion abrasion was 59,203 cm^3, equivalent to 14,567 cm^3 m^{-2} or 148.6 kg of sediment. The maximum number of impact percussions on a single sampled CAT was 42 (CAT # 2). The mean number of impact percussions for the sampled CATs (n = 10) was 21. Of the sub-sampled CATs only 1 (# 5) had no impact percussions. Except for CAT # 3,

the highest number of percussion marks consistently occurred on CATs found on morphological types A and B (Figure 11). There is no significant relationship between CAT length and number of impacts (Spearman's rho = 0.309, $P > 0.05$).

The total estimated surface area abraded during the storms (percussion + scratch) was 13.6 m^2, representing <1% of the total surface area (approx. 40,000 m^2) of the northern and central platforms where the CATs were analysed. The total estimated volume of sediment removed from the rock platform surface via abrasion (scratch and percussion) during the storms was 67,808 cm^3, equivalent to 12,943 $cm^3\ m^{-2}$ or 170 kg of sediment. The results of the impact percussion analysis indicate that the volume of platform sediment removed via percussion is almost seven times that of scratch type abrasion.

4.3.3 Clast Transport Experiments

4.3.3.1 Wind and wave data

Offshore wave data recorded by the Westwave MK3 wave buoy and wind data recorded at Shannon airport for the clast experiments are shown in Table 1.

During the August deployment maximum and mean on shore wave heights recorded by the pressure transducer (RBR Solo Wave) at 0m OD on T1 were 1.36 m and 0.53 m. Maximum and mean wave energies were 431 and 124 j m^{-2} respectively. At 0 m (OD) on T2, max wave height recorded was 1.26 m and mean wave height was 0.45 m. Maximum wave energy values occurred during peak tide were 381 with a mean value of 106 j m^{-2} (Figure 12).

During the November deployment period, maximum and mean wave heights recorded by the pressure transducer at 1.4 m OD on T2 were 1.7 m and 1.1 m. Maximum and mean wave energies recorded were 143 and 31 j m^{-2} (Figure 12). The PT located on T1 at 1.5 m OD failed to record any data during the monitoring period. Lower wave energy and shorter inundation period recorded during the November experiment can be partially explained by increased elevation in the tidal frame and increased distance from the platform edge relative to the August deployment. Maximum wave energy for both deployments occurred during peak tide.

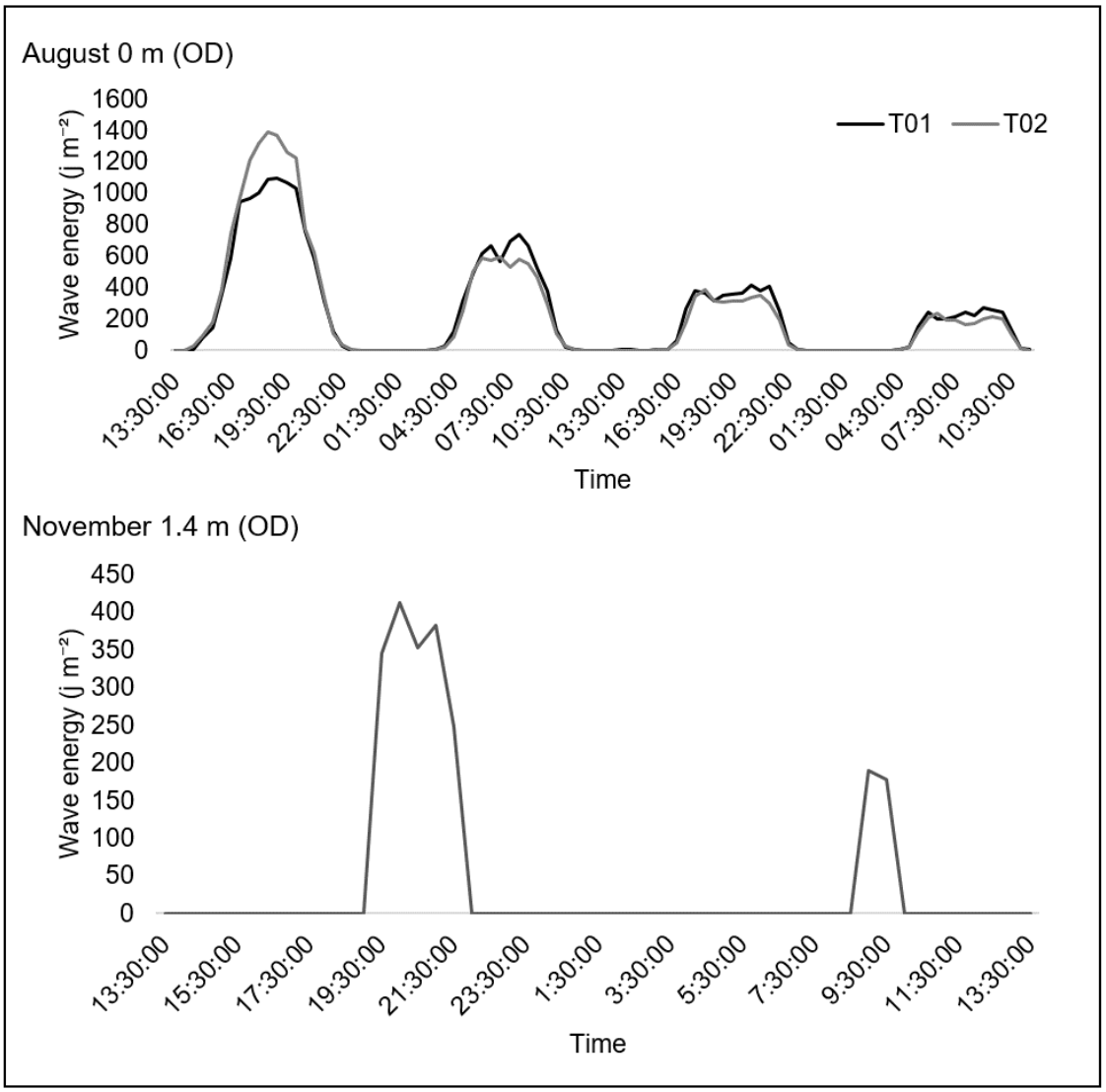

Figure 12. Wave energy (j m^{-2}) measured by the pressure transducers deployed during the August and November clast deployments at 0 m OD on T1 and T2 (August) and 1.4 m OD on T2 (November).

4.3.3.2 Clast transport under non-storm conditions

All clasts were transported during the August (relatively low energy) experiment. Only four of the eight clasts remained on the platform (Figure 13). The remaining four were not recovered and are presumed to have been transported offshore. The recovered clasts were the heaviest clasts deployed (Table 4). Net transport direction for recovered clasts was 72 degrees. Maximum Net Transport Distance (NTD) for an individual clast was 73.8 m (T2iv) and minimum NTD was 44.1 m (T1iii). Mean NTD for recovered clasts was 59.8 m. The maximum increase in boulder elevation during the monitoring period was 2.53 m (T1iii). Both T1iii and T2iv were found in small (0.1 m^2) areas with microtopographic variability associated with Type B morphology which acted as a trap (Figure 13d and e).

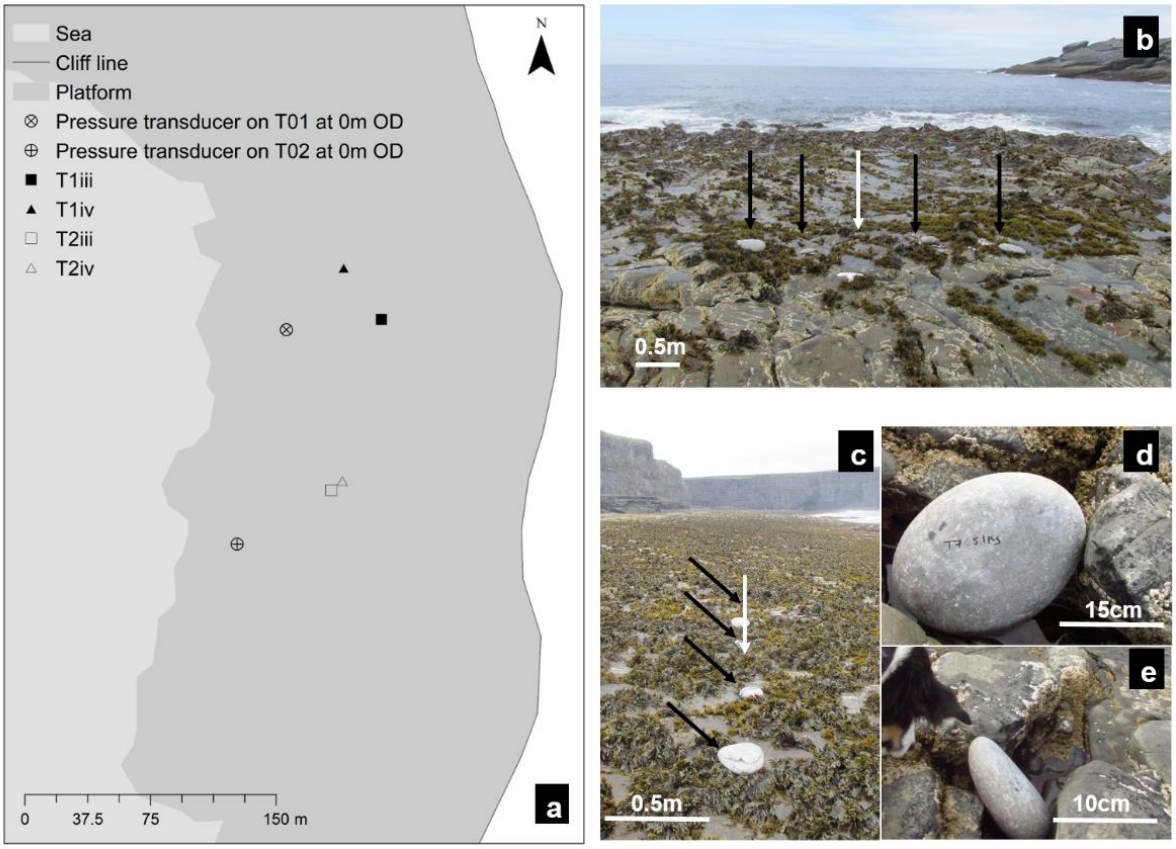

Figure 13. a) The location of the pressure transducers (circles) where clasts were deployed at 0 m OD and the finishing positions (outline and solid symbols) of the clasts deployed during the August pilot experiment. The experimental setup on T1 (b) and T2 (c) showing the pre-transport setting of deployed clasts (black arrows) and the location of the pressure transducers (white arrows). Note the hummocky morphology (Type B) seaward of the boulder line in b. Figures d and e show the respective finishing positions of T1iii and T2iv in small boulder traps.

All 14 clasts were transported during the November deployment (Figure 14). Nine clasts were recovered. Three were found in a cluster together at the base of a 0.5 m step in the platform (Figure 14a). Similar to the August deployment, recovered clasts comprised the heaviest of those deployed (7.8 - 17.5 kg) (Table 4). Net transport direction for recovered clasts was 51

degrees. Maximum NTD for individual clasts was significantly larger at 232.7 m which also overtopped a 0.5 m high step in the platform. Minimum NTD was 28.7 m. Maximum increase in elevation for deployed clasts during the monitoring period was 2.07 m.

No statistically significant relationship was found between clast weight and NTD (Spearman's rho = -0.250, $P > 0.05$) or clast weight and net transport direction Spearman's rho = -0.576, $P > 0.05$) for either deployment.

Table 4. The characteristics of clasts deployed in August and November. FC = fine cobble, CC = coarse cobble and FB = fine boulder.

Clast ID	Weight	Axis length			Net Transport		Shape	Size
		A	B	C	Direction	Distance		
	(Kg)	(cm)	(cm)	(cm)	(degrees)	(m)		
August								
T1i*	0.5	10	7	3	No data	No data	Disc	FC
T1ii*	2	12	11	4	No data	No data	Disc	FC
T1iii	5.2	18	16	5	87	44.1	Disc	CC
T1iv	7.8	24	20	12	83	57.4	Disc	CC
T2i*	0.5	9	8	4	No data	No data	Disc	FC
T2ii*	2	13	12	5	No data	No data	Disc	FC
T2iii	5.2	12	11	7	61	64.2	Disc	FC
T2iv	7.8	27	21	9	58	73.8	Disc	FB
November								
T1v *	0.5	11	8	3	No data	No data	Disc	FC
T1vi*	2.5	20	13	7	No data	No data	Blade	CC
T1vii*	5.2	22	21	7	No data	No data	Disc	CC
T1viii	7.8	27	25	8	48	71.1	Disc	CC
T1ix	11.5	29	24	9	39	78.5	Disc	CC
T1x	15.2	32	25	14	44	77	Disc	CC
T1xi	17.5	46	28	13	52	51	Blade	FB
T2v*	0.5	15	11	16	No data	No data	Sphere	FC
T2vi*	2.5	19	14	18	No data	No data	Sphere	CC
T2vii	5.2	23	21	16	17	232.7	Sphere	CC
T2viii	7.8	28	24	8	64	57.5	Disc	CC
T2ix	11.5	27	22	10	30	209.9	Disc	CC
T2x	15.2	32	31	8	72	46.6	Disc	FB
T2xi	17.5	37	26	12	93	28.7	Disc	FB

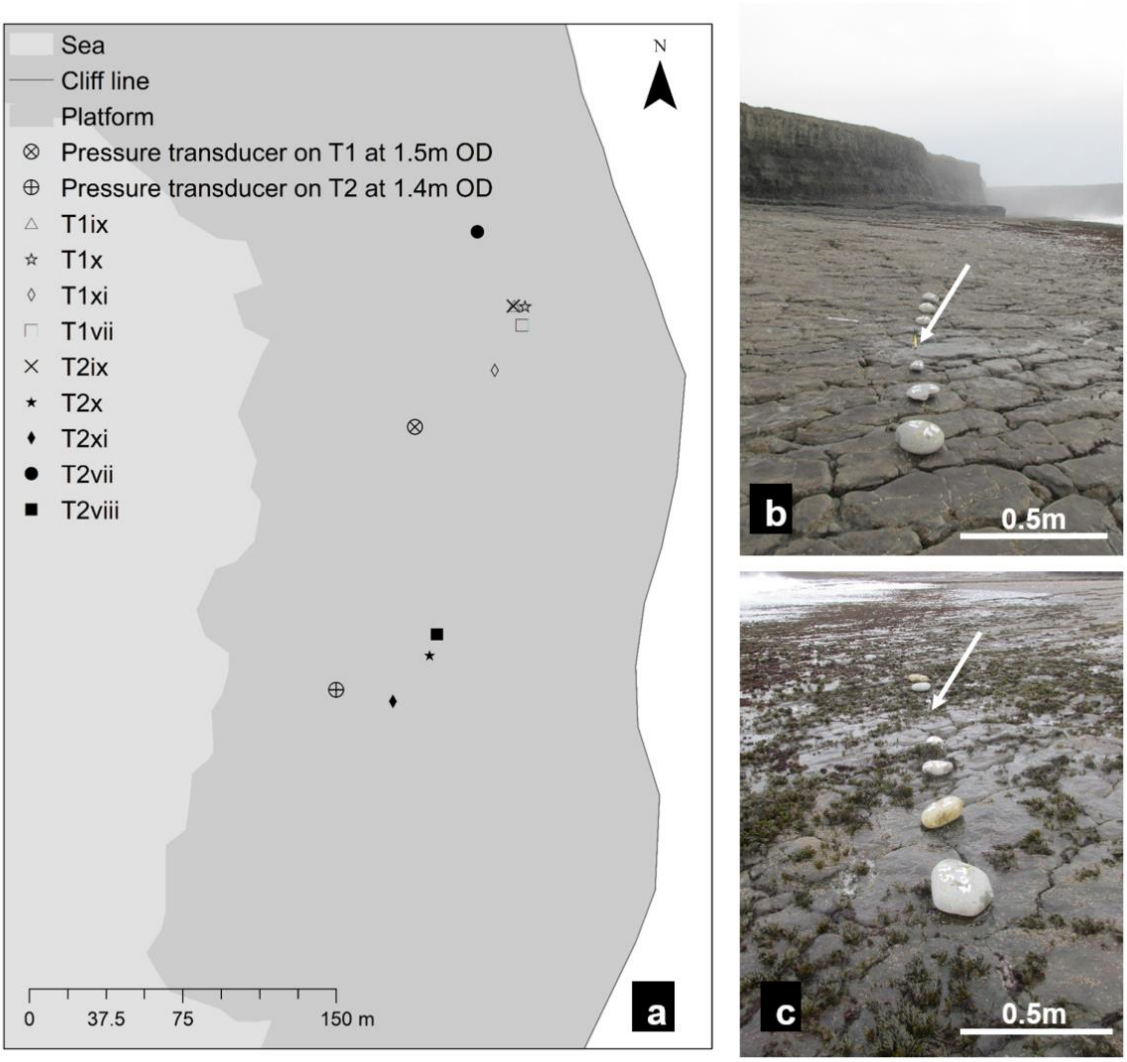

Figure 14. a) The location of the pressure transducers (circles) where clasts were deployed and finishing positions (hollow and solid symbols) of the clasts deployed during the November experiment. b and c) The starting setup for the November experiment on T1 (b) and T2 (c) showing the pre-transport setting of deployed clasts and the location of the pressure transducers (white arrows).

Evidence of geomorphic work carried out by clast transport was found following both clast deployments (August and November) where we observed both percussion and scratch marks (Figure 15a-e). Many of the fresh abrasion features were superimposed on, or adjacent to, older abrasion features (Figure 15a, c and d).

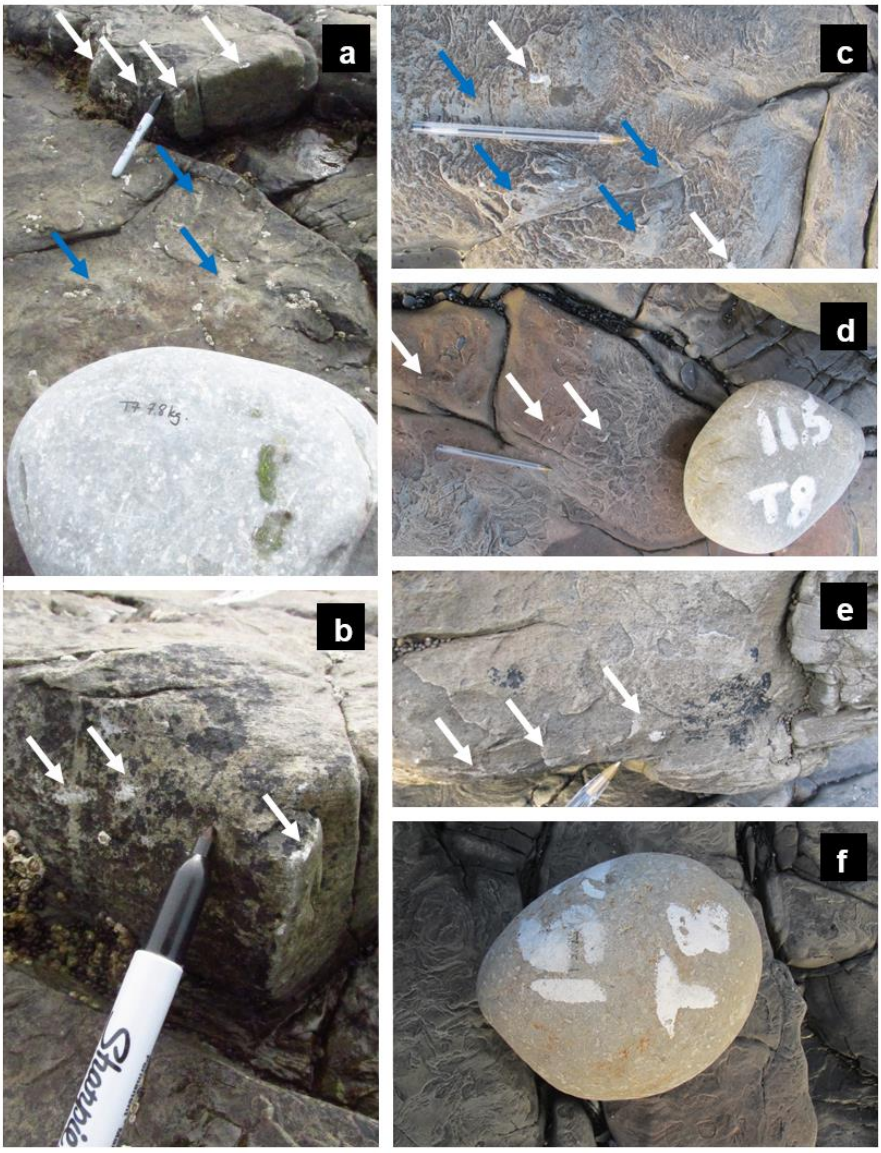

Figure 15. a) Example of fresh abrasion features (white arrows) from boulder (T2iv) and older abrasion marks (blue arrows). b) Zoomed in perspective of abrasion features (edge and face percussion) shown in a. c) Fresh abrasion features formed by boulder (T1xi) (shown in d) superimposed on and adjacent to older abrasion marks. e) Edge abrasion features made by boulder (T1x) (shown in f).

4.4 Discussion

Abrasion of shore platforms by clasts has been considered largely restricted to a narrow zone with supply of abrasive material limited to depositional strips of sand or pebbles at the cliff toe and or trapped in topographic depressions (Blanco Chao et al., 2007). This study demonstrates that abrasion by clast transport, can be an effective geomorphic erosional agent that extends from the cliff toe to the intertidal zone which, at the study site, is up to 120 m wide. Simple CATs were found on all platform morphological types (A-D). With few exceptions, CATs become less obvious in the intertidal zone. The lack of conspicuous abrasion trails in the intertidal zone is likely to be a combination of bioprotection and clast strength. We have directly observed the role of biological cover in mediating the ability of clasts to both scratch and percuss the platform (Figure 10c). We find that clasts at the study site sourced from the cliff are more friable than clast derived from the platform and tend to break up into smaller fragments, either *in situ* in rockfall deposits, or as they are transported across the platform.

A conservative estimate of 13.6 m^2 of platform surface was eroded by clast abrasion during three storms in a winter season. This value is conservative as it excludes abrasion estimates for complex CATs formed during the three storms. The common practice of reporting erosion rates on shore platforms in mm $yr.^{-1}$ of downwearing implies a uniform rate of vertical erosion across the platform. In a rare example, Stephenson et al. (2010) also report the volume of material eroded using micro erosion meter data by also calculating the surface area of the different platform types studied in order to estimate a sediment budget for the Kaikoura Peninsula, Australia. However, our study has demonstrated that abrasion by clast transport is not uniform across the platform and thus supports the recommendations by Naylor et al. (2012) for reporting volume of material eroded via specific processes. In doing so, the

volumes reported here are more easily compared to other processes of shore platform erosion which are similar in scale and spatial variability. A direct comparison to other processes of erosion on shore platforms, e.g. bioerosion, is still problematic as studies rarely report the percentage area of platform surface occupied by bio erosive species (Naylor et al., 2012). Without these data it is difficult to make useful comparisons between our study and studies of other erosive processes. As such, we can only compare our data to other data as it is reported in the literature, whilst also providing additional key information in the hope that this will help more robust comparisons in the future. In research which highlighted the benefits of reporting erosion as a volume, Naylor et al. (2012) reported 6795 cm^3 of fine sediment produced by piddocks in 26 rock pools on a limestone shore platform in Glamorgan, Wales. Pinn et al. (2005) estimated a volume of 2909 cm^3 m^{-2} $yr.^{-1}$ of erosion by piddocks on a shore platform at Lyme Regis in south of England. However, the authors do not state what percentage of the total platform area was occupied by piddocks. Andrews and Williams (2000) calculated theoretical erosion of 328 cm^3 m^{-2} $yr.^{-1}$ by limpets on a chalk shore platform on the Sussex coast based on the measured rate of grazing and population densities of 100 limpets per m^2. Again, the percentage area of the total platform affected by limpet grazing was not explicitly stated. Despite this limitation, the values for bioerosion stated above serve to demonstrate the relative importance of abrasion by clast transport as an erosive agent with respect to volumes of sediment removed from the platform surface.

Although the surface area of measured CATs represents less than 1% of the total platform area, abrasion features described in this study frequently occur adjacent to or superimposed on older abrasion features (Figure 15). A previous study of boulder dynamics on a shore platform in Donegal (Knight and Burningham, 2011) documented weathering of freshly quarried boulder sockets. The authors noted that rapid weathering in the coastal zone rendered these sockets almost indistinguishable from the surrounding platform in a relatively short period of time (c. 5 yrs.). This suggests that visible abrasion features at the study site

are likely to have been formed within the last 5 - 10 years. These data support the findings of the experimental trials where clasts were observed to move over and abrade the platform during non-storm conditions. While we have measured the erosion of the platform surface by clast transport during storms, the clast transport experiments demonstrate that this erosion process also occurs during all diurnal tidal cycles (subject to sediment availability).

The volume of platform erosion reported here (for storm conditions), suggests that CATs can be significant components of platform erosion over longer time scales. Assuming similar clast availability and clast transport dynamics over longer timescales, a minimum volume of 67,808 cm^3 per year over an area of 0.4 km^2 is equivalent to 70 m^3 or 170 tonnes of sediment in 10^3 years. This is likely to be an underestimate of the actual volumes given that our data only include simple CATs formed during three storms and does not account for abrasion by clast transport under non-storm conditions, as shown by the clast transport experiments. We acknowledge that, globally, the efficacy of this process is likely to vary between locations and is contingent on supply of clasts to the platform. Furthermore, we were unable to monitor clast transport under extreme storm conditions and as such were unable to determine the size of clasts transported during the storms representing a limitation of this study with respect to clast transport dynamics under more extreme storm conditions. Based on results discussed here, specifically geomorphic work done by the transport of clasts during the storms and geomorphic work done during non-storm conditions, it is difficult to determine the relative efficacy of erosion via clast transport under varying wave energy conditions with respect to the relative efficacy of high frequency, low magnitude wave energy events versus low frequency, high magnitude wave energy events.

The absence of any significant relationship between scratched surface area or percussion frequency and CAT length suggests that there are other factors which control the type and frequency of abrasion features. Among these will be the influence of clast size and shape (Imamura et al., 2008, Nandasena et al., 2011). However, we were unable to determine these

parameters for clasts in the storm study and found no significant relationship between size, shape and net transport distance during the clast transport experiments.

It is possible to infer mode of transport based on our observations of the type of abrasion features observed. Scratch marks are formed through prolonged periods of contact between the moving clast and the platform i.e. via dragging or rolling of clasts across the platform surface. Percussion marks are formed through brief contact, single or repeated, between the clast and the in situ bedrock via saltation, tumbling or skimming (Allen, 1982). This understanding, in combination with quantitative measurements of platform roughness and the spatial distribution of scratch and percussion marks, provide insight on relationships between platform morphology, i.e. roughness, transport mode and abrasion feature types. Our data suggest that surface roughness not only influences the entrainment of clasts as noted by Weiss and Diplas (2015), but also strongly influences the transport mode and as such, the distribution and frequency of abrasion feature types. We propose that platforms with higher macro-roughness are more susceptible to abrasion via percussion as higher roughness would likely favour more frequent saltation and tumbling of clasts as they traverse across an uneven topography. As such, the presence of edges owing to higher roughness also enhances the potential for percussion type abrasion. Favouring saltation and tumbling as transport modes in areas with high macro-roughness would also partially explain the lower frequency of scratch type abrasion observed for CATs found on type A morphology. CATs found in areas with type D morphology and low microtopographic variability had lower frequency of both scratches and percussions. The lower frequency of percussions on CATs found in areas of the platform with lower roughness can be explained using the same logic as that discussed above i.e. the effect of roughness on transport mode. The importance of geomorphological controls on clast transport reported by previous research (Naylor et al., 2016a) are also readily supported by the clast transport experiments where heavier clasts were transported further than lighter

clasts of similar size, shape and pre-transport setting which had been trapped in topographic depressions on the platform.

Research on boulder dynamics has been largely confined to studies relating to entrainment and transport of boulders by storm and tsunami waves (e.g. Mastronuzzi and Sansò, 2004, Scheffers et al., 2009, Etienne and Paris, 2010, Switzer and Burston, 2010, Cox et al., 2012, Nandasena et al., 2013). However, the results of the clast transport experiments show that cobble and fine boulder sized clasts can be entrained and transported significant distances under non-storm conditions with observable, geomorphic effects in a short period of time (two tidal cycles). Although we were unable to determine threshold wave energy, given the large net transport distances measured for clasts during both deployments and the expected dissipation of wave energy across the platform, wave energy needed to entrain and transport the clasts to final positions is likely to be significantly less than the maximum values recorded during the deployment periods. The shortest net transport distance recorded for one of the heaviest clasts on T2 in November suggests that the maximum wave energy value recorded by the PT at 1.4 m OD in November is close to the lower limit of wave energy required to entrain and transport this size and shape of clast in this setting. There is potential to compare wave energy, measured here using PTs, to offshore wave buoy data to establish a relationship between offshore wave energy and the wave energy measured using PTs to allow for more detailed analysis of wave energy transformation.

Abrasion by clast transport at the study site is supply limited. We suggest that the lack of sediment accumulation on the platform is related partially to the low rate of onshore sediment supply in addition to rapid rates of clast breakdown from cliff rockfalls and the effective and frequent removal of material (as demonstrated in the clast transport experiments). These factors are conjunctive with the presence of a sub tidal cliff at the seaward edge (Type B after Sunamura, 1992). This break in slope inhibits re-deposition of clasts back onto the platform once they are transported over the sub tidal cliff, thus limiting accumulation of clasts on the

platform at the study site. However, recent field validation of Ireland's shore platform locations and types (Bourke et al., 2016) has shown that the cobble to fine boulder sized material used in the clast transport experiments are commonly found on shore platforms on the west coast of Ireland and that CATs are also frequently observed on these platforms. These clasts may be repeatedly entrained and transported at wave energies well below storm values. We acknowledge that specific entrainment threshold values will depend on size, shape and pre transport setting of clasts (Nott, 2003, Imamura et al., 2008, Nandasena et al., 2011), while geomorphological setting will also exert a strong control (Naylor et al., 2016a). However, we find that there is significant potential for abrasion of shore platforms via clast transport under non-storm conditions.

While the role of the connectivity of the cliff to the platform is an area that requires further study, we have shown here that sediment supply from the cliff to the platform provides an effective abradant of the platform surface. This is not a process that is exclusive to cliff-sourced sediment as clasts quarried from the platform (while restricted to higher magnitude events) also form CATs. Given the modelled increase in the frequency of more extreme storms (Mölter et al., 2016), then it follows that that abrasion by clast transport may become an increasingly important geomorphic process on shore platforms as higher intensity storms will likely result in an increase in the number of clasts produced via quarrying. In addition, given that climate change will increase not only potential wave energy on the platform but also weathering rates of cliffs from increased rainfall receipts – more frequent rockfalls will provide additional clasts for abrasion of the platform.

4.5 Conclusions

This work is the first quantitative estimate of abrasion on a shore platform by clast transport. Although we measured erosion which occurred via this process during storms, we find that abrasion by clast transport is not limited to storm events. The efficacy of abrasion by clast transport as a mechanism for platform erosion is strongly influenced by availability of clasts, wave energy regime and geomorphological controls. The volumes of erosion reported here are comparable to those reported for other forms of erosion (e.g., bioerosion) operating at a similar spatial scale. As previously suggested by Naylor et al. (2012), we suggest that future research of erosional processes on shore platforms include an estimate of the surface area affected so that the relative efficacy of different processes within and between sites can be more robustly assessed and models of platform evolution better informed. Our findings also support the recommendation of Stephenson et al. (2010) for adopting techniques which capture erosion of shore platform at a range of scales to complement micro erosion meter data. To this end we advocate the use of SfM Photogrammetry as a practical method for investigating meso-scale erosion on shore platforms.

In agreement with previous research we find that geomorphological controls strongly influence clast transport dynamics. Weiss and Diplas (2015) provided evidence that surface roughness in the vicinity of a clasts influences clast entrainment, while Naylor et al. (2016a) determined that topographic variability across a platform surface had a strong influence on entrainment and transport distance of clasts. We add to this our observation that surface roughness also influences transport mode and in doing so determines the type of abrasion feature observed. Increasing evidence for relationships between geomorphological controls and clast transport dynamics has implications for paleo-storm reconstructions and strengthens previous calls (e.g. Weiss and Diplas, 2015, Naylor et al., 2016a) for consideration of platform roughness in models of clast entrainment and transport on intertidal platforms.

Acknowledgements

We would like to thank the following people for their contributions. Dr. Larissa Naylor (University of Glasgow) for the loan of the pressure transducers, Ciaran Nash, Archie McCauley, Floriano Goffo and Caoimhe Bourke for their help with field work and Ankit Verma for his expertise. We would also like to thank the Geological Survey of Ireland (GSI) for supporting field work costs via the GSI Short Call program (Award no. 2015-sc-064).

References

Agisoft, L. P.: Professional Edition, Version 1.0. 0, 2013. 2013.

Allen, J.: Sedimentary structures, their character and physical basis, Elsevier, Netherlands, 1982.

Andrews, C. and Williams, R. B.: Limpet erosion of chalk shore platforms in southeast England, Earth Surface Processes and Landforms, 25, 1371-1381, 2000.

Balaguer-Puig, M., Marqués-Mateu, Á., Lerma, J. L., and Ibáñez-Asensio, S.: Estimation of small-scale soil erosion in laboratory experiments with Structure from Motion photogrammetry, Geomorphology, doi: doi: 10.1016/j.geomorph.2017.04.035, 2017. 2017.

Barlow, J., Lim, M., Rosser, N., Petley, D., Brain, M., Norman, E., and Geer, M.: Modeling cliff erosion using negative power law scaling of rockfalls, Geomorphology, 139, 416-424, 2012.

Barron, S., Delaney, A., Perrin, P., Martin, J., O'Neill, F., De Jongh, A., O'Neill, L., Perrin, P., Barron, S., and Roche, J.: National survey and assessment of the conservation status of Irish sea cliffs, National Parks and Wildlife Service, 2011.

Blair, T. C. and McPherson, J. G.: Grain-size and textural classification of coarse sedimentary particles, Journal of Sedimentary Research, 69, 1999.

Bourke, M. C., Brearley, J. A., Haas, R., and Viles, H. A.: A photographic atlas of rock breakdown features in geomorphic environments, Planetary Science Institute, 2007.

Bourke, M. C., Naylor, L. A., Flood, R., Nash, C., Cullen, N. D., Goffo, F., and Migge, K.: Investigation of Ireland's Shore Platforms: Location, type and coastal protection. , Geological Survey of Ireland., Dublin, Ireland, 2016.

Bowen, D., Phillips, F., McCabe, A., Knutz, P., and Sykes, G.: New data for the last glacial maximum in Great Britain and Ireland, Quaternary Science Reviews, 21, 89-101, 2002.

Brasington, J., Langham, J., and Rumsby, B.: Methodological sensitivity of morphometric estimates of coarse fluvial sediment transport, Geomorphology, 53, 299-316, 2003.

Brasington, J., Rumsby, B., and McVey, R.: Monitoring and modelling morphological change in a braided gravel-bed river using high resolution GPS-based survey, Earth Surface Processes and Landforms, 25, 973-990, 2000.

Brunier, G., Fleury, J., Anthony, E. J., Gardel, A., and Dussouillez, P.: Close-range airborne Structure-from-Motion Photogrammetry for high-resolution beach morphometric surveys: Examples from an embayed rotating beach, Geomorphology, 261, 76-88, 2016a.

Brunier, G., Fleury, J., Anthony, E. J., Pothin, V., Vella, C., Dussouillez, P., Gardel, A., and Michaud, E.: Structure-from-Motion photogrammetry for high-resolution coastal and fluvial geomorphic surveys, Géomorphologie: relief, processus, environnement, 22, 147-161, 2016b.

Buyer, A. and Schubert, W.: Extraction of discontinuity orientations in point clouds, Rock Mechanics and Rock Engineering: From the Past to the Future, 2, 1133-1138, 2016.

Carbonneau, P. E., Lane, S. N., and Bergeron, N. E.: Catchment-scale mapping of surface grain size in gravel bed rivers using airborne digital imagery, Water resources research, 40, 2004.

Carrivick, J. L., Smith, M. W., and Quincey, D. J.: Structure from Motion in the Geosciences, John Wiley & Sons, 2016.

Chandler, J.: Effective application of automated digital photogrammetry for geomorphological research, Earth Surface Processes and Landforms, 24, 51-63, 1999.

Chandler, J., Ashmore, P., Paola, C., Gooch, M., and Varkaris, F.: Monitoring river-channel change using terrestrial oblique digital imagery and automated digital photogrammetry, Annals of the Association of American Geographers, 92, 631-644, 2002.

Cignoni, P., Rocchini, C., and Scopigno, R.: Metro: measuring error on simplified surfaces, 1998, 167-174.

Collinson, J. D., Martinsen, O., Bakken, B., and Kloster, A.: Early fill of the Western Irish Namurian Basin: a complex relationship between turbidites and deltas, Basin Research, 3, 223-242, 1991.

Corominas, J., Mavrouli, O., and Ruiz-Carulla, R.: Magnitude and frequency relations: are there geological constraints to the rockfall size?, Landslides, 2017. 1-17, 2017.

Cox, R., Zentner, D. B., Kirchner, B. J., and Cook, M. S.: Boulder ridges on the Aran Islands (Ireland): recent movements caused by storm waves, not tsunamis, The Journal of geology, 120, 249-272, 2012.

Cruslock, E. M., Naylor, L. A., Foote, Y. L., and Swantesson, J. O.: Geomorphologic equifinality: A comparison between shore platforms in Höga Kusten and Fårö, Sweden and the Vale of Glamorgan, South Wales, UK, Geomorphology, 114, 78-88, 2010.

Cullen, N. D. and Bourke, M. C.: Clast abrasion of a rock shore platform on the Atlantic coast of Ireland, Earth Surface Processes and Landforms, 43 (12) 2627-2641, 2018.

Dahl, A. L.: Surface area in ecological analysis: quantification of benthic coral-reef algae, Marine Biology, 23, 239-249, 1973.

Dasgupta, R.: Determination of the fractal dimension of a shore platform profile, Journal of the Geological Society of India, 81, 122-128, 2013.

Dasgupta, R.: Whither shore platforms?, Progress in Physical Geography, 35, 183-209, 2011.

Dasgupta, R.: Whither shore platforms?, Progress in Physical Geography, 2010. 2010.

Devoy, R. J.: Coastal vulnerability and the implications of sea-level rise for Ireland, Journal of Coastal research, 2008. 325-341, 2008.

Dornbusch, U., Moses, C., Robinson, D. A., and Williams, R.: Soft copy photogrammetry to measure shore platform erosion on decadal timescales, Journal of Coastal Conservation, 11, 193-200, 2008.

Dussauge-Peisser, C., Helmstetter, A., Grasso, J.-R., Hantz, D., Desvarreux, P., Jeannin, M., and Giraud, A.: Probabilistic approach to rock fall hazard assessment: potential of historical data analysis, Natural Hazards and Earth System Science, 2, 15-26, 2002.

Edwards, A. B.: Storm-wave platforms, Jour. Geomorphology, 4, 223-236, 1941.

Ellis, N.: Morphology, process and rates of denudation on the chalk shore platform of East Sussex, 1986. Brighton Polytechnic, PhD Thesis, 1986.

Erdmann, W., Kelletat, D., and Scheffers, A.: Boulder transport by storms–Extreme-waves in the coastal zone of the Irish west coast, Marine Geology, 2018. 2018.

Etienne, S. and Paris, R.: Boulder accumulations related to storms on the south coast of the Reykjanes Peninsula (Iceland), Geomorphology, 114, 55-70, 2010.

EUrosion: Living with coastal erosion in Europe: Sediment and Space for Sustainability. Part 2 Maps and Statistics. , Europe, 2004.

Farrell, E. J., Granja, H., Cappietti, L., Ellis, J. T., Li, B., and Sherman, D. J.: Wave transformation across a rock platform, Belinho, Portugal, Journal of Coastal Research, 2009. 44-48, 2009.

Fonstad, M. A., Dietrich, J. T., Courville, B. C., Jensen, J. L., and Carbonneau, P. E.: Topographic structure from motion: a new development in photogrammetric measurement, Earth Surface Processes and Landforms, 38, 421-430, 2013.

Foote, Y., Plessis, E., Robinson, D., Hénaff, A., and Costa, S.: Rates and patterns of downwearing of chalk shore platforms of the Channel: comparisons between France and England, Zeitschrift Fur Geomorphologie, 144, 93-115, 2006.

Furukawa, Y., Curless, B., Seitz, S. M., and Szeliski, R.: Towards internet-scale multi-view stereo, 2010, 1434-1441.

Gallagher, S., Tiron, R., and Dias, F.: A detailed investigation of the nearshore wave climate and the nearshore wave energy resource on the west coast of Ireland, 2013, V008T009A046-V008T009A046.

Gallagher, S., Tiron, R., and Dias, F.: A long-term nearshore wave hindcast for Ireland: Atlantic and Irish Sea coasts (1979–2012), Ocean Dynamics, 64, 1163-1180, 2014.

Gardner, J.: Rockfall frequency and distribution in the Highwood Pass area, Canadian Rocky Mountains, Zeitshrift fur Geomorphologie, NF, 27, 311-324, 1983.

Gardner, J. S.: Frequency, magnitude and spatial distribution of mountain rockfalls and rockslides in the Highwood Pass area, Alberta, Canada, Thresholds in Geomorphology. Allen and Unwin, New York, 1980. 267-295, 1980.

Girardeau-Montaut, D., Roux, M., Marc, R., and Thibault, G.: Change detection on points cloud data acquired with a ground laser scanner, International Archives of Photogrammetry, Remote Sensing and Spatial Information Sciences, 36, W19, 2005.

Gómez-Gutiérrez, Á., Schnabel, S., Berenguer-Sempere, F., Lavado-Contador, F., and Rubio-Delgado, J.: Using 3D photo-reconstruction methods to estimate gully headcut erosion, Catena, 120, 91-101, 2014.

Gómez-Pujol, L., Stephenson, W. J., and Fornós, J. J.: Two-hourly surface change on supra-tidal rock (Marengo, Victoria, Australia), Earth Surface Processes and Landforms, 32, 1-12, 2007.

Goudie, A.: Encyclopedia of geomorphology, Psychology Press, 2004.

Guidi, G., Gonizzi, S., and Micoli, L.: Image pre-processing for optimizing automated photogrammetry performances, 2014, 145-152.

Guthrie, R. and Evans, S.: Magnitude and frequency of landslides triggered by a storm event, Loughborough Inlet, British Columbia, Natural Hazards and Earth System Science, 4, 475-483, 2004.

Guzzetti, F., Ardizzone, F., Cardinali, M., Rossi, M., and Valigi, D.: Landslide volumes and landslide mobilization rates in Umbria, central Italy, Earth and Planetary Science Letters, 279, 222-229, 2009.

Guzzetti, F., Malamud, B. D., Turcotte, D. L., and Reichenbach, P.: Power-law correlations of landslide areas in central Italy, Earth and Planetary Science Letters, 195, 169-183, 2002.

Hall, A. M.: Storm wave currents, boulder movement and shore platform development: a case study from East Lothian, Scotland, Marine Geology, 283, 98-105, 2011.

Hall, A. M., Hansom, J. D., and Jarvis, J.: Patterns and rates of erosion produced by high energy wave processes on hard rock headlands: The Grind of the Navir, Shetland, Scotland, Marine Geology, 248, 28-46, 2008.

Hampton, M. A., Griggs, G. B., Edil, T. B., Guy, D. E., Kelley, J. T., Komar, P. D., Mickelson, D. M., and Shipman, H. M.: Processes that govern the formation and evolution of coastal cliffs, US Geological Survey professional paper, 1693, 7-38, 2004.

Hanna, F.: A technique for measuring the rate of erosion of cave passages, Proceedings University of Bristol Spelaeology Society, 83-86, 1966.

Hemmingsen, S. A., Eikaas, H. S., and Hemmingsen, M. A.: The influence of seasonal and local weather conditions on rock surface changes on the shore platform at Kaikoura Peninsula, South Island, New Zealand, Geomorphology, 87, 239-249, 2007.

Hodson, F. and Lewarne, G. C.: A mid-Carboniferous (Namurian) basin in parts of the counties of Limerick and Clare, Ireland, Quarterly Journal of the Geological Society, 117, 307-333, 1961.

Hovius, N., Stark, C. P., Hao-Tsu, C., and Jiun-Chuan, L.: Supply and removal of sediment in a landslide-dominated mountain belt: Central Range, Taiwan, The Journal of Geology, 108, 73-89, 2000.

Hudson, J. A. and Harrison, J.: Engineering rock mechanics, vol. I. Pergamon, 1997.

Hungr, O., Evans, S., and Hazzard, J.: Magnitude and frequency of rock falls and rock slides along the main transportation corridors of southwestern British Columbia, Canadian Geotechnical Journal, 36, 224-238, 1999.

Hungr, O., McDougall, S., Wise, M., and Cullen, M.: Magnitude–frequency relationships of debris flows and debris avalanches in relation to slope relief, Geomorphology, 96, 355-365, 2008.

Imamura, F., Goto, K., and Ohkubo, S.: A numerical model for the transport of a boulder by tsunami, Journal of Geophysical Research: Oceans, 113, 2008.

James, M. R., Robson, S., and Smith, M. W.: 3-D uncertainty-based topographic change detection with structure-from-motion photogrammetry: precision maps for ground control and directly georeferenced surveys, Earth Surface Processes and Landforms, doi: doi:10.1002/esp.4125, 2017. 2017.

Javernick, L., Brasington, J., and Caruso, B.: Modeling the topography of shallow braided rivers using Structure-from-Motion photogrammetry, Geomorphology, 213, 166-182, 2014.

Johnson, D. W.: Shore processes and shoreline development, John Wiley & Sons, Incorporated, 1919.

Jones, E. V., Rosser, N., and Brain, M.: Alongshore variability in wave energy transfer to coastal cliffs, Geomorphology, 2018. 2018.

Kaiser, A., Neugirg, F., Rock, G., Müller, C., Haas, F., Ries, J., and Schmidt, J.: Small-scale surface reconstruction and volume calculation of soil erosion in complex Moroccan gully morphology using structure from motion, Remote Sensing, 6, 7050-7080, 2014.

Kazhdan, M. and Hoppe, H.: Screened poisson surface reconstruction, ACM Transactions on Graphics (ToG), 32, 29, 2013.

Kemeny, J. and Post, R.: Estimating three-dimensional rock discontinuity orientation from digital images of fracture traces, Computers & Geosciences, 29, 65-77, 2003.

Kirby, E. and Ouimet, W.: Tectonic geomorphology along the eastern margin of Tibet: Insights into the pattern and processes of active deformation adjacent to the Sichuan Basin, Geological Society, London, Special Publications, 353, 165-188, 2011.

Kirby, E. and Whipple, K. X.: Expression of active tectonics in erosional landscapes, Journal of Structural Geology, 44, 54-75, 2012.

Knight, J. and Burningham, H.: Boulder dynamics on an Atlantic-facing rock coastline, northwest Ireland, Marine Geology, 283, 56-65, 2011.

Knight, J., Burningham, H., and Barrett-Mold, C.: The geomorphology and controls on development of a boulder-strewn rock platform, NW Ireland, Journal of Coastal Research, 2009. 1646-1650, 2009.

Lague, D., Brodu, N., and Leroux, J.: Accurate 3D comparison of complex topography with terrestrial laser scanner: Application to the Rangitikei canyon (NZ), ISPRS journal of photogrammetry and remote sensing, 82, 10-26, 2013.

Lane, S. N., Westaway, R. M., and Murray Hicks, D.: Estimation of erosion and deposition volumes in a large, gravel-bed, braided river using synoptic remote sensing, Earth Surface Processes and Landforms, 28, 249-271, 2003.

Larsen, I. J., Montgomery, D. R., and Korup, O.: Landslide erosion controlled by hillslope material, Nature Geoscience, 3, 247, 2010.

Lim, M., Rosser, N. J., Allison, R. J., and Petley, D. N.: Erosional processes in the hard rock coastal cliffs at Staithes, North Yorkshire, Geomorphology, 114, 12-21, 2010.

Lowe, D. G.: Distinctive image features from scale-invariant keypoints, International journal of computer vision, 60, 91-110, 2004.

Malamud, B. D., Turcotte, D. L., Guzzetti, F., and Reichenbach, P.: Landslide inventories and their statistical properties, Earth Surface Processes and Landforms, 29, 687-711, 2004.

Malinverno, A.: A simple method to estimate the fractal dimension of a self-affine series, Geophysical Research Letters, 17, 1953-1956, 1990.

Marine Institute: Irish National Tide Gauge Network Real Time Data., Marine Institute, RInville, Oranmore, Galway., 2016.

Marshall, R. J. and Stephenson, W. J.: The morphodynamics of shore platforms in a micro-tidal setting: Interactions between waves and morphology, Marine Geology, 288, 18-31, 2011.

Mastronuzzi, G. and Sansò, P.: Large boulder accumulations by extreme waves along the Adriatic coast of southern Apulia (Italy), Quaternary International, 120, 173-184, 2004.

Matasci, B., Jaboyedoff, M., Loye, A., Pedrazzini, A., Derron, M.-H., and Pedrozzi, G.: Impacts of fracturing patterns on the rockfall susceptibility and erosion rate of stratified limestone, Geomorphology, 241, 83-97, 2015.

Mc Keown, L., Bourke, M., and McElwaine, J.: Experiments On Sublimating Carbon Dioxide Ice And Implications For Contemporary Surface Processes On Mars, Scientific reports, 7, 14181, 2017.

McCartney, M., Abernethy, G., and Gault, L.: The Divider Dimensions of the Irish Coast, Irish Geography, 43, 277-284, 2010.

McKenna, J.: Morphodynamics and sediments of basalt shore platforms, 1990. University of Ulster, 1990.

McKenna, J., Carter, R., and Bartlett, D.: Coast Erosion in Northeast Ireland:-Part II Cliffs and Shore Platforms, Irish Geography, 25, 111-128, 1992.

Micheletti, N., Chandler, J. H., and Lane, S. N.: Investigating the geomorphological potential of freely available and accessible structure-from-motion photogrammetry using a smartphone, Earth Surface Processes and Landforms, 40, 473-486, 2015a.

Micheletti, N., Chandler, J. H., and Lane, S. N.: Structure from Motion (SfM) Photogrammetry. In: Geomorphlogical Techniques, 2 (2.2), British Society for Geomorphology, Loondon, 2015b.

Milan, D. J., Heritage, G. L., and Hetherington, D.: Application of a 3D laser scanner in the assessment of erosion and deposition volumes and channel change in a proglacial river, Earth

Surface Processes and Landforms: The Journal of the British Geomorphological Research Group, 32, 1657-1674, 2007.

Mölter, T., Schindler, D., Albrecht, A. T., and Kohnle, U.: Review on the projections of future storminess over the North Atlantic European Region, Atmosphere, 7, 60, 2016.

Moses, C., Robinson, D., and Barlow, J.: Methods for measuring rock surface weathering and erosion: A critical review, Earth-Science Reviews, 135, 141-161, 2014.

Moses, C. A.: The origin and implications of microsolutional features on the surface of limestone, 1993. Queen's University of Belfast, 1993.

Moses, C. A.: The rock coast of the British Isles: shore platforms, Geological Society, London, Memoirs, 40, 39-56, 2014.

Nandasena, N., Paris, R., and Tanaka, N.: Numerical assessment of boulder transport by the 2004 Indian ocean tsunami in Lhok Nga, West Banda Aceh (Sumatra, Indonesia), Computers & geosciences, 37, 1391-1399, 2011.

Nandasena, N., Tanaka, N., Sasaki, Y., and Osada, M.: Boulder transport by the 2011 Great East Japan tsunami: Comprehensive field observations and whither model predictions?, Marine Geology, 346, 292-309, 2013.

Naylor, L.: Geomorphological control on boulder transport and coastal erosion before, during and after an extreme extra-tropical cyclone, Earth Surface Processes and Landforms, 2016. 2016.

Naylor, L. and Stephenson, W.: On the role of discontinuities in mediating shore platform erosion, Geomorphology, 114, 89-100, 2010.

Naylor, L., Stephenson, W., and Trenhaile, A.: Rock coast geomorphology: recent advances and future research directions, Geomorphology, 114, 3-11, 2010.

Naylor, L. A., Coombes, M. A., and Viles, H. A.: Reconceptualising the role of organisms in the erosion of rock coasts: A new model, Geomorphology, 157, 17-30, 2012.

Naylor, L. A., Stephenson, W. J., Smith, H., Way, O., Mendelssohn, J., and Cowley, A.: Geomorphological control on boulder transport and coastal erosion before, during and after an extreme extra-tropical cyclone, Earth Surface Processes and Landforms, 2016. 2016.

Nott, J.: Waves, coastal boulder deposits and the importance of the pre-transport setting, Earth and Planetary Science Letters, 210, 269-276, 2003.

Ogawa, H.: Observation of wave transformation on a sloping type B shore platform under wind-wave and swell conditions, Geo-Marine Letters, 33, 1-11, 2013.

Ogawa, H., Dickson, M., and Kench, P.: Wave transformation on a sub-horizontal shore platform, Tatapouri, North Island, New Zealand, Continental Shelf Research, 31, 1409-1419, 2011.

Ogawa, H., Kench, P., and Dickson, M.: Field Measurements of Wave Characteristics on a Near-Horizontal Shore Platform, Mahia Peninsula, North Island, New Zealand, Geographical Research, 50, 179-192, 2012.

Özyeşil, O., Voroninski, V., Basri, R., and Singer, A.: A survey of structure from motion*, Acta Numerica, 26, 305-364, 2017.

Palamara, D., Dickson, M., and Kennedy, D.: Defining shore platform boundaries using airborne laser scan data: a preliminary investigation, Earth Surface Processes and Landforms, 32, 945-953, 2007.

Paris, R., Naylor, L. A., and Stephenson, W. J.: Boulders as a signature of storms on rock coasts, Marine Geology, 283, 1-11, 2011.

Pérez-Alberti, A., Trenhaile, A., Pires, A., López-Bedoya, J., Chaminé, H., and Gomes, A.: The effect of boulders on shore platform development and morphology in Galicia, north west Spain, Continental Shelf Research, 48, 122-137, 2012.

Peters, J. L., Benetti, S., Dunlop, P., Cofaigh, C. Ó., Moreton, S. G., Wheeler, A. J., and Clark, C. D.: Sedimentology and chronology of the advance and retreat of the last British-Irish Ice Sheet on the continental shelf west of Ireland, Quaternary Science Reviews, 140, 101-124, 2016.

Pinn, E. H., Richardson, C., Thompson, R., and Hawkins, S.: Burrow morphology, biometry, age and growth of piddocks (Mollusca: Bivalvia: Pholadidae) on the south coast of England, Marine Biology, 147, 943-953, 2005.

Poate, T., Masselink, G., Austin, M. J., Dickson, M., and McCall, R.: The role of bed roughness in wave transformation across sloping rock shore platforms, Journal of Geophysical Research: Earth Surface, 123, 97-123, 2018.

Porter, N. J. and Trenhaile, A.: Short-term rock surface expansion and contraction in the intertidal zone, Earth Surface Processes and Landforms, 32, 1379-1397, 2007.

Prémaillon, M., Regard, V., and Dewez, T.: How to explain variations in sea cliff erosion rate?, 2017, 8012.

Priest, S. and Hudson, J.: Estimation of discontinuity spacing and trace length using scanline surveys, 1981, 183-197.

Pulham, A.: Controls on internal structure and architecture of sandstone bodies within Upper Carboniferous fluvial-dominated deltas, County Clare, western Ireland, Geological Society, London, Special Publications, 41, 179-203, 1989.

Richardson, K. and Carling, P. A.: A typology of sculpted forms in open bedrock channels, Geological Society of America Special Papers, 392, 1-108, 2005.

Rider, M.: The Namurian of West County Clare, 1974, 125-142.

Riquelme, A., Tomás, R., Cano, M., Pastor, J. L., and Abellán, A.: Automatic Mapping of Discontinuity Persistence on Rock Masses Using 3D Point Clouds, Rock Mechanics and Rock Engineering, 2018. 1-24, 2018.

Riquelme, A. J., Abellán, A., and Tomás, R.: Discontinuity spacing analysis in rock masses using 3D point clouds, Engineering Geology, 195, 185-195, 2015.

Riquelme, A. J., Abellán, A., Tomás, R., and Jaboyedoff, M.: A new approach for semi-automatic rock mass joints recognition from 3D point clouds, Computers & Geosciences, 68, 38-52, 2014.

Riquelme, A. J., Tomás, R., and Abellán, A.: Characterization of rock slopes through slope mass rating using 3D point clouds, International Journal of Rock Mechanics and Mining Sciences, 84, 165-176, 2016.

Risk, M. J.: Fish diversity on a coral reef in the Virgin Islands, The Smithsonian Institution,, Washington, Atoll Research Bulletin, Report No. 153, 1972.

Rosser, N., Lim, M., Petley, D., Dunning, S., and Allison, R.: Patterns of precursory rockfall prior to slope failure, Journal of geophysical research: earth surface, 112, 2007.

Rosser, N. J., Brain, M. J., Petley, D. N., Lim, M., and Norman, E. C.: Coastline retreat via progressive failure of rocky coastal cliffs, Geology, 41, 939-942, 2013.

Rosser, N. J., Petley, D. N., Lim, M., Dunning, S., and Allison, R. J.: Terrestrial laser scanning for monitoring the process of hard rock coastal cliff erosion, Quarterly Journal of Engineering Geology and Hydrogeology, 38, 363-375, 2005.

Santana, D., Corominas, J., Mavrouli, O., and Garcia-Sellés, D.: Magnitude–frequency relation for rockfall scars using a Terrestrial Laser Scanner, Engineering geology, 145, 50-64, 2012.

Scheffers, A., Scheffers, S., Kelletat, D., and Browne, T.: Wave-Emplaced Coarse Debris and Megaclasts in Ireland and Scotland: Boulder Transport in a High-Energy Littoral Environment, The Journal of Geology, 117, 553-573, 2009.

Schindelin, J., Arganda-Carreras, I., Frise, E., Kaynig, V., Longair, M., Pietzsch, T., Preibisch, S., Rueden, C., Saalfeld, S., and Schmid, B.: Fiji: an open-source platform for biological-image analysis, Nature methods, 9, 676-682, 2012.

Scott, D. N. and Wohl, E. E.: Bedrock Fracture Influences on Geomorphic Process and Form Across Process Domains and Scales, Earth Surface Processes and Landforms, 2018. 2018.

Slob, S.: Automated rock mass characterisation using 3-D terrestrial laser scanning, 2010. TU Delft, Delft University of Technology, 2010.

Slob, S., Hack, R., and Turner, A. K.: An approach to automate discontinuity measurements of rock faces using laser scanning techniques, 2002.

Slob, S., Van Knapen, B., Hack, R., Turner, K., and Kemeny, J.: Method for automated discontinuity analysis of rock slopes with three-dimensional laser scanning, Transportation research record: journal of the transportation research board, 2005. 187-194, 2005.

Smith, M., Carrivick, J., and Quincey, D.: Structure from motion photogrammetry in physical geography, Progress in Physical Geography, 40, 247-275, 2016.

Snavely, N.: Bundler: SfM for unordered image collections. GitHub, 2006.

Spate, A., Jennings, J., Smith, D., and Greenaway, M.: The micro-erosion meter: use and limitations, Earth Surface Processes and Landforms, 10, 427-440, 1985.

Stephenson, W.: Shore platforms: remain neglected coastal feature?, Progress in Physical Geography, 24, 311-327, 2000.

Stephenson, W. and Finlayson, B.: Measuring erosion with the micro-erosion meter—contributions to understanding landform evolution, Earth-Science Reviews, 95, 53-62, 2009.

Stephenson, W., Kirk, R., Hemmingsen, S., and Hemmingsen, M.: Decadal scale micro erosion rates on shore platforms, Geomorphology, 114, 22-29, 2010.

Stephenson, W. and Naylor, L.: Geological controls on boulder production in a rock coast setting: insights from South Wales, UK, Marine Geology, 283, 12-24, 2011a.

Stephenson, W. and Naylor, L.: Within site geological contingency and its effect on rock coast erosion, Journal of Coastal Research, 61, 831-835, 2011b.

Stephenson, W. J.: Improving the traversing micro-erosion meter, Journal of Coastal Research, doi: . 1997. 236-241, 1997.

Stephenson, W. J., Dickson, M. E., and Trenhaile, A. S.: Rock Coasts. In: Treatise on Geomorphology, Shroder, J. F. (Ed.), Elsevier, 2013.

Stephenson, W. J. and Kirk, R. M.: Measuring erosion rates using the micro-erosion meter: 20 years of data from shore platforms, Kaikoura Peninsula, South Island, New Zealand, Marine Geology, 131, 209-218, 1996.

Stephenson, W. J. and Kirk, R. M.: Surface swelling of coastal bedrock on inter-tidal shore platforms, Kaikoura Peninsula, South Island, New Zealand, Geomorphology, 41, 5-21, 2001.

Stockamp, J., Li, Z., Bishop, P., Hansom, J., Rennie, A., Petrie, E., Tanaka, A., Bingley, R., and Hansen, D.: Investigating Glacial Isostatic Adjustment in Scotland with InSAR and GPS Observations, 2015.

Sunamura, T.: Geomorphology of rocky coasts, John Wiley & Son Ltd, 1992.

Sunamura, T.: Rock control in coastal geomorphic processes, 1995, 103A.

Suzuki, T.: Rock control in geomorphological processes: research history in Japan and perspective, Transactions, Japanese Geomorphological Union, 23, 161-199, 2002.

Swantesson, J., Moses, C., Berg, G., and Jansson, K. M.: Methods for measuring shoreplatform micro-erosion; a comparison of the micro-erosion meter and the laser scanner, Zeitschrift fur Geomorphologie Supplementband, 144, 1-17, 2006.

Switzer, A. D. and Burston, J. M.: Competing mechanisms for boulder deposition on the southeast Australian coast, Geomorphology, 114, 42-54, 2010.

Thoeni, K., Giacomini, A., Murtagh, R., and Kniest, E.: A comparison of multi-view 3D reconstruction of a rock wall using several cameras and a laser scanner, The International Archives of Photogrammetry, Remote Sensing and Spatial Information Sciences, 40, 573, 2014.

Thornbush, M. J.: A site-specific index based on weathering forms visible in Central Oxford, UK, Geosciences, 2, 277-297, 2012.

Trenhaile, A.: Tidal wetting and drying on shore platforms: an experimental study of surface expansion and contraction, Geomorphology, 76, 316-331, 2006.

Trenhaile, A. S.: The geomorphology of rock coasts, Oxford University Press, USA, 1987.

Trenhaile, A. S.: Modeling shore platforms: present status and future developments. In: Advances in Coastal Modeling. Amsterdam: Elsevier, Lakhan, V. C. (Ed.), Elsevier Science B.V. , 2003.

Tressler, C.: From hillslopes to canyons, studies of erosion at differing time and spatial scales within the Colorado River drainage, 2011. 2011.

Trudgill, S.: Measurement of erosional weight loss of rock tablets, British Geomorphological Research Group Technical Bulletin, 13-20 pp., 1975.

Trudgill, S., High, C., and Hanna, F.: Improvements to the micro-erosion meter, British Geomorphological Research Group Technical Bulletin, 3-17 pp., 1981.

Turowski, J. M. and Cook, K. L.: Field techniques for measuring bedrock erosion and denudation, Earth Surface Processes and Landforms, 42, 109-127, 2017.

Verma, A. K. and Bourke, M. C.: A Structure from Motion photogrammetry-based method to generate sub-millimetre resolution Digital Elevation Models for investigating rock breakdown features, Earth Surf. Dynam. Discuss., https://doi.org/10.5194/esurf-2018-53, in review, 2018.
.

Viles, H. A.: Scale issues in weathering studies, Geomorphology, 41, 63-72, 2001.

Walkden, M. and Hall, J.: A predictive mesoscale model of the erosion and profile development of soft rock shores, Coastal Engineering, 52, 535-563, 2005.

Warke, P. A. and McKinley, J.: Scale issues in geomorphology, Geomorphology, 130, 1-4, 2011.

Weiss, R. and Diplas, P.: Untangling boulder dislodgement in storms and tsunamis: Is it possible with simple theories?, Geochemistry, Geophysics, Geosystems, 16, 890-898, 2015.

Wentworth, C. K.: A scale of grade and class terms for clastic sediments, The Journal of Geology, 30, 377-392, 1922.

Westoby, M., Brasington, J., Glasser, N., Hambrey, M., and Reynolds, J.: 'Structure-from-Motion'photogrammetry: A low-cost, effective tool for geoscience applications, Geomorphology, 179, 300-314, 2012.

Whadcoat, S. K.: Numerical modelling of rockfall evolution in hard rock slopes, 2017. Durham University, 2017.

Wheaton, J. M., Brasington, J., Darby, S. E., and Sear, D. A.: Accounting for uncertainty in DEMs from repeat topographic surveys: improved sediment budgets, Earth Surface Processes and Landforms, 35, 136-156, 2010.

Williams, J. G., Rosser, N. J., Hardy, R. J., Brain, M. J., and Afana, A. A.: Optimising 4-D surface change detection: an approach for capturing rockfall magnitude–frequency, Earth surface dynamics., 6, 101-119, 2018.

Williams, R.: DEMs of difference. In: Geomorphological Techniques, 2 (3.2), British Society for Geomorphology, London, UK, 2012.

XLSTAT: Data Analysis and Statistical Solution for Microsoft Excel. . Addinsoft, Paris, France., 2017.

Yatsu, E.: The nature of weathering: an introduction, Sozosha Tokyo, 1988.

Yatsu, E.: Rock control in geomorphology, Sozosha, 1966.

Zingg, T.: Beitrag zur schotteranalyse, 1935. 1935.

4.6 Supplementary tables

Table S1. Clast Abrasion Trail (CAT) scratch inventory with the CAT ID and photo ID (CAT_ID_Photo ID), number of scratches in the image and the total abraded surface area for the scratches in the photo used in the volume calculations of abraded surface area.

CAT ID_Photo ID	SA	Scratches	CAT ID_Photo ID	SA	Scratches	CAT ID_Photo ID	SA	Scratches
	m^2	n		m^2	n		m^2	n
01_0019	2.50E-03	3	01_0042	1.70E-03	6	01_0067	1.91E-03	3
01_0020	9.47E-03	5	01_0043	7.15E-03	7	01_0068	5.00E-03	2
01_0021	2.52E-03	7	01_0044	1.48E-02	7	01_0069	3.75E-03	2
01_0022	5.64E-03	10	01_0045	5.86E-03	9	01_0070	1.23E-02	10
01_0023	3.63E-03	13	01_0046	4.12E-03	5	01_0071	8.24E-03	11
01_0024	7.86E-03	10	01_0049	3.33E-03	8	01_0072	3.57E-03	7
01_0025	3.54E-03	10	01_0050	1.17E-03	3	01_0073	3.46E-03	7
01_0026	1.97E-02	20	01_0051	1.66E-03	5	01_0074	7.31E-05	1
01_0027	4.15E-03	6	01_0052	7.87E-03	19	01_0075	1.52E-03	2
01_0028	3.85E-03	10	01_0053	8.90E-03	16	01_0076	2.47E-03	12
01_0029	3.73E-03	6	01_0054	1.11E-02	16	01_0077	7.65E-03	15
01_0030	6.07E-03	13	01_0055	7.17E-03	14	01_0078	6.15E-03	5
01_0031	7.56E-03	24	01_0056	5.60E-03	10	01_0079	9.58E-03	9
01_0032	5.67E-03	22	01_0057	5.61E-03	5	01_0080	4.87E-03	9
01_0033	5.68E-03	20	01_0058	3.06E-03	5	01_0081	6.30E-03	16
01_0034	2.77E-03	8	01_0059	4.33E-03	7	01_0082	7.07E-03	9
01_0035	2.73E-03	3	01_0060	4.02E-02	18	01_0083	2.29E-04	1
01_0036	2.54E-03	8	01_0061	1.81E-02	7	01_0084	6.11E-04	6
01_0037	4.82E-03	17	01_0062	1.03E-02	9	01_0086	1.63E-03	10
01_0038	4.56E-03	10	01_0063	3.06E-03	7	01_0087	1.68E-03	6
01_0039	4.35E-03	6	01_0064	8.01E-03	4	01_0088	8.79E-04	1
01_0040	2.47E-03	13	01_0065	4.28E-03	2	01_0089	6.80E-03	10
01_0041	3.85E-03	5	01_0066	8.73E-03	3	01_0090	3.32E-03	4

Table S1 continued.

CAT ID_Photo ID	SA	Scratches	CAT ID_Photo ID	SA	Scratches	CAT ID_Photo ID	SA	Scratches
	m^2	n		m^2	n		m^2	n
01_0091	4.63E-03	11	01_0115	6.21E-03	11	01_0139	5.57E-03	7
01_0092	6.90E-03	6	01_0116	2.47E-03	5	01_0140	2.20E-03	3
01_0093	2.94E-03	6	01_0117	4.03E-03	9	01_0141	7.86E-04	2
01_0094	9.32E-03	22	01_0118	7.39E-03	9	01_0142	1.12E-02	12
01_0096	7.89E-03	12	01_0119	1.31E-03	3	01_0143	4.49E-03	8
01_0097	7.54E-03	9	01_0120	2.15E-03	6	01_0144	5.60E-03	15
01_0098	1.01E-02	13	01_0121	1.18E-02	9	01_0145	4.61E-03	7
01_0099	1.25E-02	9	01_0122	5.43E-03	6	01_0146	8.12E-03	9
01_0100	2.70E-03	7	01_0123	5.43E-03	6	01_0147	5.54E-03	13
01_0101	8.43E-03	12	01_0124	6.45E-03	11	01_0148	7.15E-03	11
01_0102	7.94E-03	6	01_0126	3.78E-03	5	01_0149	5.67E-03	10
01_0103	3.60E-03	13	01_0127	6.07E-03	5	01_0150	7.25E-03	12
01_0104	6.94E-04	1	01_0128	7.34E-03	7	01_0151	5.39E-03	13
01_0105	8.86E-03	17	01_0129	4.55E-03	7	01_0152	4.46E-03	14
01_0106	6.94E-03	14	01_0130	7.64E-03	11	01_0153	5.71E-03	14
01_0107	4.15E-03	9	01_0131	1.00E-02	2	01_0154	5.44E-03	10
01_0108	5.06E-03	4	01_0132	1.23E-02	15	01_0155	2.80E-03	13
01_0109	3.08E-03	10	01_0133	6.85E-03	4	01_0156	1.07E-03	2
01_0110	8.70E-03	8	01_0134	2.19E-04	2	01_0157	2.16E-03	4
01_0111	2.92E-03	5	01_0135	5.43E-03	3	01_0159	3.44E-03	3
01_0112	3.61E-03	6	01_0136	2.46E-03	6	01_0160	2.77E-03	10
01_0113	3.89E-03	12	01_0137	3.71E-03	9	01_0162	3.95E-03	5
01_0114	1.51E-03	5	01_0138	2.70E-03	7	01_0163	3.11E-03	8

Table S1 continued.

CAT ID_Photo ID	SA m^2	Scratches n	CAT ID_Photo ID	SA m^2	Scratches n	CAT ID_Photo ID	SA m^2	Scratches n
01_0164	4.22E-03	11	02_0187	3.55E-03	7	02_0210	1.93E-03	3
01_0165	6.42E-03	6	02_0188	2.82E-03	2	02_0211	1.35E-02	7
01_0166	2.13E-03	6	02_0189	1.81E-02	9	02_0212	1.27E-02	13
01_0167	7.63E-04	4	02_0190	5.42E-03	7	02_0213	5.90E-03	11
01_0168	9.57E-03	19	02_0191	2.37E-03	7	02_0214	2.17E-03	7
01_0169	2.67E-04	2	02_0192	4.38E-03	9	02_0215	3.46E-03	5
01_0170	2.29E-03	10	02_0193	1.93E-02	19	02_0216	1.26E+02	12
01_0171	2.24E-03	6	02_0194	1.27E-02	10	02_0217	5.82E-03	14
01_0172	4.06E-03	5	02_0195	2.70E-03	5	02_0218	6.70E-04	1
01_0173	2.47E-04	3	02_0196	1.19E-02	14	02_0219	2.27E-03	10
01_0174	2.15E-03	7	02_0197	1.21E-02	16	02_0220	2.39E-03	9
01_0175	3.37E-03	9	02_0198	6.01E-03	7	02_0221	2.01E-03	5
01_0176	2.21E-03	2	02_0199	2.28E-03	3	02_0222	4.90E-03	7
01_0177	6.52E-04	4	02_0200	3.82E-03	10	02_0223	7.34E-04	3
02_0178	5.44E-03	9	02_0201	5.48E-03	5	02_0224	1.28E-03	9
02_0179	1.52E-03	7	02_0202	1.01E-02	13	02_0225	5.94E-04	7
02_0180	1.28E-02	5	02_0203	6.91E-03	12	02_0227	8.36E-04	8
02_0181	6.15E-03	14	02_0204	8.72E-03	7	02_0228	3.27E-04	4
02_0182	5.08E-03	14	02_0205	9.39E-03	16	02_0229	8.86E-03	8
02_0183	2.77E-03	9	02_0206	9.80E-03	17	02_0230	7.09E-03	4
02_0184	8.44E-03	6	02_0207	6.65E-03	14	02_0231	3.08E-03	3
02_0185	1.28E-02	13	02_0208	4.83E-03	4	02_0232	1.25E-03	2
02_0186	5.51E-03	6	02_0209	6.08E-03	5	02_0233	5.80E-03	13

Table S1 continued.

CAT ID_Photo ID	SA m^2	Scratches n	CAT ID_Photo ID	SA m^2	Scratches n	CAT ID_Photo ID	SA m^2	Scratches n
02_0234	1.00E-03	1	03_266	3.00E-03	2	03_290	2.15E-04	4
02_0235	6.60E-03	6	03_267	1.57E-03	5	03_291	9.24E-04	4
03_244	8.85E-03	2	03_268	2.60E-03	3	03_292	3.48E-04	4
03_245	4.10E-03	3	03_269	4.46E-03	8	03_293	1.00E-03	9
03_247	4.22E-03	21	03_270	1.60E-02	7	03_294	5.75E-04	8
03_248	7.25E-03	19	03_271	1.59E-03	7	03_295	9.36E-04	11
03_249	5.23E-03	21	03_272	4.39E-04	3	03_296	8.04E-04	7
03_250	6.61E-03	16	03_273	6.43E-03	4	03_297	1.00E-03	14
03_251	9.13E-03	11	03_274	3.00E-03	1	03_298	2.01E-03	20
03_252	2.10E-03	8	03_275	4.06E-03	6	03_299	1.07E-03	11
03_253	2.89E-03	6	03_277	2.18E-03	2	03_300	3.54E-04	8
03_254	3.14E-03	12	03_278	5.74E-04	10	03_301	1.80E-04	4
03_255	3.49E-03	11	03_279	1.20E-03	6	03_302	4.86E-04	10
03_256	6.62E-03	5	03_280	5.55E-04	1	03_303	1.30E-04	4
03_257	3.95E-03	9	03_281	2.00E-03	1	04_0335	1.10E-02	21
03_258	3.14E-03	10	03_282	1.16E-03	7	04_0336	5.63E-03	17
03_259	3.99E-03	6	03_283	4.48E-04	3	04_0337	2.49E-03	3
03_260	3.48E-03	12	03_284	7.78E-04	3	04_0338	2.95E-03	20
03_261	5.41E-03	7	03_285	2.87E-04	2	04_0339	2.02E-03	8
03_262	3.10E-03	5	03_286	5.88E-04	5	04_0340	2.93E-03	12
03_263	4.80E-03	15	03_287	5.85E-04	7	04_0341	1.42E-02	10
03_264	2.28E-03	12	03_288	5.20E-04	4	04_0342	1.19E-02	17
03_265	5.09E-03	15	03_289	1.23E-04	3	04_0343	9.00E-03	19

Table S1 continued.

CAT ID_Photo ID	SA m^2	Scratches n	CAT ID_Photo ID	SA m^2	Scratches n	CAT ID_Photo ID	SA m^2	Scratches n
04_0344	1.29E-02	21	04_0370	1.12E-04	6	05_0395	1.24E-03	6
04_0345	4.33E-03	7	04_0371	9.76E-03	11	05_0396	2.03E-03	13
04_0346	5.92E-03	11	04_0372	9.28E-03	4	05_0397	5.12E-03	11
04_0347	4.74E-03	3	05_0375	8.29E-03	14	05_0398	5.88E-03	13
04_0348	1.94E-03	5	05_0376	4.64E-03	2	05_0399	5.36E-03	13
04_0351	5.89E-03	6	05_0377	1.53E-03	6	05_0400	2.47E-03	4
04_0352	7.66E-03	12	05_0378	1.61E-03	8	05_0401	2.69E-03	9
04_0353	7.49E-03	9	05_0379	4.38E-03	16	05_0402	4.14E-03	8
04_0354	1.68E-02	16	05_0380	1.61E-02	19	05_0403	3.65E-03	11
04_0355	1.22E-03	7	05_0381	9.54E-03	14	05_0404	3.81E-03	11
04_0356	2.65E-03	7	05_0382	7.69E-03	15	05_0405	1.88E-03	8
04_0357	1.10E-03	2	05_0383	1.46E-02	16	05_0406	3.06E-03	15
04_0359	1.63E-03	7	05_0384	1.01E-03	3	05_0407	2.05E-03	9
04_0360	1.18E-03	2	05_0385	4.67E-03	15	05_0408	3.32E-03	17
04_0361	3.48E-03	8	05_0386	2.37E-03	18	05_0409	3.70E-03	17
04_0362	3.82E-03	10	05_0387	5.39E-03	16	05_0410	2.62E-03	7
04_0363	1.93E-03	11	05_0388	1.84E-03	10	05_0411	2.95E-03	15
04_0364	3.87E-03	12	05_0389	5.46E-03	21	05_0412	3.33E-03	17
04_0365	2.87E-03	4	05_0390	4.13E-03	13	05_0413	5.52E-03	16
04_0366	5.96E-04	5	05_0391	7.57E-04	5	05_0414	1.18E-03	7
04_0367	1.02E-03	15	05_0392	1.35E-02	20	05_0415	6.49E-03	14
04_0368	1.63E-03	22	05_0393	2.18E-03	15	05_0416	5.30E-04	4
04_0369	1.44E-03	14	05_0394	4.02E-03	16	05_0417	1.46E-03	3

Table S1 continued.

CAT ID_Photo ID	SA m^2	Scratches n	CAT ID_Photo ID	SA m^2	Scratches n	CAT ID_Photo ID	SA m^2	Scratches n
06_0425	8.76E-05	3	06_0453	1.00E-03	1	06_0476	9.13E-04	30
06_0426	7.57E-03	5	06_0454	1.41E-02	6	06_0478	8.72E-05	1
06_0427	1.06E-02	17	06_0455	1.38E-03	2	06_0479	1.09E-04	7
06_0428	9.83E-03	34	06_0456	6.63E-03	7	06_0481	1.29E-04	4
06_0429	1.27E-02	36	06_0457	5.99E-04	5	06_0482	9.99E-04	9
06_0430	1.96E-02	45	06_0458	9.47E-04	3	06_0485	4.32E-04	3
06_0431	1.57E-03	7	06_0459	2.18E-03	2	06_0486	6.57E-04	3
06_0432	3.48E-02	39	06_0460	6.81E-03	4	06_0487	2.47E-04	1
06_0433	2.66E-03	19	06_0461	1.27E-03	2	06_0489	3.46E-03	9
06_0434	1.00E-02	41	06_0462	7.00E-04	8	06_0492	2.38E-04	13
06_0435	8.91E-03	41	06_0463	1.50E-03	8	06_0495	4.61E-04	3
06_0436	6.48E-04	4	06_0464	5.63E-04	5	06_0496	6.13E-05	5
06_0437	6.13E-03	16	06_0465	1.50E-03	8	06_0497	7.44E-05	4
06_0439	2.30E-03	17	06_0466	3.58E-04	3	06_0498	7.13E-05	4
06_0440	9.06E-03	43	06_0467	1.33E-03	3	06_0499	1.21E-03	3
06_0441	3.33E-03	24	06_0468	1.38E-03	2	06_0500	2.74E-04	1
06_0442	4.38E-03	2	06_0469	2.65E-04	1	06_0502	2.22E-04	2
06_0443	3.33E-04	3	06_0470	1.15E-04	2	07_0719	1.98E-03	6
06_0444	4.72E-03	11	06_0471	2.53E-04	10	07_0721	7.35E-03	26
06_0447	1.30E-03	5	06_0472	2.46E-04	4	07_0722	1.61E-03	9
06_0448	2.58E-03	4	06_0473	5.11E-04	13	07_0724	2.85E-03	6
06_0449	6.95E-03	9	06_0474	3.00E-04	7	07_0725	2.88E-03	7
06_0450	1.70E-02	12	06_0475	7.12E-04	8	07_0726	4.93E-03	16

Table S1 continued.

CAT ID_Photo ID	SA m^2	Scratches n	CAT ID_Photo ID	SA m^2	Scratches n	CAT ID_Photo ID	SA m^2	Scratches n
07_0727	1.73E-03	11	07_0750	3.08E-04	1	08_0942	1.98E-03	9
07_0728	1.81E-03	5	07_0751	5.54E-03	13	08_0943	3.17E-03	7
07_0729	9.89E-03	6	07_0752	1.86E-03	5	08_0944	7.48E-03	8
07_0730	1.02E-03	9	08_0920	4.02E-03	6	08_0945	1.40E-03	4
07_0731	4.22E-03	15	08_0922	1.58E-03	10	08_0946	3.51E-03	14
07_0732	1.36E-03	5	08_0923	1.21E-02	35	08_0947	3.36E-03	8
07_0733	2.02E-03	11	08_0924	5.09E-03	20	08_0948	3.96E-03	6
07_0734	2.57E-03	10	08_0925	3.53E-03	14	08_0949	5.51E-03	9
07_0735	1.99E-03	9	08_0926	2.51E-03	6	08_0950	5.39E-03	5
07_0736	3.66E-03	10	08_0927	9.82E-03	16	08_0951	4.80E-04	4
07_0737	6.92E-03	12	08_0928	1.51E-03	4	08_0952	6.83E-03	12
07_0738	2.11E-03	7	08_0929	1.85E-03	6	08_0954	7.47E-03	11
07_0739	6.99E-03	11	08_0930	9.32E-04	6	08_0955	3.26E-03	9
07_0740	4.05E-03	7	08_0932	1.96E-03	9	08_0956	2.44E-03	4
07_0741	2.59E-03	10	08_0933	2.17E-03	10	08_0957	1.03E-03	8
07_0742	4.07E-03	7	08_0934	1.21E-03	6	08_0958	1.89E-03	7
07_0743	4.90E-03	14	08_0935	1.64E-03	3	08_0959	1.14E-03	4
07_0744	3.00E-03	2	08_0936	5.55E-03	21	08_0960	5.06E-03	10
07_0745	3.04E-03	8	08_0937	7.00E-03	18	08_0962	1.05E-03	5
07_0746	1.39E-03	8	08_0938	1.89E-03	7	08_0964	6.47E-03	6
07_0747	2.76E-03	9	08_0939	1.54E-03	4	09_0109	1.42E-03	3
07_0748	2.32E-03	6	08_0940	3.69E-03	8	09_0110	1.36E-02	8
07_0749	6.24E-03	13	08_0941	8.74E-03	17	09_0111	4.27E-03	5

Table S1 continued.

CAT ID_Photo ID	SA m^2	Scratches n	CAT ID_Photo ID	SA m^2	Scratches n	CAT ID_Photo ID	SA m^2	Scratches n	CAT ID_Photo ID	SA m^2	Scratches n
09_0112	1.11E-02	11	09_0136	3.46E-04	2	10_0001	4.16E-03	3	10_0025	1.53E-03	8
09_0113	5.25E-03	7	09_0138	5.02E-04	1	10_0002	3.80E-04	3	10_0026	3.44E-03	6
09_0114	3.22E-03	8	09_0139	5.01E-04	1	10_0003	9.71E-03	8	10_0027	1.51E-03	6
09_0115	8.91E-04	2	09_0140	2.67E-03	3	10_0004	8.32E-03	15	10_0028	5.29E-04	2
09_0116	7.05E-03	4	09_0141	1.06E-03	2	10_0005	1.87E-03	3	10_0029	2.43E-03	4
09_0117	2.05E-03	4	09_0142	2.28E-03	9	10_0006	2.65E-03	4	10_0030	4.31E-03	8
09_0118	1.58E-03	4	09_0143	1.16E-03	5	10_0007	8.89E-03	11	10_0031	3.09E-03	5
09_0119	2.96E-03	7	09_0144	3.61E-03	4	10_0008	4.79E-03	8	10_0032	6.03E-04	2
09_0120	1.98E-03	3	09_0145	2.76E-03	9	10_0009	4.00E-03	11	10_0033	2.55E-03	11
09_0121	4.13E-04	5	09_0146	8.25E-04	1	10_0010	3.30E-03	6	10_0034	9.75E-04	3
09_0122	1.09E-03	4	09_0147	4.22E-03	5	10_0011	7.82E-03	5	10_0035	2.67E-03	10
09_0123	1.08E-03	2	09_0148	1.61E-03	7	10_0012	5.37E-03	5	10_0036	1.76E-04	1
09_0124	2.32E-03	8	09_0149	2.81E-04	4	10_0013	2.10E-03	8			
09_0125	8.45E-04	1	09_0150	1.83E-03	8	10_0015	6.12E-04	4			
09_0126	2.22E-03	7	09_0151	2.72E-03	5	10_0016	4.92E-03	13			
09_0128	1.89E-03	9	09_0152	5.92E-04	5	10_0017	2.18E-03	9			
09_0129	9.95E-04	3	09_0153	1.56E-03	8	10_0018	3.40E-03	10			
09_0130	1.39E-03	4	09_0154	1.27E-03	2	10_0019	5.47E-03	9			
09_0131	9.73E-04	7	09_0155	4.61E-04	4	10_0020	3.93E-03	14			
09_0132	3.48E-03	14	09_0156	5.39E-03	6	10_0021	9.29E-04	3			
09_0133	5.13E-04	4	09_0157	1.18E-04	1	10_0022	2.85E-03	6			
09_0134	1.87E-03	6	09_0158	1.46E-04	1	10_0023	2.25E-04	1			
09_0135	3.56E-04	5	09_0159	4.61E-04	1	10_0024	1.18E-03	4			

Table S2. Percussion ID, surface area and volume of sampled percussions (n=29) used in the calculation of total percussion volume.

Percussion ID	Vol (m3) m^3	SA m^2	Percussion ID	Vol (m3) m^3	SA m^2
01A	6.20E-05	9.57E-03	06B	9.00E-04	1.60E-03
01b	1.30E-05	2.21E-03	06C	3.40E-05	3.72E-03
01C	6.55E-05	5.83E-03	06D	8.00E-06	1.98E-03
01D	7.40E-05	6.78E-03	06E	3.00E-06	8.68E-04
01E	5.00E-06	1.63E-03	07A	5.12E-05	1.03E-02
01F	2.57E-04	3.18E-02	07B	6.00E-06	1.76E-03
2A	5.00E-06	2.19E-03	07C	2.60E-05	9.05E-03
2B	2.22E-05	5.88E-03	07D	7.20E-05	5.17E-03
03A	2.72E-04	1.97E-02	07E	2.80E-05	4.76E-03
03B	1.47E-06	1.96E-04	08A	9.00E-06	2.52E-04
04A	2.00E-06	3.76E-04	9A	2.30E-05	2.84E-03
04B	2.00E-06	4.80E-04	10A	1.30E-05	2.92E-03
04C	1.33E-06	1.21E-03	10B	3.00E-06	7.28E-04
04D	4.60E-05	4.36E-03	10C	2.00E-06	7.81E-04
06A	1.00E-05	1.41E-03			

Chapter 5: A comparison of Structure from Motion Photogrammetry and the Traversing Micro Erosion Meter for measuring erosion on rock shore platforms.

Cullen, N.D., Verma, A.K. and Bourke, M.C., 2018. A comparison of structure from motion photogrammetry and the traversing micro-erosion meter for measuring erosion on shore platforms. *Earth Surface Dynamics*, *6*(4), pp.1023-1039.

Abstract

For decades researchers have used the Micro Erosion Meter and it successor the Traversing Micro Erosion Meter to measure microscale rates of vertical erosion (downwearing) on shore platforms. Difficulties with 'upscaling' of microscale field data in order to explain long-term platform evolution have led to calls to introduce other methods which allow measurement of platform erosion at different scales. Structure from Motion Photogrammetry is fast emerging as a reliable, cost-effective tool for geomorphic change detection, providing a valuable means for detecting micro to meso-scale geomorphic change over different terrain types. Here we present the results of an experiment where we test the efficacy of Structure from Motion Photogrammetry for measuring change on shore platforms due to different erosion processes (sweeping abrasion, scratching and percussion). Key to this approach is the development of the Coordinate Reference System used to reference and scale the models, and which can be easily deployed in the field. Experiments were carried out on three simulated platform surfaces with low to high relative rugosity to assess the influence of surface roughness. We find that a Structure from Motion Photogrammetry can be used to reliably detect micro (sub-mm) and meso (cm) scale erosion on shore platforms with a low Rugosity Index. As topographic complexity increases, the scale of detection is reduced. We also provide a detailed comparison of the two methods across a range of categories including cost, data collection, analysis and output. We find that Structure from Motion offers several advantages over the

Micro Erosion Meter, most notably the ability to detect and measure erosion of shore platforms at different scales.

Keywords

Shore platforms, Structure from Motion Photogrammetry, Traversing/Micro Erosion Metre, erosion.

Author contributions

N.D.C. prepared and wrote the main body of the manuscript with discussion and contributions from A.K.V. and M.C.B. N.D.C. designed the experiment with input from A.K.V. and M.C.B. A.K.V. designed the original coordinate reference system, and N.D.C designed the field adapted version with input from A.K.V and M.C.B. N.D.C and A.K.V carried out the experiments. A.K.V. processed images and generated the digital elevation models. N.D.C. carried out data analysis. A.K.V. and M.C.B reviewed and edited the final manuscript.

5.1 Introduction

There are numerous methods employed for measuring natural rates of change on rock surfaces. For decades researchers were restricted to direct measurement of change relative to a datum, however this method has been largely superseded by techniques which fall into two general categories: contact methods which utilise erosion meters, and non-contact methods such as Terrestrial Laser Scanning (TLS) and Structure from Motion (SfM) Photogrammetry (Moses et al., 2014). On shore platforms, the Micro Erosion Meter (MEM) and its successor the Transverse Micro Erosion Meter (TMEM) are the most frequently applied instruments for quantifying micro-scale erosion. However, SfM Photogrammetry is fast emerging as a valuable tool for detecting and quantifying geomorphic change across a range of scales and environments and represents a potential alternative to the MEM and TMEM for measuring erosion on shore platforms if a suitable level of resolution, accuracy and repeatability can be achieved. There is a large body of literature focused on each of these methods (e.g. Hanna, 1966, Trudgill, 1975, Trudgill et al., 1981, Stephenson and Kirk, 2001, Snavely, 2006., Trenhaile, 2006, Stephenson and Finlayson, 2009, Stephenson et al., 2010, Westoby et al., 2012, Gómez-Gutiérrez et al., 2014, Kaiser et al., 2014, Carrivick et al., 2016, Smith et al., 2016). A brief overview of the two methods is given below.

5.1.1 The Micro Erosion Meter and the Traversing Micro Erosion Meter

The MEM was developed and described by Hanna (1966) and High and Hanna (1970) as a tool for measuring relatively slow lowering rates of bedrock surfaces. Since its inception, the MEM and its modified successor, the TMEM (Trudgill et al., 1981) (hereafter T/MEM) have been used by numerous researchers to measure rates of surface lowering on shore platforms of varying lithologies. The spatial and temporal variability of measured erosion rates for shore platforms have allowed a more detailed understanding of processes operating on shore

platform, contributing to the ongoing debate on the origin of shore platforms and the relative contributions of marine, biological and subaerial processes which drive their evolution (See Stephenson and Finlayson (2009), for a more detailed review of the contribution of the T/MEM to rock coast research). The popularity of the T/MEM stems from the ability to detect sub-mm changes over very short time scales (hours) as is the case with platform swelling and timescales comparative with the duration of many research projects (1-3 years), which are also considered representative of longer-term (decadal) measurements (Stephenson et al., 2010). Add to this, the often cited low cost of construction and portability of the instrument and its popularity among rock coast researchers is easily understood.

Moses et al. (2014) outlined some limitations associated with the T/MEM that had been identified by previous research (e.g. Spate et al., 1985, Ellis, 1986, Andrews and Williams, 2000, Trenhaile, 2003, Foote et al., 2006, Swantesson et al., 2006). Authors studying erosion on (relatively soft) chalk platforms noted that the probe might cause erosion of the platform surface. This 'probe erosion' was also noted early on by Spate (1985). However, this does not constitute a problem where erosion rates are rapid (Foote et al., 2006; Swantesson et al., 2006). In addition, Moses et al., (2014) also pointed to previous research which showed that where rapid rates of erosion occur, this may result in the loosening or dislodgement of the bolts on which the T/MEM is placed on annual (Ellis, 1986; Andrews, 2000), or decadal timescales (Stephenson and Kirk, 1996). Trenhaile (2003) noted that although the T/MEM records small amounts of platform downwearing, it cannot record wave quarrying of larger blocks or loss of rock fragments due to frost riving.

Additional significant limitations have also been identified. For example, the location of a T/MEM measurement station is limited to surfaces with low topographic complexity. This is an issue for shore platforms with highly variable meso and macro scale roughness and which only broadly conform to the Sunamura's (1992) traditional Type A and Type B classification. Excluding these more complex platform morphologies significantly limits our ability to quantify

rates and identify processes and styles of shore platform erosion across the complete spectrum of platform morphologies. Second, while decades of measuring micro-scale erosion using the T/MEM have provided valuable insights into rates and processes of downwearing on shore platforms, there are difficulties associated with 'up-scaling' these field data to explain meso and macro-scale landform development (Warke and McKinley, 2011). Stephenson and Naylor (2011b) noted a tendency towards micro and macro scale studies of shore platform erosion. A recent study that reviewed 95 publications on shore platforms (Cullen and Bourke, 2018) also highlighted this concentration of micro and macro scale studies.

In comparison, meso-scale processes have received less attention, although research at this scale has increased significantly in the last two decades (Cullen and Bourke, 2018). Indeed, Stephenson et al. (2010) advocated the introduction of new techniques which capture the full range of scales of erosion on shore platforms. SfM Photogrammetry is one such technique that has this potential.

5.1.2 Structure from Motion Photogrammetry

Significant developments in digital photogrammetry techniques over the last decade have revolutionised the collection of 3D topographic data in the geosciences. Traditional photogrammetry requires a knowledge of the 3D location and orientation of the camera and accurate 3D information of control points in the scene of interest. While methods which allow the accurate calibration of non-metric cameras and reliable automation of the photogrammetric process have enhanced the use of photogrammetry in the geosciences (e.g. Chandler, 1999, Chandler et al., 2002, Carbonneau et al., 2004), it still requires expert understanding and practice (Carrivick et al., 2016). In the last decade, there have been significant workflow advancements which have dramatically reduced the expertise required.

Structure from Motion (SfM) photogrammetry uses a standard camera for collecting image data of a three-dimensional (3D) landform.

Multiple overlapping images are taken from different spatial positions and used to reconstruct the 3D geometry of the target. Unlike traditional photogrammetry, the SfM workflow does not require prior knowledge of the 3D location, the camera orientation or 3D information on control points before reconstruction of scene geometry. Rather, Scale Invariant Feature Detection (SIFT) (Lowe, 2004) is used to match points between images, and a least square bundle adjustment algorithm is used to align images and produce a 'sparse' point cloud representing the most prominent features in the images. A further development utilises Multi-View Stereo (SfM-MVS) algorithms (e.g. Furukawa et al., 2010) to intensify the sparse cloud and merge the resulting 3D point cloud into a single dense point-based model. This can then be used to generate a high-resolution ortho-photo, mesh or Digital Elevation Model (DEM). Successive point clouds and DEMs of the same location or feature can be analysed utilising widely available GIS software (e.g. ESRI ArcGIS desktop or QGIS) and other programs (e.g. CloudCompare) used for geomorphic change detection to quantify erosion and deposition. A large amount of literature has been published on SfM, and the reader is referred to Walkden and Hall (2005), Westoby et al. (2012), (Fonstad et al., 2013), Thoeni et al. (2014), Micheletti et al. (2015a), Micheletti et al. (2015b), Smith et al. (2016), Carrivick et al. (2016), Özyeşil et al. (2017) and Verma and Bourke (2018) for more detailed discussions of SfM techniques and workflows.

The SfM-MVS workflow has been widely applied in the geosciences at varying scales of resolution from small scale (mm - cm's) studies of soil erosion to morphodynamic studies of beaches, coastal cliffs and braided rivers (e.g. Lim et al., 2010, Javernick et al., 2014, Kaiser et al., 2014, Brunier et al., 2016a, Brunier et al., 2016b, Balaguer-Puig et al., 2017). SfM-MVS offers several advantages over traditional surveying techniques, specifically its relatively low cost and portability of required equipment, i.e. a camera, compared to that of TLS. In addition,

the availability of free and relatively low cost commercial software, a semi-automated workflow and the decreasing cost of high-end desktop computers have resulted in the increasing application of this method in geomorphological research. While SfM MVS offer significant advantages at a range of scales, it it worth noting that the scale of some processes operating on shore platforms, for example, platform swelling, operate at resolution currently not obtainable using SfM MVS, and other tried and tested approaches (i.e. the T/MEM) remain the most suitable method of measurement .

It is worth noting that the accuracy and resolution of SfM-MVS derived DEMs relies heavily on the quality of the images used and the accuracy of the coordinate reference system. For work on shore platforms, the accuracy of the DEM is limited by the accuracy of the Ground Control Points (GCPs) used. These are often determined using a Differential GPS (dGPS) or total stations which have reported accuracies of centimetres and millimetres respectively. However, a number of rock breakdown processes, such as granular disintegration (Viles, 2001) and features, such as weathering pits (Viles, 2001, Bourke et al., 2007, Thornbush, 2012) occur at cm to sub-mm scale.

Our work has three foci: First, to test the SfM-MVS for measuring micro-scale erosion on shore platforms. Second to determine the potential of SfM-MVS for meso-scale geomorphic change detection. Third, to provide a robust assessment and comparison of the two methods (T/MEM and SfM-MVS) for measuring erosion on shore platforms. Key to our approach is to adapt the local coordinate reference system (CRS), and SfM-MVS workflow developed by Verma and Bourke (2018). Their system was developed to generate sub-mm scale DEMs of rock surfaces (<10 m^2) in difficult to access terrains (e.g., cliffs and steep-sided impact crater walls). Their method can produce high resolution (sub-mm) DEMs with sub-mm accuracy. We advance this work through the design and manufacture of a field-hardy Coordinate Reference

System (CRS) which can be quickly deployed, repeatedly at the same site. Our approach will enable the application of SfM-MVS for geomorphic change detection on shore platforms at both the micro and meso scale.

In this paper, we present the results of a series of experiments on simulated platform surfaces using our newly developed CRS.

5.2 Methods

5.2.1 A manufactured Coordinate Reference System for SfM-MVS

We have adapted the local coordinate reference system of Verma and Bourke (2018) which utilises a precisely measured equilateral triangle with a coded marker (downloaded from Agisoft Photoscan) attached at each vertex (Figure 1a and b). The x, y and z coordinates of each coded marker are calculated using trigonometry and serve as the GCPs for generating the DEMs in the SfM-MVS workflow. When used for a small surface area (≤ 6.76 m^2), this method has been proved to produce high resolution (0.5 mm per pixel) DEMs with sub-mm accuracy (Verma and Bourke 2018).

We mounted the coded markers onto a specifically designed stainless-steel platform (Fig. a and b) based on the design of Verma and Bourke (2018). The platform consists of a 15 cm equilateral triangle with three square steel plates (4 cm x 4 cm x 0.5 cm) and a specially machined leg. Each plate is engineered so that the centre of a plate is fixed precisely (± 0.01mm) on one vertex of the triangular base. The centre of each plate is also permanently

marked during manufacture to aid the application of coded markers. The base of the leg is machined to fit a stainless-steel square head bolt to a depth of 1.5 cm and is fixed at the centre of gravity on the underside of the triangular base plate.

In the field, the square headed bolt is fixed to the platform by drilling a hole and fixing the bolt with marine grade epoxy resin, using a digital inclinometer to make sure the bolt head is level. This is similar to the approach used to install T/MEM stations. When mounted onto the bolt, this design secures the base plate with the coordinate system in place with a high degree of relocation precision (see section 5.3.2). This permits repeated measurements and the georeferencing of DEMs for high resolution change detection of field sites.

5.2.2 The experiments

The experiments were designed to capture different scales of erosion from the granular scale (sub-mm) abrasion of the platform surface to the removal of rock fragments (mm -cm). The accuracy of the SfM-MVS generated DEMs used to calculate DEMs of Difference (DoDs) for geomorphic change detection were assessed by means of horizontal and vertical checkpoints. We also investigated the influence of surface roughness on the accuracy of DEMs and resultant DoDs.

The experiment was set up outdoors on a level table (1.2 m x 0.6 m). Two scaled coded markers (0.25 m) and a series of 2.5 cm x 2.5 cm and 1 cm x 1 cm checkboard pattern, non-coded markers and eight, evenly spaced wooden blocks of known dimensions were fixed onto the table surface (Figure 1 C). These were used to calculate the horizontal and vertical error of the DEMs (as recommended by Verma and Bourke 2018). Four simulated platform surface blocks were constructed using moulds and gypsum plaster. Stainless steel, square-headed bolts for mounting the CRS, as described above, were installed on each block. A digital inclinometer (Examobile Bubble Level for iPhone) was used to ensure the surface of the bolt

was level. The surface of the experimental blocks was constructed to represent a range of micro (<mm - mm) to meso scale >mm - cm) roughness that is observed in the field. These include low (B1), medium (B2) and high (B2) relative surface roughness (Figure 1 D-F). All blocks were sprayed with matte grey paint to allow easy identification of 'erosion' areas and provide additional visual validation of the models. A set of three 1 cm x 1 cm checkboard non-coded markers were fixed to each experimental block to serve as additional checkpoints for horizontal error. One block (B-con) was used as a control. The remaining three blocks (B1, B2 and B3) were used to carry out the experiment. Each block was placed at the centre of the table when acquiring images.

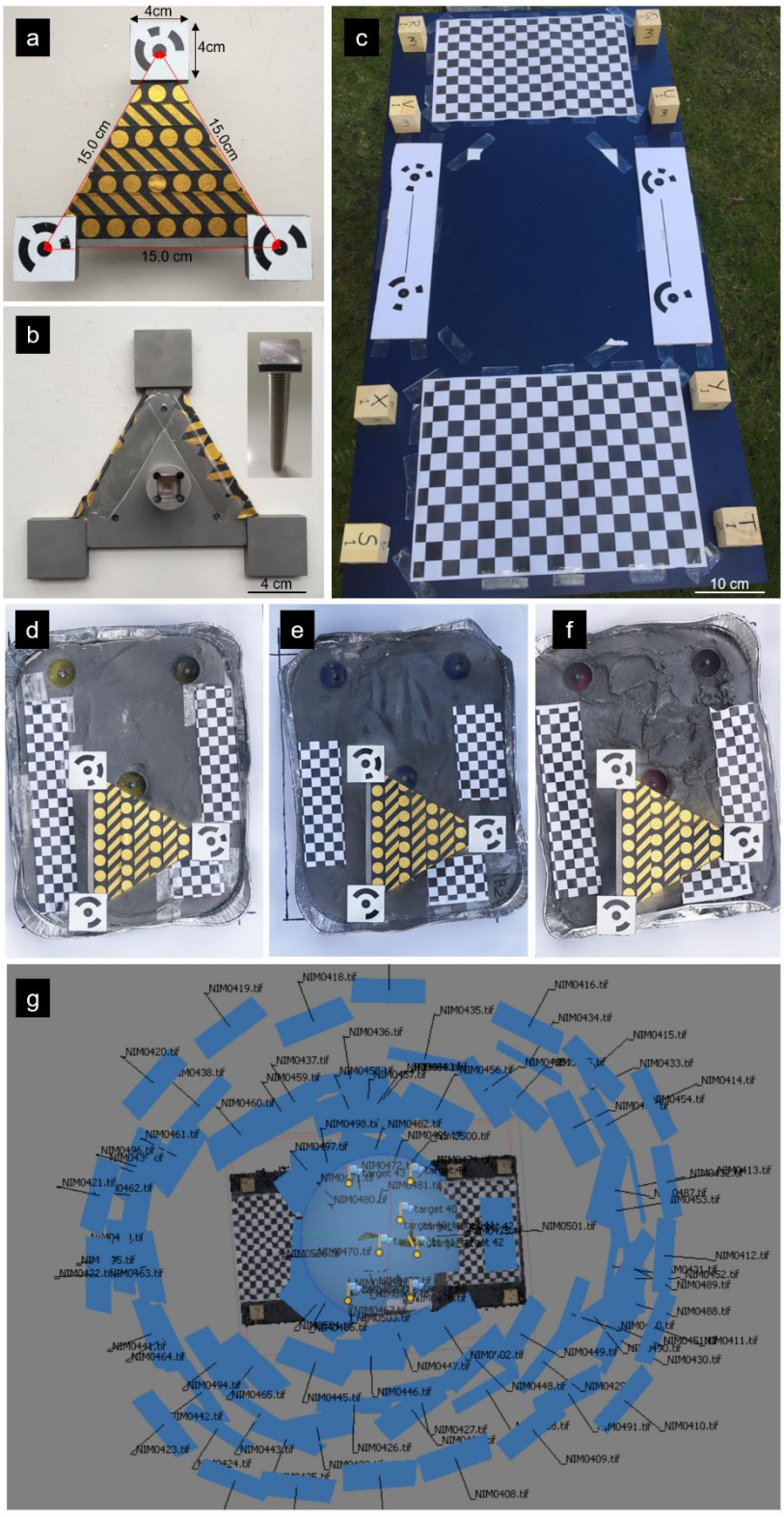

Figure 1. The experimental setup. a) The CRS top view with scale shown and b) underside with the square headed bolt (inset) c) The experimental platform with markers and wooden

blocks used to calculate the horizontal and vertical error. d, e, f) The simulated platform and g) example of the camera positions for image acquisition.

5.2.3 Data collection

In order to replicate field conditions as closely as possible, all images of the experimental blocks were acquired outdoors during a single day. The CRS was placed on the pre-installed square head bolt (Stig Fasteners , SQHM8x75) , and orientation was noted. We used a Nikon D5500 with a variable zoom lens set up at 24 mm focal length, on a tripod to reduce effects of handshake. Approximately 100 images of each block were obtained. This number of images was required to capture the full extent of the table with the non-coded markers and the wooden blocks used for the error analysis. We expect that 40-50 images would be sufficient to generate a high-resolution DEM for a smaller area (e.g. <0.5 m^2) in the field. In this study, ~70 images were acquired at a distance of ~1m from the experimental blocks with the camera mounted on a tripod to reduce the effect of handshake on image quality, and then a series (25-30 images) of close-range shots at <0.5 m (Figure 1). All three experimental blocks and the control block were imaged on the table prior to simulating erosion on the blocks.

Recent work has demonstrated the potential efficacy of smaller-scale physical erosion processes (e.g. abrasion, scratching, perussion impact) on high energy Atlantic shore platforms (Cullen and Bourke, 2018). However accurate quantification of these features has not been possible. We, therefore, tested simulations of three known types of erosion: 1. Sweeping abrasion was simulated by gently abrading the surface of all three blocks with medium grit sandpaper to variable depths up to approximately 1 mm. 2. Scratches were simulated using a screwdriver 3. Impact percussion marks were simulated on one block using a hammer and chisel.

The CRS was removed and replaced between each stage of data collection, as would be practical for carrying out repeat surveys in the field. Images of the blocks were taken following simulated erosion as outlined above.

5.2.4 Repeatability

The utility of this approach for microscale change detection using the CRS developed for this study is contingent on the exact replacement of the CRS during successive surveys in the field. To test the repeatability of this approach, we used a control block to acquire images for DEM generation using the data collection and processing procedure outlined above. At the end of the experiment, the CRS was replaced and the second series of images were acquired for DEM generation for comparison. DEM accuracy and error propagation were calculated as described below.

5.2.5 Data processing

5.2.5.1 Digital Elevation Models

All the images were acquired in the raw format during the experiment. RAW images were converted to 14-bit uncompressed tiff format with AdobeRGB colour space in Adobe Lightroom. We used Agisoft Photoscan (version 1.4.1). Image quality (Q) was assessed using the Estimate Image Quality tool in AgiSoft and images with Q values < 0.5 were removed. The CRS was used to scale and georeference the model. Baseline DEMs and orthophoto mosaics for each block were generated and exported at the highest, common pixel resolution (0.3mm/pixel) and common pixel coordinates.

5.2.5.2 DEMs of Difference

DEMs were exported in ArcMap, and a polygon shapefile was drawn over the area of interest for each block. The area of interest, i.e. the erosion area of the simulated platform surface, was extracted for analysis using the Extract by Mask' tool in Spatial Analyst tools. DoDs were generated using the Raster was Math tool (minus) in ArcMap (version 10.5) using Eq. (1),

$$B1\ DoD_1 = B1\ DEM_1 - B1\ DEM_0 \quad (1)$$

where the subscript refers to the experimental stage.

5.2.5.3 Rugosity

To permit evaluation of the impact of different degrees of surface roughness on the accuracy and reliability of our generated DEMs, a rugosity index for each block was calculated in ArcMap using the standard Surface Area ratio method (Risk, 1972, Dahl, 1973) where,

$$Rugosity = \frac{Contoured\ area}{Planar\ area} \quad (2)$$

A rugosity index (RI) of 1 indicates a planar surface while increasingly higher values indicate increasingly 'rougher' surfaces. The contoured area for each block was calculated using the relevant baseline DEM. A TIN surface was generated using the Raster to TIN tool in ArcMap. The contoured surface area for the specified region was calculated using the Polygon Volume tool in ArcMap. The planar surface area of the same region was derived using the calculate

geometry tool assuming negligible change in slope over the specified area. The RI was calculated using Eq. (2).

5.2.5.4 DEM accuracy and error propagation

The coded and non-coded markers fixed to the table were used as checkpoints to determine the horizontal (XY) error of the DEMs produced using the CRS developed by Verma and Bourke (2018). For each DEM, the model and its respective orthophoto were imported into ArcMap (version 10.5) and the distance between 30 randomly selected checkpoints and the two coded scale bars (Figure 1) were measured using the measurement tool. The horizontal error was calculated as the Root Mean Square Error (RMSE) of the difference between the measured length and known length.

To determine the vertical accuracy of the DEMs, eight wooden blocks were used as checkpoints (Figure 1). The DEMs and orthophotos were imported in ArcMap where the height of wooden blocks were measured using the Interpolate Line tool, by drawing a line across one of the sides of the wooden block and extending it to the ground surface. We ensured that the line drawn was straight. Height was estimated as the difference in mean elevation between wooden block top surface and the surrounding ground surface on each side. The actual height of wooden blocks was measured by an electronic digital Vernier Caliper. The Vernier Caliper has an accuracy of 0.03 mm and measurement repeatability of 0.01 mm. We obtained five measurements along the same side of wooden block measured in ArcMap. We used the mean of these five measurements to calculate the height of the wooden block. The actual height was subtracted from the estimated DEM height to calculate the vertical error.

The calculation of a DoD can result in propagation of error associated with the DEMs used in the computation process. As such, an error analysis is required to increase confidence in the DoD results. This is particularly important when the scale of geomorphic change being detected is of similar magnitude to uncertainties of the DEMs used in the DoD calculation.

We determined the minimum level of detection as the most suitable method of error analysis for this study as the development of shore platforms is primarily an erosional process and as such, the spatial coherence of erosion and deposition (Wheaton et al., 2010) is unsuitable as a method for error analysis in this study. Additionally, while probabilistic approaches produce reliable estimates of morphological change (e.g. Brasington et al., 2000, Brasington et al., 2003, Lane et al., 2003), small changes in elevation, such as those measured in this experiment, may be disguised as noise (Williams, 2012). The minimum Level of Detection (LoD) uses the quadratic composition of errors in the original DEMs to estimate the propagated error of the calculated DoD (Brasington et al., 2003, Lane et al., 2003, Wheaton et al., 2010, Gómez-Gutiérrez et al., 2014, Williams, 2012):

$$E_{DoD_{1-2}} = \sqrt{(E_{DEM_1}{}^2 + E_{DEM_2}{}^2)} \quad (3)$$

Where $E_{DoD_{1-2}}$ refers to the LoD calculated as the square root of the combined squared errors of the DEMs used to generate the DoD. If values of E_{DEM_1} and E_{DEM_2} are known, this method can be applied at a global or local scale where the spatial variability of the error terms are known (Lane et al., 2003). We applied Eq. (3) to determine the minimum threshold of detection for each DEM (Williams, 2012) for each stage of the experiment. Changes detected that fall within the limits of detection (+ LOD_{min} or – LOD_{min}) calculated using Eq. (1) are considered noise and interpreted as no change.

5.3 Results

5.3.1 Accuracy and error propagation

DEM generation resulted in a maximum and minimum horizontal (XY) RMSE of 0.23 mm and 0.03 mm respectively. Maximum vertical (Z) RMSE was 0.52 mm with a minimum of 0.23 mm. The minimum limit of detection was calculated at 0 ± 0.27 mm while the maximum LoD was 0 ± 0.71 mm.

Table 1. The horizontal (XY) and vertical (Z) RMSE error for the control block (B-con) and the experimental blocks B1, B2 and B3. LoD for each DoD is also shown.

DEM	**XY RMSE** (mm)	**Z RMSE** (mm)	**LoD** (0 ± mm)
B-con			
1	0.03	0.45	N/A
2	0.12	0.23	0.27
B1			
Stage 0	0.23	0.37	N/A
Stage 1	0.12	0.39	0.54
Stage 2	0.22	0.44	0.56
Stage 3	0.12	0.52	0.71
B2			
Stage 0	0.1	0.40	N/A
Stage 1	0.2	0.46	0.53
Stage 2	0.1	0.35	0.49
Stage 3	0.2	0.45	0.56
B3			
Stage 0	0.2	0.39	N/A
Stage 1	0.1	0.37	0.54
Stage 2	0.1	0.39	0.54
Stage 3	0.1	0.45	0.60

5.3.2 Repeatability

The change in vertical elevation for the control block calculated from the DoD is shown in Figure 2 below. The maximum change in elevation (- 0.29 mm) is within the LoD and is interpreted as no change.

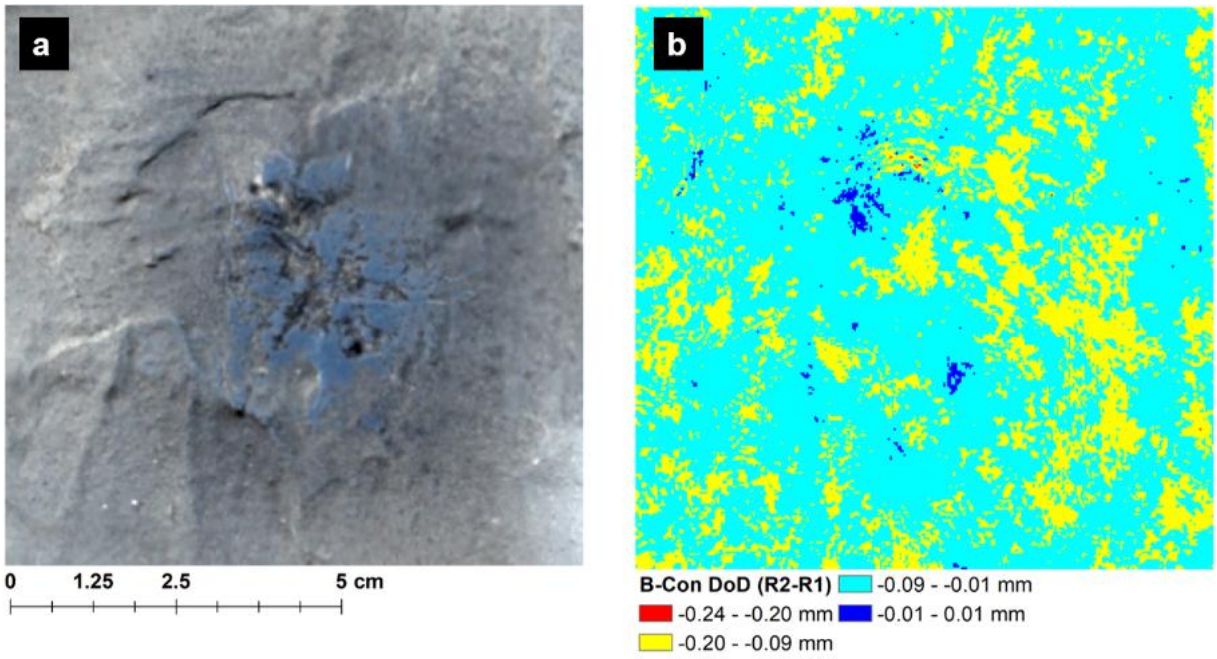

Figure 2. (a) The control block (B-Con) orthophoto and (b) DoD showing a change in surface elevation between successive DEMs. Note that detected change is within the calculated LoD (± 0.27 mm).

5.3.3 Rugosity

The RI calculated for each block is shown in Table 2. The control block (B-con) had the lowest rugosity (planar surface) while B1 had a very low RI followed by B2 and B3 in order of increasing rugosity.

Table 2. Contoured surface area (SA), planar surface area and Rugosity Index (RI) for each of the experimental blocks.

Block ID	**Contoured SA** (cm)	**Planar SA** (cm)	**R Index**
B-con	8.9	8.9	1.00
B1	9.0	8.9	1.01
B2	11.7	10.9	1.07
B3	9.9	8.2	1.21

5.3.3.1 Very low rugosity platform: B1

The results for experimental block B1 are shown in Figure 3 (a-i). The surface area of B1 used in the analysis is shown in (a) where light grey indicates the area of abrasion. For B1 Abrasion, a maximum negative surface change of 1.06 mm was detected, while an increase of 0.30 mm was observed (b) before the LoD was applied. The area of negative surface change between 0.1 mm and 1.06 mm corresponds to the actual area abraded. After thresholding at the LoD, the area of change detected is significantly lower (less than half) the area where the actual change occurred. No increase in surface elevation was detected. For B1 Scratches, the scratched surface is shown in d (black arrows). Before thresholding, the maximum negative change on the surface of B2 was 0.35 mm while an increase in surface elevation of 0.26 mm was detected. Negative changes corresponded well to the observed locations of scratches. After thresholding at the LoD, no changes were detected on the block surface (f). For B1 impact percussions, the locations where block fragments were removed are shown in G (black arrows). Maximum negative change detected, i.e. predicted the depth of percussions, was

1.49 mm, while a positive change in surface elevation of 0.30 mm was detected before thresholding (H). After thresholding, no positive change in surface elevation was detected and predicted negative change corresponded well to the actual location of percussions (i).

To summarise, for a simulated platform with a very low RI, sweeping abrasion and chips were reliably detected in the thresholded DoD. Scratch depths were less than the LoD and as such were not detected in the thresholded model.

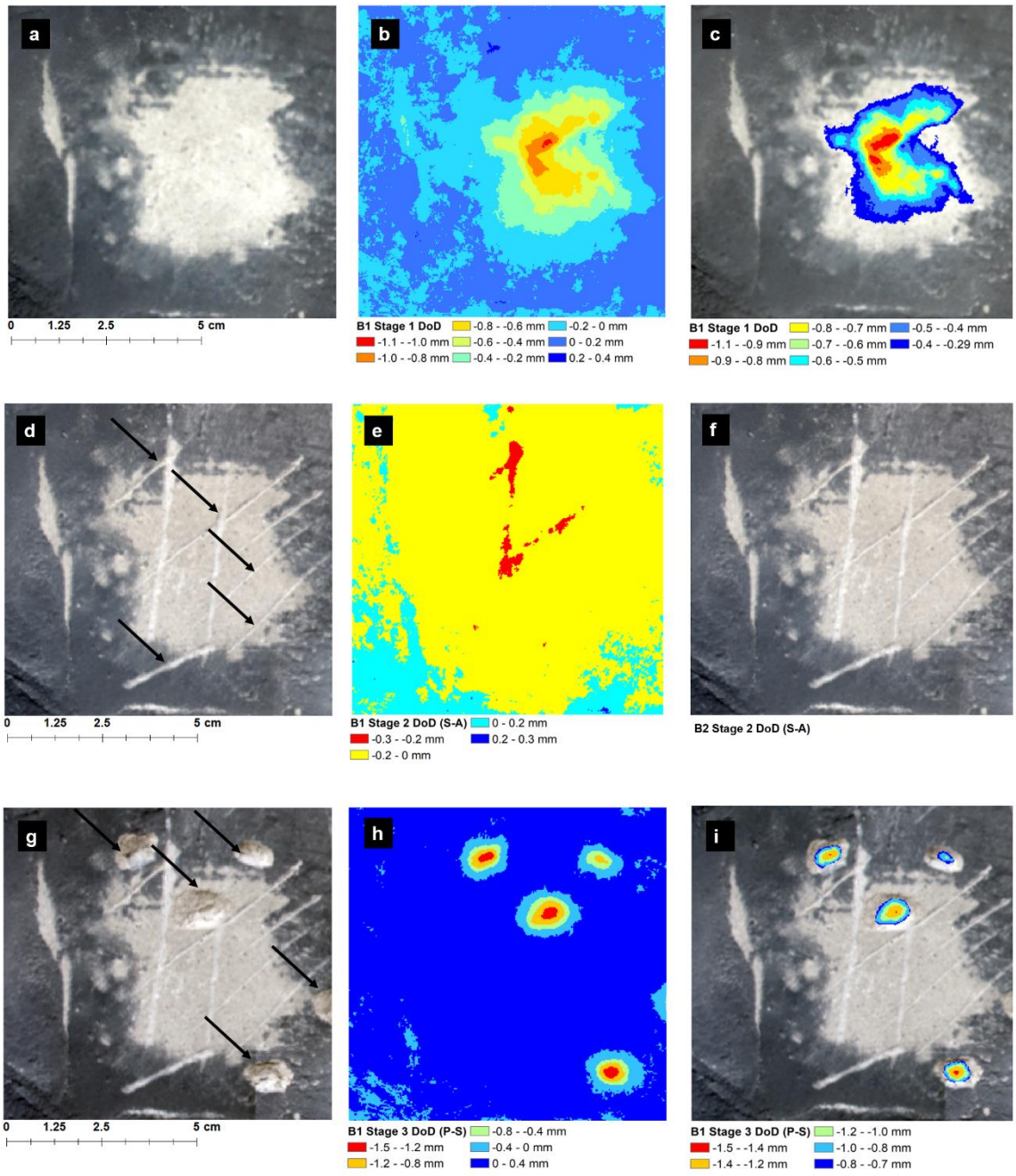

Figure 3. (a) B1 Stage 1 Orthophoto showing abraded surface of simulated platform surface (light grey). (b DoD for B1 Stage 1 before thresholding at LoD and the thresholded DoD (c. (d) B1 Stage 2 orthophoto showing location of scratches, (e) B1 Stage 2 DoD before thresholding and (f) DoD shown in E thresholded at LoD. (g) B1 Stage 3 orthophoto showing locations of percussions. (h) B1 Stage 2 DoD before thresholding at the LoD and the thresholded DoD (I).

The topographic profiles of erosion features on B1 for stages 1, 3 and 3 are shown in Figure 4. The profiles show the geometry (i.e. max depth and width) of erosion features on B1 which are similar in scale for all experimental blocks.

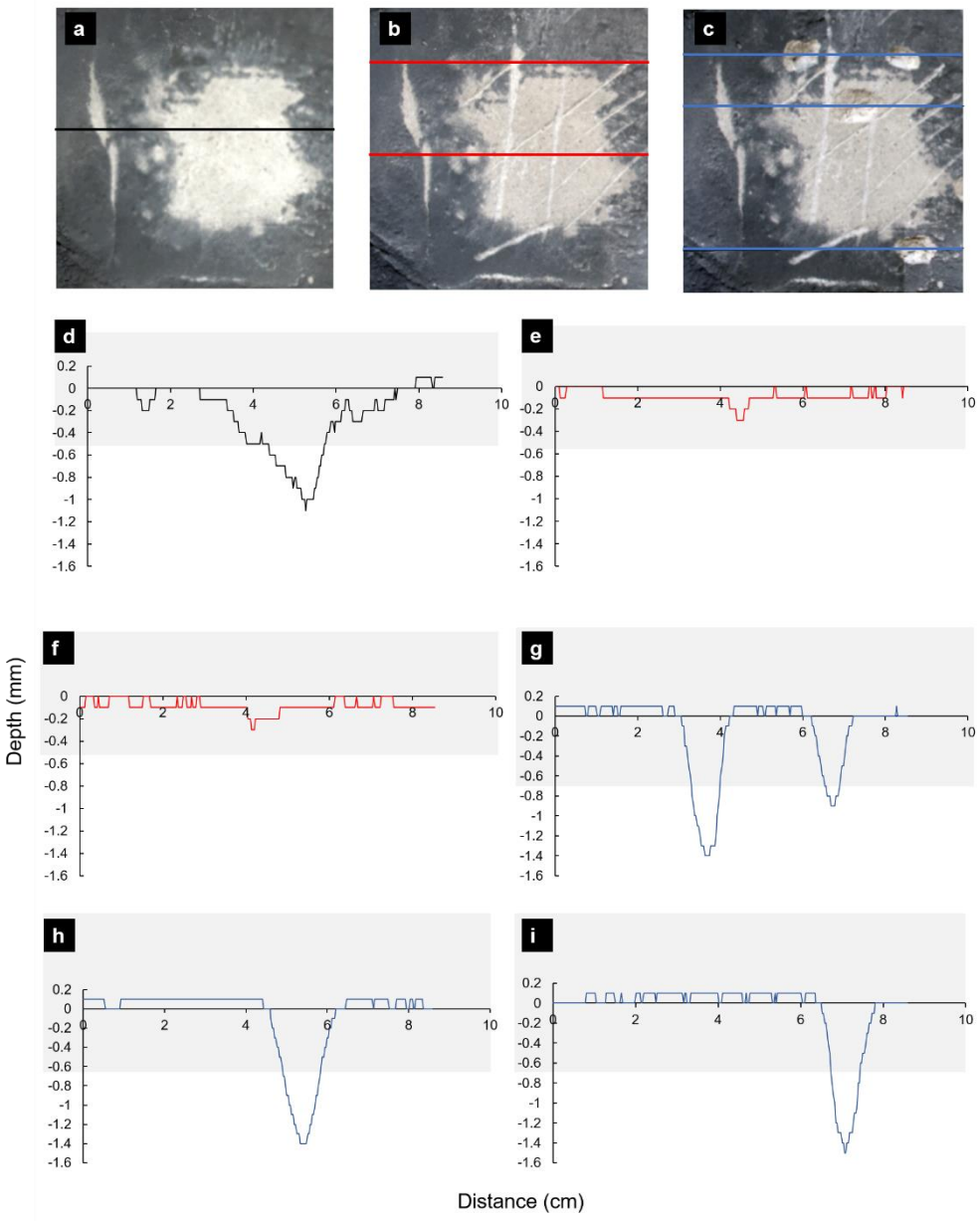

Figure 4. Location and topographic profiles of 'erosion' features on the simulated platform surface of B1 for (a) stage 1 (profile shown in d), (b) stage 2 (e and f, top and bottom respectively shown in b) and (c) stage 3 (g, h and i, top, middle and bottom profiles respectively shown in b). Grey shaded areas in d-i show the LoD.

5.3.3.2 Moderate rugosity platform (B2)

The results for experimental block B2 are shown in Figure 5 (a-i). The abraded surface area is indicated by lighter tone areas in Figure 5a. While this abrasion is visible in the DOD (Figure 5b), a significant component of the detected change occurred where no change was expected. This corresponds to 'shadow zones' associated with topographic highs. This result was not affected by thresholding at the LoD (Fig. 5c).

Scratches are evident in Figure 5d. Furthermore, the location of negative change corresponds well to the location of scratches (Fig. 5e). However, similar to B1, a small area of change is detected around the deepest scratch where none is expected (Fig. 5f). The impact percussion features are shown in (Fig. 5g). The maximum negative change in the surface elevation detected (i.e. the depth of percussions), was 3.35 mm, while the maximum positive change was 0.57 mm (h). Following thresholding, no positive change in elevation was detected (Fig. 5i) and negative change corresponded well to the actual location of percussions.

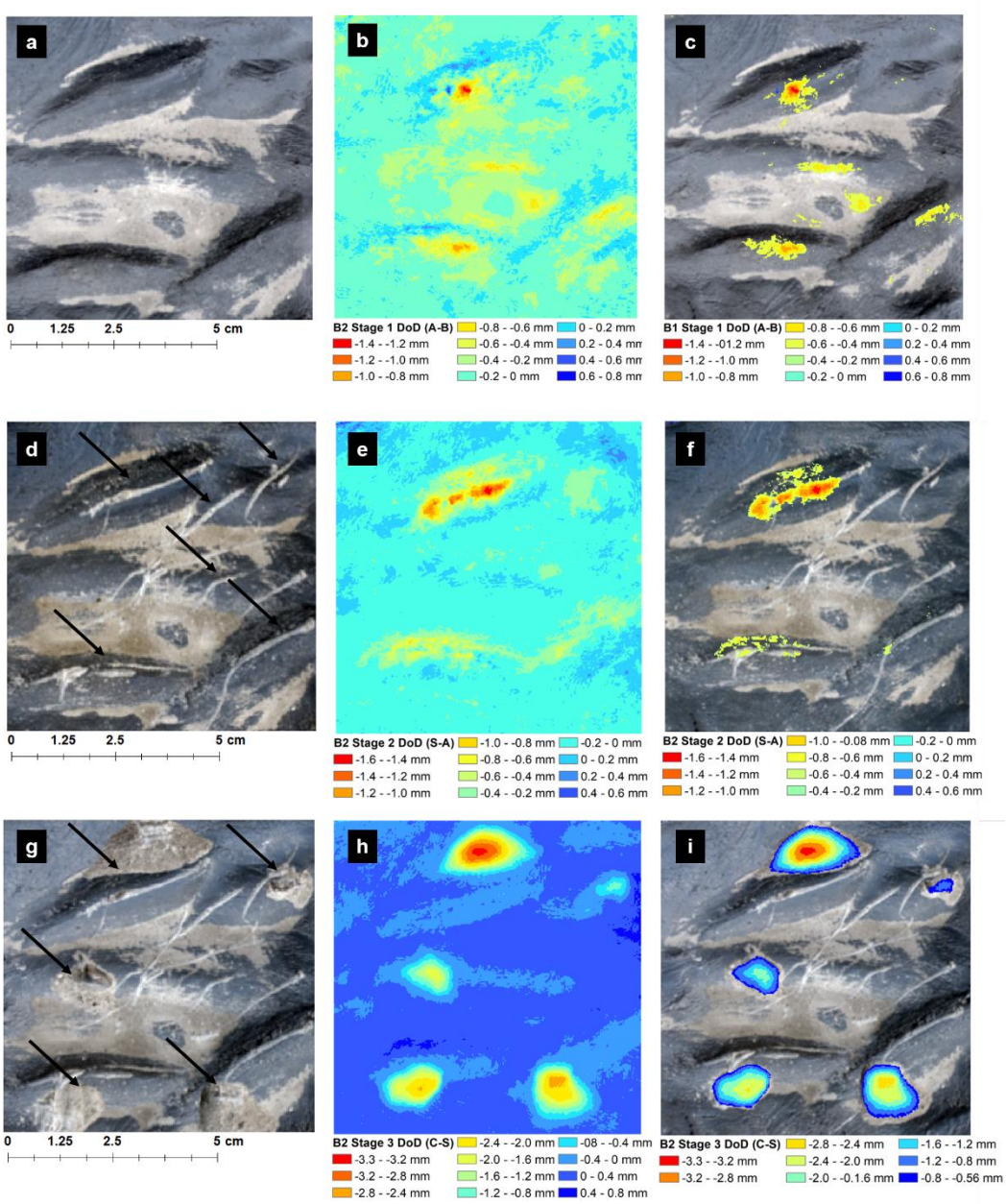

Figure 5**.** (a) B2 Stage 1 Orthophoto showing abraded area (light grey) of simulated platform surface, (b) B2 Stage 1 DoD before thresholding at LoD and the thresholded DoD (c). (d) B2 Stage 2 orthophoto showing scratched surface of B2 (black arrows). (e) B2 Stage 2 DoD before thresholding and (f) DoD shown in E thresholded at LoD. Note change detected in shadow zones in F (white arrow) where none is expected. (g) B2 Stage 3 orthophoto percussed surface. (h) DoD before thresholding at LoD and (i) DoD thresholded using calculated LoD.

To summarise, for a simulated platform with a moderate RI, only scratches and impacts were detected in the thresholded DoD.

5.3.2.3 Relatively high rugosity platform (B3)

The results for B3 are shown in Figure 6 (a-i). The light-toned areas in (a) indicate the abraded surface of the experimental block. In general, the maximum negative change detected (red and orange areas in b) correspond well to the abraded area. However, there are significant increases and decreases (>3 mm) in surface elevation where no change was expected. As above, the largest of these errors generally occurred in 'shadow zones'. Thresholding did not significantly improve the resultant DoD (i). For scratches (Fig. 6d)there was a reduction in surface elevation of 3.45 mm detected where no change was expected. As with the previous stage, these changes were observed to occur in shadow zones. Thresholding at the LoD did not improve the resultant DoD, and both increases and decreases were recorded where no change was expected (white arrows in i). The location percussions are shown in Figure 6g. Maximum negative change detected corresponded mainly to the location of percussion however negative change was recorded where none was expected (h). As before, an abnormal change occurred in shadow zones. Thresholding improved the resultant DoD (i), and the majority of negative change observed corresponded well to the location of percussions, except in some small areas (white arrows in i), associated with shadow zones. Maximum percussion depth was recorded at 5.43 mm.

To summarise, for a simulated platform with a relatively high RI, only impacts were reliably detected in the thresholded DoD. However, there were errors (larger than in B2) in the data, which are concentrated in topographic 'shadows'.

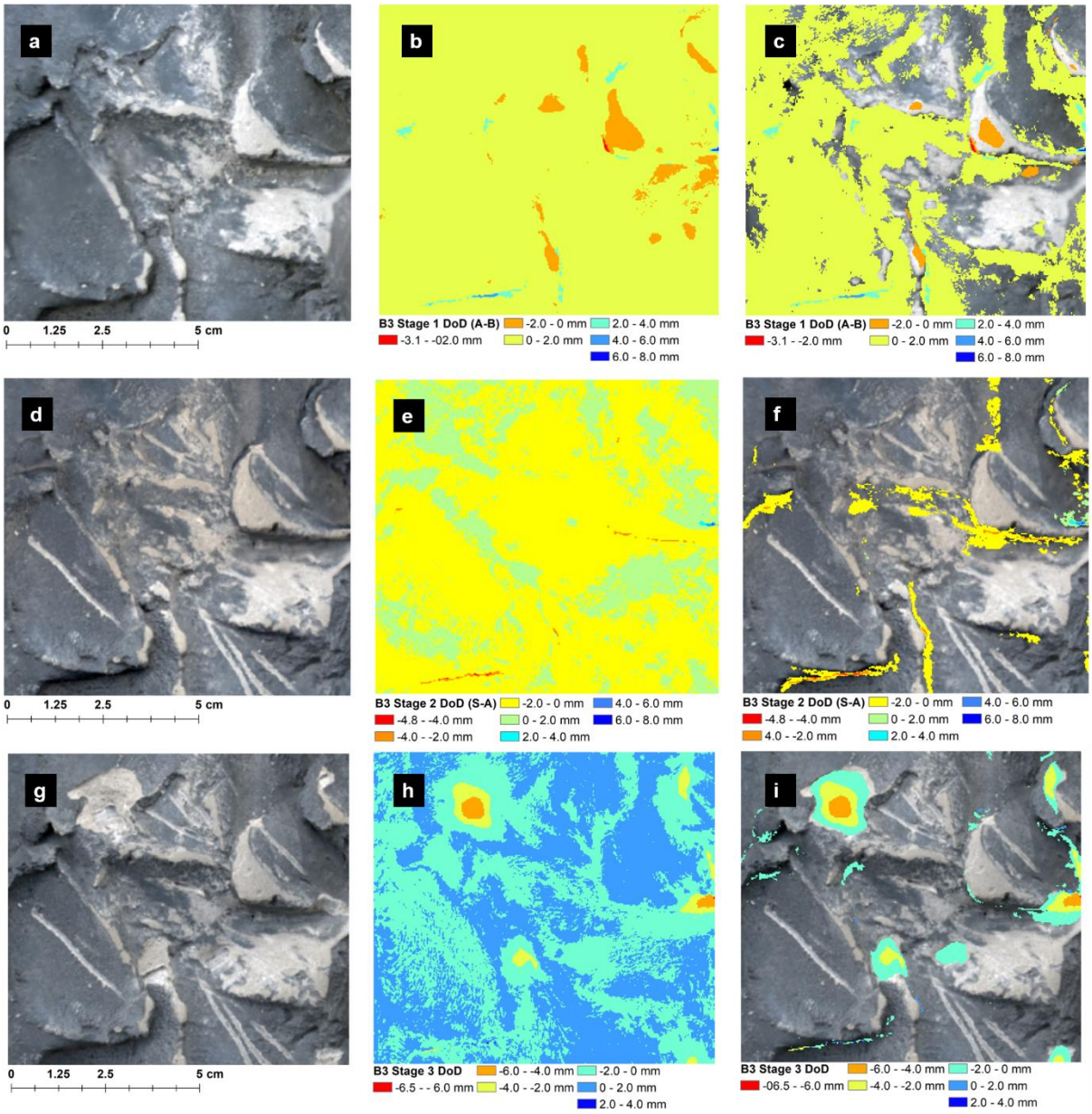

Figure 6**.** (a) B3 Stage 1 Orthophoto showing abraded surface area (light grey) of simulated platform surface. (b) DoD for B3 Stage 3 before thresholding and (c) DoD at LoD shown at 50% transparency overlain onto the orthophoto shown in A. Note significant geomorphic change detected in shadow zones (white arrows) where no change is expected. (d) B3 Stage 2 orthophoto showing scratched the surface of the simulated platform (black arrows), (e) DoD before thresholding and (f) DoD thresholded at LoD. As in C, note change higher than the LoD

detected in shadow zones (white arrows) in f where no change is expected. (g) B3 Stage 3 orthophoto showing the location of percussions (black arrows), (h) B3 Stage 3 DoD before thresholding at LoD and (i) B3 Stage 3 DoD thresholded using calculated LoD. Note shadow zones (white arrows) where DoD indicates change, but none is expected.

5.3.4 Comparison of the T/MEM and SfM-MVS for measuring erosion on shore platforms

The T/MEM has, over decades, cemented its position as a low-cost method for measuring microscale erosion on shore platforms, while SfM-MVS is fast emerging as a valuable tool in the geomorphologists toolkit for the detection and measurement of geomorphic change at a range of scales. Both approaches have advantages and limitations, and the choice for use one method over another will depend on a number of factors such as cost, the ease of data collection, quality and value of the data required to answer a specific research question.

We have compared our experience of using the T/MEM to that of the SfM-MVS (based on the CRS and workflow used in this study) as a means for detecting geomorphic change on shore platforms under the following headings. We evaluated both techniques for; ease of data acquisition (including both installation and data collection), data processing, hardware costs, software costs, model resolution, accuracy and overall ease of use. Our reported installation, data collection and data processing times refer to a single measurement station. Hardware costs for the TMEM are based on initial outlay for SDS drill, drill bits, the TMEM platform and engineers gauge. Hardware for the SfM-MVS workflow described in this study refers to initial outlay for the manufacture of CRS and cost of the camera. Basic hardware costs (e.g. computer for processing) are not included. Overall ease of use for each method is based on our experience of data acquisition in the field (installation and collection) and data processing.

An overall comparison is provided based on the above factors in addition to the value of the data obtained.

A comparison of the TMEM and the SfM-MVS approach as a means for detecting geomorphic change on shore platforms is shown in Figure 7. Both methods have clear advantages and disadvantages, and the comparison is intended to be a guide to assist researchers in choosing the most appropriate method for specific project deliverables.

5.3.3.1 Installation

To install a single T/MEM measurement station, three holes are drilled at the apex of an equilateral triangle and pins set into each hole with a marine grade epoxy resin. The time needed to install a single TMEM station varies between 20 and 80 minutes depending on operator experience and rock hardness. For the workflow used in this study, the time needed to install a single bolt to mount the CRS will take approximately one-third of the time.

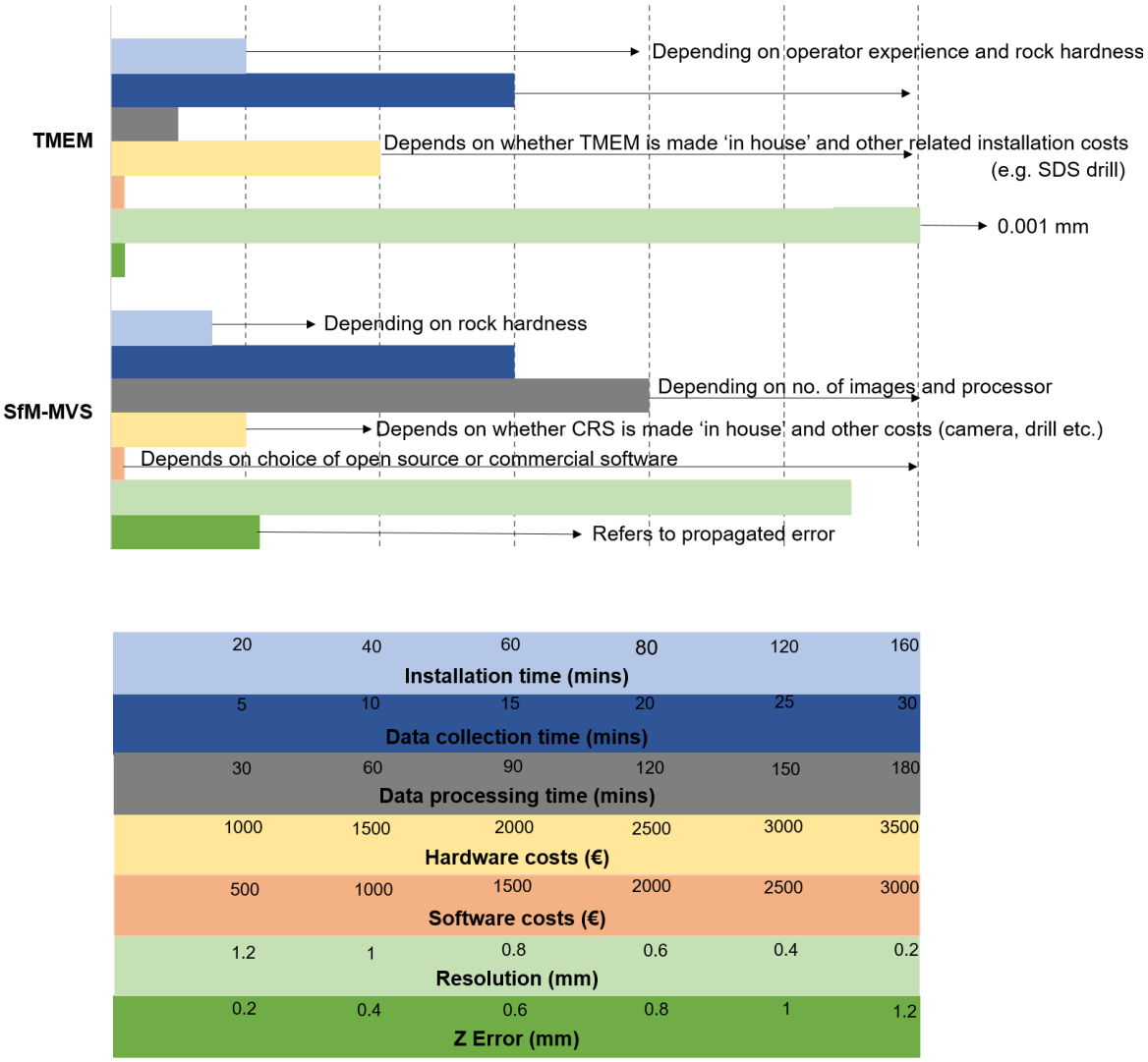

Figure 7. Comparison of TMEM and the SfM – MVS workflow presented in this study under different categories. Values showed (cost, time etc) increase from left to right apart from 'Resolution' where decreasing values from left to right indicate increasing resolution.

5.3.3.2 Data collection

In our experience, the time needed to collect data from a single station (based on 100 measurements) using a TMEM varies between 15-30 mins (grey bar in figure 6). This will depend on whether the digital gauge being used has a USB memory, which automatically stores measurements as they are taken (e.g. Stephenson, 1997), or whether measurements are recorded manually which increases the time required. In comparison, acquiring the 40-50 images as are necessary for SfM-MVS took approximately 15 minutes.

5.3.3.3 Data processing

The time required to process TMEM data will depend on the number of measurements collected and the method used to record data in the field, i.e. whether they are stored automatically (e.g. Stephenson, 1997) or manually. Automatic recording reduces the time needed to process data however manual processing can take up to 30 minutes per station (based on 100 measurements). Data processing takes significantly longer for SfM-MVS (2-3 hours per DEM) depending on a number of images and the processor used.

5.3.3.4 Hardware costs

The cost of a TMEM platform varies considerably depending on whether it is made in-house or commercially. In-house construction is considerably less (~€900 for materials and labour), while a commercial TMEM costs approximately €2000 (based on 2017 prices). The cost of the digital gauge also varies depending on the manufacturer, model, resolution, accuracy and Ingress Protection (IP) needed and range from €200-€500. Most rock types will also require an SDS drill with masonry bits which cost in the region of €600. The cost of the 316 stainless steel pins also varies depending on whether they are constructed ‘in-house’ or purchased commercially.

5.3.3.5 Software costs

Software cost for TMEM data processing is negligible while there are free open source software available for processing of images for SfM–MVS (e.g. Visual SfM). However, commercial packages such as Agisoft Photoscan can cost between €600 and €3500 depending on the licence type (e.g. Pro, Standard, Educational, Stand alone or Floating).

5.3.3.6 Resolution and Error

Depending on the digital gauge used, TMEM measurements can have a resolution of up to 0.001 mm with a reported measurement error of ± 0.005 mm (Gómez-Pujol et al., 2007). This resolution permits detection of change at a scale not currently achievable using the SfM MVS approach described here. Resolution for SfM-MVS (achieved in this study) was 0.3 mm per pixel. For some DEMs it was less than this (0.15 mm per pixel) however differencing of DEMs requires that pixel resolution be the same for both DEMs being compared. The CRS and SfM-MVS workflow employed for this study achieved maximum XY and Z RMSE errors of 0.2 mm and 0.5 mm respectively.

5.4 Discussion

The T/MEM has contributed significantly to our understanding of microscale erosion processes on shore platforms. Measurements of microscale platform erosion using a T/MEM are limited to repeated point measurements over time which provides a mean rate of surface downwearing within the measurement area for that measurement period with the dominant process(es) being inferred from the spatial and temporal variation in downwearing rates (Trenhaile, 2003). However, the method's inability to measure erosion at different scales was noted by Stephenson and Finlayson (2009) as a limitation and the authors advocated the introduction of new methods for measuring shore platform erosion at a range of scales. We have developed a CRS which can be quickly deployed by researchers in the field for detection of micro and meso-scale erosion on shore platforms using SfM-MVS Photogrammetry and a geomorphic change detection approach. The CRS described in this study permits rigorous georeferencing of DEMs derived using the SfM-MVS workflow. Although we demonstate the potential of the method on a simulated shore platform, the approach is not limited to shore platforms and has potential as a means for measuring bedrock erosion at similar scales in other environemnts (see Turowski and Cook, 2017 for examples).

We have demonstrated that SfM-MVS Photogrammetry can be used to reliably detect sub-mm changes on shore platforms where the platform surface has a low RI. This approach successfully detected 0.3 mm downwearing of the simulated platform surface of B1 caused by abrasion of the surface. While we were also able to identify shallow scratches on the surface of the experimental block, applying the LoD obscured this finding due to the shallow depth of scratches (< 0.3 mm). However, we were able to detect loss of mm-cm sized rock effectively. This demonstrates that our approach offers a method for cross scalar analysis of erosion on shore platforms, offering a much-needed means to examine relationships between micro and meso-scale processes of shore platform erosion and morphologies.

Our results indicate that as RI increases, the reliability of SfM-MVS for detection of fine scale (sub-mm) erosion is reduced due to increased topographic complexity. Despite areas of reduced elevation, i.e. erosion, aligning well with areas where the surface had been abraded, there were areas of change where clearly none was expected. Despite this, our approach successfully detected the loss of rock fragments on the simulated platform surface of B2 (higher RI) once the LoD was applied. Similarly, for B3, which had the highest RI, fine-scale erosion and scratches were not detected reliably, and while the loss of rock fragments was detected, the effect of complex topography in creating shadows zones produced abnormal change. The orthophotos were important in this regard as they provided visual validation of the models and highlighted the influence of shadow zones in introducing error into the models. The additional uncertainty introduced into the models due to the surface complexity was not accounted for using the LoD approach. This resulted in abnormal change detection associated with meso scale (> 1mm) slopes and troughs. Indeed, this is a well recognised limitation of SfM MVS approach to geomorphic change detection, and appropriate solutions (e.g. precision mapping) have been proposed. While the strong influence of surface complexity may be considered a limitation, it should be noted that the T/MEM is largely restricted to measurements of downwearing on small surface areas with low topographic complexity. As such, it does not exclude this approach as an alternative for measuring change on this type of surface.

Precision mapping (James et al., 2017) offers a potential approach to address this as there is an opportunity to increase confidence in the accuracy of point clouds derived for more complex platform morphologies. While the LoD assumes a global uniform distribution of error, precision mapping explicitly accounts for the spatially variable precision characteristic of photo-based surveys (James et al., 2017) and has been demonstrated to improve change detection in areas with complex topography. Future work will test this approach.

Another possible contributor to the erroneous results may be variable lighting conditions and specular reflection. In a study by Guidi et al. (2014) demonstrated that the use of polarising filter and digital pre-processing with HDR imaging could help to homogenise brightness over the subject subsequently improving image matching We recommend these approaches to overcome this problem.

This study and our experience in the field using a TMEM suggest that the time required for data collection (installation and acquisition) collection is shorter using an SfM-MVS approach compared to the TMEM. The requirement of just one bolt per measurement site for the CRS described here, compared to three bolts per measurement site for the TMEM, reduces the time needed for initial installation in the field. Add to that the time required to collect images for the SfM-MVS workflow compared to the time needed to obtain 100 TMEM measurements, and SfM–MVS has notable advantages. This reduced installation and data acquisition time are of particular worth for shore platforms with meso to macro tidal ranges, where time in the intertidal zone is limited to, at most, a couple of hours either side of low tide. For larger platforms, where a number of measurement stations are located in the intertidal zone, time is a limiting factor, and methods which allow rapid installation data collection are preferable. Regarding data processing, the time required depends on the gauge used to collect the TMEM data, i.e. manual or automatic and the desired output (point measurements or 3D surface). Regardless, the processing time required for SfM-MVS is significantly higher (2-3 hours per DEM generated). Nevertheless, batch processing options in Photoscan mean that DEM generation process/steps can be automated and the user time on the computer is reduced. With respect to image acquisition for SfM-MVS, we used a Nikon D5500 and had included this in our overall analysis however expensive cameras are not a prerequisite. For example, in a recent experimental study of surface features in sand caused by sublimation of CO_2 ice, of a similar scale to this study, Mc Keown et al. (2017) used an iPhone to acquire images and

utilised the same CRS developed by Verma and Bourke (2018) to scale and reference DEMs, achieving similar accuracy and resolution (<1 mm).

It is important to note that the resolution of the SfM MVS approach, while capable of detecting sub-mm scale change, is still 2 orders of magnitude lower than that achievable with a T/MEM. The T/MEM offers considerable resolution and accuracy for measurements of very small surface changes, which is particularly useful for measuring very slow rates of downwearing and detection of very small changes due to processes which operate at much finer spatial scales such as platform swelling (e.g. Stephenson and Kirk, 2001, Gómez-Pujol et al., 2007, Trenhaile, 2006, Hemmingsen et al., 2007, Porter and Trenhaile, 2007). For faster-eroding rocks, the precision obtainable using a T/MEM is not required (Stephenson and Finlayson, 2009). While the highest common resolution of the DEMs produced for this study were 0.3 mm/pixel, this is demonstrated to be sufficient for measuring micro-scale and meso scale erosion on surfaces with low RI and loss of rock fragments on more topographically complex surfaces.

In terms of data output, the TMEM produces a series of surface point measurements. These can be compared directly to point measurements made from previous surveys or plotted as a digital elevation model for 3D visualisation of the surface at the bolt site (e.g. Stephenson, 1997). The spatial and temporal variation in downwearing rates can be used to infer the efficacy of erosion processes. In this, we suggest that SfM–MVS has a clear and important geomorphic advantage. The technique produces point clouds and DEMs which can be used to identify and classify surface features as well as detect geomorphic change at different scales. This added value in the approach is significant. Orthophotograph mosaics offer additional means for validating meso scale changes on the rock surface and identifying erosion styles.

5.5 Conclusions

1. This study demonstrates that SfM can be used to detect sub-mm changes due to erosion on shore platforms. However, we find that as the complexity of the rock surface topography increases, the reliability of SfM to detect sub-mm changes decreases. We note that the application of TMEM is also limited to relatively planar surfaces. Future work will test the precision mapping approach of James et al. (2017) to determine the spatial distribution of error and increase confidence in results on more topographically complex platform surfaces.

2. While TMEM has higher resolution and accuracy compared to SfM, if offers a limited number of point measurments over a small area. In comparison, SfM produces 3D topographic data from dense point clouds and DEMs which can be used to identify, classify and quantify different styles and scales of erosion.

3. In this study, we have provided a detailed comparison between TMEM and SfM methods to measure change due to erosion of rock surfaces in the coastal environment. The approach is not limited to shore platforms and has potential as a means for measuring erosion at similar scales in a range of environments.

Acknowledgements

N.D.C and A.K.V were supported by the Trinity College Dublin Postgraduate Studentship, Faculty of Engineering, Mathematics and Science. The authors would also like to thank the Geography Department at Trinity College Dublin for additional support in carrying out this research. Our thanks also to Neil Dawson from J.F. Dunne Engineering for expertise in the manufacture of the field adapted coordinate reference system used in the experiment.

References

Adams, P. N.: Nearshore wave-induced cyclical flexing of sea cliffs, Journal of Geophysical Research, 110, 2005.

Adams, P. N., Anderson, R. S., and Revenaugh, J.: Microseismic measurement of wave-energy delivery to a rocky coast, Geology, 30, 895-898, 2002.

Adams, P. N., Storlazzi, C. D., and Anderson, R. S.: Nearshore wave-induced cyclical flexing of sea cliffs, Journal of Geophysical Research: Earth Surface (2003–2012), 110, 2005.

Agisoft, L. P.: Professional Edition, Version 1.0. 0, 2013. 2013.

Allen, J.: Sedimentary structures, their character and physical basis, Elsevier, Netherlands, 1982.

Andrews, C. and Williams, R. B.: Limpet erosion of chalk shore platforms in southeast England, Earth Surface Processes and Landforms, 25, 1371-1381, 2000.

Balaguer-Puig, M., Marqués-Mateu, Á., Lerma, J. L., and Ibáñez-Asensio, S.: Estimation of small-scale soil erosion in laboratory experiments with Structure from Motion photogrammetry, Geomorphology, doi: doi: 10.1016/j.geomorph.2017.04.035, 2017. 2017.

Barlow, J., Lim, M., Rosser, N., Petley, D., Brain, M., Norman, E., and Geer, M.: Modeling cliff erosion using negative power law scaling of rockfalls, Geomorphology, 139, 416-424, 2012.

Barron, S., Delaney, A., Perrin, P., Martin, J., O'Neill, F., De Jongh, A., O'Neill, L., Perrin, P., Barron, S., and Roche, J.: National survey and assessment of the conservation status of Irish sea cliffs, National Parks and Wildlife Service, 2011.

Battjes, J. A. and Janssen, J.: Energy loss and set-up due to breaking of random waves. In: Coastal Engineering 1978, 1978.

Beetham, E. P. and Kench, P. S.: Field observations of infragravity waves and their behaviour on rock shore platforms, Earth Surface Processes and Landforms, 36, 1872-1888, 2011.

Blair, T. C. and McPherson, J. G.: Grain-size and textural classification of coarse sedimentary particles, Journal of Sedimentary Research, 69, 1999.

Booij, N., Ris, R., and Holthuijsen, L. H.: A third-generation wave model for coastal regions: 1. Model description and validation, Journal of geophysical research: Oceans, 104, 7649-7666, 1999.

Bourke, M. C., Brearley, J. A., Haas, R., and Viles, H. A.: A photographic atlas of rock breakdown features in geomorphic environments, Planetary Science Institute, 2007.

Bourke, M. C., Naylor, L. A., Flood, R., Nash, C., Cullen, N. D., Goffo, F., and Migge, K.: Investigation of Ireland's Shore Platforms: Location, type and coastal protection. , Geological Survey of Ireland., Dublin, Ireland, 2016.

Bowen, D., Phillips, F., McCabe, A., Knutz, P., and Sykes, G.: New data for the last glacial maximum in Great Britain and Ireland, Quaternary Science Reviews, 21, 89-101, 2002.

Brain, M. J., Rosser, N. J., Norman, E. C., and Petley, D. N.: Are microseismic ground displacements a significant geomorphic agent?, Geomorphology, 207, 161-173, 2014.

Brasington, J., Langham, J., and Rumsby, B.: Methodological sensitivity of morphometric estimates of coarse fluvial sediment transport, Geomorphology, 53, 299-316, 2003.

Brasington, J., Rumsby, B., and McVey, R.: Monitoring and modelling morphological change in a braided gravel-bed river using high resolution GPS-based survey, Earth Surface Processes and Landforms, 25, 973-990, 2000.

Brodu, N. and Lague, D.: 3D terrestrial lidar data classification of complex natural scenes using a multi-scale dimensionality criterion: Applications in geomorphology, ISPRS Journal of Photogrammetry and Remote Sensing, 68, 121-134, 2012.

Brunier, G., Fleury, J., Anthony, E. J., Gardel, A., and Dussouillez, P.: Close-range airborne Structure-from-Motion Photogrammetry for high-resolution beach morphometric surveys: Examples from an embayed rotating beach, Geomorphology, 261, 76-88, 2016a.

Brunier, G., Fleury, J., Anthony, E. J., Pothin, V., Vella, C., Dussouillez, P., Gardel, A., and Michaud, E.: Structure-from-Motion photogrammetry for high-resolution coastal and fluvial geomorphic surveys, Géomorphologie: relief, processus, environnement, 22, 147-161, 2016b.

Buyer, A. and Schubert, W.: Extraction of discontinuity orientations in point clouds, Rock Mechanics and Rock Engineering: From the Past to the Future, 2, 1133-1138, 2016.

Carbonneau, P. E., Lane, S. N., and Bergeron, N. E.: Catchment-scale mapping of surface grain size in gravel bed rivers using airborne digital imagery, Water resources research, 40, 2004.

Carrivick, J. L., Smith, M. W., and Quincey, D. J.: Structure from Motion in the Geosciences, John Wiley & Sons, 2016.

Chandler, J.: Effective application of automated digital photogrammetry for geomorphological research, Earth Surface Processes and Landforms, 24, 51-63, 1999.

Chandler, J., Ashmore, P., Paola, C., Gooch, M., and Varkaris, F.: Monitoring river-channel change using terrestrial oblique digital imagery and automated digital photogrammetry, Annals of the Association of American Geographers, 92, 631-644, 2002.

Cignoni, P., Rocchini, C., and Scopigno, R.: Metro: measuring error on simplified surfaces, 1998, 167-174.

Collinson, J. D., Martinsen, O., Bakken, B., and Kloster, A.: Early fill of the Western Irish Namurian Basin: a complex relationship between turbidites and deltas, Basin Research, 3, 223-242, 1991.

Compare, C.: Cloud Compare. 2013.

Corominas, J., Mavrouli, O., and Ruiz-Carulla, R.: Magnitude and frequency relations: are there geological constraints to the rockfall size?, Landslides, 2017. 1-17, 2017.

Cox, R., Zentner, D. B., Kirchner, B. J., and Cook, M. S.: Boulder ridges on the Aran Islands (Ireland): recent movements caused by storm waves, not tsunamis, The Journal of geology, 120, 249-272, 2012.

Cruslock, E. M., Naylor, L. A., Foote, Y. L., and Swantesson, J. O.: Geomorphologic equifinality: A comparison between shore platforms in Höga Kusten and Fårö, Sweden and the Vale of Glamorgan, South Wales, UK, Geomorphology, 114, 78-88, 2010.

Cullen, N. D. and Bourke, M. C.: Clast abrasion of a rock shore platform on the Atlantic coast of Ireland, Earth Surface Processes and Landforms, 43 (12) 2627-2641, 2018.

Dahl, A. L.: Surface area in ecological analysis: quantification of benthic coral-reef algae, Marine Biology, 23, 239-249, 1973.

Dasgupta, R.: Determination of the fractal dimension of a shore platform profile, Journal of the Geological Society of India, 81, 122-128, 2013.

Dasgupta, R.: Whither shore platforms?, Progress in Physical Geography, 2010. 2010.

Dasgupta, R.: Whither shore platforms?, Progress in Physical Geography, 35, 183-209, 2011.

Devoy, R. J.: Coastal vulnerability and the implications of sea-level rise for Ireland, Journal of Coastal research, 2008. 325-341, 2008.

Dickson, M. E. and Pentney, R.: Micro-seismic measurements of cliff motion under wave impact and implications for the development of near-horizontal shore platforms, Geomorphology, 151-152, 27-38, 2012.

Dornbusch, U., Moses, C., Robinson, D. A., and Williams, R.: Soft copy photogrammetry to measure shore platform erosion on decadal timescales, Journal of Coastal Conservation, 11, 193-200, 2008.

Dussauge-Peisser, C., Helmstetter, A., Grasso, J.-R., Hantz, D., Desvarreux, P., Jeannin, M., and Giraud, A.: Probabilistic approach to rock fall hazard assessment: potential of historical data analysis, Natural Hazards and Earth System Science, 2, 15-26, 2002.

Earlie, C. S.: Field observations of wave induced coastal cliff erosion, Cornwall, UK, 2015. 2015.

Edwards, A. B.: Storm-wave platforms, Jour. Geomorphology, 4, 223-236, 1941.

Éireann, M.: Met Eireann. Shannon Airport 1971–2000 averages Met Éireann, Dublin, Ireland., 2015.

Eldeberky, Y. and Battjes, J. A.: Spectral modeling of wave breaking: Application to Boussinesq equations, Journal of Geophysical Research: Oceans, 101, 1253-1264, 1996.

Elgar, S. and Guza, R.: Observations of bispectra of shoaling surface gravity waves, Journal of Fluid Mechanics, 161, 425-448, 1985.

Ellis, N.: Morphology, process and rates of denudation on the chalk shore platform of East Sussex, 1986. Brighton Polytechnic, PhD Thesis, 1986.

Erdmann, W., Kelletat, D., and Scheffers, A.: Boulder transport by storms–Extreme-waves in the coastal zone of the Irish west coast, Marine Geology, 2018. 2018.

Ester, M., Kriegel, H.-P., Sander, J., and Xu, X.: A density-based algorithm for discovering clusters in large spatial databases with noise, 1996, 226-231.

Etienne, S. and Paris, R.: Boulder accumulations related to storms on the south coast of the Reykjanes Peninsula (Iceland), Geomorphology, 114, 55-70, 2010.

EUrosion: Living with coastal erosion in Europe: Sediment and Space for Sustainability. Part 2 Maps and Statistics. , Europe, 2004.

Faro: *Faro Scene cloud processing software* (version 6.2) [software] Available at https://www.faro.com/products/product-design/faro-scene, 2016. 2016.

Farrell, E. J., Granja, H., Cappietti, L., Ellis, J. T., Li, B., and Sherman, D. J.: Wave transformation across a rock platform, Belinho, Portugal, Journal of Coastal Research, 2009. 44-48, 2009.

Fonstad, M. A., Dietrich, J. T., Courville, B. C., Jensen, J. L., and Carbonneau, P. E.: Topographic structure from motion: a new development in photogrammetric measurement, Earth Surface Processes and Landforms, 38, 421-430, 2013.

Foote, Y., Plessis, E., Robinson, D., Hénaff, A., and Costa, S.: Rates and patterns of downwearing of chalk shore platforms of the Channel: comparisons between France and England, Zeitschrift Fur Geomorphologie, 144, 93-115, 2006.

Freilich, M. and Guza, R.: Nonlinear effects on shoaling surface gravity waves, Phil. Trans. R. Soc. Lond. A, 311, 1-41, 1984.

Furukawa, Y., Curless, B., Seitz, S. M., and Szeliski, R.: Towards internet-scale multi-view stereo, 2010, 1434-1441.

Gallagher, S., Tiron, R., and Dias, F.: A detailed investigation of the nearshore wave climate and the nearshore wave energy resource on the west coast of Ireland, 2013, V008T009A046-V008T009A046.

Gallagher, S., Tiron, R., and Dias, F.: A long-term nearshore wave hindcast for Ireland: Atlantic and Irish Sea coasts (1979–2012), Ocean Dynamics, 64, 1163-1180, 2014.

Gardner, J.: Rockfall frequency and distribution in the Highwood Pass area, Canadian Rocky Mountains, Zeitshrift fur Geomorphologie, NF, 27, 311-324, 1983.

Gardner, J. S.: Frequency, magnitude and spatial distribution of mountain rockfalls and rockslides in the Highwood Pass area, Alberta, Canada, Thresholds in Geomorphology. Allen and Unwin, New York, 1980. 267-295, 1980.

Girardeau-Montaut, D., Roux, M., Marc, R., and Thibault, G.: Change detection on points cloud data acquired with a ground laser scanner, International Archives of Photogrammetry, Remote Sensing and Spatial Information Sciences, 36, W19, 2005.

Gómez-Gutiérrez, Á., Schnabel, S., Berenguer-Sempere, F., Lavado-Contador, F., and Rubio-Delgado, J.: Using 3D photo-reconstruction methods to estimate gully headcut erosion, Catena, 120, 91-101, 2014.

Gómez-Pujol, L., Stephenson, W. J., and Fornós, J. J.: Two-hourly surface change on supra-tidal rock (Marengo, Victoria, Australia), Earth Surface Processes and Landforms, 32, 1-12, 2007.

Gorrell, L., Raubenheimer, B., Elgar, S., and Guza, R.: SWAN predictions of waves observed in shallow water onshore of complex bathymetry, Coastal Engineering, 58, 510-516, 2011.

Goto, K., Miyagi, K., Kawana, T., Takahashi, J., and Imamura, F.: Emplacement and movement of boulders by known storm waves—field evidence from the Okinawa Islands, Japan, Marine Geology, 283, 66-78, 2011.

Goto, K., Okada, K., and Imamura, F.: Characteristics and hydrodynamics of boulders transported by storm waves at Kudaka Island, Japan, Marine Geology, 262, 14-24, 2009.

Goto, K., Okada, K., and Imamura, F.: Numerical analysis of boulder transport by the 2004 Indian Ocean tsunami at Pakarang Cape, Thailand, Marine Geology, 268, 97-105, 2010.

Goudie, A.: Encyclopedia of geomorphology, Psychology Press, 2004.

Guidi, G., Gonizzi, S., and Micoli, L.: Image pre-processing for optimizing automated photogrammetry performances, 2014, 145-152.

Guthrie, R. and Evans, S.: Magnitude and frequency of landslides triggered by a storm event, Loughborough Inlet, British Columbia, Natural Hazards and Earth System Science, 4, 475-483, 2004.

Guzzetti, F., Ardizzone, F., Cardinali, M., Rossi, M., and Valigi, D.: Landslide volumes and landslide mobilization rates in Umbria, central Italy, Earth and Planetary Science Letters, 279, 222-229, 2009.

Guzzetti, F., Malamud, B. D., Turcotte, D. L., and Reichenbach, P.: Power-law correlations of landslide areas in central Italy, Earth and Planetary Science Letters, 195, 169-183, 2002.

Hall, A. M.: Storm wave currents, boulder movement and shore platform development: a case study from East Lothian, Scotland, Marine Geology, 283, 98-105, 2011a.

Hall, A. M.: Storm wave currents, boulder movement and shore platform development: A case study from East Lothian, Scotland, Marine Geology, 283, 98-105, 2011b.

Hall, A. M., Hansom, J. D., and Jarvis, J.: Patterns and rates of erosion produced by high energy wave processes on hard rock headlands: The Grind of the Navir, Shetland, Scotland, Marine Geology, 248, 28-46, 2008.

Hampton, M. A., Griggs, G. B., Edil, T. B., Guy, D. E., Kelley, J. T., Komar, P. D., Mickelson, D. M., and Shipman, H. M.: Processes that govern the formation and evolution of coastal cliffs, US Geological Survey professional paper, 1693, 7-38, 2004.

Hanna, F.: A technique for measuring the rate of erosion of cave passages, Proceedings University of Bristol Spelaeology Society, 83-86, 1966.

Hansom, J., Barltrop, N., and Hall, A.: Modelling the processes of cliff-top erosion and deposition under extreme storm waves, Marine Geology, 253, 36-50, 2008.

Hasselmann, K., Barnett, T., Bouws, E., Carlson, H., Cartwright, D., Enke, K., Ewing, J., Gienapp, H., Hasselmann, D., and Kruseman, P.: Measurements of wind-wave growth and swell decay during the Joint North Sea Wave Project (JONSWAP), Ergänzungsheft 8-12, 1973. 1973.

Hemmingsen, S. A., Eikaas, H. S., and Hemmingsen, M. A.: The influence of seasonal and local weather conditions on rock surface changes on the shore platform at Kaikoura Peninsula, South Island, New Zealand, Geomorphology, 87, 239-249, 2007.

Hodson, F. and Lewarne, G. C.: A mid-Carboniferous (Namurian) basin in parts of the counties of Limerick and Clare, Ireland, Quarterly Journal of the Geological Society, 117, 307-333, 1961.

Hovius, N., Stark, C. P., Hao-Tsu, C., and Jiun-Chuan, L.: Supply and removal of sediment in a landslide-dominated mountain belt: Central Range, Taiwan, The Journal of Geology, 108, 73-89, 2000.

Hudson, J. A. and Harrison, J.: Engineering rock mechanics, vol. I. Pergamon, 1997.

Hungr, O., Evans, S., and Hazzard, J.: Magnitude and frequency of rock falls and rock slides along the main transportation corridors of southwestern British Columbia, Canadian Geotechnical Journal, 36, 224-238, 1999.

Hungr, O., McDougall, S., Wise, M., and Cullen, M.: Magnitude–frequency relationships of debris flows and debris avalanches in relation to slope relief, Geomorphology, 96, 355-365, 2008.

Hutchinson, J.: Field and laboratory studies of a fall in Upper Chalk cliffs at Joss Bay, Isle of Thanet, 1972, 692-706.

Imamura, F., Goto, K., and Ohkubo, S.: A numerical model for the transport of a boulder by tsunami, Journal of Geophysical Research: Oceans, 113, 2008.

James, M. R., Robson, S., and Smith, M. W.: 3-D uncertainty-based topographic change detection with structure-from-motion photogrammetry: precision maps for ground control and directly georeferenced surveys, Earth Surface Processes and Landforms, doi: doi:10.1002/esp.4125, 2017. 2017.

Janssen, P. A.: Quasi-linear theory of wind-wave generation applied to wave forecasting, Journal of Physical Oceanography, 21, 1631-1642, 1991.

Janssen, P. A.: Wave-induced stress and the drag of air flow over sea waves, Journal of Physical Oceanography, 19, 745-754, 1989.

Javernick, L., Brasington, J., and Caruso, B.: Modeling the topography of shallow braided rivers using Structure-from-Motion photogrammetry, Geomorphology, 213, 166-182, 2014.

Johnson, D. W.: Shore processes and shoreline development, John Wiley & Sons, Incorporated, 1919.

Jones, E. V., Rosser, N., and Brain, M.: Alongshore variability in wave energy transfer to coastal cliffs, Geomorphology, 2018. 2018.

Kaiser, A., Neugirg, F., Rock, G., Müller, C., Haas, F., Ries, J., and Schmidt, J.: Small-scale surface reconstruction and volume calculation of soil erosion in complex Moroccan gully morphology using structure from motion, Remote Sensing, 6, 7050-7080, 2014.

Kanyaya, J. I. and Trenhaile, A. S.: Tidal wetting and drying on shore platforms: an experimental assessment, Geomorphology, 70, 129-146, 2005.

Kazhdan, M. and Hoppe, H.: Screened poisson surface reconstruction, ACM Transactions on Graphics (ToG), 32, 29, 2013.

Kemeny, J. and Post, R.: Estimating three-dimensional rock discontinuity orientation from digital images of fracture traces, Computers & Geosciences, 29, 65-77, 2003.

Knight, J. and Burningham, H.: Boulder dynamics on an Atlantic-facing rock coastline, northwest Ireland, Marine Geology, 283, 56-65, 2011.

Knight, J., Burningham, H., and Barrett-Mold, C.: The geomorphology and controls on development of a boulder-strewn rock platform, NW Ireland, Journal of Coastal Research, 2009. 1646-1650, 2009.

Lague, D., Brodu, N., and Leroux, J.: Accurate 3D comparison of complex topography with terrestrial laser scanner: Application to the Rangitikei canyon (NZ), ISPRS journal of photogrammetry and remote sensing, 82, 10-26, 2013.

Lane, S. N., Westaway, R. M., and Murray Hicks, D.: Estimation of erosion and deposition volumes in a large, gravel-bed, braided river using synoptic remote sensing, Earth Surface Processes and Landforms, 28, 249-271, 2003.

Larsen, I. J., Montgomery, D. R., and Korup, O.: Landslide erosion controlled by hillslope material, Nature Geoscience, 3, 247, 2010.

Leica: *Leica Cyclone, 3D point cloud processing software*. (version 8.1) [software] Available at http://hds.leica-geosystems.com/en/Leica-Cyclone_6515.htm. 2015.

Lim, M., Rosser, N. J., Allison, R. J., and Petley, D. N.: Erosional processes in the hard rock coastal cliffs at Staithes, North Yorkshire, Geomorphology, 114, 12-21, 2010.

Lim, M., Rosser, N. J., Petley, D. N., and Keen, M.: Quantifying the controls and influence of tide and wave impacts on coastal rock cliff erosion, Journal of Coastal Research, 27, 46-56, 2011.

Lowe, D. G.: Distinctive image features from scale-invariant keypoints, International journal of computer vision, 60, 91-110, 2004.

Malamud, B. D., Turcotte, D. L., Guzzetti, F., and Reichenbach, P.: Landslide inventories and their statistical properties, Earth Surface Processes and Landforms, 29, 687-711, 2004.

Malinverno, A.: A simple method to estimate the fractal dimension of a self-affine series, Geophysical Research Letters, 17, 1953-1956, 1990.

Marine Institute: Irish National Tide Gauge Network Real Time Data., Marine Institute, RInville, Oranmore, Galway., 2016.

Marshall, R. J. and Stephenson, W. J.: The morphodynamics of shore platforms in a micro-tidal setting: Interactions between waves and morphology, Marine Geology, 288, 18-31, 2011.

Mastronuzzi, G. and Sansò, P.: Large boulder accumulations by extreme waves along the Adriatic coast of southern Apulia (Italy), Quaternary International, 120, 173-184, 2004.

Matasci, B., Jaboyedoff, M., Loye, A., Pedrazzini, A., Derron, M.-H., and Pedrozzi, G.: Impacts of fracturing patterns on the rockfall susceptibility and erosion rate of stratified limestone, Geomorphology, 241, 83-97, 2015.

Mc Keown, L., Bourke, M., and McElwaine, J.: Experiments On Sublimating Carbon Dioxide Ice And Implications For Contemporary Surface Processes On Mars, Scientific reports, 7, 14181, 2017.

McCartney, M., Abernethy, G., and Gault, L.: The Divider Dimensions of the Irish Coast, Irish Geography, 43, 277-284, 2010.

McKenna, J.: Morphodynamics and sediments of basalt shore platforms, 1990. University of Ulster, 1990.

McKenna, J., Carter, R., and Bartlett, D.: Coast Erosion in Northeast Ireland:-Part II Cliffs and Shore Platforms, Irish Geography, 25, 111-128, 1992.

Micheletti, N., Chandler, J. H., and Lane, S. N.: Investigating the geomorphological potential of freely available and accessible structure-from-motion photogrammetry using a smartphone, Earth Surface Processes and Landforms, 40, 473-486, 2015a.

Micheletti, N., Chandler, J. H., and Lane, S. N.: Structure from Motion (SfM) Photogrammetry. In: Geomorphlogical Techniques, 2 (2.2), British Society for Geomorphology, Loondon, 2015b.

Milan, D. J., Heritage, G. L., and Hetherington, D.: Application of a 3D laser scanner in the assessment of erosion and deposition volumes and channel change in a proglacial river, Earth Surface Processes and Landforms: The Journal of the British Geomorphological Research Group, 32, 1657-1674, 2007.

Mölter, T., Schindler, D., Albrecht, A. T., and Kohnle, U.: Review on the projections of future storminess over the North Atlantic European Region, Atmosphere, 7, 60, 2016.

Moses, C., Robinson, D., and Barlow, J.: Methods for measuring rock surface weathering and erosion: A critical review, Earth-Science Reviews, 135, 141-161, 2014.

Moses, C. A.: The origin and implications of microsolutional features on the surface of limestone, 1993. Queen's University of Belfast, 1993.

Moses, C. A.: The rock coast of the British Isles: shore platforms, Geological Society, London, Memoirs, 40, 39-56, 2014.

Nandasena, N., Paris, R., and Tanaka, N.: Numerical assessment of boulder transport by the 2004 Indian ocean tsunami in Lhok Nga, West Banda Aceh (Sumatra, Indonesia), Computers & geosciences, 37, 1391-1399, 2011.

Nandasena, N. and Tanaka, N.: Boulder transport by high energy: Numerical model-fitting experimental observations, Ocean Engineering, 57, 163-179, 2013.

Nandasena, N., Tanaka, N., Sasaki, Y., and Osada, M.: Boulder transport by the 2011 Great East Japan tsunami: Comprehensive field observations and whither model predictions?, Marine Geology, 346, 292-309, 2013.

Naylor, L.: Geomorphological control on boulder transport and coastal erosion before, during and after an extreme extra-tropical cyclone, Earth Surface Processes and Landforms, 2016. 2016.

Naylor, L. and Stephenson, W.: On the role of discontinuities in mediating shore platform erosion, Geomorphology, 114, 89-100, 2010.

Naylor, L., Stephenson, W., and Trenhaile, A.: Rock coast geomorphology: recent advances and future research directions, Geomorphology, 114, 3-11, 2010.

Naylor, L. A., Coombes, M. A., and Viles, H. A.: Reconceptualising the role of organisms in the erosion of rock coasts: A new model, Geomorphology, 157, 17-30, 2012.

Naylor, L. A., Stephenson, W. J., Smith, H., Way, O., Mendelssohn, J., and Cowley, A.: Geomorphological control on boulder transport and coastal erosion before, during and after an extreme extra-tropical cyclone, Earth Surface Processes and Landforms, 2016a. 2016a.

Naylor, L. A., Stephenson, W. J., Smith, H. C., Way, O., Mendelssohn, J., and Cowley, A.: Geomorphological control on boulder transport and coastal erosion before, during and after an extreme extra-tropical cyclone, Earth Surface Processes and Landforms, 41, 685-700, 2016b.

Norman, E. C., Rosser, N. J., Brain, M. J., Petley, D. N., and Lim, M.: Coastal cliff-top ground motions as proxies for environmental processes, Journal of Geophysical Research: Oceans, 118, 6807-6823, 2013.

Nott, J.: Waves, coastal boulder deposits and the importance of the pre-transport setting, Earth and Planetary Science Letters, 210, 269-276, 2003.

Ogawa, H.: Observation of wave transformation on a sloping type B shore platform under wind-wave and swell conditions, Geo-Marine Letters, 33, 1-11, 2013.

Ogawa, H.: Observation of wave transformation on a sloping type B shore platform under wind-wave and swell conditions, Geo-Marine Letters, 33, 1-11, 2012.

Ogawa, H., Dickson, M., and Kench, P.: Wave transformation on a sub-horizontal shore platform, Tatapouri, North Island, New Zealand, Continental Shelf Research, 31, 1409-1419, 2011.

Ogawa, H., Dickson, M. E., and Kench, P. S.: Generalised observations of wave characteristics on near-horizontal shore platforms: Synthesis of six case studies from the North Island, New Zealand, New Zealand Geographer, 72, 107-121, 2016.

Ogawa, H., Kench, P., and Dickson, M.: Field Measurements of Wave Characteristics on a Near-Horizontal Shore Platform, Mahia Peninsula, North Island, New Zealand, Geographical Research, 50, 179-192, 2012.

Özyeşil, O., Voroninski, V., Basri, R., and Singer, A.: A survey of structure from motion*, Acta Numerica, 26, 305-364, 2017.

Palamara, D., Dickson, M., and Kennedy, D.: Defining shore platform boundaries using airborne laser scan data: a preliminary investigation, Earth Surface Processes and Landforms, 32, 945-953, 2007.

Paris, R., Naylor, L. A., and Stephenson, W. J.: Boulders as a signature of storms on rock coasts, Marine Geology, 283, 1-11, 2011.

Pérez-Alberti, A., Trenhaile, A., Pires, A., López-Bedoya, J., Chaminé, H., and Gomes, A.: The effect of boulders on shore platform development and morphology in Galicia, north west Spain, Continental Shelf Research, 48, 122-137, 2012.

Peters, J. L., Benetti, S., Dunlop, P., Cofaigh, C. Ó., Moreton, S. G., Wheeler, A. J., and Clark, C. D.: Sedimentology and chronology of the advance and retreat of the last British-Irish Ice Sheet on the continental shelf west of Ireland, Quaternary Science Reviews, 140, 101-124, 2016.

Pinn, E. H., Richardson, C., Thompson, R., and Hawkins, S.: Burrow morphology, biometry, age and growth of piddocks (Mollusca: Bivalvia: Pholadidae) on the south coast of England, Marine Biology, 147, 943-953, 2005.

Poate, T., Masselink, G., Austin, M., Dickson, M., and Kench, P.: Observation of Wave Transformation on Macro-tidal Rocky Platforms, Journal of Coastal Research, 75, 602-606, 2016.

Poate, T., Masselink, G., Austin, M. J., Dickson, M., and McCall, R.: The role of bed roughness in wave transformation across sloping rock shore platforms, Journal of Geophysical Research: Earth Surface, 123, 97-123, 2018.

Porter, N. J. and Trenhaile, A.: Short-term rock surface expansion and contraction in the intertidal zone, Earth Surface Processes and Landforms, 32, 1379-1397, 2007.

Prémaillon, M., Regard, V., and Dewez, T.: How to explain variations in sea cliff erosion rate?, 2017, 8012.

Prémaillon, M., Regard, V., Dewez, T. J., and Auda, Y.: GlobR2C2 (Global Recession Rates of Coastal Cliffs): a global relational database to investigate coastal rocky cliff erosion rate variations, Earth Surface Dynamics, 6, 651-668, 2018.

Priest, S. and Hudson, J.: Estimation of discontinuity spacing and trace length using scanline surveys, 1981, 183-197.

Pulham, A.: Controls on internal structure and architecture of sandstone bodies within Upper Carboniferous fluvial-dominated deltas, County Clare, western Ireland, Geological Society, London, Special Publications, 41, 179-203, 1989.

Richardson, K. and Carling, P. A.: A typology of sculpted forms in open bedrock channels, Geological Society of America Special Papers, 392, 1-108, 2005.

Rider, M.: The Namurian of West County Clare, 1974, 125-142.

Riquelme, A., Tomás, R., Cano, M., Pastor, J. L., and Abellán, A.: Automatic Mapping of Discontinuity Persistence on Rock Masses Using 3D Point Clouds, Rock Mechanics and Rock Engineering, 2018. 1-24, 2018.

Riquelme, A. J., Abellán, A., and Tomás, R.: Discontinuity spacing analysis in rock masses using 3D point clouds, Engineering Geology, 195, 185-195, 2015.

Riquelme, A. J., Abellán, A., Tomás, R., and Jaboyedoff, M.: A new approach for semi-automatic rock mass joints recognition from 3D point clouds, Computers & Geosciences, 68, 38-52, 2014.

Riquelme, A. J., Tomás, R., and Abellán, A.: Characterization of rock slopes through slope mass rating using 3D point clouds, International Journal of Rock Mechanics and Mining Sciences, 84, 165-176, 2016.

Risk, M. J.: Fish diversity on a coral reef in the Virgin Islands, The Smithsonian Institution,, Washington, Atoll Research Bulletin, Report No. 153, 1972.

Rosser, N., Lim, M., Petley, D., Dunning, S., and Allison, R.: Patterns of precursory rockfall prior to slope failure, Journal of geophysical research: earth surface, 112, 2007.

Rosser, N. J., Brain, M. J., Petley, D. N., Lim, M., and Norman, E. C.: Coastline retreat via progressive failure of rocky coastal cliffs, Geology, 41, 939-942, 2013.

Rosser, N. J., Petley, D. N., Lim, M., Dunning, S., and Allison, R. J.: Terrestrial laser scanning for monitoring the process of hard rock coastal cliff erosion, Quarterly Journal of Engineering Geology and Hydrogeology, 38, 363-375, 2005.

Sallenger Jr, A. H., Krabill, W., Brock, J., Swift, R., Manizade, S., and Stockdon, H.: Sea-cliff erosion as a function of beach changes and extreme wave runup during the 1997–1998 El Niño, Marine Geology, 187, 279-297, 2002.

Sanders, N.: Wave tank experiments on erosion of rocky coasts, 1968, 11-18.

Santana, D., Corominas, J., Mavrouli, O., and Garcia-Sellés, D.: Magnitude–frequency relation for rockfall scars using a Terrestrial Laser Scanner, Engineering geology, 145, 50-64, 2012.

Scheffers, A., Scheffers, S., Kelletat, D., and Browne, T.: Wave-Emplaced Coarse Debris and Megaclasts in Ireland and Scotland: Boulder Transport in a High-Energy Littoral Environment, The Journal of Geology, 117, 553-573, 2009.

Schindelin, J., Arganda-Carreras, I., Frise, E., Kaynig, V., Longair, M., Pietzsch, T., Preibisch, S., Rueden, C., Saalfeld, S., and Schmid, B.: Fiji: an open-source platform for biological-image analysis, Nature methods, 9, 676-682, 2012.

Scott, D. N. and Wohl, E. E.: Bedrock Fracture Influences on Geomorphic Process and Form Across Process Domains and Scales, Earth Surface Processes and Landforms, 2018. 2018.

Silverman, B. W.: Density estimation for statistics and data analysis, Routledge, 2018.

Slob, S.: Automated rock mass characterisation using 3-D terrestrial laser scanning, 2010. TU Delft, Delft University of Technology, 2010.

Slob, S., Hack, R., and Turner, A. K.: An approach to automate discontinuity measurements of rock faces using laser scanning techniques, 2002.

Slob, S., Van Knapen, B., Hack, R., Turner, K., and Kemeny, J.: Method for automated discontinuity analysis of rock slopes with three-dimensional laser scanning, Transportation research record: journal of the transportation research board, 2005. 187-194, 2005.

Smith, M., Carrivick, J., and Quincey, D.: Structure from motion photogrammetry in physical geography, Progress in Physical Geography, 40, 247-275, 2016.

Snavely, N.: Bundler: SfM for unordered image collections. GitHub, 2006.

Spate, A., Jennings, J., Smith, D., and Greenaway, M.: The micro-erosion meter: use and limitations, Earth Surface Processes and Landforms, 10, 427-440, 1985.

Stephenson, W.: Shore platforms: remain neglected coastal feature?, Progress in Physical Geography, 24, 311-327, 2000.

Stephenson, W. and Finlayson, B.: Measuring erosion with the micro-erosion meter—contributions to understanding landform evolution, Earth-Science Reviews, 95, 53-62, 2009.

Stephenson, W., Kirk, R., Hemmingsen, S., and Hemmingsen, M.: Decadal scale micro erosion rates on shore platforms, Geomorphology, 114, 22-29, 2010.

Stephenson, W. and Naylor, L.: Geological controls on boulder production in a rock coast setting: insights from South Wales, UK, Marine Geology, 283, 12-24, 2011a.

Stephenson, W. and Naylor, L.: Within site geological contingency and its effect on rock coast erosion, Journal of Coastal Research, 61, 831-835, 2011b.

Stephenson, W. J.: Improving the traversing micro-erosion meter, Journal of Coastal Research, doi: . 1997. 236-241, 1997.

Stephenson, W. J., Dickson, M. E., and Trenhaile, A. S.: Rock Coasts. In: Treatise on Geomorphology, Shroder, J. F. (Ed.), Elsevier, 2013.

Stephenson, W. J. and Kirk, R. M.: Development of shore platforms on Kaikoura Peninsula, South Island, New Zealand: Part one: the role of waves, Geomorphology, 32, 21-41, 2000.

Stephenson, W. J. and Kirk, R. M.: Measuring erosion rates using the micro-erosion meter: 20 years of data from shore platforms, Kaikoura Peninsula, South Island, New Zealand, Marine Geology, 131, 209-218, 1996.

Stephenson, W. J. and Kirk, R. M.: Surface swelling of coastal bedrock on inter-tidal shore platforms, Kaikoura Peninsula, South Island, New Zealand, Geomorphology, 41, 5-21, 2001.

Stephenson, W. J., Naylor, L. A., Smith, H., Chen, B., and Brayne, R. P.: Wave transformation across a macrotidal shore platform under low to moderate energy conditions, Earth Surface Processes and Landforms, 43, 298-311, 2018.

Stockamp, J., Li, Z., Bishop, P., Hansom, J., Rennie, A., Petrie, E., Tanaka, A., Bingley, R., and Hansen, D.: Investigating Glacial Isostatic Adjustment in Scotland with InSAR and GPS Observations, 2015.

Sunamura, T.: Geomorphology of rocky coasts, John Wiley & Son Ltd, 1992.

Sunamura, T.: A relationship between wave-induced cliff erosion and erosive force of waves, The Journal of Geology, 85, 613-618, 1977.

Sunamura, T.: Rock control in coastal geomorphic processes, 1995, 103A.

Suzuki, T.: Rock control in geomorphological processes: research history in Japan and perspective, Transactions, Japanese Geomorphological Union, 23, 161-199, 2002.

Swantesson, J., Moses, C., Berg, G., and Jansson, K. M.: Methods for measuring shoreplatform micro-erosion; a comparison of the micro-erosion meter and the laser scanner, Zeitschrift fur Geomorphologie Supplementband, 144, 1-17, 2006.

Swirad, Z., Rosser, N., and Brain, M.: Identifying mechanisms of shore platform erosion using Structure-from-Motion (SfM) Photogrammetry, Earth surface Processes and Landforms, *In review*. *In review*.

Switzer, A. D. and Burston, J. M.: Competing mechanisms for boulder deposition on the southeast Australian coast, Geomorphology, 114, 42-54, 2010.

Teledyne: River Ray ADCP Guide.

Teledyne Marine, 2015.

Thoeni, K., Giacomini, A., Murtagh, R., and Kniest, E.: A comparison of multi-view 3D reconstruction of a rock wall using several cameras and a laser scanner, The International Archives of Photogrammetry, Remote Sensing and Spatial Information Sciences, 40, 573, 2014.

Thornbush, M. J.: A site-specific index based on weathering forms visible in Central Oxford, UK, Geosciences, 2, 277-297, 2012.

Trenhaile, A.: Modeling the development of wave-cut shore platforms, Marine Geology, 166, 163-178, 2000.

Trenhaile, A.: Tidal wetting and drying on shore platforms: an experimental study of surface expansion and contraction, Geomorphology, 76, 316-331, 2006.

Trenhaile, A. and Porter, N. J.: Can shore platforms be produced solely by weathering processes?, Marine Geology, 241, 79-92, 2007.

Trenhaile, A. S.: The development of subhorizontal shore platforms by waves and weathering in microtidal environments, Zeitschrift für Geomorphologie, 52, 105-124, 2008.

Trenhaile, A. S.: The geomorphology of rock coasts, Oxford University Press, USA, 1987.

Trenhaile, A. S.: Modeling shore platforms: present status and future developments. In: Advances in Coastal Modeling. Amsterdam: Elsevier, Lakhan, V. C. (Ed.), Elsevier Science B.V. , 2003.

Trenhaile, A. S. and Kanyaya, J. I.: The role of wave erosion on sloping and horizontal shore platforms in macro-and mesotidal environments, Journal of Coastal Research, 2007. 298-309, 2007.

Trudgill, S.: Measurement of erosional weight loss of rock tablets, British Geomorphological Research Group Technical Bulletin, 13-20 pp., 1975.

Trudgill, S., High, C., and Hanna, F.: Improvements to the micro-erosion meter, British Geomorphological Research Group Technical Bulletin, 3-17 pp., 1981.

Turowski, J. M. and Cook, K. L.: Field techniques for measuring bedrock erosion and denudation, Earth Surface Processes and Landforms, 42, 109-127, 2017.

Verma, A. K. and Bourke, M. C.: A Structure from Motion photogrammetry-based method to generate sub-millimetre resolution Digital Elevation Models for investigating rock breakdown features, Earth Surf. Dynam. Discuss., https://doi.org/10.5194/esurf-2018-53, in review, 2018.
.

Verma, A. K. and Bourke, M. C.: A Structure from Motion photogrammetry-based method to generate sub-millimetre resolution Digital Elevation Models for investigating rock breakdown features, Earth Surf. Dynam. Discuss., 4, 5, 2018.

Viles, H. A.: Scale issues in weathering studies, Geomorphology, 41, 63-72, 2001.

Walkden, M. and Hall, J.: A predictive mesoscale model of the erosion and profile development of soft rock shores, Coastal Engineering, 52, 535-563, 2005.

Warke, P. A. and McKinley, J.: Scale issues in geomorphology, Geomorphology, 130, 1-4, 2011.

Weiss, R. and Diplas, P.: Untangling boulder dislodgement in storms and tsunamis: Is it possible with simple theories?, Geochemistry, Geophysics, Geosystems, 16, 890-898, 2015.

Wentworth, C. K.: A scale of grade and class terms for clastic sediments, The Journal of Geology, 30, 377-392, 1922.

Westoby, M., Brasington, J., Glasser, N., Hambrey, M., and Reynolds, J.: 'Structure-from-Motion'photogrammetry: A low-cost, effective tool for geoscience applications, Geomorphology, 179, 300-314, 2012.

Whadcoat, S. K.: Numerical modelling of rockfall evolution in hard rock slopes, 2017. Durham University, 2017.

Wheaton, J. M., Brasington, J., Darby, S. E., and Sear, D. A.: Accounting for uncertainty in DEMs from repeat topographic surveys: improved sediment budgets, Earth Surface Processes and Landforms, 35, 136-156, 2010.

Williams, J. G., Rosser, N. J., Hardy, R. J., Brain, M. J., and Afana, A. A.: Optimising 4-D surface change detection: an approach for capturing rockfall magnitude–frequency, Earth surface dynamics., 6, 101-119, 2018.

Williams, R.: DEMs of difference. In: Geomorphological Techniques, 2 (3.2), British Society for Geomorphology, London, UK, 2012.

XLSTAT: Data Analysis and Statistical Solution for Microsoft Excel. . Addinsoft, Paris, France., 2017.

Yatsu, E.: The nature of weathering: an introduction, Sozosha Tokyo, 1988.

Yatsu, E.: Rock control in geomorphology, Sozosha, 1966.

Young, A. P., Adams, P. N., O'Reilly, W. C., Flick, R. E., and Guza, R.: Coastal cliff ground motions from local ocean swell and infragravity waves in southern California, Journal of Geophysical Research: Oceans, 116, 2011.

Young, A. P. and Ashford, S. A.: Instability investigation of cantilevered seacliffs, Earth Surface Processes and Landforms: The Journal of the British Geomorphological Research Group, 33, 1661-1677, 2008.

Young, A. P., Guza, R. T., Adams, P. N., O'Reilly, W. C., and Flick, R. E.: Cross-shore decay of cliff top ground motions driven by local ocean swell and infragravity waves, Journal of Geophysical Research, 117, 2012.

Young, A. P., Guza, R. T., Dickson, M. E., O'Reilly, W. C., and Flick, R. E.: Ground motions on rocky, cliffed, and sandy shorelines generated by ocean waves, Journal of Geophysical Research: Oceans, 118, 6590-6602, 2013.

Zingg, T.: Beitrag zur schotteranalyse, 1935. 1935.

Chapter 6: Synthesis

In this chapter, the significance of the research in the context of the wider field of rock coast geomorphology and the implications for future research are considered.

The role of discontinuities in local rates of rock cliff erosion (Research aim 1)

Although the role of discontinuities in reducing the resisting force of a rock mass is widely accepted, this study is the first time that the characteristics of discontinuity sets and their relationship to the spatial distribution of coastal cliff erosion have been investigated. The findings of this study build and expand on previous studies of rock coast erosion and provide new insights and empirical evidence for the importance of discontinuities in mediating coastal cliff erosion rates. The results indicate that the spacing density of discontinuities exerts a strong control on the size of rockfalls and their spatial distribution. Lower spacing density is associated with larger less frequent rockfalls while higher spacing density produces, lower magnitude failures more frequently. Geomorphologically, the frequency of rockfalls over the during the period (n = 540, t = 1 yr) is high regardless of rockfall size. The results also highlight a stronger influence of larger rockfalls on the rate of cliff erosion. Where larger failures dominate, rates of erosion are higher. Therefore, the spacing density of discontinuities also pays a critical role in mediating the rate of cliff erosion. The findings also suggest that the assumption of full discontinuity persistence which is widely used to assess rock mass stability may be incorrect for fractured, heterogenous rock masses. This is of particular importance for engineering projects where structural assessments are carried out based on the assumption of full discontinuity persistence.

This study is the first empirical measurement of cliff erosion on Ireland's rock dominated coastline. The rate of erosion is 2 orders of magnitude greater than that previously estimated

0.37 cm yr^{-1} here compared 0.001 m per century (Devoy, 2008). This measured rate of erosion is for embayed coastline and rates may be greater for more exposed coastlines depending on lithology, wave climate near and foreshore characteristics (Chapter 3). Again, we acknowledge the limitation of this study with respect to the time scale of the study period compared to the time scale of erosion processes operating on rock coasts. Hence, we apply a note of caution with respect to application of the erosion rate calculate here to estimate long term rates of erosion, particularly given the stochastic nature of rock coast erosion. We do however, note that the erosion rate calculated here is a similar order of magnitude when compared to globally averaged rates of erosion for rocks of medium hardness and as such is a reasonable estimate despite the relatively short period of study

We find that semi-automated discontinuity set extraction techniques, such as those described in this thesis, provide significant opportunity for coastal researchers to include discontinuity set characteristics as part of their research when trying to explain variations in the spatial distribution of erosion on coastal cliffs. These findings are also of relevance for future coastal management strategies and planning with respect to coastal infrastructures and communities.

In an Irish context, there is a critical need to expand on the findings and measure rates of coastal erosion at other locations and for other lithologies so that we can establish a better understanding of the geological control on current rates of erosion. Currently, the lack of high spatial and temporal resolution 3D data sets (e.g. lidar) for Ireland's coastline represents a substantial weakness in our ability to measure erosion rates at meaningful resolution. This significantly hampers our ability to predict the coastline to projected accelerate rates of coastal erosion in response to climate change. A concerted effort is required the obtain these data sets, one which has already been achieved with respect to Irelands offshore bathymetry. The INFOMAR project is a prime example of how such a focused effort can produce extensive high-resolution data sets which are fast proving a valuable asset for research and marine spatial planning. A similar effort is required for coastal cliffs but on a repeat basis whereby

surveys are carried out on an annual or biennial basis and following large storms. This will not only allow accurate measurement of erosion rates but also assessment of the impact of storms on rock coasts, which is key to understanding how rock coasts will respond to predicted increases in the frequency of more intense storms due to climate change. These data sets will also provide opportunity for the application of semi-automated discontinuity set extraction techniques which will help to identify locations which are more sensitive to coastal erosion based on the discontinuity sets characteristics. These data are of critical importance for management of coastal infrastructure and future project planning for hazard risk and vulnerability.

Globally, the application of semi-automated discontinuity set extraction for quantification of discontinuity characteristics can be applied retrospectively on data sets with sufficiently high spatial resolution. This will help validate this approach as a means for explaining the variability of coastal erosion rates and identify areas which may more vulnerable to coastal erosion.

Future work should also investigate our finding regarding the validity of assuming full persistence of discontinuities when characterising a rock mass for slope stability assessments.

The role of wave energy in the rate and spatial distribution of cliff erosion (Research aim 2)

The model results indicate a large variability in the alongshore distribution of significant wave height, used here as a proxy for wave energy. The highest wave energy potential was found consistently in the southern half of the bay and lowest in the northern half where the current erosion rate is greatest. This variability in alongshore distribution of wave energy is due to differences in nearshore characteristics and differences in offshore wave characteristics such as significant wave height, period and direction). With respect to nearshore characteristics, greater variability in near shore topography induces greater shoaling of waves and the

production of relatively higher significant wave height, compared to nearshore bathymetry with relatively lower topographic variability.

No obvious relationship between alongshore wave energy and the spatial distribution of cliff erosion was found. This demonstrates the additional importance of foreshore characteristics on wave energy delivery to the cliff. In this case, cliff toe elevation exerts a strong control and determines how often waves reach the cliff toe. Although simulated wave energy increases from north to south, cliff toe elevation also increases from north to south to elevations well above normal tidal range. As a result, under average conditions, less wave energy is delivered to the cliff toe. The planform of the cliff supports a lower overall rate of erosion in the southern half of the bay. The influence of nearshore characteristics on the alongshore variability of wave energy was observed to decrease with increasing offshore significant wave height.

These findings demonstrate the strong role that offshore wave climate, near and foreshore characteristics play in the alongshore variability of wave energy and delivery of wave energy to the cliff toe for erosion. Previous research on wave energy to the cliff toe has largely ignored alongshore variability of near and foreshore characteristics. Future work examining the alongshore variability in cliff erosion rates will benefit from inclusion of offshore wave climate along with near and foreshore characteristics, to explain variations in wave energy delivery to, and subsequent erosion of, coastal cliffs. Currently in Ireland, a limited number of bays have high resolution bathymetric data available. Increasing the number and spatial distribution of nearshore bathymetric surveys to incorporate varying coastal planforms will provide greater opportunity to assess the variability of wave energy available for erosion. These data can be combined with pressure transducers (for measuring wave dissipation across the foreshore), microseismometers (for measuring wave energy delivery to the cliff toe) and measurements of cliff erosion using coastal lidar (see above) to provide analysis of the combined influence of

offshore wave climate, near and foreshore characteristics on wave energy delivery to the cliff toe, and their relationships to cliff erosion rates.

The efficacy of meso-scale erosion on the platform (Research aim 3)

The results indicate that meso scale abrasion of the platform via the transport of clasts can be an effective geomorphic agent under storm and non-storm conditions, limited only by sediment supply. The process is comparable in volume of material removed to other processes which are considered important geomorphic agents on rocky shorelines, such as bioerosion. Although for the period of study < 1% of the platform was affected by clast abrasion, the abrasion features often occur adjacent or superimposed on older abrasion features which are likely to have been formed in the last 5-10 years, suggesting that the process is an important geomorphic agent of erosion on timescale relevant for rock coast erosion, potentially producing 170 tonnes of sediment in 10^3 years.

Earlier studies of clast transport on shore platforms have been largely concerned with the transport of clasts during Tsunami and storm conditions. However, the experiments described in this thesis demonstrate that large clasts can be transported significant distances in a short period of time (2 tidal cycles) under average wave conditions. The lack of any significant relationship between transport distance and clast size illustrates the role that platform morphology plays in clast transport. Previous research has demonstrated the role that clast size and shape, pre-transport setting and slope play in clast transport dynamics. With respect to clast transport mode, the study described in this thesis highlights the additional importance of platform roughness, whereby higher platform roughness facilitates greater saltation and tumbling of clast as they traverse uneven topography. Platform roughness also influences the type of abrasion feature observed with a higher frequency of impact type abrasion on areas of the platform with higher roughness, and a higher proportion of scratch type abrasion features observed on areas with low platform roughness.

The findings highlight the potential importance of abrasion by clast transport as a geomorphic agent on shore platforms. The data supports previous calls for cross scalar investigation of platform erosion, particularly at meso scale, to help bridge the geomorphology gap between microscale process-based studies and studies of macro scale landform, or long-term landscape, evolution. Structure from Motion Photogrammetry is one such technique which can help to bridge this gap (discussed below). The effect of platform roughness on transport mode and hence abrasion feature type, adds to the increasing evidence of the role of geomorphological controls on clast transport dynamics. This warrants future inclusion of platform roughness in models of clast transport dynamics and has implications for paleo environmental reconstructions.

Methods for measuring erosion on shore platforms and development of cross scalar investigation technique (Research aim 4).

The study demonstrates the potential of SfM Photogrammetry as a means for cross scalar investigation of erosion on shore platforms. Cross scalar measurements of erosion are critical for improved understanding of the relative efficacy of processes which operate and interact over a range of spatial scales. The approach will allow collection of erosion data in difficult environments with relative ease compared to the traditional approach using a TMEM. The SfM Photogrammetry approach described demonstrates a technique which can resolve sub mm scale change on a simulated platform surface. The CRS described in the chapter has been developed for deployment on shore platforms and permits high resolution DEMs for cross scalar geomorphic change detection. This approach allows measurement and identification of erosion features and styles which is not possible using traditional method of measuring erosion on shore platform, the T/MEM. Although the T/MEM is well established as a mean for measuring micro erosion on shore platforms it is limited to point measurements of the surface

of interest with variable rates of erosion between locations interpreted as representing the relative importance of different erosion processes (e.g. sweeping abrasion, sub aerial weathering). Critically the TMEM is restricted to measurements of micro scale erosion and is unlikely to record loss of rock fragments. These measurements must be upscaled to meso scale landforms and macroscale landscape development, the inherent complications of which are well known (the efficacy and importance of meso scale erosion on shore platform have been discussed in chapter 4). Furthermore, the TMEM is largely restricted to quasi planar surfaces resulting in exclusion of many different platform morphologies. Notably however, the extremely high resolution of TMEM measurements, which is two orders of magnitude greater than that currently possible using SfM Photogrammetry, has allowed researchers to identify phenomena such as platform swelling which is unlikely to be captured by SfM Photogrammetry. Additionally, the results of the SfM Photogrammetry experiments indicate that increasing platform surface roughness results in an increasing level of error when using SfM Photogrammetry. However, new methods for assessing DEM accuracy and the spatial distribution of error may assist in addressing this issue. The ability of SfM photogrammetry to capture and measure sub mm scale abrasion, in addition capture larger scale erosion such as loss of rock fragments, represents a significant advantage over the TMEM.

Future work will test the SfM Photogrammetry approach using the CRS described here under field conditions. Further work will also test approaches for measuring the spatial distribution of error on rougher surfaces to increase confidence in the results. With respect to the wider field of geomorphology, the approach represents a much-needed, cost effective approach for measuring cross scalar erosion on rock surfaces.

Concluding remarks

Previous studies of rock coast erosion have tended to focus on either the cliff or the platform This study demonstrates an important link between cliff erosion and erosion of the platform.

whereby material supplied by the cliff abrades the platform. Furthermore, the spatial distribution of cliff erosion, and hence the supply of clasts their spatial distribution and characteristics on the platform, are strongly influenced by discontinuity set characteristics (Chapter 2), demonstrating another important link between the cliff and the platform. In turn, platform width, roughness and elevation relative to the tidal frame control the delivery of wave energy to the cliff toe.

The findings highlight the need to study coastal cliffs and their contiguous platforms as a single landform, which itself is strongly connected to and influenced by the characteristics of the nearshore environment.